A Thermodynamic Approach to Constitutive Modelling of Concrete using Damage Mechanics and Plasticity Theory

by

Giang Dinh Nguyen

Trinity College

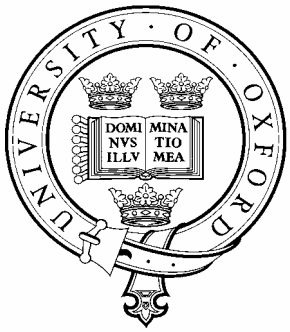

A Thesis submitted for the degree of
Doctor of Philosophy
at the University of Oxford

Trinity Term 2005

Abstract

A Thermodynamic Approach to Constitutive Modelling of Concrete using Damage Mechanics and Plasticity Theory

A Thesis submitted for the degree of Doctor of Philosophy

Giang Dinh Nguyen
Trinity College, University of Oxford
Trinity Term, 2005

Recent advances in computational mechanics have opened the potential of carrying out the analysis and design of concrete structures in a realistic manner with the use of nonlinear concrete models. This encourages the development of more capable and realistic constitutive models, based on a rigorous approach, for the analysis and design of concrete structures. This research focuses on the development of a thermodynamic approach to constitutive modelling of concrete, with emphasis on the rigour and consistency both in the formulation of constitutive models, and in the identification of model parameters based on experimental tests.

The key feature of the thermodynamic framework used in this study is that all behaviour of the defined model can be derived from two specified energy potentials. In addition, the derivation of a constitutive model within this framework merely follows procedures established beforehand. The proposed constitutive model here is based on continuum damage mechanics, in combination with plasticity theory, hence enabling the macroscopic material behaviour observed in experiments to be appropriately modelled.

Damage-induced softening is the cause of many problems in numerical failure simulations based on conventional continuum mechanics. The resolution of these problems requires an appropriate special treatment for the constitutive modelling which, in this study, is based on nonlocal theory, and realized through the nonlocality of energy terms in the damage loading functions. For practical applications in structural analysis, the model requires a minimum number of parameters, which can be identified from experimental tests. All the above features of the model have been incorporated in a unified and consistent thermodynamic approach, which also distinguish the approach from existing ones.

Numerical implementation and application are important parts of the study. A suitable implicit scheme is adapted here for the integration of the nonlocal rate constitutive equations. For the solution of systems of nonlinear algebraic equations in finite element analysis, the arc-length method in combination with local constraint equations employing dominant displacements is implemented, and proves its reliability in this study. Application of the proposed constitutive models in the analysis and design of concrete structures is straightforward, with several numerical examples showing the practical aspects of the proposed modelling.

Acknowledgements

My gratitude goes to Professor Guy Houlsby for the opportunity to work in the Civil Engineering Group at Oxford University, and for his supervision, and guidance during my study at Oxford. I am also very grateful to my College advisor, Dr Alexander Korsunsky, for his advice and support during my study and my job application.

My special thanks also go to Dr Harvey Burd and Professor Guy Houlsby for allowing me to use the OXFEM finite element code, and for their help in using and developing the code; to Drs Quoc-Viet Bui (University of Liege, Belgium), Angelo Amorosi (Politecnico di Bari, Italy), Athanasios Makrodimopoulos (Civil Engineering Group) and Mr Bac Van Nguyen (University of Birmingham) for many stimulating discussions; to Dr Byron Byrne for letting me use his powerful computer for the finite element analysis; to Dr Brendan Ruck, a former member of the Civil Engineering Group, for the careful proof reading of chapters 2 and 3; to Alison Payne and Karen James for the administrative and computing support; to Ms Anne Greig, the librarian of Engineering Science library, for always being willing to deal with my requests for additional research materials. I am also grateful to useful comments from the examiners (Drs Harvey Burd, Oxford University, and Anthony Jefferson, Cardiff University).

The financial support (the Peter Jenks Vietnam scholarship) from the Jenks family in the United States, is gratefully acknowledged. I also would like to thank Trinity College for providing me with computing facilities, accommodation and financial support during my time at Oxford.

To many members of the Civil Engineering Group, who have made my time at Oxford unforgettable. In particular, I would like to thank Miguel Pena and Kaori Kuribayashi for being my long-hour working office mates and for always being willing to help; Nick Melin and Lam Nguyen-Sy for many discussions and arguments about political issues; John Pickhaver and Suched Likitlersuang for sharing their ideas in using and developing the OXFEM code; Jackie Sim for the proof reading of chapter 2 and for introducing me to some extracurricular activities in Oxford. Special thanks also to John Pickhaver for always being willing to correct my English.

To all my Vietnamese friends at Oxford, my College friends, Mr and Mrs Mowat and other friends in Commonwealth house, Oxford, for their direct or indirect helps.

I am also grateful to Dr Cong-Luan Ngo-Tran for introducing me to Oxford University Civil Engineering Group. Encouragement from Professor Luong-Dung Nguyen (HCMC University of Technology, Vietnam), and Dr Quang Nguyen, my math teacher at the HCMC University of Architecture (Vietnam), is also acknowledged.

Finally my special thanks go to my wife, Nga, for her love, understanding, and endurance during my years away from home and especially during the last months of my study at Oxford. We both are very grateful to our parents for their love and encouragement during the course of my DPhil study.

Contents

List of symbols

(only the most frequently used symbols are listed)

a_{ijkl}, **a**	elastic moduli tensor
c	constant in the expression of the equivalent plastic strain rate $\dot{\varepsilon}_p$
C_i	constraint in the dissipation function d
C^t_{ijkl}	tangent moduli tensor
d	dissipation function (rate of dissipation)
d_d	part of the dissipation function d, associated with damage
d_p	part of the dissipation function d, associated with plasticity
$d_{\max}$	maximum aggregate size
D_c	slope at peak stress in the cohesive crack model (bilinear softening)
D_{ijkl}	elastic compliance moduli tensor
D^{st}_{ijkl}	compliance moduli tensor which is tangent with respect to plasticity and secant with respect to damage
D^{sc}_{ijkl}	secant compliance moduli tensor
E	elasticity modulus
E_c	tangent modulus at peak stress of the stress-strain curve (uniaxial tension, bilinear softening), corresponding to the slope D_c in cohesive crack model
E_{c0}	initial softening modulus of the uniaxial compressive stress-strain curve
E_{ep}	elasto-plastic tangent stiffness in uniaxial compression (in pre-peak hardening regime)
E_{pc}	parameter in the tensile damage loading function y^c_d
E_{pt}	parameter in the tensile damage loading function y^t_d
E_t	tangent modulus of the uniaxial tensile stress-strain curve
E_{t0}	initial softening modulus of the uniaxial tensile stress-strain curve
E_{cu}	unloading modulus at a point on the uniaxial compressive stress-strain curve, corresponding to ε_{cu} and α^c_{du}
E_{tu}	unloading modulus at a point on the uniaxial tensile stress-strain curve, corresponding to ε_{tu} and α^t_{du}
f	Helmholtz specific free energy
f_{c0}	yield stress in uniaxial compression
f_{cy}	evolving yield stress in uniaxial compression
f_{ty}	evolving yield stress in uniaxial tension

f_c'	ultimate tensile stress in uniaxial compression
f_t'	ultimate tensile stress in uniaxial tension
F_1	function governing the damage process in isotropic damage model (only in Chapter 3)
F_1^c	function governing the compressive damage process
F_1^t	function governing the tensile damage process
F_3	function used to smooth out the transition between compression and tension
F_4^c	function used in the decomposition of the equivalent plastic strain ε_p
F_4^t	function used in the decomposition of the equivalent plastic strain ε_p
$\mathbf{F}_i$	out of balance force at the end of the i^{th} iteration
g	Gibbs free energy
g_F	total specific (or volumetric, or local) fracture energy in tension
g_f	initial specific fracture energy in tension, used for bilinear softening law
g_{fnl}	initial specific fracture energy in tension, used for nonlinear softening law
g_p	elastic energy density at peak stress
g_c	specific fracture energy in compression
G_c	fracture energy in compression
G_f	initial fracture energy in tension, associated with cohesive crack model
G_F	total fracture energy in tension, associated with cohesive crack model
G_{Fa}	apparent fracture energy in tension
h	enthalpy
H	hardening modulus, for model with a single hardening mechanism
$H(x)$	Heaviside function
H_c	hardening modulus, for compressive hardening
H_t	hardening modulus, for tensile hardening
I_1	first invariant of the stress tensor σ_{ij}
J_2	second invariant of the deviatoric stress tensor σ'_{ij}
J_3	third invariant of the deviatoric stress tensor σ'_{ij}
k	parameter of the parabolic Drucker-Prager yield criterion
k, k_t	ratio between the crack bandwidth w_t and nonlocal radius R
k_c	ratio between the crack bandwidth w_c and nonlocal radius R
$\mathbf{K}_i$	global tangent stiffness matrix at the i^{th} iteration
l_c	compressive internal (or characteristic) length of nonlocal continuum
l_t	tensile internal (or characteristic) length of nonlocal continuum
m_c	parameter in the compressive damage function y_d^c

n_c parameter in the compressive damage function y_d^c

n_t parameter in the tensile damage function y_d^t

p_c parameter in the compressive damage function y_d^c, controlling the shape of the compressive damage loading surface

p_t parameter in the tensile damage function y_d^t, controlling the shape of the tensile damage loading surface

P nonlocality residual

$\mathbf{P}$ load vector

q_k heat flux

$\dot{Q}$ heat supply to a volume element

r factor controlling the deviation of the plastic strain rate vector $\dot{\alpha}_{ij}$ from the normal vector to the yield surface

R nonlocal interaction radius

$\mathbf{R}_i$ internal force vector at the i^{th} iteration

s entropy

t parameter relating g_{fnl} and g_F ($t = g_{fnl} / g_F$)

u internal energy function

u_c critical crack opening in cohesive crack model, corresponding to ε_{cc} and w_c in compression

u_t critical crack opening in cohesive crack model, corresponding to ε_{tc} and w_t in tension

$\mathbf{U}_i$ updated displacement vector at the i^{th} iteration

$\mathbf{U}_i^P$ displacement vector at the i^{th} iteration, resulted from the fixed load vector $\mathbf{P}$ and the tangent stiffness matrix $\mathbf{K}_i$

w_c width of an imaginary and uniformly damaged crack band in compression, corresponding to u_t and ε_{tc}

w_t width of an imaginary and uniformly damaged crack band in tension, corresponding to u_c and ε_{cc}

$\dot{W}$ rate of mechanical work input

y_d damage surface in isotropic damage model (only in Chapter 3)

y_p yield surface in dissipative generalized stress space χ_{ij}

y_p^* yield surface in true stress space σ_{ij}

y_d^c damage loading surface, for compressive behaviour

y_d^t damage loading surface, for tensile behaviour

α_{ij}, $\boldsymbol{\varepsilon}^p$ plastic strain tensor

α'_{ij}	deviatoric part of the plastic strain tensor α_{ij}
α_{kk}	volumetric part of the plastic strain tensor α_{ij}
α_p	uniaxial plastic strain
α_d , D	scalar damage variable, in isotropic damage model (only in Chapters 2 and 3)
α_d^t , D_t	scalar damage variable for tensile damage mechanism
α_d^c , D_c	scalar damage variable for compressive damage mechanism
α_{du}^c	compressive damage measure at a point on the uniaxial tensile stress-strain curve, corresponding to E_{cu} and ε_{cu}
α_{du}^t	tensile damage measure at a point on the uniaxial compressive stress-strain curve, corresponding to E_{tu} and ε_{tu}
β	parameter of the parabolic Drucker-Prager yield criterion
δ_{ij}	Kronecker delta
$\delta\mathbf{U}_i$	iterative displacement vector at the i^{th} iteration
$\delta\mathbf{U}_i^F$	iterative displacement vector at the i^{th} iteration, resulted from the tangent stiffness matrix $\mathbf{K}_{\text{i}}$ and the out of balance force $\mathbf{F}_{i\text{-}1}$ at the end of the $(i\text{-}1)^{\text{th}}$ iteration
$\Delta\mathbf{U}_i$	incremental displacement vector at the i^{th} iteration
$\Delta\lambda_i$	incremental load factor at the i^{th} iteration
ε_{ij} , $\boldsymbol{\varepsilon}$	total strain tensor
$\bar{\varepsilon}_{ij}$, $\bar{\boldsymbol{\varepsilon}}$	effective strain tensor
ε_{ij}^e , $\boldsymbol{\varepsilon}^e$	elastic strain tensor
ε_p	equivalent plastic strain, for model with a single hardening mechanism
ε_p^t	equivalent plastic strain, for tensile hardening
ε_p^c	equivalent plastic strain, for compressive hardening
ε_{tc}	uniaxial tensile strain at rupture, corresponding to u_t and w_t
ε_{cc}	uniaxial compressive strain at rupture, corresponding to u_c and w_c
ε_{c0}	strain at compressive peak stress f'_c
ε_{cu}	strain at a point on the uniaxial compressive stress-strain curve, corresponding to E_{cu} and α_{du}^c
ε_{tu}	strain at a point on the uniaxial tensile stress-strain curve, corresponding to E_{tu} and α_{du}^t
θ	temperature; Lode angle
λ_i	load factor at the i^{th} iteration
λ_p	plasticity multiplier

λ_d	scalar multiplier in the damage loading function
Λ_i	Lagrangean multiplier associated with the constraint C_i in the dissipation function d
κ	hardening parameter
ν	Poisson's ratio
ξ	coordinate of the Haigh-Westergard space ($\xi = I_1/\sqrt{3}$)
ρ	mass density; coordinate of the Haigh-Westergard space ($\rho = \sqrt{2J_2}$)
ρ_t	tensile meridian, corresponding to Lode angle $\theta = 0^{\mathrm{o}}$
ρ_c	compressive meridian, corresponding to Lode angle $\theta = 60^{\mathrm{o}}$
ρ_s	shear meridian, corresponding to Lode angle $\theta = 30^{\mathrm{o}}$
σ_1	first principal stress
σ_2	second principal stress
σ_3	third principal stress
σ_m , p	mean stress, $\sigma_m = p = I_1/3$
σ_{ij} , $\boldsymbol{\sigma}$	total stress tensor
$\overline{\sigma}_{ij}$, $\overline{\boldsymbol{\sigma}}$	effective stress tensor
σ'_{ij} , $\boldsymbol{\sigma}'$	deviatoric stress tensor
σ^+_{ij} , $\boldsymbol{\sigma}^+$	positive part of the stress tensor σ_{ij}
σ^-_{ij} , $\boldsymbol{\sigma}^-$	negative part of the stress tensor σ_{ij}
φ	plastic potential
$\overline{\chi}_d$	generalized stress conjugate to the damage variable α_d
$\overline{\chi}_{ij}$	generalized stress conjugate to the plastic strain tensor α_{ij}
$\overline{\chi}^t_d$	generalized stress conjugate to the damage variable α^t_d
$\overline{\chi}^c_d$	generalized stress conjugate to the damage variable α^c_d
χ_d	dissipative generalized stress conjugate to the damage variable α_d
χ_{ij}	dissipative generalized stress conjugate to the plastic strain tensor α_{ij}
χ^t_d	dissipative generalized stress conjugate to the damage variable α^t_d
χ^c_d	dissipative generalized stress conjugate to the damage variable α^c_d

Chapter 1: Introduction

1.1 Aims and scope of the study

Constitutive modelling of concrete materials has been a theme of research for some decades. Nevertheless, the complex behaviour of concrete, due to its composite nature, cannot always be faithfully reflected in any models dedicated to the constitutive modelling of the material. This study centres on the development of a thermodynamic approach to constitutive modelling of concrete, with emphasis on the rigour and consistency both in the formulation of constitutive models, and in the identification of model parameters based on experimental tests. Only isotropic damage is considered in this study. The constitutive model formulated within this approach can, to some extent, capture the main macroscopic features in the behaviour of the material, while still maintaining its applicability through the use of few model parameters, each identifiable from standard tests. This model is of macroscopic nature, with the underlying micromechanical processes being characterized by a few representative macroscopic quantities. Therefore, it can only capture the macroscopically observed behaviour of concrete materials in an approximate manner. In addition, as the nonlinearity in the material behaviour normally takes place under very small strain, continuum mechanics with the small strain assumption is used throughout the study.

Thermodynamics plays an important role in the formulation and development of constitutive models. To avoid thermodynamically unrealistic results, the first and second laws of thermodynamics should be the basis for any approach to constitutive modelling. Although the requirements for the thermodynamic admissibility of a constitutive model can be applied retrospectively, it is more rigorous and consistent to build a constitutive model within a well-established thermomechanical framework. This way of developing constitutive models helps avoid introducing any further *ad hoc* assumptions during the model formulation. Therefore it is pursued in this study, with an existing thermomechanical framework (Houlsby and Puzrin, 2000) being extensively used as a basis for the construction of constitutive models. The formulation and development of a model within this framework then follows procedures established

beforehand, reducing the possibilities of introducing more assumptions during the model formulation. However, thermodynamics in this case only provides a general framework, as well as restrictions on the development of constitutive models. Details of the models must be based on experiments and/or the micromechanical analysis of the behaviour and interaction of all the material constituents.

Continuum damage mechanics has been used extensively for the constitutive modelling of concrete. Prior to the establishment of damage theories with a thermodynamic and micromechanics basis in the 1970s, the nonlinear response of concrete could only be captured using plasticity theory, nonlinear elasticity theory or, more recently, fracturing theory (Dougill, 1976). Although on their own those theories can yield adequate results, which match those of experiments in some cases (e.g. in monotonic loading), a combination of them would be a better choice in the constitutive modelling of concrete. A coupled damage-plasticity approach is therefore adopted in this study. In the combined approach, the strain softening and stiffness degradation can be modelled by damage mechanics, while the residual strains and some other macroscopic features are seen to be related to and captured by plasticity theory. In relation to the micromechanical processes, the representative macroscopic variables characterizing the material behaviour at microscopic level are the damage indicators and plastic strains. In thermodynamic terminology, those quantities are considered as internal variables of the dissipation processes taking place in the material. However, the combination of damage and plasticity theories should only be regarded here as one of the possible ways of constitutive modelling. It has the advantage of using well established theories, but still needs more experimental evidence for the identification of model parameters as well as validation of numerical simulation results.

Softening-related problems should always be considered in constitutive modelling of quasi-brittle materials based on continuum mechanics. These problems are direct consequences of the failure of conventional continuum mechanics in capturing the material behaviour at a scale below a certain level. From the mathematical point of view, softening leads to the loss of ellipticity of the governing partial differential equations in static analysis and results in ill-posed boundary problems. The solution of the boundary value problem therefore loses its uniqueness, with several pathological features [e.g. infinitely small softening zone and mesh-dependent solutions in finite

element analysis (Jirasek and Bazant, 2002)]. In the numerical simulation, localization of deformation takes place in the smallest softening zone that can be captured by the numerical disretization. In structural analysis, this zone is termed the fracture process zone for cohesive materials such as rocks and concrete or the shear band for frictional materials like soils. As a consequence of this localization, the numerical solution becomes mesh-dependent and the energy dissipation in the softening zone may approach zero upon mesh refinement. Use of classical continuum mechanics in this case has been proved to be inadequate (Peerlings, 1999; Comi, 2001; Jirasek and Bazant, 2002). Therefore, special treatments, termed regularization techniques, are required for the resolution of the problem. In general, the aim of these techniques is to prevent the localization of deformation into a zero volume zone and therefore remedy the pathological problems (e.g. mesh-dependent numerical solutions, infinitely small softening zone) encountered in the analysis using conventional continuum mechanics.

Various forms of regularization techniques have been proposed, encompassing both the simple and more mathematically complicated types of regularization. The term simple here refers to techniques such as fracture energy regularizations (e.g. use of smeared crack or crack band models) applied at structural level, which can help remove the mesh dependence of the numerical solutions but preserves the ill-posedness of the boundary problem. In other words, loss of ellipticity of the governing partial differential equations in this case still accompanies softening. In contrast with this is the fully mathematical regularization (e.g. nonlocal and gradient approaches, rate-dependent regularization), which aims at preserving the ellipticity of the governing partial differential equations throughout the analysis and hence automatically removes all softening-related problems in the numerical simulation. The nonlocal treatment is used in this study. With the introduction of spatial terms in the nonlocal constitutive relations, the ellipticity of the governing partial differential equations (in rate-independent material models) is kept unchanged throughout the analysis. This helps to avoid the pathological aspects encountered with the use of classical continuum mechanics.

The constitutive models in this study are constructed within a well-established thermodynamic framework, and can accommodate both damage and plastic dissipation mechanisms. Many of the important macroscopic behavioural features of concrete,

which will be briefly presented in the next chapter, can be captured and characterized by the proposed constitutive models. It should be mentioned here that for the continuum mechanics approach adopted in this study, the material behaviour to be modelled should be interpreted as the averaged response over a certain volume element, governed by several underlying microstructural phenomena. To deal with softening-related problems, a nonlocal regularization technique is employed and realized through the nonlocality of energy terms in the tensile and compressive damage loading functions. This nonlocal feature of the constitutive modelling can be readily incorporated in the thermodynamic approach used in this study, although the physical interpretation is not very clear. Therefore, it can be considered as a pure mathematical method used to remedy the problems of continuum mechanics in dealing with softening.

Numerical aspects are also important in the constitutive modelling, with the proposal of an appropriate integration scheme for the constitutive relations and the employment of relevant numerical algorithms for the nonlinear finite element analysis. However, the aim of this research is not to carry out exact numerical simulations of structural problems, but to propose and develop a consistent and rigorous approach with promising potential of application in the constitutive modelling of concrete materials. Further investigation and research are still required to work out the proposed modelling.

1.2 Outline of the thesis

The starting point of this study is a brief review on the behaviour of concrete and the constitutive modelling of that material, all of which are presented in Chapter 2. Emphasis here is placed on capturing faithfully important features of the material behaviour in the constitutive modelling, and the identification of model parameters based on standard experiments. This results in the advocacy of combined approaches employing both damage mechanics and plasticity theory, with a tight connection between the model parameters and the experimentally-measured material properties.

Chapter 3 of this thesis addresses the thermodynamic aspects of the constitutive modelling and presents a general formulation for constitutive models based on an established thermodynamic framework. Constitutive models with both damage and plastic dissipation mechanisms are constructed and discussed. It is also shown in this

Chapter that both stress- and strain-based damage-plasticity formulations can readily be accommodated in the existing framework.

Chapter 4 of the thesis is concerned with the combined damage-plasticity approach for two-dimensional applications. To capture the different responses in tension and compression, the approach makes use of the separation of tensile and compressive behaviour, achieved through the decomposition of stress tensor and integrated in the thermomechanical framework. The dissipation process therefore consists of three separate dissipation mechanisms: tensile and compressive damage coupled with plasticity. Schematic presentation of the failure surfaces in biaxial loading shows the combined behaviour of the proposed constitutive model. The identification of model parameters from simplest (pure tensile damage) to most complicated cases (tensile and compressive damage coupled with plasticity) is also carried out. Some numerical examples are used at the end of the Chapter to show the capability of the proposed model.

In Chapter 5, we focus on softening-related problems and regularization techniques employed for the treatment of the above-mentioned pathological problems encountered in classical continuum mechanics when dealing with softening materials. Various types of regularization, with the key feature of introducing additional material characteristics, are briefly reviewed and advantages and disadvantages of those techniques in practical applications are pointed out. The nonlocal regularization method for strain softening material models is introduced to the constitutive modelling in this Chapter. The thermomechanical aspects of nonlocality are briefly presented, followed by the incorporation of nonlocality into the thermodynamic framework used in this study. Various ways of integrating nonlocality into the modelling are presented and discussed. The connection between parameters of the nonlocal model and experimentally-provided material properties is established at the end of this Chapter. This connection furnishes a consistent way of identifying parameters for nonlocal models, which is not carefully considered in many nonlocal damage models proposed by several researchers.

Numerical implementation plays an important role in the model development and is discussed in Chapter 6. An implicit integration scheme (Crisfield, 1997) for the rate constitutive equations is adopted, and modified in this Chapter for the nonlocal rate

constitutive equations. Because of the material nonlinearity, the system of algebraic equations in finite element analysis is nonlinear and its solution requires a reliable numerical algorithm. The arc-length incremental control with local constraint equations (May and Duan, 1997), in combination with Newton-Raphson iteration techniques, is adopted for the nonlinear finite element analysis. This helps to overcome limit points and snap back behaviour possibly encountered in the equilibrium paths.

In the last two Chapters, various structural problems showing the behaviour of the material from simple to combined loading cases are numerically simulated to show the performance of the developed models. Conclusions are withdrawn and further studies are proposed.

Chapter 2: Constitutive Modelling of Concrete, A Brief Review

2.1 Introduction

The complex behaviour of concrete, which comes from the composite nature of the material, necessitates the development of appropriate constitutive models. Although recently there have been a large number of noteworthy contributions, with different levels of complexity and applicability, the complete features of the material behaviour have not always been acknowledged and reflected in the modelling. Further development in the constitutive modelling of concrete materials is therefore needed, with the motivation of incorporating important experimentally-observed features of the material behaviour in the macroscopic constitutive modelling.

A brief review on the material behaviour and then an overview on the constitutive modelling of concrete along with a critical discussion are presented in this chapter. For the constitutive modelling, the focus here is mainly on continuum theories such as plasticity theory, continuum damage mechanics and damage coupled with plasticity. For the sake of simplicity, only the constitutive aspects are considered in this chapter. Softening and its related problems in the constitutive modelling and numerical simulation are included in the discussion in chapter 5. The main features, and advantages as well as shortcomings of constitutive models will be examined in this chapter to provide a general background and motivation for this study. Further details on the models and their applicability to concrete modelling can be found in the references.

2.2 Mechanical behaviour of concrete

Some important mechanical features of concrete are summarized in this section, mainly based on research available in the literature (Chen, 1982; Chen and Han, 1988). This furnishes a background for the review and further study on the constitutive modelling of concrete in the following sections. The macroscopic features of the material behaviour will only be briefly presented, with references to sources where

detailed information can be obtained. The structure of concrete such as the ratio of water to cement, the shape and size of aggregate, the kind of cement used, and other factors all have effects on the mechanical behaviour of the material. However, these are not mentioned here and the material is considered as a continuum with initial isotropic behaviour.

2.2.1 Uniaxial behaviour

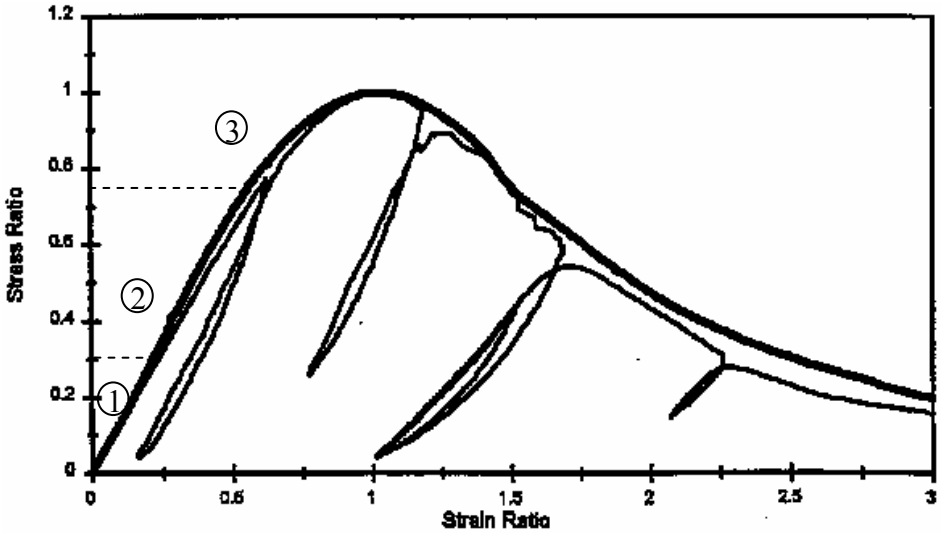

Figure 2.1: Behaviour of concrete under monotonic and cyclic compressive loading (after Bahn and Hsu, 1998)

The mechanical behaviour of concrete is highly nonlinear in both tension and compression. In uniaxial compression, three different deformational stages (figure 2.1) can be observed (Kotsovos and Newman, 1977; Chen and Han 1988). For axial stresses up to about 30% of the maximum compressive stress f_c' the uniaxial compressive behaviour of concrete can be considered linear, with existing micro-cracks in the material remaining nearly unchanged. The second stage is between $0.3f_c'$ and $0.75f_c'$, in which cracks develop due to the breakage of bonds (among constituents), and cracks at nearby aggregate surfaces start to bridge. However, the crack propagation is still stable until the stress reaches about $0.75f_c'$, which is generally termed the onset of unstable fracture propagation. Beyond this stress level is the third stage of deformation in which the mortar cracks join bond cracks at the surface of nearby aggregates and

form a fracture zone. Further deformation may be localized, followed by major cracks parallel to the direction of applied load, resulting in failure of the specimen.

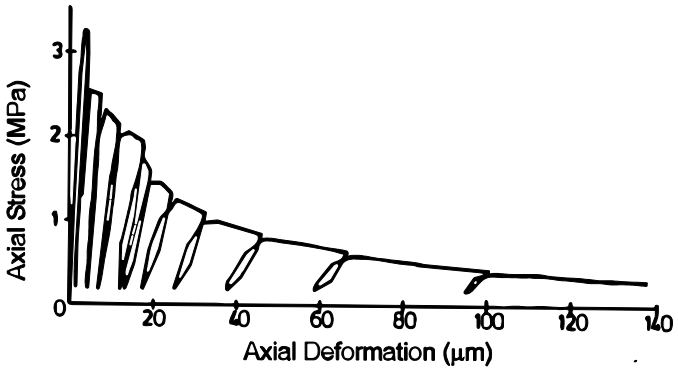

Figure 2.2: Stress-deformation curve of concrete subjected to uniaxial cyclic tensile loading (Reinhardt *et al.*, 1986)

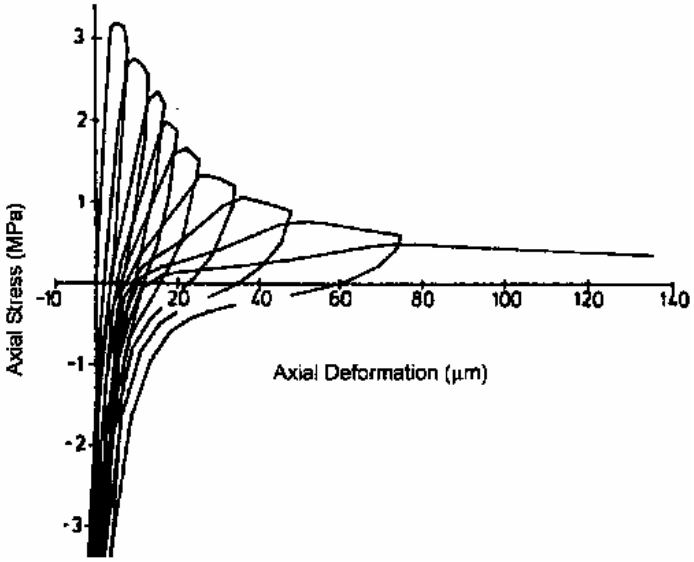

Figure 2.3: Stress-deformation curve of concrete subjected to reversed cyclic tensile loading (Reinhardt *et al.*, 1986)

However, in uniaxial tension, the experimentally observed deformation process is different from that in compression. The low tensile strength of concrete is primarily due to the low tensile strength of the aggregate-mortar interface, which has a significantly lower strength than the mortar. This interface is known to be the weakest link in this composite material, with cracks usually occurring at the interface. Since the existing microcracks remain nearly unchanged under a stress less than 60% to 80% of the ultimate tensile strength f_t', this stress level can be regarded as the limit of elasticity in tension. However, the stress-deformation curve of the material in tension is almost

linear until the peak stress is reached (figures 2.2 and 2.3). Hence, the uniaxial tensile strength of the material is usually adopted as the elastic limit in constitutive modelling.

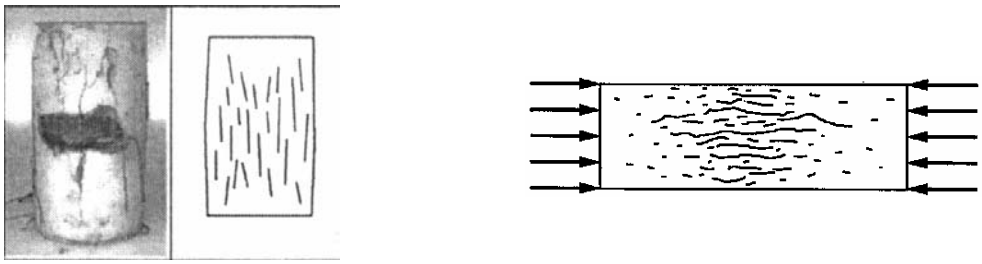

(a) Sfer *et al.* (2002) (b) Jansen and Shah (1997)

Figure 2.4: Failure of concrete in uniaxial compression
with cracks parallel to the loads applied

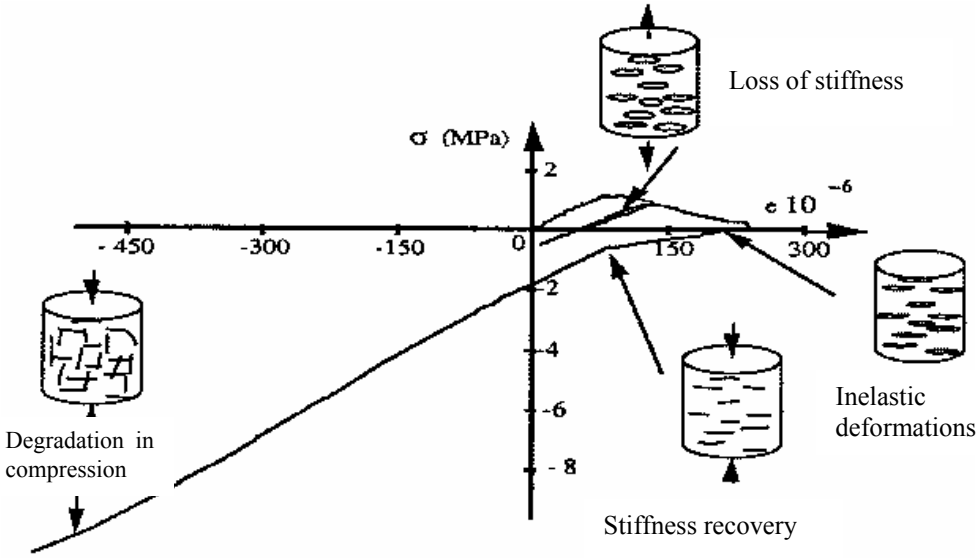

Figure 2.5: Uniaxial behaviour of concrete under cyclic loading
(Ramtani, 1990; as presented by Nechnech, 2000)

Unlike in a compressive test, where splitting cracks are parallel to the direction of the compressive stress (figure 2.4) or in the form of a zig-zag band depending on the specimen height (figure 2.6a), the direction of crack propagation in a tensile test is transverse to the stress direction (figure 2.5). This leads to a reduction of the load-carrying area followed by an increase in the stress concentration at critical crack tips. In addition, unstable crack propagation in tension starts very soon, resulting in the brittle nature of concrete in tension (figures 2.2 and 2.3).

Also experimentally observed in concrete under loading is the permanent deformation, both in tension and compression (figures 2.1, 2.2 and 2.3). At the macroscopic level, that permanent deformation can be considered as a result of "yielding" taking place in the material under continuous loading. Although similarity with metal plasticity is observed at the macroscopic level through the residual strains, the actual dissipation mechanisms in the two materials are completely different. In metallic materials, plastic deformation is the result of slips due to dislocations occurring at the microscopic level. However, dissipations due to friction in pulling out of aggregates and fragments, interfacial slips between mortar and aggregate when macro cracks are formed and crushing of the mortar can be regarded as main causes of irreversible strains in concrete.

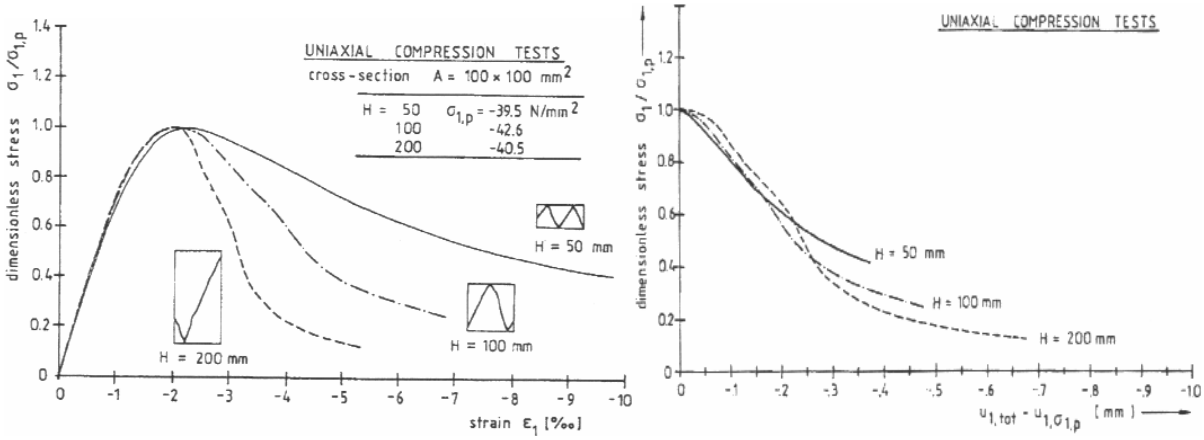

Figure 2.6: (a) Influence of specimen height on the uniaxial stress-strain curve in compression; (b) corresponding stress-displacement diagrams (Van Mier, 1986)

Like other geomaterials such as soils and rocks, concrete also exhibits a significant strain-softening behaviour beyond the peak stress, in both tension and compression (see figures 2.1 and 2.2). The localization of deformations is a direct consequence of this softening behaviour of the material, making the determination of the material stress-strain curve impossible. In fact, there is no unique stress-strain relationship (Gopalaratnam and Shah, 1985) and the softening branch of a stress-strain curve is generally considered as a mixed material-structural property (Chen and Han, 1988). This is illustrated in the experiments by Van Mier (1986) with different average strains obtained from compressive tests on specimens with different heights. In all three tests (figure 2.6a), the post-peak strains are localized in small regions of the specimens, while the average strain for each specimen is calculated by dividing the corresponding post-

peak deformation (or the localized deformation, in the form of the difference between the total deformation $u_{1,tot}$ and the deformation at peak $u_{1,\sigma 1p}$), which have the same value in this case (figure 2.6b), by the specimen height.

The stiffness degradation in concrete, both in tension and compression (figures 2.1 and 2.2), is mainly due to the material damage, especially in the post-peak range (Chen and Han, 1988). The fact that concrete is a composite material made of aggregates and cement paste makes its mechanical behaviour complex. The microcracks caused by shrinkage, thermal expansion and other factors are initially invisible but will progress to become visible cracks with the application of external loads. From the thermomechanical point of view, the input energy is dissipated during the failure process through microcracks formed due to the loss of cohesion between the mortar and the aggregate, frictional slip at interface between the aggregate and the mortar, or crushing of the mortar.

As mentioned above the mechanical behaviour of concrete is significantly different in tension and compression, with the ultimate compressive stress being about 10 to 20 times as big as that in uniaxial tension (Chen, 1982; see also figure 2.5). However, the intact elasticity modulus in both loading cases was experimentally shown to be comparable, with that in uniaxial tension being somewhat higher (Chen, 1982). Nevertheless, failure under compression, e.g. crushing and microcracks through the mortar, is believed to have profound effects on the tensile behaviour of the material, through the compression-induced stiffness degradation in tension. In other words, the elasticity modulus changes during load reversal from compression to tension, of course after a certain failure degree in compression. However, this stiffness reduction does not happen in tension-compression load reversal. Physically, microcracks, which open under tension loading, will close upon load reversal, resulting in the stiffness recovery in compression (figures 2.3 and 2.5).

2.2.2 Multiaxial behaviour

The above experimental observations on uniaxial tensile and compressive behaviour of the material are also applicable in general multi-axial stress states (Chen and Han, 1988). The strength envelope of the material and the evolution of the envelope are used to characterize the material behaviour in those stress states. However, two

separate kinds of envelopes should be distinguished: the elastic-limit surface defining the elastic region, and the failure surface characterizing the maximum-strength envelope of the material (figure 2.7).

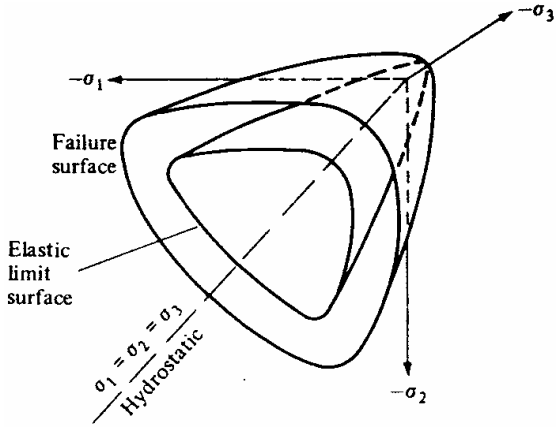

Figure 2.7: Failure surface and elastic-limit surface in principal stress space (Chen, 1982)

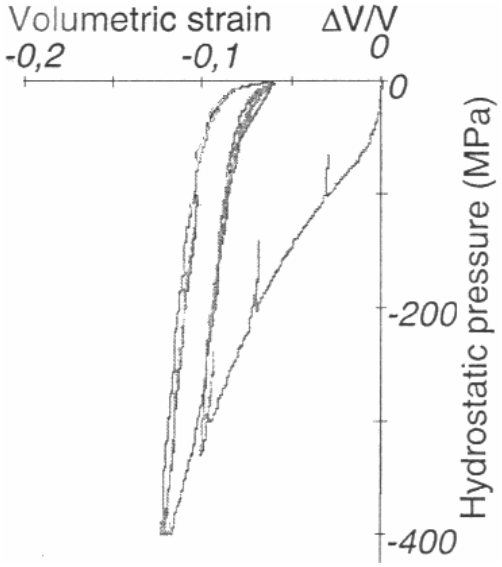

Figure 2.8: Behaviour of concrete under hydrostatic compression (after Burlion *et al.*, 2000)

For the assumption of isotropic behaviour (Chen and Han, 1988), the equations for both surfaces can be expressed in terms of the stress invariants I_1, J_2 and J_3, and/or in terms of the three principal stresses σ_1, σ_2 and σ_3. The Haigh-Westergaard space is used to define the failure surface in principal stress space, in which the position of a stress point is determined by three coordinates ξ, ρ and θ:

$$\xi = \frac{I_1}{\sqrt{3}} \text{; where } I_1 = \delta_{ij}\sigma_{ij} = \sigma_{11} + \sigma_{22} + \sigma_{33} \tag{2.1}$$

$$\rho = \sqrt{2J_2} \text{; where } J_2 = \frac{1}{2}\sigma'_{ij}\sigma'_{ij}, \text{ and } \sigma'_{ij} = \sigma_{ij} - \frac{1}{3}\delta_{ij}\sigma_{kk} \tag{2.2}$$

$$\cos 3\theta = \frac{3\sqrt{3}}{2}\frac{J_3}{J_2^{3/2}} \text{; where } J_3 = \frac{1}{3}\sigma'_{ij}\sigma'_{jk}\sigma'_{ki} \tag{2.3}$$

For reference, a comprehensive presentation of tensors and their invariants and the Haigh-Westergaard stress space can be found in Chen and Han (1988). Although the casting direction obviously has effects on the initial anisotropy of the material (Van Mier, 1986), it is not discussed here. The above assumption on the initial isotropy of the

material behaviour has been accepted and confirmed in several experiments (figure 2.10), indicating that concrete has a fairly consistent failure surface in three-dimensional principal stress space (Chen, 1982).

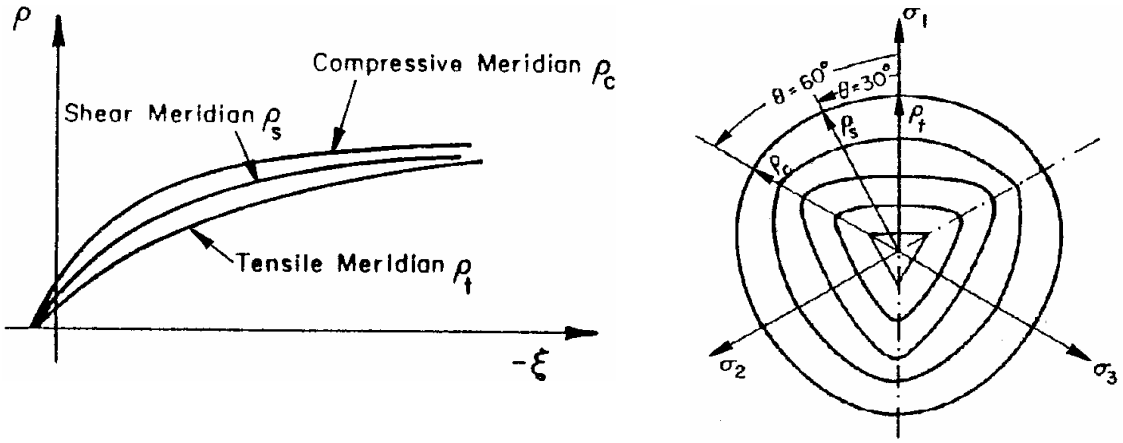

(a). Meridian sections (b). Deviatoric sections

Figure 2.9: Failure surface in the meridian and deviatoric planes (Chen and Han, 1988)

From experimental studies (see figure 2.10), it can be seen that the failure surface is of open shape, while the elastic-limit surface (or the initial yield surface) is believed to exhibit "cap behaviour" (figure 2.12), confirmed through the nonlinear behaviour of concrete under hydrostatic compression (figure 2.8). Under pure hydrostatic compression, the elastic-limit surface expands and gradually opens towards the negative hydrostatic axis (figure 2.12; see also figure 2.17b) and finally coincides with the failure surface. This is illustrated in figure (2.8) where there is no strength reduction observed on the mean stress–volumetric strain curve of concrete material under very high hydrostatic pressure (about 10 times the normal uniaxial compressive strength).

The shapes of the failure surface in the meridian and deviatoric planes are shown in figure (2.9). As can be seen in the figure, the deviatoric sections of the failure surface are different in both shape and size, depending on the value of the hydrostatic pressure. The meridian $\rho_f = \rho_f(\sigma_m, \theta)$, where $\sigma_m = I_1/3$ is the mean stress and θ the Lode angle, defines the failure envelope on the deviatoric planes and can be experimentally determined (figure 2.10). In figure (2.9), the meridians ρ_t, ρ_s, and ρ_c correspond to the values of the Lode angle θ of 0^0, 30^0 and 60^0, respectively. On the deviatoric planes, the ratio ρ_c/ρ_t is about 0.5 near the π-plane (the deviatoric plane passing through the origin) and increases to about 0.8 for $\xi \approx -7f_c'$ (Chen and Han, 1988; figure 2.9).

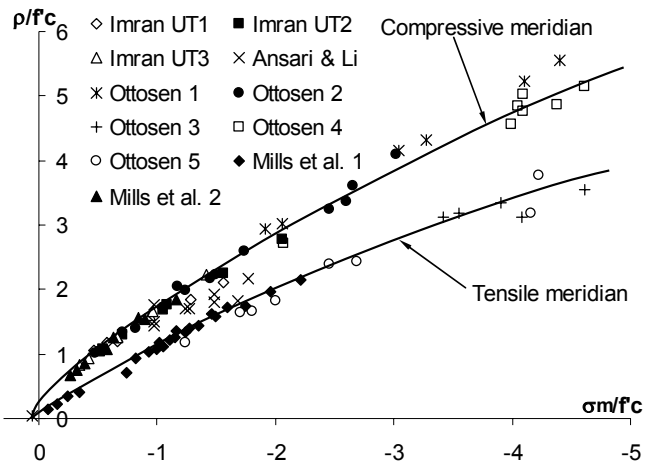

Figure 2.10: Tensile and compressive meridians of the failure envelope (data from Ansari and Li, 1998; Imran and Pantazopoulou, 1996; Ottosen, 1977; and Mills *et al.*, 1970; as presented by Chen and Han, 1988 and Imran and Pantazopoulou, 2001)

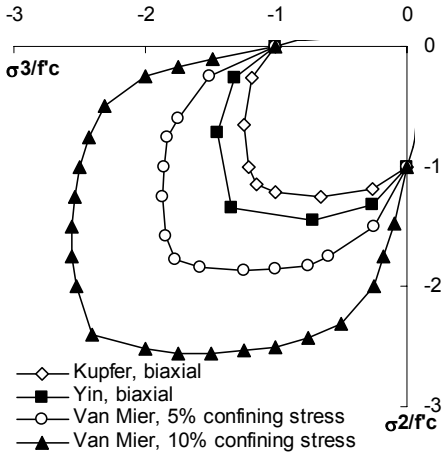

Figure 2.11: Biaxial compressive failure surface for concrete under low confining pressure (data from Kupfer *et al.*, 1969; Yin *et al.*, 1989; and Van Mier, 1986; as presented by Lowes, 1999)

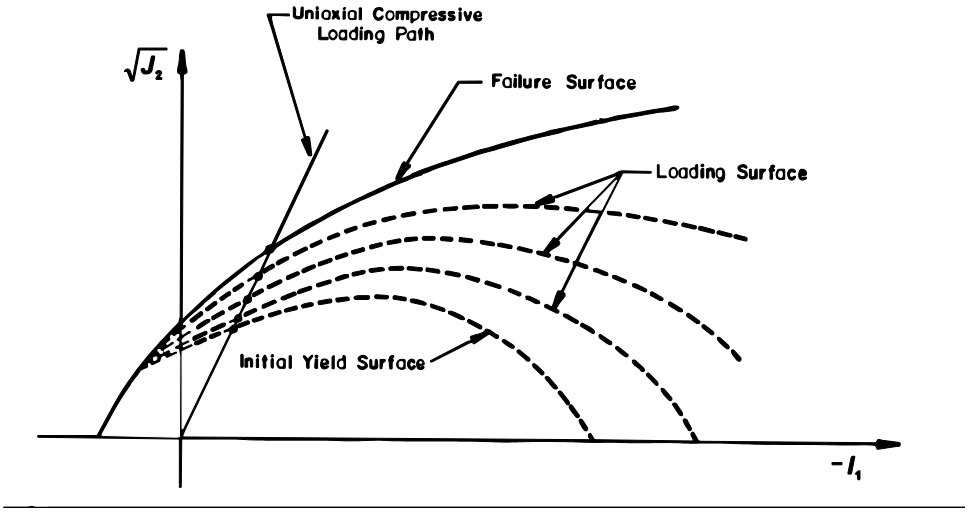

Figure 2.12: Evolution of the yield surface (Chen and Han, 1988)

The gradual change of the deviatoric sections with respect to hydrostatic pressure was also confirmed by Van Mier (1986) in biaxial loading tests, in which rather small confining pressures in the out-of-plane direction can significantly increase the material strength in the plane of primary loading (figure 2.11).

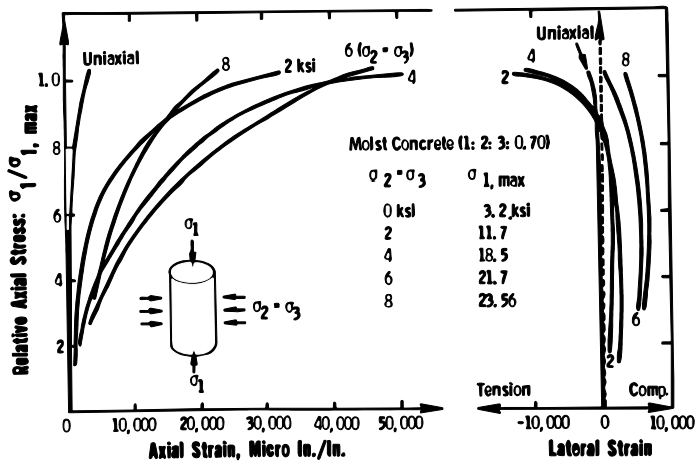

Figure 2.13: Stress versus axial strain and lateral strains curves

(Palaniswamy and Shah, 1974)

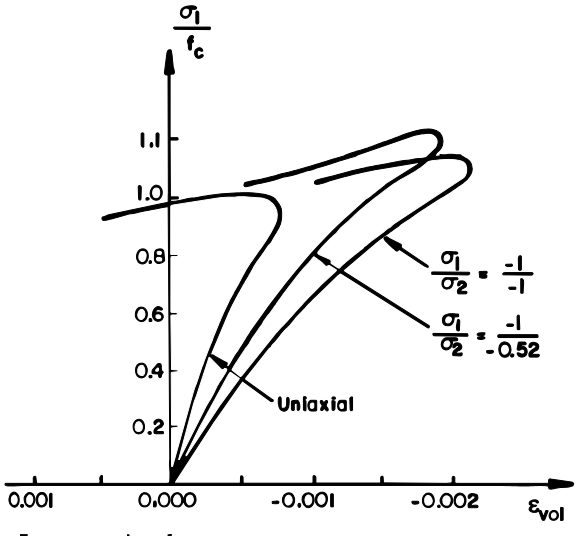

Figure 2.14: Volumetric expansion under biaxial compression

(data from Kupfer *et al.*, 1969; as presented by Chen and Han, 1988)

Experiments (Kupfer, 1969; Palaniswamy and Shah, 1974) have also shown that the deformational behaviour of a concrete specimen is significantly affected by the confining pressure. As can be seen in figure (2.13), the axial and lateral strains at failure increase with increasing confining pressure. However, at a certain level, further increase of lateral stress results in the decrease in the values of axial strains at failure (figure 2.13). In addition, under confining pressure the axial and lateral strains at failure are much larger that those in uniaxial compression. This shows that concrete in compression exhibits a certain degree of ductility before failure.

It was found experimentally (Shah and Chandra, 1968) that in concrete the cement paste itself does not expand under compressive loading. However, the composite nature of concrete, which is a mixture of cement paste and aggregates, results in its dilation at a certain level of stress. That stress level is also found to be related to the onset of a considerable increase of microcracks through the mortar. This is illustrated in figure (2.14), showing the expansion of concrete under biaxial compression through the increase of the volumetric strain near peak loads.

2.3 Constitutive modelling of concrete materials

In principle, it is desired that the above-mentioned macroscopic features of the material behaviour be reflected in any constitutive models dedicated to concrete modelling. However, it is quite difficult to incorporate all of these aspects of material behaviour in a constitutive model. Those experimentally observed features are all of macroscopic nature, which can only be characterized through some material and structural quantities and cannot always represent what truly happens at the microscopic level. This is the disadvantage of the macroscopic approach to constitutive modelling. In another aspect, the applicability of the proposed constitutive models is also of importance. Simple models with pure damage dissipation, i.e. models employing scalar damage variables, can be used in relevant cases thanks to their simplicity in the formulation, implementation and parameter identification. Complicated constitutive models should only be adopted with much care applied to the physical interpretation and identification of model parameters, which can only be done in combination with experimental work.

Constitutive models proposed and used so far (Willam and Warnke, 1975; Simo and Ju, 1987; Mazars and Pijaudier-Cabot, 1989; Yazdani and Schreyer, 1990; Feenstra and de Borst, 1995; Lee and Fenves, 1998; Imran and Pantazopoulou, 2001; Grassl *et al.*, 2002; Addessi *et al.*, 2002; Jirasek *et al.*, 2004; Salari *et al.*, 2004), although having achieved great success in the numerical simulations of concrete structures, all have their own limitations and cannot always be universally used without much care. A brief review will follow, in which main features as well as limitations of models are pointed out. The focus here is only the behavioural features of the constitutive models based on continuum mechanics in capturing the macroscopic responses observed in experiments. From the point of view of continuum mechanics, these responses can be characterized

through the evolution laws of the failure envelope of the material behaviour in multi-axial loading. Details of the constitutive models with appropriate treatments for softening-related problems will be presented in chapter 5.

2.3.1 Plasticity theory

In summary, any model based on conventional plasticity always requires an elastic constitutive relationship, the assumption of total strain decomposition, the definition of a yield surface with an evolution rule, and a flow rule. For plasticity models with a linear stress-strain relationship in the elastic region, the first two requirements are the same but the last two differ.

Regarding the distinction of the yield surface and the failure surface (figures 2.7 and 2.12), we can see that these two surfaces coincide in plasticity theory. In other words, a single loading surface acts as a yield-failure surface in plasticity theory. This combined surface is often a scaled down version of the failure envelope of the material. Numerous forms of yield surfaces have been proposed and can be classified based on either the number of model parameters (Chen and Han, 1988) or on the shape of the surface in principal stress space. The Von Mises and Tresca criteria are two typical examples of one-parameter pressure-independent yield surfaces, which were initially intended for metallic materials and are incapable of modelling the different responses in tension and compression. For the constitutive modelling of concrete, they can be augmented by tensile cut-off surfaces and should be used in combination with a non-associated flow rule to reflect the plastic volumetric expansion observed in experiments (figure 2.14). An example of the augmentation using Rankine's criterion was given by Feenstra and de Borst (1995), in which the failure of the material model is governed by a composite failure surface of the form

$$y_c = \sqrt{3J_2} - \bar{\sigma}_c(\kappa_c) = 0 \tag{2.4}$$

$$y_t = \sigma_1 - \bar{\sigma}_t(\kappa_t) = 0 \tag{2.5}$$

where σ_1 is the major principal stress; $\bar{\sigma}_c(\kappa_c)$ and $\bar{\sigma}_t(\kappa_t)$ are two equivalent stress functions governing the size of the yield/failure surfaces in compression and tension respectively; and κ_c and κ_t are two internal parameters. This augmentation for Von Mises and Tresca criteria is however only adequate in biaxial loading, as these criteria

are pressure-independent and therefore cannot reflect faithfully the behaviour of the material under compression.

Among the two-parameter models, the Mohr-Coulomb and Drucker-Prager surfaces (figure 2.15) are probably the simplest types of pressure-dependent criteria (Chen and Han, 1988). However the shortcoming of these surfaces is that they assume a linear relationship between $\sqrt{J_2}$ and I_1 ($\sqrt{2J_2} = \rho$ and $I_1/\sqrt{3} = \xi$ in the meridian plane), although this relationship has been experimentally shown to be nonlinear (see figure 2.10). Moreover the lack of dependence of the deviatoric section on the Lode angle θ is another shortcoming of the Drucker-Prager surface, even though it can be modified to have nonlinear relationships between $\sqrt{J_2}$ and I_1, i.e. the parabolic Drucker-Prager presented in the next chapter.

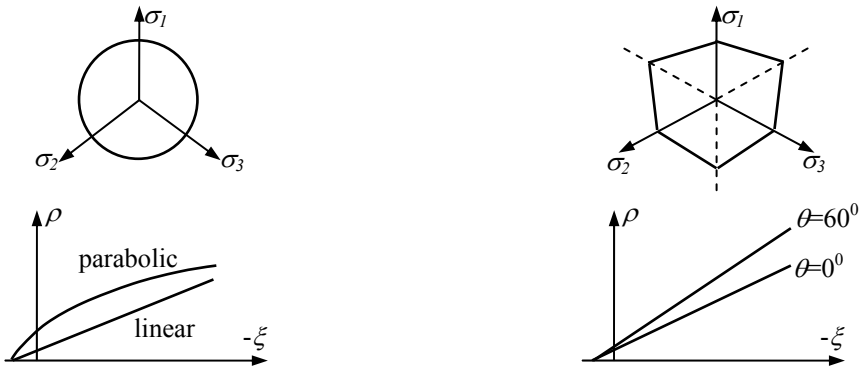

(a). Drucker-Prager (b). Mohr-Coulomb

Figure 2.15: Drucker-Prager and Mohr-Coulomb failure surfaces

Other failure criteria with nonlinear relationship between $\sqrt{J_2}$ and I_1 and the dependence on the Lode angle θ have been proposed: Hsieh-Ting-Chen (see Chen and Han, 1988), Ottosen (1977), Willam and Warnke (1975), Kang and Willam (1999), Imran and Pantazopoulou (2001), Grassl *et al.* (2002). Details on these models can be found in the relevant papers (Kang and Willam, 1999; Imran and Pantazopoulou, 2001; Grassl *et al.* 2002) and books by Chen (1982) and Chen and Han (1988). The typical deviatoric and meridian sections of those failure surfaces are shown in figure (2.16).

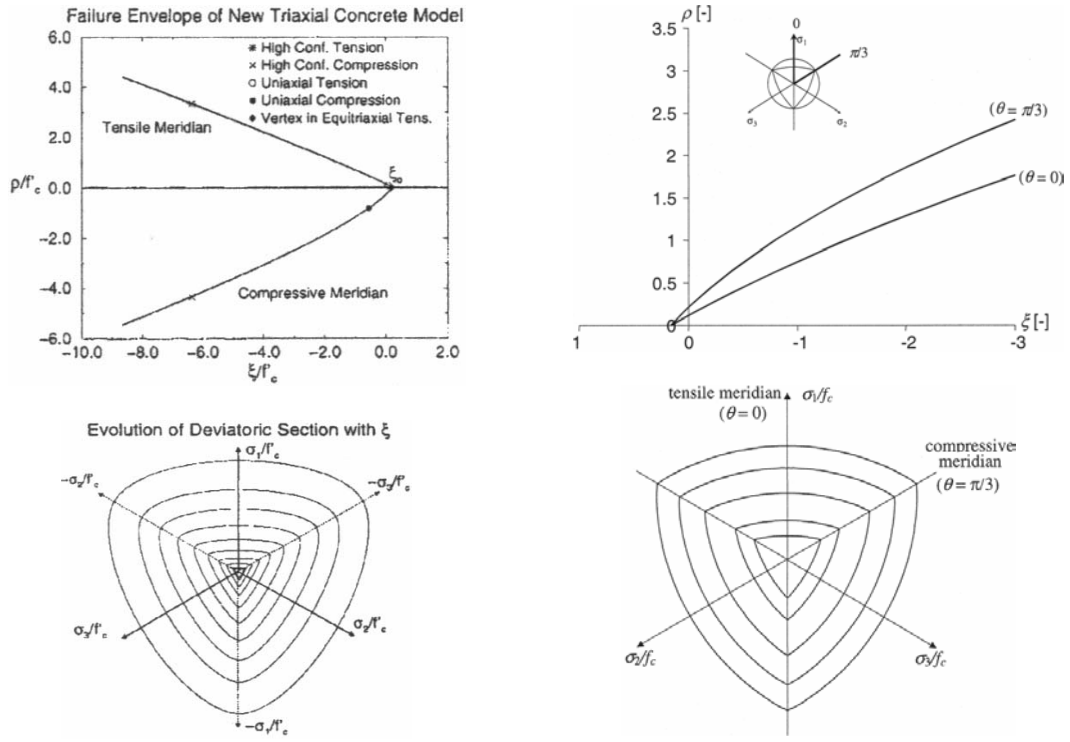

(a) Kang and Willam (1999) (b) Grassl *et al.* (2002)

Figure 2.16: Deviatoric and meridian sections of two typical failure surfaces

The above is a brief presentation of some typical failure criteria in the literature, aiming at setting a general background for the discussion on the use of plasticity theory for the constitutive modelling. In plasticity theory, the definition of a yield surface, the shape of which is usually similar to that of the failure surface (i.e. the yield surface by Grassl *et al.*, 2002), is required. However, as pointed out by Chen and Han (1988), yield surfaces as scaled down versions of failure surfaces at maximum loading are inadequate for concrete modelling. The open shape of such yield surfaces does not reflect the true behaviour of concrete under hydrostatic loading. A solution for this is the use of an additional "cap surface" for the behaviour of the model under hydrostatic compressive pressure (Simo and Ju, 1987; Sfer *et al.*, 2002). Slightly different from the use of "cap surface" is the direct modification of the equation of the open-shape yield surface so that plastic deformation under hydrostatic loading can be captured. Following the modification, the initial yield surface has a closed shape and, under loading, eventually opens towards the negative hydrostatic axis. This is the approach adopted by Kang and Willam (1999) and Imran and Pantazopoulou (2001), and illustrated in figure (2.17).

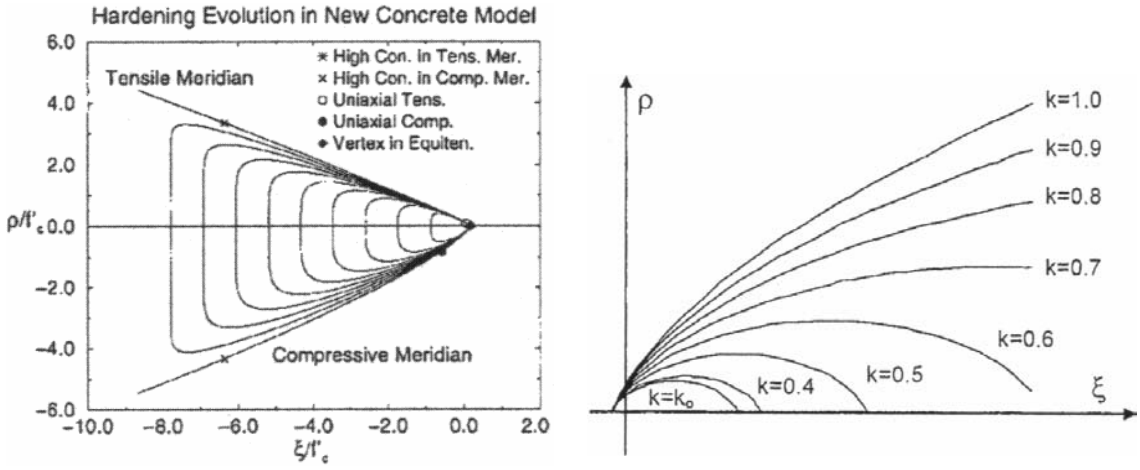

(a) Kang and Willam (1999) (b) Imran and Pantazopoulou (2001)

Figure 2.17: Modification of the yield surface to account for the nonlinear behaviour of the material under hydrostatic pressure

In addition to the disadvantage described in the preceding paragraph, the similar shape of the yield surface with respect to the failure surface results in uniform distribution of the elasto-plastic zone between the yield surface and the failure surface. As a consequence, the plastic strains can be overestimated in tension while being underestimated in compression (Chen and Han, 1988). One of the solutions to overcome these shortcomings is to use models with a yield surface of variable shape (or nonuniform hardening plasticity model; Han and Chen, 1987). In this model the yield surface consists of several parts representing different responses in tensile and compressive loading of concrete. Based on the independent hardening rule, Ohtani and Chen (1988) also proposed a model called multiple hardening plasticity. The key feature of this model is that the yield surface is allowed to expand independently in different directions due to the independent hardening parameters.

The volumetric expansion of concrete under compression makes the application of the associated flow rule for concrete inappropriate. In addition, to avoid excessive inelastic dilatancy when using pressure-dependent yield criteria, a non-associated flow rule, which is defined by the plastic potential other than the yield function, should be used instead. Models which employ this feature include that of Chen and Han (1988), Lee and Fenves (1998a, 1998b), Kang and Willam (1999), and Grassl *et al.* (2002).

In concrete both the proliferation and coalescence of microcracks, which exist within concrete even before loading, are believed to have an impact on the integrity of

the material at a macroscopic scale. The nonlinear behaviour of concrete is therefore partially or fully caused by the propagation and coalescence of these existing microcracks as well as the initiation of new microcracks. This leads inevitably to a progressive modification in the mechanical properties of concrete. Such aspects should be included in any theory designed to predict failures in concrete. Unfortunately, they cannot be modelled using conventional plasticity theory, which was originally developed for metallic materials and then modified to fit the experimental data of concrete without accounting for the underlying microscopic failure mechanisms of the material.

To overcome this shortcoming, Bazant and Kim (1979), and Chen and Han (1988) have proposed a combination of plasticity theory and progressive fracturing theory (Dougill, 1976). The fundamental assumption of progressive fracturing theory is the loss of material stiffness due to progressive fracturing during the deformation process. This is characterized through the evolution of the constitutive tensor under loading, and resembles the loss of stiffness in the modelling using continuum damage theory. In fact the fracturing theory can be formulated in the context of continuum damage theory with the constitutive tensor being considered as internal damage variable (Kratzig and Polling, 1998). A brief presentation of the fracturing theory and its comparison with damage theory can be found in Kratzig and Polling (1998). However, upon unloading, no permanent plastic strain remains and the material returns to its zero-strain and stress-free state. Combination of plasticity theory and progressive fracturing theory resolves their corresponding deficiencies in each individually attempting to model the behaviour of the material. However, without a consistent thermomechanical and micromechanical basis, this can be regarded as an *ad hoc* treatment in remedying approaches based on plasticity theory.

2.3.2 Models based on damage mechanics

The basic concepts of damage-based models are outlined in this part of the chapter. By the term “damage-based”, we also include a class of smeared crack models, i.e. fixed crack models, multiple fixed crack models, rotating crack models and, the closely related microplane models (see Carol and Bazant, 1997; Weihe *et al.*, 1998; Ohmenhauser *et al.*, 1999; and de Borst, 2002 for a brief review on those models). The appealing feature of this class of smeared crack models models is the introduction of the

failure plane (or plane of degradation, POD) in a reduced space, from which a constitutive law is postulated. The complex constitutive behaviour of the material is then obtained by transforming the constitutive relations in the reduced space (2-D plane of degradation) to the 3-D continuum level. This transformation can be of geometric nature (fixed crack models) or based on the principle of virtual work (microplane models). As can be seen, the anisotropic nature of damage is implicitly taken into account in smeared crack models. Nevertheless, more formal treatment of these models can be conceived within the framework of continuum damage mechanics, as illustrated by de Borst (2002). In this study, as only scalar damage models are considered, the above-mentioned smeared crack models will not be further discussed.

The definition of damage indicator, following Lemaitre (1992), can be seen as the most widely used, as it covers the micromechanical, thermodynamic and geometrical aspects of the macroscopic representation of the material deterioration. It is therefore adopted here and briefly presented to furnish a basis for the review in this chapter. More details can be found in the books by Lemaitre and Chaboche (1990); and Lemaitre (1992).

2.3.2.1 Concepts of damage mechanics

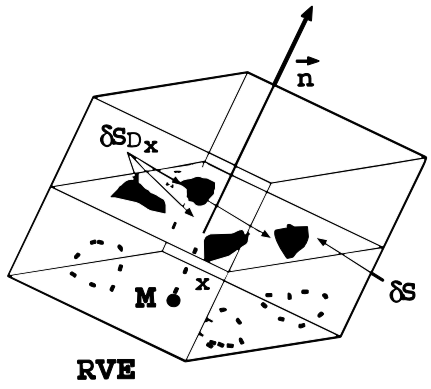

Figure 2.18: Definition of damage variable (after Lemaitre, 1992)

The idea of continuously representing material damage was first proposed by Kachanov (Lemaitre and Chaboche 1990; Lemaitre, 1992) and then a further contribution was given by Rabotnov (Lemaitre, 1992) with the concept of effective stress. However the basic development of Continuum Damage Mechanics only began in the 1970s and then in the 1980s with a more rigorous basis, based on thermodynamics

and micromechanics. Since then there have been numerous Continuum Damage Mechanics models proposed for the constitutive modelling of materials in general and concrete in particular.

The quantities of continuum mechanics are defined at a mathematical point. However, from the physical point of view, and accounting for the heterogeneity of the material in reality, these quantities should be considered to have been averaged over a certain volume called a "Representative Volume Element" whose size depends on each material (Lemaitre, 1992). As a consequence, the stress and strain in continuum mechanics should be physically interpreted as mean quantities over this volume element. In a similar way, to define the material damage at a mathematical point M, let us consider a Representative Volume Element (RVE) oriented by a plane defined by its normal $\vec{n}$ and its abscissa x along the direction $\vec{n}$. The damage value $D(M,\vec{n},x)$ at point M in the direction $\vec{n}$ and at abscissa x is defined as:

$$D(M,\vec{n},x)=\frac{\delta S_{D_x}}{\delta S} \tag{2.6}$$

in which δS is the area of intersection of the considered plane and the RVE; and δS_{D_x} is the effective area of intersections of all microcracks and microcavities in δS (see figure 2.18). It can readily be seen that the value of damage $D(M,\vec{n},x)$ ranges from zero (undamaged) to unity (totally damaged). The failure of the RVE in direction $\vec{n}$ is defined at the most damaged intersection area.

$$D(M,\vec{n})=\max_{x} D(M,\vec{n},x)=\frac{\delta S_D}{\delta S} \tag{2.7}$$

where δS_D is the most damaged intersection area. Since the damage of the RVE depends on the direction $\vec{n}$, the anisotropic nature of damage is also enclosed in that definition. Damage theories provide us with an effective means to characterize the material deterioration at microscopic level by quantities at the macroscopic level. If microcracks and cavities are uniformly distributed in the RVE, it is adequate to assume the isotropy of damage, as the damage variable $D(M,\vec{n},x)$ in this case does not depend on the direction. We restrict ourselves to the case of scalar damage variable in this study.

The concept of "effective stress", which is used here in a different sense from that used in metal plasticity and in geotechnical engineering, can be derived directly from

the above definition. For the sake of simplicity let us consider the case of uniaxial tension with scalar damage variable. Due to damage the cross sectional area is reduced and becomes the effective cross sectional area $S - S_D$ in which S is the original cross sectional area and S_D is the total area of microcracks. The stress is no longer $\sigma = F/S$ but replaced by the effective stress $\bar{\sigma} = F/(S - S_D) = \sigma/(1 - D) \geq \sigma$. The extension of the concept to multi-axial stress state with scalar damage variable is straightforward since damage in this case does not depend on the direction $\vec{n}$. Therefore we still have $\bar{\sigma}_{ij} = \sigma_{ij}/(1 - D)$ where σ_{ij} and $\bar{\sigma}_{ij}$ are now the stress and effective stress tensors respectively. In unloading from tension to compression, due to the crack closure effect, the effective cross sectional area is larger than $S - S_D$. In particular, if all the defects close ($S_D = 0$), it is equal to S and the stress σ and effective stress $\bar{\sigma}$ are now equal. This unilateral behaviour should always be accounted for in the constitutive modelling of concrete materials.

The principle of strain equivalence (Lemaitre, 1971; see figure 2.19) follows directly the effective stress concept and helps us to avoid a micromechanical analysis for each type of defect and each type of damage mechanism (Lemaitre, 1992). It is stated: "*Any strain constitutive equation for a damaged material may be derived in the same way as for a virgin material except that the usual stress is replaced by the effective stress*"

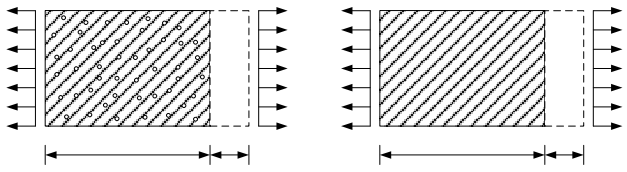

Figure 2.19: Schematic representation of the hypothesis of strain equivalence

Application of the strain equivalence hypothesis results in the state coupling between damage and elasticity (Lemaitre, 1992). This coupling comes from the physical observation that damage due to the breakage of bonds in the material directly results in changes in the elastic properties of the material. In the constitutive modelling, this coupling can be written for uniaxial case as: $\sigma = (1 - D)E\varepsilon$. This expression is in fact in accordance with that observed in experiments (Lemaitre, 1992), with the effective elasticity modulus $\bar{E}$ being dependent on the damage measure: $\bar{E} = (1 - D)E$.

Continuum damage models, like models based on conventional plasticity theory, can also be developed within two alternative frameworks. In the strain-based formulation, damage is characterized through the effective stress concept along with the hypothesis of strain equivalence. Dual with this, in a stress-based formulation, the hypothesis of stress equivalence is proposed (Simo and Ju, 1987; see figure 2.20) and damage is presented through the effective strain concept, in which the effective strain tensor in the case of isotropic damage is: $\bar{\varepsilon}_{ij} = (1-D)\varepsilon_{ij}$. The hypothesis of stress equivalence (Simo and Ju, 1987) states: "*The stress associated with a damaged state under the applied strain is equivalent to the stress associated with its undamaged state under the effective strain*"

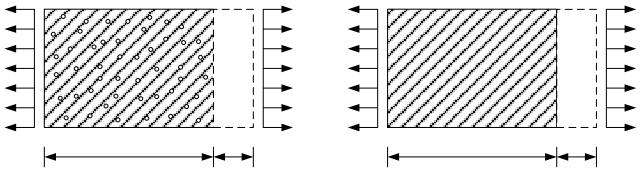

Figure 2.20: Schematic representation of the hypothesis of stress equivalence

Application of these two principles (of strain and stress equivalence) to the constitutive modelling based on damage mechanics and plasticity theory will be presented later.

Models based on continuum damage mechanics are usually formulated within a thermodynamic framework, though in principle damage theory can be developed by simply stating a damage-related stress-strain law and a yield/damage criterion (Lee and Fenves, 1998; Addessi *et al.*, 2002; see section 2.3.3 for details). This way of developing a constitutive model, however, is like using arbitrary assumptions in progressive fracturing theory (Kratzig and Polling, 1998). Although the thermodynamic admissibility of such models can be verified later using the Clausius-Duhem inequality, those kinds of approaches are not advocated in this study. For the discussion here, only constitutive aspects of damage-based approaches are considered; the thermodynamic issues will be presented in the next chapter.

In principle, the choice of the damage variable D is arbitrary, provided that the laws of thermodynamics are strictly obeyed. In addition to the above presented definition of damage (Lemaitre, 1992), there have been several ways of representing the damage measure D, which can be a single scalar for isotropic damage and a tensor for

anisotropic damage. It can be represented as a variable characterizing the material deterioration with the concepts of effective stress or effective strain (Simo and Ju, 1987; Mazars and Pijaudier-Cabot, 1989; Lemaitre and Chaboche, 1990; Lemaitre, 1992; Lee and Fenves, 1998; Peerlings, 1999; Jirasek *et al.*, 2004); or as a function in terms of the position of the loading surface in stress space between the initial and bounding surfaces (Li and Ansari, 1999); or even it can be a decreasing function (Addessi *et al.*, 2002) representing the damage experienced by the material and can hardly be directly related to the geometrical definition of damage in (2.2). In fact, in macroscopic constitutive modelling, physical interpretation of damage variables is not always straightforward. However, the convincing physical interpretation of the damage variable D depends on the identification of the microscopic mechanism underlying the observed macroscopic response (DeSimone *et al*, 2001). The definition of damage variable D following the concepts of effective stress and effective strain, which has been presented above, is probably the most well-known and widely used in literature.

2.3.2.2 Damage mechanics in constitutive modelling of concrete

The continuum Damage Mechanics approach has been shown and proved by many authors to be appropriate for constitutive models of concrete (Krajcinovic and Fonseka, 1981; Simo and Ju, 1987; Mazars and Pijaudier-Cabot, 1989; Peerlings, 1999; Geers *et al.*, 2000; Jirasek *et al.*, 2004). Due to the anisotropic nature of damage, even for initially isotropic materials, the damage measure D requires a tensorial representation. However damage models employing scalar damage variables are still preferred because of their simplicity in the formulation, numerical implementation and parameter identification (Burlion *et al.*, 2000). We restrict ourselves to the case of scalar damage in this study.

From the point of view of constitutive modelling, continuum damage mechanics alone can be used exclusively in the case that the structures analyzed are under monotonic loading, as it can reproduce the softening response of the material without necessarily paying attention to capturing the permanent deformation. In addition, the stiffness degradation, although overestimated in pure damage models, can also be seen as an important feature to be reflected in the constitute modelling of concrete materials. These features confirm the applicability of pure damage models in the constitutive

modelling of concrete materials, with promising results obtained in the literature (Peerlings, 1999; Comi, 2001; Comi and Perego, 2001; Jirasek *et al.*, 2004).

A constitutive model based on damage theory is usually formulated based on a stress-strain law with the presence of a damage variable to characterize the material deterioration, and a damage criterion and/or an evolution law for damage. The evolution law of damage, which plays a very important role in any damage-based model, is different for many Continuum Damage Mechanics models. However it is possible to group almost all existing approaches into three categories: one with imposed damage evolution laws (e.g. Faria *et al.*, 1998; Peerlings, 1999; Jirasek and Patzak, 2002; Jirasek *et al.*, 2004); one in which damage evolution laws are obtained from a dissipation potential, of which the existence is postulated (Lemaitre and Chaboche, 1990; Lemaitre, 1992) and one using implicitly defined damage evolution laws (Luccioni *et al.*, 1996; Comi, 2001; Comi and Perego, 2001; Nguyen, 2002; Nguyen and Houlsby, 2004; Salari *et al.*, 2004). Besides the simple bilinear softening laws, explicit nonlinear softening laws have been used by several researchers (Peerlings, 1999; Jirasek and Patzak, 2002; Jirasek *et al.*, 2004; Comi and Perego, 2001), with their parameters being related to relevant experimental tensile tests for the material properties.

In Jirasek and Patzak (2002) and Jirasek *et al.* (2004), an exponential curve was proposed and can be calibrated based on the uniaxial behaviour of the material, with the area under the uniaxial stress-strain curve representing the local (or specific) fracture energy g_F (see chapter 4 for details). The damage evolution is of the form:

$$D = g(\kappa) = \begin{cases} 0 & \text{if } \kappa \le \varepsilon_0 \\ 1 - \dfrac{\varepsilon_0}{\kappa} \exp\left(- \dfrac{\kappa - \varepsilon_0}{\varepsilon_f - \varepsilon_0} \right) & \text{if } \kappa \ge \varepsilon_0 \end{cases} \tag{2.8}$$

where $\varepsilon_0 = f_t'/E$ is the strain at peak stress and ε_f a model parameter controlling the initial slope of the softening curve (figure 2.21). This evolution law is in fact associated with a damage criterion: $y_d(\boldsymbol{\varepsilon}, \kappa) = \tilde{\varepsilon}(\boldsymbol{\varepsilon}) - \kappa = 0$. The history variable κ here represents the maximum previously reached value of the equivalent strain $\tilde{\varepsilon}$, which is defined as (Jirasek *et al.*, 2004):

$$\tilde{\varepsilon}(\boldsymbol{\varepsilon}) = \frac{1}{E} \sqrt{(\bar{\boldsymbol{\sigma}})^+ : (\bar{\boldsymbol{\sigma}})^+} \tag{2.9}$$

where $\bar{\boldsymbol{\sigma}} = \mathbf{a} : \boldsymbol{\varepsilon}$ is the effective stress tensor ($\mathbf{a}$ is the elastic stiffness tensor), and $\bar{\boldsymbol{\sigma}}^{+}$ denotes the positive part of the effective stress tensor.

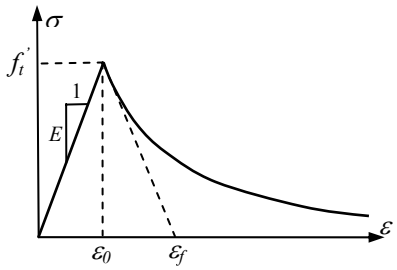

Figure 2.21: Exponential softening law (after Jirasek *et al.*, 2004)

As can be seen, the decomposition of the effective stress tensor $\bar{\boldsymbol{\sigma}}$ (see chapter 4 for details) is used in this model to properly capture the tensile behaviour of the material. In addition, the damage loading function is only used to define a failure criterion and does not play any role in the evolution law of damage. Although using arbitrary assumptions in the formulation, the model here was shown to be adequate in capturing the behaviour of the material in tensile-dominated stress states (Jirasek *et al.*, 2004). However, it was also admitted (Jirasek *et al.*, 2004) that the model parameters cannot be uniquely evaluated based solely on the input fracture energy g_F. This is because there are several stress-strain curves producing the same g_F and the problem of evaluating model parameters becomes ill-conditioned unless additional constraints are introduced. This non-uniqueness of the model parameters can also be observed in several damage-based models (Comi, 2001; Comi and Perego, 2001; Borino *et al.*, 2003). Details on this and simple remedies will be presented in chapters 4 and 5 of this thesis.

Alternatively, implicitly defined damage evolution laws have also been used (Luccioni *et al.*, 1996; Comi, 2001; Comi and Perego, 2001; Nguyen, 2002; Nguyen and Houlsby, 2004; Salari *et al.*, 2004), in which the damage growth and the plastic strain evolution are implicitly embedded in the coupling yield and/or damage loading functions. The evolution laws of damage in this case are derived using the consistency conditions of the loading functions. This is in fact a special form of deriving the damage evolution law from a damage-dissipation potential, which coincides with the damage loading function in this case. For example, in Comi (2001), the increments of tensile and compressive damage are determined from the consistency conditions of the damage

functions $y_d^t(D_t, D_c, \boldsymbol{\varepsilon}) = 0$ and $y_d^c(D_t, D_c, \boldsymbol{\varepsilon}) = 0$, in which D_t and D_c are two separate damage variables in tension and compression, respectively:

$$\dot{y}_d^t = \frac{\partial y_d^t}{\partial D_t}\dot{D}_t + \frac{\partial y_d^t}{\partial D_c}\dot{D}_c + \frac{\partial y_d^t}{\partial \boldsymbol{\varepsilon}} : \dot{\boldsymbol{\varepsilon}} = 0 \tag{2.10}$$

$$\dot{y}_d^c = \frac{\partial y_d^c}{\partial D_t}\dot{D}_t + \frac{\partial y_d^c}{\partial D_c}\dot{D}_c + \frac{\partial y_d^c}{\partial \boldsymbol{\varepsilon}} : \dot{\boldsymbol{\varepsilon}} = 0 \tag{2.11}$$

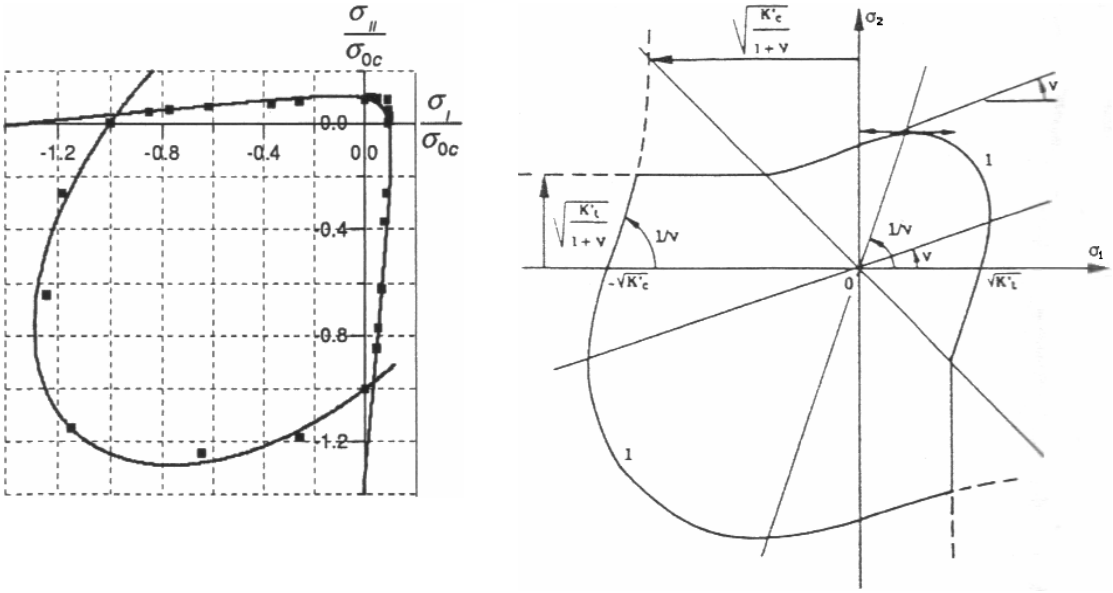

(a) Comi and Perego (2001)

(b) Mazars and Pijaudier-Cabot (1989); as presented by Chaboche (1992)

Figure 2.22: Composite failure surfaces in biaxial stress states

Different responses of concrete under tension and compression (see section 2.2) require special treatment in the constitutive modelling. This feature can be modelled mainly through two different ways, both of which use two separate damage variables (see 2.10 and 2.11 as an example) to capture the stiffness degradations in tension and compression. The first way is to use separate damage criteria for compressive and tensile response (Comi, 2001; Comi and Perego, 2001; see figure 2.22a). In this case the two damage criteria can be expressed (Comi and Perego, 2001) in the following form in stress space:

$$y_d^t(D_t, D_c, \boldsymbol{\sigma}) = J_2 - a_t {I_1}^2 + b_t h_t I_1 - (1 - \alpha D_c) k_t {h_t}^2 = 0 \tag{2.12}$$

$$y_d^c(D_t, \boldsymbol{\sigma}) = J_2 + a_c {I_1}^2 + b_c h_c I_1 - k_c {h_c}^2 = 0 \tag{2.13}$$

In the above expressions, a_i, b_i, k_i (i stands for t or c) and α are non-negative model parameters determined based on the experimental failure envelope and properties of the material. The effect of compressive damage on the tensile strength of the material is also accounted for through the presence of the compressive damage variable D_c in the tensile damage criteria. The evolutions of the two failure surfaces are governed by two isotropic hardening-softening functions $h_t(D_t)$ and $h_c(D_c)$ (see Comi and Perego, 2001 for details).

Alternatively, based on the decomposition of stress/strain into positive and negative parts (Ladeveze, 1983; Ortiz, 1985; Simo and Ju, 1987; Mazars and Pijaudier-Cabot, 1989), two separate damage loading surfaces can also be defined. In Mazars and Pijaudier-Cabot (1989), the composite damage surface is expressed as a double-criterion using two thermodynamic forces associated with the tensile and compressive damage variables. The Gibbs free energy function in this case is decomposed into two parts corresponding to the tensile and compressive behaviour of the material (see chapter 4 for details on the decomposition):

$$g = \frac{1}{2}\left\{\begin{array}{l} \dfrac{1}{E(1-D_t)}\left[(1+\nu)\boldsymbol{\sigma}^+ : \boldsymbol{\sigma}^+ - \nu\left[(\mathrm{Tr}\boldsymbol{\sigma})^+\right]^2\right] \\ + \dfrac{1}{E(1-D_c)}\left[(1+\nu)\boldsymbol{\sigma}^- : \boldsymbol{\sigma}^- - \nu\left[(\mathrm{Tr}\boldsymbol{\sigma})^-\right]^2\right] \end{array}\right\} \tag{2.14}$$

The resulting thermodynamic forces associated with damage are:

$$Y_t = \frac{\partial g}{\partial D_t} = \frac{1}{2E(1-D_t)^2}\left[(1+\nu)\boldsymbol{\sigma}^+ : \boldsymbol{\sigma}^+ - \nu\left[(\mathrm{Tr}\boldsymbol{\sigma})^+\right]^2\right] \tag{2.15}$$

$$Y_c = \frac{\partial g}{\partial D_c} = \frac{1}{2E(1-D_c)^2}\left[(1+\nu)\boldsymbol{\sigma}^- : \boldsymbol{\sigma}^- - \nu\left[(\mathrm{Tr}\boldsymbol{\sigma})^-\right]^2\right] \tag{2.16}$$

The damage criteria are defined as:

$$y_d^t = Y_t - K_t(D_t) = 0 \tag{2.17}$$

$$y_d^c = Y_c - K_c(D_c) = 0 \tag{2.18}$$

where $K_t(D_t)$ and $K_c(D_c)$ are two hardening-softening functions. The combination of these two damage criteria creates a composite failure surface in multi-axial loading (see figure 2.22b). However, in the case that the compressive behaviour of the material can be neglected (i.e. in tensile-dominated stress states) and no unloading-reloading cycle is

considered, the compressive damage criterion can be disabled and the constitutive model reduces to a much simpler form (see Jirasek and Patzak, 2002; Jirasek *et al.*, 2004).

Different responses of concrete under arbitrary loadings should be reflected in the non-uniform expansion/contraction of the failure surface, through the use of a multiple or tensorial form of damage indicator. This is, however, difficult to achieve in constitutive modelling using only two scalar damage indicators for tensile and compressive behaviour, due to the lack of experimental data. Instead, the two independent hardening/softening processes (in tension and compression) are always assumed to be isotropic, resulting in the uniform expansion/contraction of the tensile/compressive failure surface. This evolution of the failure surfaces has been adopted by several researchers (Jirasek and Patzak, 2002; Jirasek *et al.*, 2004; Comi and Perego, 2001) and is usually based on the uniaxial behaviour of the material, with the areas under the uniaxial stress-strain curves in tension and compression representing the local fracture energies of the material. For the restriction to isotropic damage and proportional loading in this study, this adoption of evolution law is acceptable.

From the point of view of continuum mechanics, the multi-axial behaviour of concrete should be carefully taken into account in the constitutive modelling. In other words, the initial shape of the damage criteria in stress/strain space should be in accordance with experiments. This was, however, not always respected (e.g. in Peerlings, 1999; Jirasek and Patzak, 2002; Addessi *et al.*, 2002). In those models, it is simple for the model formulation to declare a stress-strain relationship with scalar damage variables, along with a damage criterion and an evolution law for the damage indicator. No special attention has been paid to the macroscopic material behaviour in multi-axial loading, e.g. calibrating the failure envelope of the model against that of the material behaviour (see figure 2.28 in section 2.3.3). This inevitably restricts the capability of the models in capturing the material behaviour faithfully.

The above-mentioned pure damage models, although applicable in several cases, are just attempts to capture the tensile and compressive behaviour of the material without paying careful attention to all the observed macroscopic features of the material behaviour. In addition, assigning all the dissipation energy only to damage mechanisms results in the inability of the model to capture the irreversible strains of the material

under loading. Fortunately, this deficiency of the model becomes serious only when an unloading-reloading cycle is to be considered. However, the inability to capture the permanent deformation of the material is in fact contrary to experimental observations, even in pure tension. Coupling between damage and plasticity is therefore an essential way to take into account the important macroscopic features of the material behaviour, which have been briefly presented at the start of this chapter.

2.3.3 Coupling between damage and plasticity

From the aspects of constitutive modelling, the changes of the internal variables (i.e. damage variable and/or plastic strains) used in a constitutive model characterize the micro-structural phenomena of the material. For concrete, these microstructural changes are the decohesion in aggregate and mortar, or between them, slips along the surface of decohesion, and crushing of the mortar. These phenomena lead to irreversible strains and material deterioration observed at the macro scale. Two kinds of coupling can be distinguished in the constitutive modelling (Lemaitre, 1992): state coupling between damage and elasticity, and indirect coupling (or kinetic coupling) between damage and plasticity. This comes from the physical observations that damage due to the breakage of bonds in the material directly results in changes in the elastic properties of the material (state coupling). On the other hand, it is also observed that the material deterioration leads to a decrease in the elementary area of resistance and hence the reduction of the material strength, resulting in the indirect coupling between damage and plasticity.

In the constitutive modelling of concrete using damage mechanics, the concept of effective stress (section 2.3.2.1) furnishes a way to introduce coupling between damage and elasticity. However, coupling between damage and plasticity can be implicitly embedded in the yield and damage criteria (Luccioni *et al.*, 1996; Nguyen, 2002; Nguyen and Houlsby, 2004; Salari *et al*, 2004), with the material strength being a decreasing function with respect to the damage variable D. This implicit coupling characterizes the strength reduction due to the material deterioration and is equivalent to introducing effective instead of nominal stress into the yield function (Lemaitre and Chaboche, 1990; Lemaitre, 1992). Therefore, the concept of effective stress is still applicable in this case. This way of introducing coupling enables the constitutive modelling to use separate yield and failure criteria, helping to remedy the problems

encountered in using only one combined yield-failure criterion for the dissipation process (see section 2.3.1). The corresponding internal variables (damage variable and plastic strains for the coupled model) of the model do not explicitly depend on each other. Nevertheless, the parameter identification becomes more difficult as the model responses in this case are governed by all the internal variables used in the coupled model.

An alternative type of coupling has been used by some other researchers (Lemaitre, 1992; Lee and Fenves, 1998; Faria *et al.*, 1998; Lemaitre, 2000), in which only one loading function is specified and used to control the dissipation process. This function can be a damage loading function (Faria *et al.*, 1998) or a yield function (Lemaitre, 1992; Lee and Fenves, 1998; Lemaitre, 2000). In the first case with a damage loading function governing the dissipation process, an evolution law for the plastic strain is required (Faria *et al.*, 1998). For the use of a yield function, the damage measures, activated based on a simple damage criterion [i.e. a threshold based on the equivalent plastic strain in Lemaitre (1992)], are expressed in terms of other internal variables controlling the plastic flow process. Despite the restrictions in modelling the material behaviour using only one loading surface, this is obviously much simpler than the coupling using two separate damage and yield surfaces. Nevertheless, many *ad hoc* assumptions are usually used during the formulation of constitutive models (see Lee and Fenves, 1998; Faria *et al.*, 1998).

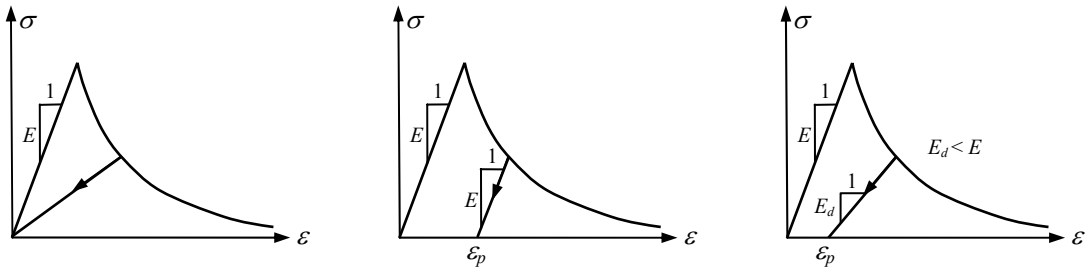

Damage Plasticity Coupled Damage-Plasticity

Figure 2.23: Uniaxial stress-strain behaviour of constitutive models

Use of coupling between damage and plasticity in theoretical modelling is an essential way to capture the observed phenomenological behaviour of concrete. In this study, true coupling is used instead of *ad hoc* modification of a pure damage model to capture the permanent strains in cyclic loading (i.e. in models by Hordijk, 1992; and

Hatzigeorgiou and Beskos, 2002). In the combined approach, damage theory is used to model the material deterioration, while the permanent deformation, as well as the volumetric expansion under compression and some other features (section 2.2), can be captured using plasticity theory (see figure 2.23). All features of the two theories can be incorporated in this combined approach, making it very promising for use in the constitutive modelling. Despite the complexity, this approach to the constitutive modelling of concrete has been widely adopted by several researchers, e.g. Simo and Ju (1987), Yazdani and Schreyer (1990), Luccioni *et al.* (1996), Lee and Fenves (1998a, 1998b), Hansen *et al.* (2001), Addessi *et al.* (2002), Ung-Quoc (2003), Jefferson (2003), Salari *et al.* (2004). Reviews on some selected coupled damage-plasticity models are presented hereafter.

2.3.3.1 Model of Yazdani and Schreyer (1990)

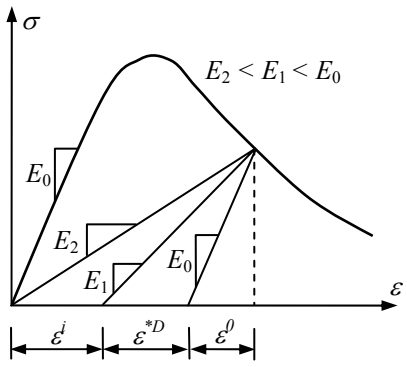

Figure 2.24: Separation of total strain in uniaxial case
(after Yazdani and Schreyer, 1990)

In the approach by Yazdani and Schreyer (1990), the pressure-dependent damage surface is used as a failure surface, and enhanced with a Von Mises yield surface. In principal stress space, this yield surface covers the damage surface in the positive hydrostatic axis, and lies almost entirely inside the damage surface in the opposite direction (figure 2.25). Attention was also paid to the multi-axial behaviour of the model, with the failure surface being calibrated to account for the strength enhancement and ductility under increasing lateral confinement (figure 2.25).

Bypassing intermediate details on the model derivation, the constitutive relations of the model can be rewritten as follows. The stress-strain relationship is

$$\boldsymbol{\varepsilon} = \mathbf{C}^0 : \boldsymbol{\sigma} + \mathbf{C}^c(D) : \boldsymbol{\sigma} + \boldsymbol{\varepsilon}^i = \boldsymbol{\varepsilon}^0 + \boldsymbol{\varepsilon}^{*D} + \boldsymbol{\varepsilon}^i \tag{2.19}$$

$$\dot{\boldsymbol{\varepsilon}}^{i} = \dot{\boldsymbol{\varepsilon}}^{r}\left(D\right) + \dot{\boldsymbol{\varepsilon}}^{p}\left(\varepsilon_{p}\right) \tag{2.20}$$

in which $\mathbf{C}^{0}$ denotes the compliance tensor for the uncracked material; $\mathbf{C}^{c}\left(D\right)$ is the added flexibility tensor due to damage; $\boldsymbol{\varepsilon}^{0}$ is the elastic strain tensor and $\boldsymbol{\varepsilon}^{*D}$ the additional recoverable strain due to elastic damage. The inelastic strain tensor is denoted as $\boldsymbol{\varepsilon}^{i}$ and arises from two irreversible sources: inelastic damage ($\boldsymbol{\varepsilon}^{r}$) and plastic flow ($\boldsymbol{\varepsilon}^{p}$) (see figure 2.24).

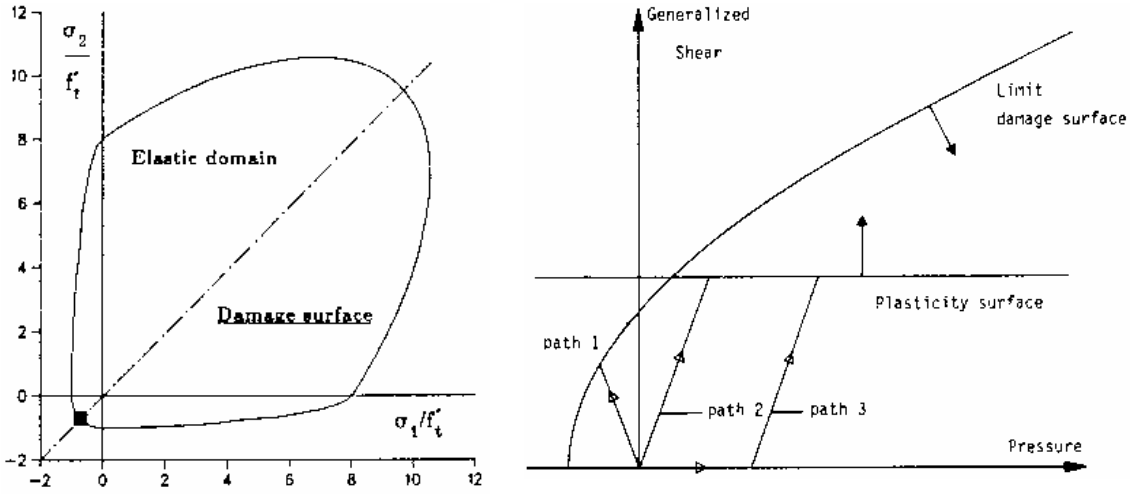

(a). Biaxial strength envelope (b). Loading surfaces in shear-pressure space

Figure 2.25: Schematic view of coupled damage-plasticity model by Yazdani and Schreyer (1990)

The yield criterion is defined as:

$$y_{p}\left(\boldsymbol{\sigma}, \varepsilon_{p}\right) = \left(\frac{3}{2}\boldsymbol{\sigma} : \boldsymbol{\sigma}\right)^{1/2} - \tau\left(\varepsilon_{p}\right) = 0 \tag{2.21}$$

where $\varepsilon_{p} = \int \left(d\boldsymbol{\varepsilon}^{p} : d\boldsymbol{\varepsilon}^{p}\right)^{1/2}$ is defined as the plastic strain path invariant (or the equivalent plastic strain), and function $\tau\left(\varepsilon_{p}\right)$ defines the hardening rule. The associated flow rule is assumed here.

The damage surface of the model is of the form:

$$\begin{aligned} y_{d}\left(\boldsymbol{\sigma}, D\right) = {} & \frac{1}{2}\boldsymbol{\sigma}^{+} : \boldsymbol{\sigma}^{+} + \frac{\omega}{2}\boldsymbol{\sigma}^{-} : \frac{\tilde{\boldsymbol{\sigma}} \otimes \tilde{\boldsymbol{\sigma}}}{\tilde{\boldsymbol{\sigma}} : \tilde{\boldsymbol{\sigma}}} : \boldsymbol{\sigma}^{-} + \omega\left(\mathbf{S}^{-} + \beta\mathbf{S}^{+}\right) : \boldsymbol{\sigma} \\ & + \frac{\omega}{2}\alpha\mu H\left(-\tilde{\lambda}\right)\boldsymbol{\sigma} : \boldsymbol{\sigma} - \frac{9\omega\alpha}{2}H\left(-\tilde{\lambda}\right)p^{2} - \frac{1}{2}t^{2}\left(D\right) = 0 \end{aligned} \tag{2.22}$$

In the above expression, the positive part of the stress tensor $\boldsymbol{\sigma}$ is denoted as $\boldsymbol{\sigma}^{+}$ and is obtained by removing the eigen vectors associated with negative eigen values of $\boldsymbol{\sigma}$ (see

chapter 4 for details); $p = \mathrm{Tr}\boldsymbol{\sigma}/3$ is the mean pressure; ω, α, β and μ are model parameters; $\mathbf{S}^+$ and $\mathbf{S}^-$ are respectively positive part and negative part of the deviatoric stress tensor $\left(\boldsymbol{\sigma}^-\right)'$ (the deviatoric stress of $\boldsymbol{\sigma}^-$); $\tilde{\boldsymbol{\sigma}}$ is the stress tensor defined by $\tilde{\boldsymbol{\sigma}} = \boldsymbol{\sigma}^- - \lambda\mathbf{i}$ with $\mathbf{i}$ denoting the second-order identity tensor and λ the maximum eigenvalue of $\boldsymbol{\sigma}^-$; $\tilde{\lambda}$ and H are the minimum eigen value of $\tilde{\boldsymbol{\sigma}}$ and the Heaviside function, respectively; $t(D)$ is the function controlling the damage process.

The evolution of the flexibility tensor $\mathbf{C}^c(D)$ in the model is defined as

$$\dot{\mathbf{C}}^c(D) = \dot{D}\,\mathbf{R}_{\mathrm{I}}(\boldsymbol{\sigma}) + \dot{D}\,\mathbf{R}_{\mathrm{II}}(\boldsymbol{\sigma}) \tag{2.23}$$

where $\mathbf{R}_{\mathrm{I}}$ and $\mathbf{R}_{\mathrm{II}}$ are two fourth-order tensors determining the direction of incurring damage in mode I (opening) and mode II (shearing) cracking respectively (see Yazdani and Schreyer, 1988; and Yazdani and Schreyer, 1990). It can be noted that the anisotropic nature of damage is accounted for using these two stress-dependent tensors.

Compared to other coupled damage-plasticity models, this model is able to capture the irrecoverable strains using inelastic damage mechanism to account for the misfit of crack surfaces. The evolution equation for the strain rate due to inelastic damage is postulated as follows:

$$\dot{\boldsymbol{\varepsilon}}^r(D) = \dot{D}\omega\mathbf{S}^- + \dot{D}\omega\beta\mathbf{S}^+ \tag{2.24}$$

Nevertheless, this capability is restricted to compressive mode of cracking only (Yazdani and Schreyer, 1990). As a consequence, with a pure damage mechanism activated in tension, the model exhibits an inability to capture the observed permanent deformation in tensile loading.

2.3.3.2 Model of Lee and Fenves (1998a, 1998b)

Lee and Fenves (1998a) developed their coupling damage-plasticity model for the numerical analysis of concrete dam. The stress $\boldsymbol{\sigma}$ and effective stress $\bar{\boldsymbol{\sigma}}$ in this model are given by

$$\boldsymbol{\sigma} = (1-D)\mathbf{a} : \left(\boldsymbol{\varepsilon} - \boldsymbol{\varepsilon}^p\right) \tag{2.25}$$

$$\bar{\boldsymbol{\sigma}} = \mathbf{a} : \left(\boldsymbol{\varepsilon} - \boldsymbol{\varepsilon}^p\right) \tag{2.26}$$

where $\mathbf{a}$ denotes the rank-four elasticity stiffness tensor; $\boldsymbol{\varepsilon}^e$ and $\boldsymbol{\varepsilon}^p$ are the elastic part and plastic part of the total strain tensor $\boldsymbol{\varepsilon}$, respectively; and D represents the damage

measure. In this model, a combined yield-failure surface is defined and evolves with damage variables, for which the evolution laws are postulated. This yield-failure surface is of the form (see figure 2.26):

$$y_p = \frac{1}{1-\alpha}\left[\alpha I_1 + \sqrt{3J_2} + \beta(\boldsymbol{\kappa})\langle\hat{\sigma}_{\max}\rangle\right] - c_c(\boldsymbol{\kappa}) = 0 \tag{2.27}$$

In this yield function, $\hat{\sigma}_{\max}$ is the maximum principal stress; α is a constant parameter and β a function of the damage variable $\boldsymbol{\kappa}$, defined by

$$\beta(\boldsymbol{\kappa}) = \frac{c_c(\boldsymbol{\kappa})}{c_t(\boldsymbol{\kappa})}(1-\alpha) - (1+\alpha) \tag{2.28}$$

where $c_t(\boldsymbol{\kappa})$ and $c_c(\boldsymbol{\kappa})$ are the tensile and compressive cohesions respectively. The Macaulay bracket $\langle\ \rangle$ is used in the expression of the yield function to create the desired shape of the yield surface in two-dimensional principal stress space (figure 2.26).

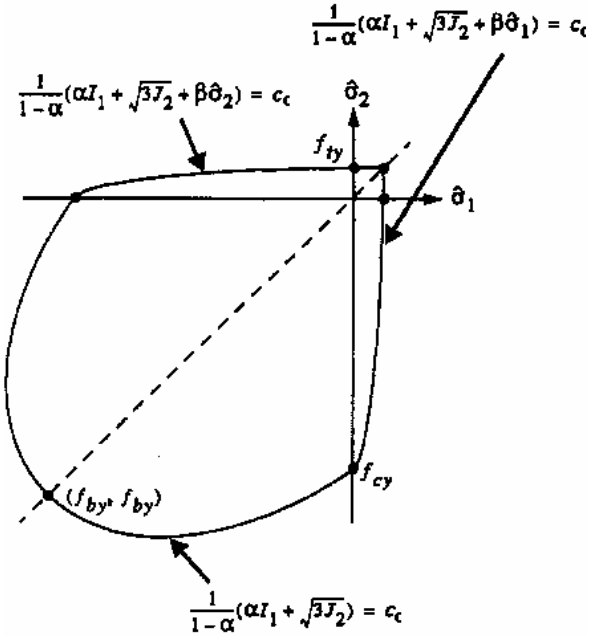

Figure 2.26: Yield surface in plane stress space (Lee and Fenves, 1998b)

The opening/closing of microcracks also features in the model, using two independent scalar damage variables κ_t and κ_c in tension and compression respectively. The vector $\boldsymbol{\kappa}$ in (2.28) is defined as: $\boldsymbol{\kappa} = [\kappa_t \quad \kappa_c]^T$. The damage measure D in (2.25) is a function expressed in term of κ_t and κ_c as

$$D = 1 - (1 - D_c(\boldsymbol{\kappa}))(1 - sD_t(\boldsymbol{\kappa})) \tag{2.29}$$

with parameter $s = s(\bar{\boldsymbol{\sigma}})$ representing the stiffness recovery, and D_t and D_c denoting the tensile and compressive damage measures. D_t and D_c in this case are defined as functions of the damage variables κ_t and κ_c.

The flow rule in the model is governed by a Drucker-Prager type plastic potential

$$\varphi = \sqrt{2J_2} + \alpha_p I_1 \tag{2.30}$$

where parameter α_p is used to control the dilatancy of the material model. Therefore the plastic strain rate is

$$\dot{\boldsymbol{\varepsilon}}^p = \dot{\lambda}\frac{\partial \varphi}{\partial \boldsymbol{\sigma}} \tag{2.31}$$

Coupling in the model is realized through the dependence of the yield threshold on the damage variables (see 2.27 and 2.28), the evolutions of which are expressed as (Lee and Fenves, 1998a)

$$\dot{\boldsymbol{\kappa}} = \dot{\lambda}\,\mathbf{H}(\bar{\boldsymbol{\sigma}}, \boldsymbol{\kappa}) \tag{2.32}$$

The forms of functions $\mathbf{H}(\bar{\boldsymbol{\sigma}}, \boldsymbol{\kappa})$ as well as $D_t(\boldsymbol{\kappa})$ and $D_c(\boldsymbol{\kappa})$ can be found in Lee and Fenves (1998a, 1998b).

The model of Lee and Fenves (1998a, 1998b) has no damage loading function. The evolution of the yield surface (2.27) is governed by the damage variables κ_t and κ_c, which in turn depend on the equivalent plastic strain ε^p (see Lee and Fenves, 1998b). Although the whole model is defined from several "pieces", its thermodynamic consistency can be readily ensured. However, the Drucker-Prager type yield criterion in this approach, although having been modified and calibrated for the biaxial test, cannot be considered appropriate for concrete modelling due to its lack of dependency on the Lode angle in the deviatoric plane.

2.3.3.3 Model of Faria *et al.* (1998)

Neglecting intermediate details in the thermodynamics-based formulation, we rewrite here the stress-strain law of the model

$$\boldsymbol{\sigma} = (1 - D_t)\bar{\boldsymbol{\sigma}}^+ + (1 - D_c)\bar{\boldsymbol{\sigma}}^- \tag{2.33}$$

In this expression, $\bar{\boldsymbol{\sigma}}^+$ and $\bar{\boldsymbol{\sigma}}^-$ are the positive and negative parts of the effective stress tensor $\bar{\boldsymbol{\sigma}}$ defined by

$$\overline{\boldsymbol{\sigma}}\left(\boldsymbol{\varepsilon}^{e}\right)=\mathbf{a}:\left(\boldsymbol{\varepsilon}-\boldsymbol{\varepsilon}^{p}\right)=\mathbf{a}:\boldsymbol{\varepsilon}^{e} \tag{2.34}$$

with **a** being the fourth order elastic stiffness tensor.

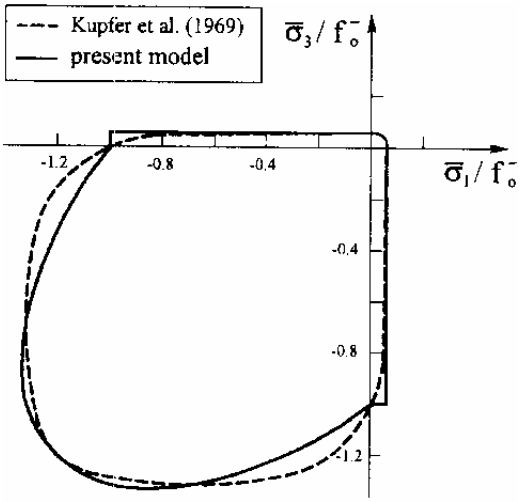

Figure 2.27: Initial 2D elastic domain (after Faria *et al.*, 1998)

Similarly to the coupled damage-plasticity of Lee and Fenves (1998a, 1998b), this model possesses only one loading surface. However, in contrast with that by Lee and Fenves (1998a, 1998b), a composite damage loading surface, instead of a yield surface, is used to govern the constitutive behaviour of the model. The two separated damage surfaces forming this composite loading surface are of the form

$$y_d^t = \overline{\tau}^+ - r^+ = 0 \tag{2.35}$$

$$y_d^c = \overline{\tau}^- - r^- = 0 \tag{2.36}$$

where r^+ and r^- are two damage thresholds controlling the size of the damage surfaces; $\overline{\tau}^+$ and $\overline{\tau}^-$ are two functions of the effective stress. The initial values r_0^+ and r_0^- of r^+ and r^-, respectively, along with $\overline{\tau}^+$ and $\overline{\tau}^-$ are all expressed as follows

$$r_0^+ = \frac{f_0^+}{\sqrt{E}} \tag{2.37}$$

$$r_0^- = \sqrt{\frac{\left(K-\sqrt{2}\right)f_0^-}{\sqrt{3}}} \tag{2.38}$$

$$\overline{\tau}^+ = \sqrt{\overline{\boldsymbol{\sigma}}^+ : \mathbf{a}^{-1} : \overline{\boldsymbol{\sigma}}^+} \tag{2.39}$$

$$\overline{\tau}^- = \sqrt{\sqrt{3}\left(K\overline{\sigma}_{oct}^- + \overline{\tau}_{oct}^-\right)} \tag{2.40}$$

In the above expressions, f_0^+ and f_0^- are defined as the uniaxial tensile and compressive stresses beyond which non-linearity becomes visible under 1D tests (Faria *et al.*, 1998). The decomposition of the effective stress tensor $\bar{\boldsymbol{\sigma}}$ is used here to distinguish the tensile and compressive responses of the model. In equation (2.40), $\bar{\sigma}_{oct}^-$ and $\bar{\tau}_{oct}^-$ are the octahedral normal stress and octahedral shear stress obtained from $\bar{\boldsymbol{\sigma}}^-$. The model parameter K in (2.38) and (2.40) is introduced to govern the ratio [about 1.16 – 1.2 based on the experimental tests by Kupfer *et al.* (1969)] between the biaxial compressive strength and its uniaxial counterpart (figure 2.27).

For the plasticity part of the coupled model, an evolution law was proposed for the plastic strain rate to capture the permanent deformations observed in experiments (Faria *et al.*, 1998):

$$\dot{\boldsymbol{\varepsilon}}^p = \beta E H\left(\dot{D}_c\right)\frac{\left\langle \bar{\boldsymbol{\sigma}} : \dot{\boldsymbol{\varepsilon}} \right\rangle}{\bar{\boldsymbol{\sigma}} : \bar{\boldsymbol{\sigma}}}\mathbf{a}^{-1} : \bar{\boldsymbol{\sigma}} \tag{2.41}$$

where β is a model parameter used to control the rate of plastic deformation. The appearance of the Heaviside step function $H\left(\dot{D}_c\right)$ here implies that permanent deformations occur in compression only. The Macaulay bracket in (2.41) is used to assure the non-negative value for the product $\bar{\boldsymbol{\sigma}} : \bar{\boldsymbol{\varepsilon}}$, which is required for the thermodynamic admissibility of the model (Faria *et al.*, 1998).

In this model the damage loading functions (2.35) and (2.36) are only used to define a strength envelope in the general loading cases. For the evolution of damage variables, the following laws are used

$$D_t = 1 - \frac{r_0^+}{r^+}\exp\left[A^+\left(1 - \frac{r^+}{r_0^+}\right)\right] \quad \text{if } r^+ \geq r_0^+ \tag{2.42}$$

$$D_c = 1 - \frac{r_0^-}{r^-}\left(1 - A^-\right) - A^-\exp\left[B^-\left(1 - \frac{r^-}{r_0^-}\right)\right] \quad \text{if } r^- \geq r_0^- \tag{2.43}$$

where A^+, A^- and B^- are all model parameters determined experimentally.

Use of two separate damage variables and damage surface in this model help to capture the unilateral behaviour of concrete, as numerically illustrated by Faria *et al.* (1998). The biaxial behaviour of the model is also calibrated against experimental data (figure 2.27). However, the introduction of plastic dissipation mechanism through the plastic strain defined in (2.41) is arbitrary. As explained by the Faria *et al.* (1998), this

is to gain algorithmic efficiency in large time consuming seismic analysis. The resulting inability of the model to capture permanent deformation in tension is obvious.

2.3.3.4 Model of Salari *et al.* (2004)

In Salari *et al.* (2004), coupling between damage and plasticity results from the decrement of plasticity threshold with respect to change of a scalar damage variable, which is equivalent to the use of effective stress in the yield function. The stress-strain relationship with a single scalar damage variable is

$$\boldsymbol{\sigma} = (1-D)\mathbf{a} : \left(\boldsymbol{\varepsilon} - \boldsymbol{\varepsilon}^{p}\right) \tag{2.44}$$

where $\mathbf{a}$ denotes the elasticity stiffness tensor. The plastic behaviour of the coupled damage-plasticity model is controlled by the following pressure-dependent Drucker-Prager yield criterion

$$y_p = \alpha I_1 + \sqrt{J_2} - (1-D)k = 0 \tag{2.45}$$

where α and k are two functions of the equivalent deviatoric plastic strain ε'_p, which are expressed as follows

$$\varepsilon'_p = \int_0^{\varepsilon'_p} d\varepsilon'_p \tag{2.46}$$

$$d\varepsilon'_p = \sqrt{\frac{2}{3} d\varepsilon'^{p}_{ij} d\varepsilon'^{p}_{ij}} \;;\; \varepsilon'^{p}_{ij} = \varepsilon^{p}_{ij} - \frac{1}{3}\delta_{ij}\varepsilon^{p}_{kk} \tag{2.47}$$

$$\alpha = \alpha_m - (\alpha_m - \alpha_0)\exp\left(-b_1 \varepsilon'_p\right) \tag{2.48}$$

$$k = k_m - (k_m - k_0)\exp\left(-b_2 \varepsilon'_p\right) \tag{2.49}$$

In the above expressions ε'^{p}_{ij} denotes the deviatoric plastic strain; b_1 and b_2 are two model parameters; α_0, α_m and k_0, k_m are the initial and maximum values of the frictional and cohesive parameters α and k, respectively, in which α_0 and k_0 can be determined directly from the uniaxial tensile and compressive strengths of the material (see Salari *et al.*, 2004).

Use of a non-associated flow rule in the model requires the definition of a plastic potential φ, which is of the form:

$$\varphi = \beta I_1 + \sqrt{J_2} \tag{2.50}$$

The dilatation parameter β is used here to control the inelastic volume expansion.

For the damage loading function, the following thermodynamic force (following the proposal by Shao *et al.*, 1998) is used to drive the damage evolution.

$$Y_v = \frac{1}{2}K^0\left\langle \varepsilon_v^e \right\rangle^2 + c\int_0^{\varepsilon_v^p} |\sigma_m| \left\langle d\varepsilon_v^p \right\rangle \tag{2.51}$$

$$c = c_t \text{ for } \varepsilon_v^e > 0$$

$$c = c_c \text{ for } \varepsilon_v^e < 0$$

in which K^0 is the bulk modulus of the intact material; ε_v^e and ε_v^p are the volumetric parts of the elastic strain and plastic strain, respectively; σ_m is the mean nominal stress; c_c and c_t are two model parameters termed plastic participation factors in damage force; and $\langle\ \rangle$ denotes the Macaulay bracket. The damage loading function is defined as

$$y_d = Y_v - r(D) = 0 \tag{2.52}$$

with $r(D)$ being the energy resistance function (Salari *et al.*, 2004). The evolutions of damage variable and plastic strain are obtained from the two consistency conditions of the yield and damage functions, which are expressed as follows:

$$\dot{y}_p = \frac{\partial y_p}{\partial \boldsymbol{\sigma}} : \dot{\boldsymbol{\sigma}} + \frac{\partial y_p}{\partial \varepsilon'_p} : \dot{\varepsilon}'_p + \frac{\partial y_p}{\partial D}\dot{D} = 0 \tag{2.53}$$

$$\dot{y}_d = \frac{\partial y_d}{\partial Y_v}\dot{Y}_v + \frac{\partial y_d}{\partial D}\dot{D} = 0 \tag{2.54}$$

The model presented above can capture the tensile and compressive behaviour of quasi-brittle materials separately, thanks to the use of different parameters in tension and compression (c_c and c_t) for the damage function. However, with only a single scalar damage indicator, this model cannot be used to model the unilateral behaviour of the material when load reversal takes place. In addition, the identification and determination of model parameters have not carefully been addressed in the development of the model, resulting in somewhat arbitrary choices of model parameters.

2.3.3.5 Model of Addessi *et al.* (2002)

The plastic nonlocal damage model proposed by Addessi *et al.* (2002) is like that of Salari *et al.* (2004) in the sense that only a single scalar damage parameter is used. For the constitutive aspects, only the local version of the model is considered here. The stress-strain law with damage is

$$\boldsymbol{\sigma} = (1-D)^2 \mathbf{a} : \left(\boldsymbol{\varepsilon} - \boldsymbol{\varepsilon}^p\right) \tag{2.55}$$

This is somewhat different from the previously reviewed models with $(1-D)^2$, instead of $(1-D)$, appearing in the stress-strain law. The definition of damage variable of Lemaitre (2.2) is therefore not applicable. However, the effective stress tensor in this case is the same as that defined in previously reviewed models (2.26 and 2.34):

$$\overline{\boldsymbol{\sigma}} = \frac{\boldsymbol{\sigma}}{(1-D)^2} = \mathbf{a} : \left(\boldsymbol{\varepsilon} - \boldsymbol{\varepsilon}^p\right) \tag{2.56}$$

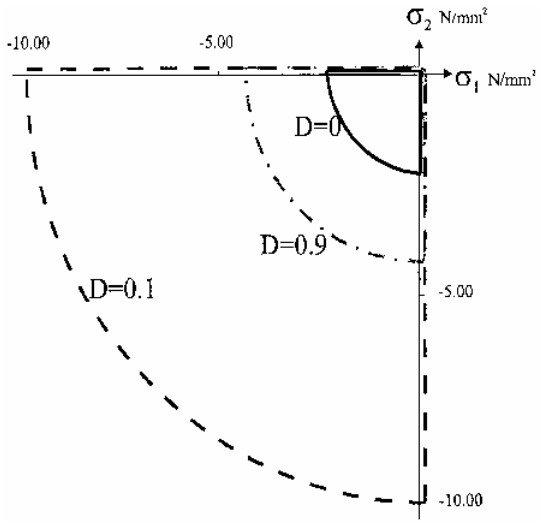

Figure 2.28: Evolution of the damage surface in 2D principal stress space (Addessi *et al.*, 2002)

For the coupling between damage and plasticity, two loading functions are defined; these being a damage function and a yield function. The damage limit function of this model is of the form

$$y_d = (Y-1) - (aY + K)D = 0 \tag{2.57}$$

In this function, K and a are two functions expressed in terms of other model parameters K_t, K_c, a_t and a_c, which in turn are strain-based functions (see Addessi *et*

al., 2002 for details). The variable Y, termed equivalent deformation, in (2.57) is defined by

$$Y = \frac{Y_t}{Y_{0t}} + \frac{Y_c}{Y_{0c}} \tag{2.58}$$

with Y_{0t} and Y_{0c} being the damage thresholds in tension and compression respectively. The equivalent tensile and compressive deformation Y_t and Y_c are functions of the equivalent elastic and total strains e_i^e and e_i, all of which are defined as:

$$Y_t = \sqrt{\sum_{i=1}^{3} \left\langle e_i^e \right\rangle^2} \; ; \; Y_c = \sqrt{\sum_{i=1}^{3} \left\langle -e_i \right\rangle^2} \tag{2.59}$$

$$e_i^e = (1-2\nu)\varepsilon_i^e + \nu \sum_{j=1}^{3} \varepsilon_j^e \; ; \; e_i = (1-2\nu)\varepsilon_i + \nu \sum_{j=1}^{3} \varepsilon_j \tag{2.60}$$

in which ε_i^e and ε_i are the elastic and total principal strains; and ν is Poisson's ratio.

For the plasticity part of the coupled model, an associated flow rule is assumed. The following yield function is used

$$y_p(\bar{\boldsymbol{\sigma}}, q) = 3\bar{J}_2 + (f_c' - f_t')\bar{I}_1 - f_c' f_t' + q = 0 \tag{2.61}$$

where $\bar{I}_1$ denotes the first invariant of the effective stress tensor and $\bar{J}_2$ the second invariant of the deviatoric part of the effective stress tensor; q is termed the thermodynamic force associated with the internal variable α by the relation $q = -\chi\alpha$, with χ being the hardening parameter of the model. This leads to the following evolution laws (Addessi *et al.*, 2002)

$$\dot{\boldsymbol{\varepsilon}}^p = \dot{\lambda} \frac{\partial y_p}{\partial \bar{\boldsymbol{\sigma}}} \tag{2.62}$$

$$\dot{\alpha} = \dot{\lambda} \frac{\partial y_p}{\partial q} = \dot{\lambda} \tag{2.63}$$

As can be seen, the above model uses the concept of effective stress to couple damage and plasticity. What is different from other reviewed models here is the flow rule (2.62), in which the differentiation of the yield function is taken with respect to the effective stress $\bar{\boldsymbol{\sigma}}$, instead of the true stress tensor $\boldsymbol{\sigma}$ (Lemaitre, 1992). The thermodynamic admissibility of the coupled model was not addressed during the model formulation. The use of a single scalar damage variable here also restricts the model

capability to capture the experimentally observed stiffness recovery in unloading from tension to compression. In addition, the true multi-axial response of the model is also not accounted for in the damage criterion (see figure 2.28), and the ductility of the material in compression under confined pressure therefore cannot be faithfully captured by the model.

2.4 Discussion

The proper choice of constitutive models for an engineering application depends on the actual need and the loading circumstances. Simple models can give satisfactory results in relevant cases, e.g. pure damage or softening plasticity models if only monotonic loading is considered. Nevertheless, this is not always the case and advanced constitutive models being able to capture faithfully the observed macroscopic behaviour of the material are often needed. In this case, coupling between damage and plasticity is advocated.

In constitutive modelling based on continuum mechanics, it is essential that the model capture faithfully the multi-axial behaviour of the material during the failure process. For isotropic damage models, at least the initial shape of the failure surface should be in accordance with the experimental failure envelope. For the macroscopic constitutive modelling pursued in this study, a yield surface and/or a failure surface with evolution laws governing the expansion/contraction of those surfaces are needed. These surfaces should account for the responses of the model in multi-axial loading. This, however, is not always respected in the modelling, e.g. models proposed by Addessi *et al.*, 2002; Jirasek and Patzak, 2002; Ung-Quoc, 2003.

Other aspects that should be mentioned are the identification and determination of model parameters. While there is no universally accepted and recommended test for the fracture properties of the material other than the standard three-point bending test of notched beam (Petersson, 1981; RILEM, 1985), for practical purpose, the identification of model parameters should be based on the recommended tests. Otherwise, new tests should be devised for the identification of model parameters. In this study, modifications of the standard three-point bending test (by Bazant, 1996) are adopted for the determination of parameters of a coupled damage-plasticity model (see chapter 4).

Along with the identification of model parameters, the evolution of the scalar damage variable is usually based on the uniaxial behaviour of the material, with the area under the stress-separation curve in a cohesive crack model (or equivalently the stress-strain curve in continuum models) representing the fracture energy in pure mode I (opening) cracking. This stress-separation curve can be in fact obtained from the standard three-point bending test of a notched beam, or possibly a direct tension test. Although it is not universal in the general loading case, this way of obtaining damage evolution laws and identifying model parameters has been widely adopted in the research community (Petersson, 1981; Saleh and Aliabadi, 1995; Meschke *et al.*, 1998; Comi and Perego, 2001; Jirasek and Patzak, 2002; Jirasek *et al.* 2004; Salari *et al.*, 2004). We will adopt it in this study without going into a debate on the importance of mode II fracture energy in the modelling. However, one important thing that should be mentioned here is that a process based solely on one experimentally-given fracture energy (mode I as adopted here) cannot give a unique response to the material model. In other words, several different stress-separation curves can produce the same given fracture energy. Furthermore, the nonlinear softening laws used in some models (Comi, 2001; Comi and Perego, 2001; Jirasek *et al.* 2004) cannot be guaranteed to give the model responses in accordance with the material behaviour in all cases with different material properties. This observation has not always been addressed in the constitutive modelling of concrete materials. Without proper care of the parameter identification, numerical simulation based on a constitutive model seems to be an *ad hoc* fitting of the responses of the numerical model to those of the real structure. We will return to this issue in chapters 4 and 5 and propose a simple but useful way, based on experimental observation, for the parameter identification of the proposed models.

Although several coupling models of damage and plasticity have been proposed and studied, there is always space for new development. This observation comes from the deficiency of current coupled damage-plasticity models in macroscopically modelling the material behaviour in a convincing manner, in which the observed material behaviour is faithfully reflected, and close connections between the proposal of the models and the identification of parameters based on experiments should be established. In addition, the complication and use of *ad hoc* assumptions in models reviewed in the preceding sections should be avoided by formulating them within a rigorously and consistently built framework. However, the development of combined

damage-plasticity models is not an easy task, as it concerns the macroscopic modelling of the complex underlying microscopic phenomena, which are difficult or even impossible to be measured experimentally. Numerical microscopic analysis of the material behaviour is an alternative way to obtain some understanding on the underlying micro-structural phenomena. This, however, makes very high computational demands, and is outside the scope of the study.

In macroscopic modelling, one possible and essential way of determining parameters for coupled damage-plasticity models is to base these on the separation of the total energy dissipated due to different dissipation mechanisms, e.g. due to microcracking processes in concrete. Those underlying microscopic processes can be observed as crack opening (mode I), sliding (mode II) or tearing (mode III) at macroscopic level. It should be noted that, the above distinction of macro cracking modes only has a relative meaning and is in the context of the macroscopic modelling, as the energy can be dissipated by several different underlying microstructural mechanisms even in pure mode I, mode II or mode III macro-cracking. For example, frictional slips at the interface between aggregate and mortar or due to aggregate interlocking can result in permanent deformations even in pure mode I cracking. As a consequence, the separation of dissipated energy should be appropriately performed, with relevant experimental tests on concrete needed to be carried out. For mode I cracking, Bazant (1996) suggested measuring the unloading slopes at sufficient number of points on the load-deflection curve in the standard three-point bending test for the separation of energies dissipated due to microcracking and frictional slips. This, however, is one simple demonstration of the suggested separation of dissipated energy, only for pure mode I cracking, which is believed to prevail in concrete even in mixed-mode cracking (Di Prisco *et al.*, 2000). The need for fracture energy in the shearing mode of cracking is still a controversial issue and therefore not considered in this study.

The brief review in the preceding sections and the above discussion have shown the need to combine damage mechanics and plasticity theory in a rigorous way without introducing any *ad hoc* assumptions during the model formulation. The combination of damage mechanics and plasticity theory within a thermodynamic framework will be focused on in the next Chapters. Thermodynamic principles will serve as a basis for the approach to constitutive modelling of the material, helping to produce

thermodynamically reasonable results in the numerical analysis. The coupled damage-plasticity model in this study is intended to capture important features of the material behaviour such as the strength reduction, stiffness degradation, and permanent deformation; all of which occurs in both tension and compression. In addition, the multi-axial behaviour along with simple mechanisms to capture the multiple hardening and the unilateral behaviour of the material will be featured in the modelling. The identification and determination of model parameters will also be addressed and discussed at length.

Chapter 3:

Thermodynamic Aspects – A Formulation of Elasto-plastic-damageable Models

3.1 Introduction

The constitutive models for concrete in this study are developed based on the thermodynamic framework proposed by Houlsby and Puzrin (2000). Modifications of the original thermodynamic framework (by Houlsby and Puzrin, 2000) to accommodate an additional internal variable for the microcracking process will be presented in this chapter, followed by the formulation of stress- and strain-based damage models. A comparison between the framework used in this study and that by Lemaitre (1992) is carried out at the end of this Chapter.

3.2 Thermodynamic aspects

This section presents a simple formulation of elasto-plastic damage models based on the thermodynamic framework for plasticity proposed by Houlsby and Puzrin (2000). Similarities, as well as differences, between this framework and the others, mainly those by Lemaitre and Chaboche (1990) and Lemaitre (1992) will also be addressed. In addition to a single internal variable of tensorial form α_{ij} in the original framework, which is identified with the plastic strain (Collins and Houlsby, 1997), a new internal variable, termed α_d instead of D to be in accordance with the terminology used in the adopted framework, is introduced to model the material deterioration. In this study, we restrict ourselves to the case of isotropic damage, so that α_d is simply a scalar internal variable. The incorporation of tensorial form of damage is in principle possible but for simplicity is left here as a future development of the proposed approach.

3.2.1 Dissipation function

The definition of internal variable here is in agreement with that of Lemaitre and Chaboche (1990), in which state variables comprising observable and internal variables define the thermodynamic state at a given point and instant of a medium. Temperature θ and total strain $\boldsymbol{\varepsilon}$ are considered as observable variables while other state variables, such as those representing the plasticity and damage processes, are regarded as internal variables. In fact these internal variables are macro variables characterizing micro-structural processes (density of dislocations, crystalline microstructure, configuration of microcracks and cavities, etc) and there are no means of measuring them by direct observation (Lemaitre and Chaboche, 1990). However, the treatment to these two kinds of variables is the same.

As mentioned in the original framework (by Houlsby and Puzrin, 2000), the generalization of the framework either to other forms of internal variable, or to multiple internal variables, is straightforward. The specific internal energy function in this case is of the form $u = u\left(\varepsilon_{ij}, \alpha_{ij}, \alpha_d, s\right)$, from which the generalized stress corresponding to the newly introduced internal kinematic variable α_d is also identified as a scalar, termed $\overline{\chi}_d$, and is defined by (Houlsby and Puzrin, 2000): $\overline{\chi}_d = -\partial u / \partial \alpha_d$. In this case the derivation of a model entirely follows the procedures in the original work by Houlsby and Puzrin (2000) and is represented here, along with some minor modifications to integrate damage-related terms into the model, merely for the sake of illustration.

Following the original work, we restate the local forms of the First and Second Laws of Thermodynamics, respectively

$$\dot{W} + \dot{Q} = \dot{u} \tag{3.1}$$

$$\dot{s} \geq -\left(\frac{q_k}{\theta}\right)_{,k} \tag{3.2}$$

in which $\dot{W} = \sigma_{ij}\dot{\varepsilon}_{ij}$ is the mechanical work input; $\dot{Q} = -q_{k,k}$ is the heat supply to a volume element, s is the entropy and q_k / θ is denoted as the entropy flux. It should also be noted here that the above rate equations are of local form and can generally be written for any given point of the whole continuum. The accommodation of nonlocality to the framework, for the treatment of softening-related problems, will be presented in

the chapter 6. We also exclude internal heat production, although some authors include it, as it is in fact contrary to the First law. Expansion of expression (3.2) then gives us

$$\theta \dot{s} + q_{k,k} - \frac{q_k \theta_{,k}}{\theta} \geq 0 \tag{3.3}$$

The dissipation here comprises two parts corresponding to the mechanical dissipation $\theta \dot{s} + q_{k,k}$ and thermal dissipation $-q_k \theta_{,k} / \theta$. As mentioned in the original framework, a more stringent law than the Second Law of Thermodynamics, can be assumed here by assuming that $\theta \dot{s} + q_{k,k} \geq 0$, using the fact that the thermal dissipation is always non-negative and small compared to the mechanical one for small thermal gradients. However, for the sake of illustration we make use of this assumption in the finally derived expression. Therefore the dissipation function, which is actually the rate of dissipation function, can be rewritten

$$d = \theta \dot{s} + q_{k,k} - \frac{q_k \theta_{,k}}{\theta} \geq 0 \tag{3.4}$$

from which and the First Law of Thermodynamics, it follows that

$$d = \theta \dot{s} + \sigma_{ij} \dot{\varepsilon}_{ij} - \dot{u} - \frac{q_k \theta_{,k}}{\theta} \geq 0 \tag{3.5}$$

In fact, this is the fundamental inequality combining the First and Second Law of Thermodynamics, which directly leads to the Clausius-Duhem inequality through the use of the Helmholtz specific free energy f, defined by

$$f = u - s\theta \tag{3.6}$$

Differentiation of f with respect to time results in

$$\dot{f} = \dot{u} - s\dot{\theta} - \theta \dot{s} \tag{3.7}$$

from which and (3.5) we obtain the inequality

$$d = \sigma_{ij} \dot{\varepsilon}_{ij} - \dot{f} - s\dot{\theta} - \frac{q_k \theta_{,k}}{\theta} \geq 0 \tag{3.8}$$

This expression embodies both the First and Second Laws of Thermodynamics and is called the Clausius-Duhem inequality. Processes satisfying the Clausius-Duhem inequality are said to be thermodynamically admissible. What is obtained here is similar to that in Lemaitre and Chaboche (1990) or Lemaitre (1992), with the only difference lying in the absence of the mass density ρ, as all the expressions here are written for a

unit volume. The Clausius-Duhem inequality here implies the thermodynamic admissibility of any non-dissipative as well as dissipative processes. Making use of the assumption that the thermal dissipation $-q_k\theta_{,k}/\theta$ is positive and small compared to the mechanical one for slow processes, and hence it can be neglected, the Clausius-Duhem inequality now reduces to a more stringent form (Houlsby and Puzrin, 2000)

$$d = \sigma_{ij}\dot{\varepsilon}_{ij} - \dot{f} - s\dot{\theta} \geq 0 \tag{3.9}$$

or in a similar form using the internal energy u

$$d = \sigma_{ij}\dot{\varepsilon}_{ij} - \dot{u} + \theta\dot{s} \geq 0 \tag{3.10}$$

3.2.2 Fundamental relations

Fundamental relations or state laws, which define links between the state variables and their associated variables, are derived in this section. The relations can be obtained either by making use of the Clausius-Duhem inequality in specific physical cases (Lemaitre and Chaboche, 1990) or, mathematically, just by comparing the expressions of $\dot{u}$ derived in two different ways (Houlsby and Puzrin, 2000). The Clausius-Duhem inequality (3.9) in this case can be interpreted as a mathematical expression for any physical processes. It can now be used with the time differentiation of the Helmholtz free energy f, which is

$$\dot{f} = \frac{\partial f}{\partial \varepsilon_{ij}}\dot{\varepsilon}_{ij} + \frac{\partial f}{\partial \theta}\dot{\theta} + \frac{\partial f}{\partial \alpha_{ij}}\dot{\alpha}_{ij} + \frac{\partial f}{\partial \alpha_d}\dot{\alpha}_d \tag{3.11}$$

to obtain

$$d = \left(\sigma_{ij} - \frac{\partial f}{\partial \varepsilon_{ij}}\right)\dot{\varepsilon}_{ij} - \left(s + \frac{\partial f}{\partial \theta}\right)\dot{\theta} - \frac{\partial f}{\partial \alpha_{ij}}\dot{\alpha}_{ij} - \frac{\partial f}{\partial \alpha_d}\dot{\alpha}_d \geq 0 \tag{3.12}$$

Physical interpretations of dissipation processes here lead to the independent cancellation of some terms in this inequality. For example, for an isothermal elastic deformation with no change in the internal variables, the dissipation is zero and hence the equality in the Clausius-Duhem inequality holds. It directly results in

$$\sigma_{ij} = \frac{\partial f}{\partial \varepsilon_{ij}} \tag{3.13}$$

In a similar way to this, for a reversible thermal process, the equality also holds, resulting in

$$s = -\frac{\partial f}{\partial \theta} \tag{3.14}$$

Finally, we have

$$d = -\frac{\partial f}{\partial \alpha_{ij}}\dot{\alpha}_{ij} - \frac{\partial f}{\partial \alpha_d}\dot{\alpha}_d \geq 0 \tag{3.15}$$

The same results can be found using some mathematical manipulations and comparisons (Houlsby and Puzrin, 2000), in which the time differentiation of the internal energy $u = u\left(\varepsilon_{ij}, \alpha_{ij}, \alpha_d, s\right)$ can be compared with (3.10), giving us similar state laws as obtained above. It can also be seen here that the associated variables with strain ε_{ij} and temperature θ are stress σ_{ij} and entropy s respectively. Therefore, in an analogous manner, the thermodynamic forces associated with the internal variables α_{ij} and α_d can be defined to be

$$\overline{\chi}_{ij} = -\frac{\partial f}{\partial \alpha_{ij}} \tag{3.16}$$

$$\overline{\chi}_d = -\frac{\partial f}{\partial \alpha_d} \tag{3.17}$$

They are called generalized stresses (Houlsby and Puzrin, 2000) and, in connection with the dissipative generalized stress defined later, are the key features for obtaining the yield and damage loading functions in this framework. Although the above laws are formulated based on the employment of the Helmholtz free energy function f, similar results for the relationships between internal and associated variables can also be obtained for any energy function through the use of the Legendre transformations. A Legendre transformation in this case involves a change in the choice of internal variables and a corresponding change in the choice of the energy function. Those energy functions can be any of the internal energy u, enthalpy h, Helmholtz free energy f or Gibbs free energy g, the use of which is interchangeable in the framework and all fundamental relations derived from which can be found in Collins and Houlsby (1997), and Houlsby and Puzrin (2000).

3.2.3 Loading functions and evolution laws

The dissipation now contains the mechanical dissipation (intrinsic dissipation) only and therefore is different from that in Lemaitre and Chaboche (1990).

$$d = \overline{\chi}_{ij}\dot{\alpha}_{ij} + \overline{\chi}_{d}\dot{\alpha}_{d} \geq 0 \tag{3.18}$$

The positiveness of the thermal dissipation $-q_k\theta_{,k}/\theta$, is automatically satisfied based on the fact that the heat flow is always in the direction of the negative thermal gradient. Moreover, this dissipation is also small compared to the mechanical ones for small thermal gradient. Neglecting the thermal dissipation hence results in a slightly more stringent condition than the Second Law of Thermodynamics but can be widely accepted (Houlsby and Puzrin, 2000). In this case, the separation of the thermal and mechanical dissipations and enforcement of the positiveness of the mechanical dissipation should only be considered as a restriction on the field of continua treated in this study.

Houlsby and Puzrin (2000) again made use of the Legendre transformation here, making this framework different from those having been developed. The evolution laws, following several thermomechanical frameworks (Lemaitre and Chaboche, 1990; Maugin, 1992; Lemaitre, 1992), are derived by differentiating the dissipation potential, which is postulated to exist. The whole problem of specifying a constitutive law is now reduced to specifying two potentials: the free energy and the dissipation potential. However, things are different here. Instead of postulating the existence of a pseudo dissipation potential, the dissipation in the original framework is assumed to be a function of the thermodynamics state of the material and the rate of change of state. It can be expressed variously as:

$$d = d^{u}\left(\varepsilon_{ij},\alpha_{ij},\alpha_{d},s,\dot{\alpha}_{ij},\dot{\alpha}_{d}\right) \geq 0 \tag{3.19a}$$

$$d = d^{f}\left(\varepsilon_{ij},\alpha_{ij},\alpha_{d},s,\dot{\alpha}_{ij},\dot{\alpha}_{d}\right) \geq 0 \tag{3.19b}$$

$$d = d^{h}\left(\varepsilon_{ij},\alpha_{ij},\alpha_{d},s,\dot{\alpha}_{ij},\dot{\alpha}_{d}\right) \geq 0 \tag{3.19c}$$

$$d = d^{g}\left(\varepsilon_{ij},\alpha_{ij},\alpha_{d},s,\dot{\alpha}_{ij},\dot{\alpha}_{d}\right) \geq 0 \tag{3.19d}$$

depending on the energy function used. Using the fact that the dissipation of a rate-independent material must be a homogeneous first order function in the rate $\dot{\alpha}_{ij}$, and $\dot{\alpha}_{d}$ (Houlsby and Puzrin, 2000), we have (Euler's theorem):

$$d = \frac{\partial d}{\partial \dot{\alpha}_{ij}}\dot{\alpha}_{ij} + \frac{\partial d}{\partial \dot{\alpha}_{d}}\dot{\alpha}_{d} = \chi_{ij}\dot{\alpha}_{ij} + \chi_{d}\dot{\alpha}_{d} \tag{3.20}$$

with the definition of the dissipative generalized stresses: $\chi_{ij} = \partial d / \partial \dot{\alpha}_{ij}$ and $\chi_d = \partial d / \partial \dot{\alpha}_d$. The consequences of keeping $\overline{\chi}_{ij}$ and χ_{ij} as well as $\overline{\chi}_d$ and χ_d separate directly follow this definition. Comparing (3.15) and (3.20), one obtains

$$(\overline{\chi}_{ij} - \chi_{ij})\dot{\alpha}_{ij} = 0 \tag{3.21}$$

$$(\overline{\chi}_d - \chi_d)\dot{\alpha}_d = 0 \tag{3.22}$$

As χ_{ij} may be a function of $\dot{\alpha}_{ij}$, it can be concluded here that $\overline{\chi}_{ij} - \chi_{ij}$ is always orthogonal to $\dot{\alpha}_{ij}$. However, as argued by Ziegler (1983) and presented by Houlsby and Puzrin (2000) and Walsh and Tordesillas (2004), a rather wide range of classes of materials can be described by enforcement of the stronger condition $\overline{\chi}_{ij} = \chi_{ij}$. This condition is equivalent to Ziegler's orthogonality condition and was adopted in the framework by Houlsby and Puzrin (2000). For the equality (3.22), with the scalar $\dot{\alpha}_d$, it is readily seen that $\overline{\chi}_d = \chi_d$ for $\dot{\alpha}_d \neq 0$.

The Legendre transformation is used for interchanging internal variables and their corresponding dissipative generalized stresses. In the original framework, since the dissipation function is homogeneous first order, the Legendre transformation is degenerate (Collins and Houlsby, 1997) and the yield function, as the transform of the dissipation function, is the result of this. However things are different here as there are two separate internal variables representing the two dissipation processes due to damage and plasticity respectively. In a similar way, we have

$$\chi_{ij}\dot{\alpha}_{ij} + \chi_d\dot{\alpha}_d - d_p - d_d = 0 \tag{3.23}$$

in which the dissipation d has been assumed to be decomposed into two parts, corresponding to the energies dissipated due to plasticity and damage mechanisms. No generality is lost here, as damage and plastic flow can be considered as independent processes and can occur alone (Lemaitre and Chaboche, 1990). This decomposition of energy dissipation has been adopted by several researchers (Simo and Ju, 1987; Ju, 1989; Lemaitre and Chaboche, 1990; Lemaitre, 1992; Walsh and Tordesillas, 2004).

For rate-independent materials, the Legendre transformation of d_p and d_d gives us the yield and damage functions (see Houlsby and Puzrin, 2000)

$$\lambda_p y_p = \chi_{ij}\dot{\alpha}_{ij} - d_p = 0 \tag{3.24}$$

$$\lambda_p y_p = \chi_d\dot{\alpha}_d - d_d = 0 \tag{3.25}$$

or, using the fact that d_p and d_d are homogeneous first order, we have

$$\lambda_p y_p = \left(\chi_{ij} - \frac{\partial d}{\partial \dot{\alpha}_{ij}} \right) \dot{\alpha}_{ij} = 0 \tag{3.26}$$

$$\lambda_d y_d = \left(\chi_d - \frac{\partial d}{\partial \dot{\alpha}_d} \right) \dot{\alpha}_d = 0 \tag{3.27}$$

where λ_p and λ_d are non-negative scalar multipliers playing the same role as that of the plasticity multiplier in conventional plasticity. Therefore, we obtain two "yield" functions, one of which is that concerned with the internal variable α_{ij} and, as in the original framework, is denoted here as the yield function. The new function here is of similar form and related to the damage process. Unlike the yield function, which can only be obtained by eliminating $\dot{\alpha}_{ij}$ from equations $\chi_{ij} - \partial d / \partial \dot{\alpha}_{ij} = 0$ (Houlsby and Puzrin, 2000), the damage function in this case can directly be obtained from (3.27). Using the fact that $\dot{\alpha}_d$ is non-zero during the damage process, we have the expression of the damage function

$$y_d = \chi_d - \frac{\partial d}{\partial \dot{\alpha}_d} = 0 \tag{3.28}$$

The flow rules can be adopted here

$$\dot{\alpha}_{ij} = \lambda_p \frac{\partial y_p}{\partial \chi_{ij}} \tag{3.29}$$

and

$$\dot{\alpha}_d = \lambda_d \frac{\partial y_d}{\partial \chi_d} \tag{3.30}$$

The above is merely a brief illustration of the adopted thermodynamic approach of the study. More details can be found in relevant papers (Collins and Houlsby, 1997; Houlsby and Puzrin, 2000; Houlsby and Puzrin, 2002). In the approach, the yield and damage functions occur naturally from the degenerate Legendre transformation of the dissipation function. This distinguishes the adopted thermodynamic approach from existing ones. The key difference, in comparison with some other thermodynamics approaches (Simo and Ju, 1987; Lemaitre and Chaboche, 1990; Lemaitre, 1992; Maugin, 1992), is the use of the fundamental constitutive assumptions ($\overline{\chi}_{ij} = \chi_{ij}$ and/or $\overline{\chi}_d = \chi_d$) equivalent to Ziegler's orthogonality conditions. Those assumptions, when

combined with the Legendre transformation, help to avoid specifying an expression for the dissipation potential and then create ways for the derivation of the yield and damage loading functions. In addition, unlike conventional plasticity, where the flow rule is obtained from the differentiation of the plastic potential (or the yield surface for associated flow rule) with respect to the stresses, in expression (3.29) the plastic strain rates are obtained by differentiating the yield surface with respect to the dissipative generalized stresses χ_{ij}. This results in the possibility of deriving non-associated plasticity within this framework (Collins and Houlsby, 1997). An illustration of this will be shown in the next section.

3.3 Formulation of elasto-plastic-damageable models

This section presents a simple formulation for continuum elasto-plastic-damageable models based on the above thermodynamic approach (by Houlsby and Puzrin, 2000). The parabolic Drucker-Prager yield criterion (Hansen *et al.*, 2001) is adopted and its derivation incorporated in the formulation. This yield criterion in this case is coupled with a damage criterion, which is based on the damage energy release rate. An isotropic hardening rule with a non-associated flow rule is assumed, thus making the stress and generalized stress in the original framework coincide. The derivation of a constitutive model here can be based on either strain- or stress-based formulation, which employs the Helmholtz or Gibbs free energy potentials respectively. They are all presented in the following sub-sections.

3.3.1 Strain-based formulation

For the strain-based formulation, the following Helmholtz energy is used

$$f = \frac{(1-\alpha_d)E}{2(1+\nu)}\left[(\varepsilon_{ij}-\alpha_{ij})(\varepsilon_{ij}-\alpha_{ij})+\frac{\nu}{(1-2\nu)}(\varepsilon_{kk}-\alpha_{kk})(\varepsilon_{ll}-\alpha_{ll})\right] \tag{3.31}$$

or in a more convenient form

$$f = \frac{1}{2}(1-\alpha_d)a_{ijkl}(\varepsilon_{ij}-\alpha_{ij})(\varepsilon_{kl}-\alpha_{kl}) \tag{3.32}$$

in which α_{ij} and α_d are internal variables characterizing the plasticity and damage processes; a_{ijkl} is the elasticity stiffness tensor expressed in terms of elasticity modulus E and Poisson's ratio ν

$$a_{ijkl} = \frac{E}{2(1+\nu)}\left[\frac{2\nu}{1-2\nu}\delta_{ij}\delta_{kl} + \delta_{ik}\delta_{jl} + \delta_{il}\delta_{jk}\right]$$

Use of loading functions (yield and damage functions) or dissipation function is interchangeable in the framework. Here, a dissipation function, which is in fact worked out from an energy-based damage function and a parabolic Drucker-Prager yield function (see section 3.3.1.2 for details), is used and takes the form

$$d = F_1(\alpha_d)\dot{\alpha}_d + \left[\frac{k}{\beta} - (1-r)\sigma_{kk}\right]\frac{\dot{\alpha}_{kk}}{3r} + \frac{3\beta r\dot{\alpha}'_{ij}\dot{\alpha}'_{ij}}{2\dot{\alpha}_{kk}} + \Lambda C \tag{3.33}$$

where $F_1(\alpha_d)$ is a positive and increasing function associated with the damage process; this function in fact decides the rate of damage dissipation; C is a constraint defining the accumulated plastic strain; Λ is the Lagrangean multiplier associated with the constraint C (see Houlsby and Puzrin, 2000 for the introduction of a constraint into the modelling); $0 < r \le 1$ is a factor related to the deviation of the plastic strain rate vector $\dot{\alpha}_{ij}$ from the normal vector to the yield surface in true stress space; β and k are parameters of the parabolic Drucker-Prager yield criterion

$$\beta(\alpha_d, \kappa) = \frac{f_{cy}(\alpha_d, \kappa) - f_{ty}(\alpha_d, \kappa)}{3} \tag{3.34}$$

$$k(\alpha_d, \kappa) = \frac{f_{cy}(\alpha_d, \kappa) f_{ty}(\alpha_d, \kappa)}{3} \tag{3.35}$$

In the above expression, f_{cy} and f_{ty} denote the yield stresses in uniaxial compression and uniaxial tension respectively. As the material undergoes two dissipation processes due to damage and plasticity, f_{cy} and f_{ty} depend on both a hardening parameter κ and damage indicator α_d. The hardening parameter κ in turn can be determined either from the accumulated plastic strain ε_p (strain hardening) or the plastic work W_p (work hardening).

In the expression of the dissipation function (3.33), it should be noted that $\dot{\alpha}_d$ must be non-negative to assure the non-negativeness of the damage dissipation $d_d = F_1(\alpha_d)\dot{\alpha}_d$. This can be enforced using the Macaulay bracket $\langle\ \rangle$ for the rate of damage $\dot{\alpha}_d$. Alternatively, a more mathematically rigorous form of the dissipation function d_d can be used here, employing the indicator function $\delta_{0+}(\dot{\alpha}_d)$ which vanishes if $\dot{\alpha}_d \ge 0$ and goes to infinity for any physically impossible value of $\dot{\alpha}_d$ (Nguyen, 2002). The damage function d_d in that case is of the form:

$d_d = F_1(\alpha_d)\dot{\alpha}_d + \delta_{0+}(\dot{\alpha}_d)$. For the sake of simplicity in the formulation, those mathematical treatments are not used here.

The strain hardening hypothesis is adopted in this study, although the formulation can also be adapted to employing work hardening plasticity without any difficulty. For strain hardening plasticity we have $\kappa = \varepsilon_p$, with the constraint C being defined

$$C = \dot{\varepsilon}_p - c\sqrt{\dot{\alpha}_{ij}\dot{\alpha}_{ij}} = 0 \tag{3.36}$$

where $c = \sqrt{2/3}$ is a constant aiming at making the definition of $\dot{\varepsilon}_p$ agree with the uniaxial plastic strain in uniaxial test. This agreement is in fact valid only for pressure-independent yield criteria (e.g. Von Mises and Tresca criteria), which is unfortunately not the case in this study. However, for simplicity, $c = \sqrt{2/3}$, as in pressure-independent plasticity, is adopted here. The resulting unwanted effects of choosing this value in the model responses will be mentioned in the next chapter.

The derivation of the constitutive models here follows standard procedures established beforehand in the original framework (Houlsby and Puzrin, 2000), and partly illustrated in the preceding sections. The stress and generalized stresses are derived from the energy function:

$$\sigma_{ij} = \frac{\partial f}{\partial \varepsilon_{ij}} = (1-\alpha_d)a_{ijkl}(\varepsilon_{kl} - \alpha_{kl}) \tag{3.37}$$

$$\overline{\chi}_{ij} = -\frac{\partial f}{\partial \alpha_{ij}} = \sigma_{ij} \tag{3.38}$$

$$\overline{\chi}_d = -\frac{\partial f}{\partial \alpha_d} = \frac{1}{2}a_{ijkl}(\varepsilon_{ij} - \alpha_{ij})(\varepsilon_{kl} - \alpha_{kl}) \tag{3.39}$$

$$\overline{\chi}_p = -\frac{\partial f}{\partial \varepsilon_p} = 0 \tag{3.40}$$

In (3.39), the thermodynamic force $\overline{\chi}_d$ conjugate to the damage indicator α_d can be identified as the strain energy release rate with respect to α_d under constant stress (Lemaitre, 1992). The dissipative generalized stresses in this case can be obtained from the dissipation function in a way similar to the above derivation of the stress and generalized stresses:

$$\chi_{ij} = \frac{\partial d}{\partial \dot{\alpha}_{ij}} = \left[\frac{k}{\beta} - (1-r)\sigma_{kk} \right] \frac{\delta_{ij}}{3r} + \frac{3\beta r \dot{\alpha}'_{ij}}{\dot{\alpha}_{kk}} - \frac{3\beta r \dot{\alpha}'_{mn} \dot{\alpha}'_{mn}}{2} \frac{\delta_{ij}}{\dot{\alpha}_{kk} \dot{\alpha}_{ll}} - \frac{c\Lambda \dot{\alpha}_{ij}}{\sqrt{\dot{\alpha}_{kl} \dot{\alpha}_{kl}}} \tag{3.41}$$

$$\chi_d = \frac{\partial d}{\partial \dot{\alpha}_d} = F_1(\alpha_d) \tag{3.42}$$

$$\chi_p = \frac{\partial d}{\partial \dot{\varepsilon}_p} = \Lambda \tag{3.43}$$

The application of the fundamental hypothesis $\overline{\chi}_p = \chi_p$ (Houlsby and Puzrin, 2000) directly leads to $\Lambda = 0$. The yield criterion in this case is derived by eliminating $\dot{\alpha}_{ij}$ from equation (3.41). It is a result of the degenerate Legendre transformation of the dissipation function, in which the true stress σ_{ij} appearing in the square bracket of (3.41) is considered as a passive variable in the transformation (see Collins and Houlsby, 1997). From the expression of χ_{ij}, the following can be obtained

$$\chi_{kk} = \left[\frac{k}{\beta r} - \frac{(1-r)\sigma_{kk}}{r} \right] - \frac{9\beta r \dot{\alpha}'_{ij} \dot{\alpha}'_{ij}}{2\dot{\alpha}_{mm} \dot{\alpha}_{nn}} \tag{3.44}$$

$$\chi'_{ij} = \frac{3\beta r \dot{\alpha}'_{ij}}{\dot{\alpha}_{kk}} \tag{3.45}$$

From (3.45), we obtain

$$\dot{\alpha}'_{mn} \dot{\alpha}'_{mn} = \frac{\chi'_{ij} \chi'_{ij} \dot{\alpha}_{kk} \dot{\alpha}_{ll}}{9\beta^2 r^2} \tag{3.46}$$

Substitution of (3.46) into (3.44) results in

$$\chi_{kk} = \left[\frac{k}{\beta r} - \frac{(1-r)\sigma_{kk}}{r} \right] - \frac{\chi'_{ij} \chi'_{ij}}{2\beta r} \tag{3.47}$$

Finally, after rearranging the above expression, we obtain the yield surface in dissipative generalized stress space

$$y_p = \beta \left[r\chi_{kk} + (1-r)\sigma_{kk} \right] + \frac{\chi'_{ij} \chi'_{ij}}{2} - k = 0 \tag{3.48}$$

This yield function can be rewritten in terms of the true stress σ_{ij}, using the condition $\chi_{ij} = \overline{\chi}_{ij} = \sigma_{ij}$ (Houlsby and Puzrin, 2000):

$$y_p^* = \beta \sigma_{kk} + \frac{\sigma'_{ij} \sigma'_{ij}}{2} - k = 0 \tag{3.49}$$

The above expression resembles the linear Drucker-Prager yield criterion. However, compared to the linear Drucker-Prager criterion, there is no square root in the second invariant of the deviatoric stress tensor in (3.49).

As mentioned in the preceding section and can be seen in (3.48), the normality of the flow rule here applies to the yield function y_p in generalized stress space χ_{ij} (Collins and Houlsby, 1997), not in true stress space σ_{ij}. This turns the flow rule into a non-associated flow rule in true stress space, with the parameter r governing the deviation of the plastic strain rate from the normal vector to the yield surface y_p^*.

$$\dot{\alpha}_{ij} = \lambda_p \frac{\partial y_p}{\partial \chi_{ij}} = \lambda_p \left(\beta\, r \delta_{ij} + \chi'_{ij} \right) = \lambda_p \left(\beta\, r \delta_{ij} + \sigma'_{ij} \right) \tag{3.50}$$

The damage criterion is derived in a way similar to the derivation of the yield function, and also as a result of the singular Legendre transformation of the dissipation function.

$$y_d = \chi_d - F_1(\alpha_d) = 0 \tag{3.51}$$

Since α_d is only a scalar variable, there is actually no "flow rule" for the damage process, and the damage multiplier, which resembles that in plasticity, coincides with the scalar damage increment $\dot{\alpha}_d$

$$\dot{\alpha}_d = \lambda_d \frac{\partial y_d}{\partial \chi_d} = \lambda_d \tag{3.52}$$

The assumption on the equality of $\overline{\chi}_d$ and χ_d also holds, turning the above damage loading function to

$$y_d = \frac{1}{2} a_{ijkl} \left(\varepsilon_{ij} - \alpha_{ij} \right) \left(\varepsilon_{kl} - \alpha_{kl} \right) - F_1(\alpha_d) = 0 \tag{3.53}$$

The obtained system of constitutive relations governing the behaviour of the proposed model can be rewritten as follows

$$\sigma_{ij} = \frac{\partial f}{\partial \varepsilon_{ij}} = (1 - \alpha_d) a_{ijkl} \left(\varepsilon_{kl} - \alpha_{kl} \right) \tag{3.54}$$

$$y_p = \beta \left[r \chi_{kk} + (1 - r) \sigma_{kk} \right] + \frac{\chi'_{ij} \chi'_{ij}}{2} - k = 0 \tag{3.55}$$

$$y_p^* = \beta\, \sigma_{kk} + \frac{\sigma'_{ij} \sigma'_{ij}}{2} - k = 0 \tag{3.56}$$

$$y_d = a_{ijkl}\left(\varepsilon_{ij} - \alpha_{ij}\right)\left(\varepsilon_{kl} - \alpha_{kl}\right) - F_1\left(\alpha_d\right) = 0 \tag{3.57}$$

with two evolution rules:

$$\dot{\alpha}_{ij} = \lambda_p \frac{\partial y_p}{\partial \chi_{ij}} = \lambda_p \left(\beta\, r \delta_{ij} + \chi'_{ij}\right) = \lambda_p \left(\beta\, r \delta_{ij} + \sigma'_{ij}\right) \tag{3.58}$$

$$\dot{\alpha}_d = \lambda_d \frac{y_d}{\partial \chi_d} = \lambda_d \tag{3.59}$$

3.3.1.1 Evolution rules of internal variables, and tangent stiffness tensor

The evolution rules of internal variables are obtained in this section. Here the difference from some other continuum damage mechanics approaches (Lee and Fenves, 1998; Peerlings, 1999; Jirasek and Patzak, 2002) lies in the fact that the evolutions of the damage indicator α_d and of plastic strain α_{ij} are implicitly defined through the relations (3.54-3.59). The procedures used here resemble those for the derivation of plastic strain increment $\dot{\alpha}_{ij}$ in conventional plasticity. Following those procedures, the system (3.54-3.59) is rewritten in general incremental form as follows

$$\dot{\sigma}_{ij} = \left(1 - \alpha_d\right) a_{ijkl}\left(\dot{\varepsilon}_{kl} - \dot{\alpha}_{kl}\right) - a_{ijkl}\left(\varepsilon_{kl} - \alpha_{kl}\right)\dot{\alpha}_d \tag{3.60}$$

$$\dot{y}^*_p = \frac{\partial y^*_p}{\partial \sigma_{ij}} \dot{\sigma}_{ij} + \frac{\partial y^*_p}{\partial \alpha_d} \dot{\alpha}_d + \frac{\partial y^*_p}{\partial \varepsilon_p} \dot{\varepsilon}_p = 0 \tag{3.61}$$

$$\dot{y}_d = a_{ijkl}\left(\varepsilon_{ij} - \alpha_{ij}\right)\left(\dot{\varepsilon}_{kl} - \dot{\alpha}_{kl}\right) - \frac{\partial F_1}{\partial \alpha_d} \dot{\alpha}_d = 0 \tag{3.62}$$

The damage increment $\dot{\alpha}_d$ can be directly obtained from equation (3.62):

$$\dot{\alpha}_d = \frac{a_{ijkl}\left(\varepsilon_{ij} - \alpha_{ij}\right)\left(\dot{\varepsilon}_{kl} - \dot{\alpha}_{kl}\right)}{\dfrac{\partial F_1}{\partial \alpha_d}} \tag{3.63}$$

It is noted that for pure damage processes, the plastic strain increments vanish and the damage evolution can be directly obtained from the above expression. Substituting (3.63), along with the stress increment (3.60), into (3.61) one gets

$$\dot{y}_p^* = \frac{\partial y_p^*}{\partial \sigma_{ij}}(1-\alpha_d)a_{ijkl}(\dot{\varepsilon}_{kl}-\dot{\alpha}_{kl}) + \frac{\partial y_p^*}{\partial \varepsilon_p}\dot{\varepsilon}_p + \left[\frac{\partial y_p^*}{\partial \alpha_d} - \frac{\partial y_p^*}{\partial \sigma_{ij}}a_{ijkl}(\varepsilon_{kl}-\alpha_{kl})\right]\frac{a_{mnpq}(\varepsilon_{mn}-\alpha_{mn})(\dot{\varepsilon}_{pq}-\dot{\alpha}_{pq})}{\frac{\partial F_1}{\partial \alpha_d}} = 0 \tag{3.64}$$

Using the flow rule (3.58) and the constraint (3.36), we obtain the increment of the accumulated plastic strain

$$\dot{\varepsilon}_p = c\sqrt{\dot{\alpha}_{ij}\dot{\alpha}_{ij}} = c\lambda_p\sqrt{\frac{\partial y_p}{\partial \chi_{ij}}\frac{\partial y_p}{\partial \chi_{ij}}} \tag{3.65}$$

The second term in (3.64) becomes

$$\frac{\partial y_p^*}{\partial \varepsilon_p}\dot{\varepsilon}_p = c\lambda_p\frac{\partial y_p^*}{\partial \varepsilon_p}\sqrt{\frac{\partial y_p}{\partial \chi_{ij}}\frac{\partial y_p}{\partial \chi_{ij}}} \tag{3.66}$$

Again, using (3.58), and substituting it into (3.64), we obtain an equation containing only λ_p as a variable to be determined. Solution of that equation gives

$$\lambda_p = \frac{M_{kl}\dot{\varepsilon}_{kl}}{M_{mn}\frac{\partial y_p}{\partial \chi_{mn}} - c\frac{\partial y_p^*}{\partial \varepsilon_p}\sqrt{\frac{\partial y_p}{\partial \chi_{ij}}\frac{\partial y_p}{\partial \chi_{ij}}}} \tag{3.67}$$

in which

$$M_{kl} = (1-\alpha_d)\frac{\partial y_p^*}{\partial \sigma_{ij}}a_{ijkl} + \left[\frac{\partial y_p^*}{\partial \alpha_d} - \frac{\partial y_p^*}{\partial \sigma_{mn}}a_{mnpq}(\varepsilon_{pq}-\alpha_{pq})\right]\frac{a_{ijkl}(\varepsilon_{ij}-\alpha_{ij})}{\frac{\partial F_1}{\partial \alpha_d}} \tag{3.68}$$

Using the computed plasticity multiplier, the evolutions of damage indicator α_d and plastic strain α_{ij} are derived as follows

$$\dot{\alpha}_d = \frac{a_{ijkl}(\varepsilon_{ij}-\alpha_{ij})}{\frac{\partial F_1}{\partial \alpha_d}}\left[\dot{\varepsilon}_{kl} - \frac{\frac{\partial y_p}{\partial \chi_{kl}}M_{mn}\dot{\varepsilon}_{mn}}{M_{pq}\frac{\partial y_p}{\partial \chi_{pq}} - c\frac{\partial y_p^*}{\partial \varepsilon_p}\sqrt{\frac{\partial y_p}{\partial \chi_{pq}}\frac{\partial y_p}{\partial \chi_{pq}}}}\right] \tag{3.69}$$

$$\dot{\alpha}_{ij} = \frac{\dfrac{\partial y_p}{\partial \chi_{ij}} M_{kl} \dot{\varepsilon}_{kl}}{M_{mn} \dfrac{\partial y_p}{\partial \chi_{mn}} - c \dfrac{\partial y_p^*}{\partial \varepsilon_p} \sqrt{\dfrac{\partial y_p}{\partial \chi_{pq}} \dfrac{\partial y_p}{\partial \chi_{pq}}}} \tag{3.70}$$

The tangent stiffness relation follows straightforwardly. We substitute (3.63) into the expression of the stress increment to obtain

$$\dot{\sigma}_{ij} = \left[(1-\alpha_d) a_{ijkl} - a_{ijpq} \left(\varepsilon_{pq} - \alpha_{pq} \right) \frac{a_{mnkl} \left(\varepsilon_{mn} - \alpha_{mn} \right)}{\dfrac{\partial F_1}{\partial \alpha_d}} \right] \left(\dot{\varepsilon}_{kl} - \dot{\alpha}_{kl} \right) \tag{3.71}$$

After substituting (3.70) into the above expression and rearranging the obtained expression, we have

$$\dot{\sigma}_{ij} = C^t_{ijrs} \dot{\varepsilon}_{rs} \tag{3.72}$$

where C^t_{ijrs} is the tangent stiffness tensor defined by

$$C^t_{ijrs} = \left[\begin{array}{l} (1-\alpha_d) a_{ijkl} - \\ a_{ijpq} \left(\varepsilon_{pq} - \alpha_{pq} \right) \dfrac{a_{mnkl} \left(\varepsilon_{mn} - \alpha_{mn} \right)}{\dfrac{\partial F_1}{\partial \alpha_d}} \end{array} \right] \left[\delta_{kr} \delta_{ls} - \frac{\dfrac{\partial y_p}{\partial \chi_{kl}} M_{rs}}{M_{tu} \dfrac{\partial y_p}{\partial \chi_{tu}} - c \dfrac{\partial y_p^*}{\partial \varepsilon_p} \sqrt{\dfrac{\partial y_p}{\partial \chi_{tu}} \dfrac{\partial y_p}{\partial \chi_{tu}}}} \right] \tag{3.73}$$

3.3.1.2 On the thermodynamic admissibility of the derived model

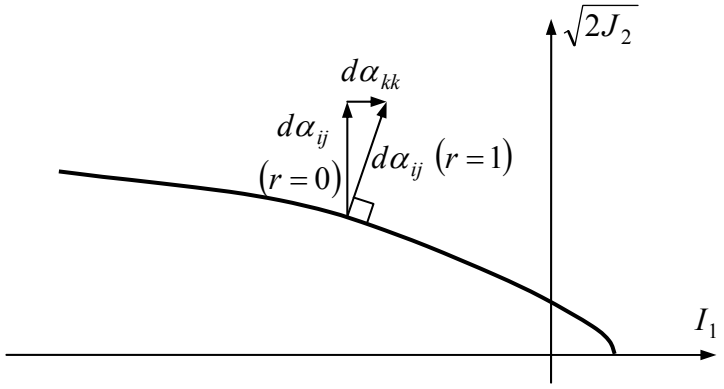

Figure 3.1: Parabolic Drucker-Prager yield surface in the meridian plane

At this point, it is necessary and worthwhile to consider the thermodynamic admissibility of the proposed model. As mentioned in the preceding section, for a thermodynamically admissible process, the Clausius-Duhem inequality, represented

here by the positiveness of the dissipation function d, must be satisfied. To simplify the condition, the thermal term can be neglected and it can be stated that the dissipations due to damage and plasticity processes (d_d and d_p, respectively) are all non-negative, which is in fact more stringent than the Second Law of Thermodynamics.

The first part of the dissipation (3.33) is that of damage process, and can be assured to be non-negative by considering the fact that damage is unrecoverable: $\dot{\alpha}_d \geq 0$, and choosing the appropriate non-negative function F_1. The dissipation due to plastic deformation consists of the second and third terms of (3.33). As can be readily seen from (3.50) and depicted in figure (3.1), $\dot{\alpha}_{kk}$ is always positive for any plastic deformation process, provided that values of r are always in the range $0 < r \leq 1$, which decides the deviation of plastic strain increment $\dot{\alpha}_{ij}$ from the vector normal to the yield surface in true stress space. Therefore, the sign of plastic dissipation only partly depends upon the expression in the square bracket of the second term of (3.33).

From the yield function y_p (see 3.48), which never admits a positive value for any plastically admissible process, one can obtain:

$$\frac{k}{\beta} - (1-r)\sigma_{kk} \geq r\chi_{kk} + \frac{\chi'_{ij}\chi'_{ij}}{2\beta} \tag{3.74}$$

This, in combination with the condition $\chi_{ij} = \overline{\chi}_{ij} = \sigma_{ij}$, shows that $k/\beta - (1-r)\sigma_{kk}$ is always positive, thus fulfilling the thermodynamic requirement on the positiveness of the dissipation function.

The inverse process, from the yield and damage functions (3.48 and 3.51) to the dissipation function (3.33), is also in principle derivable, following the procedures in Houlsby and Puzrin (2000). For the damage loading function $y_d = \chi_d - F_1(\alpha_d) = 0$ (3.51), it is easy to obtain χ_d in term of α_d and then substitute it into the dissipation expression $d_d = \chi_d \dot{\alpha}_d$ to obtain the damage dissipation function $d_d = F_1(\alpha_d)\dot{\alpha}_d$. A similar process can be carried out for the transformation from the yield function $y_p = 0$ to the dissipation function d_p of the plastic flow. For that, we rewrite the yield function (3.48) as

$$y_p = \beta\left[r\chi_{kk} + (1-r)\sigma_{kk}\right] + \frac{\chi'_{ij}\chi'_{ij}}{2} - k = 0 \tag{3.75}$$

The flow rule is

$$\dot{\alpha}_{ij} = \lambda_p \frac{\partial y_p}{\partial \chi_{ij}} = \lambda_p \left(\beta r \delta_{ij} + \chi'_{ij} \right) \tag{3.76}$$

Separating the deviatoric and volumetric components of the plastic strain rate tensor $\dot{\alpha}_{ij}$, we have

$$\dot{\alpha}_{kk} = 3\beta r \lambda_p \tag{3.77}$$

and

$$\dot{\alpha}'_{ij} = \lambda_p \chi'_{ij} \tag{3.78}$$

It follows from (3.75), (3.77) and (3.78) that

$$\chi'_{ij} = \frac{3\beta r \dot{\alpha}'_{ij}}{\dot{\alpha}_{kk}} \tag{3.79}$$

and

$$\chi_{kk} = \frac{1}{\beta r} \left[k - \beta (1-r) \sigma_{kk} - \frac{9\beta^2 r^2 \dot{\alpha}'_{ij} \dot{\alpha}'_{ij}}{2\dot{\alpha}_{kk} \dot{\alpha}_{ll}} \right] \tag{3.80}$$

The expression of the dissipation d_p is

$$d_p = \chi_{ij} \dot{\alpha}_{ij} = \chi'_{ij} \dot{\alpha}'_{ij} + \frac{1}{3} \chi_{kk} \dot{\alpha}_{kk} \tag{3.81}$$

Substitution of (3.79) and (3.80) into (3.81) gives us the dissipation function d_p

$$d_p = \frac{3\beta r \dot{\alpha}'_{ij} \dot{\alpha}'_{ij}}{2\dot{\alpha}_{kk}} + \left[\frac{k}{\beta} - (1-r) \sigma_{ll} \right] \frac{\dot{\alpha}_{kk}}{3r} \tag{3.82}$$

Additional conditions, which are that defined in (3.74) and $\dot{\alpha}_{kk} > 0$, are needed here to make (3.82) meaningful. This is due to the fact that the mathematical preservation of the conditions (3.74) and $\dot{\alpha}_{kk} > 0$ cannot be strictly assured during the transformation. In other words, it cannot be assured that those conditions are appropriately transformed following the procedures in the original framework. This motivates the use of more mathematically rigorous treatments based on convex analysis for the existing framework (Houlsby, 2004). Work on a more rigid formulation is still required, but unfortunately cannot be covered by the scope of this study.

3.3.2 Stress-based formulation

Stress-based damage-plasticity models can be derived in much the same way as that presented in the preceding section. A stress-based model here is based on the Gibbs free energy function.

$$g = -\frac{D_{ijkl}\sigma_{ij}\sigma_{kl}}{2(1-\alpha_d)} - \sigma_{ij}\alpha_{ij} \tag{3.83}$$

where

$$D_{ijkl} = \frac{1+\nu}{2E}\left(-\frac{2\nu}{1+\nu}\delta_{ij}\delta_{kl} + \delta_{ik}\delta_{jl} + \delta_{il}\delta_{jk}\right)$$

Compared to (3.33), the dissipation and its constraint in this case remain unchanged and are rewritten as follows

$$d = F_1(\alpha_d)\dot{\alpha}_d + \left[\frac{k}{\beta} - (1-r)\sigma_{kk}\right]\frac{\dot{\alpha}_{kk}}{3r} + \frac{3\beta r\dot{\alpha}'_{ij}\dot{\alpha}'_{ij}}{2\dot{\alpha}_{kk}} + \Lambda C \tag{3.84}$$

Following the same procedures (Houlsby and Puzrin, 2000) demonstrated in the preceding section on strain-based formulation, we end up here with the stress-elastic strain relationship and two loading functions, in which the yield function is exactly the same as that obtained in the strain-based formulation.

$$\varepsilon_{ij} = \frac{D_{ijkl}\sigma_{kl}}{1-\alpha_d} + \alpha_{ij} \tag{3.85}$$

$$y_p = \beta\left[r\chi_{kk} + (1-r)\sigma_{kk}\right] + \frac{\chi'_{ij}\chi'_{ij}}{2} - k = 0 \tag{3.86}$$

$$y^*_p = \beta\sigma_{kk} + \frac{\sigma'_{ij}\sigma'_{ij}}{2} - k = 0 \tag{3.87}$$

$$y_d = \frac{D_{ijkl}\sigma_{ij}\sigma_{kl}}{2(1-\alpha_d)^2} - F_1(\alpha_d) = 0 \tag{3.88}$$

The normality rules for damage and yielding processes also hold in this case, in which that for a yielding process only holds in generalized stress space. In a similar way to that in the previous section, the incremental stress-strain relationship can be derived from the above system (3.85, 3.87, and 3.88), all of which are written in incremental forms as follows

$$\dot{\varepsilon}_{ij} = \frac{D_{ijkl}\dot{\sigma}_{kl}}{1-\alpha_d} + \frac{D_{ijkl}\sigma_{kl}}{(1-\alpha_d)^2}\dot{\alpha}_d + \dot{\alpha}_{ij} \tag{3.89}$$

$$\dot{y}^*_p = \frac{\partial y^*_p}{\partial\sigma_{ij}}\dot{\sigma}_{ij} + \frac{\partial y^*_p}{\partial\alpha_d}\dot{\alpha}_d + \frac{\partial y^*_p}{\partial\varepsilon_p}\dot{\varepsilon}_p = 0 \tag{3.90}$$

$$\dot{y}_d = \frac{D_{ijkl}\sigma_{ij}\dot{\sigma}_{kl}}{(1-\alpha_d)^2} + \frac{D_{ijkl}\sigma_{ij}\sigma_{kl}}{(1-\alpha_d)^3}\dot{\alpha}_d - \frac{\partial F_1}{\partial \alpha_d}\dot{\alpha}_d = 0 \tag{3.91}$$

The plasticity multiplier λ_p, as a function of the stress increment $\dot{\sigma}_{ij}$, damage increment $\dot{\alpha}_d$ and some other quantities, can be obtained from (3.90)

$$\lambda_p = -\frac{\dfrac{\partial y_p^*}{\partial \sigma_{ij}}\dot{\sigma}_{ij} + \dfrac{\partial y_p^*}{\partial \alpha_d}\dot{\alpha}_d}{c\dfrac{\partial y_p^*}{\partial \varepsilon_p}\sqrt{\dfrac{\partial y_p}{\partial \chi_{kl}}\dfrac{\partial y_p}{\partial \chi_{kl}}}} \tag{3.92}$$

The plastic strain increment then follows

$$\dot{\alpha}_{ij} = \lambda_p \frac{\partial y_p}{\partial \chi_{ij}} = -\left[\frac{\dfrac{\partial y_p^*}{\partial \sigma_{mn}}\dot{\sigma}_{mn} + \dfrac{\partial y_p^*}{\partial \alpha_d}\dot{\alpha}_d}{c\dfrac{\partial y_p^*}{\partial \varepsilon_p}\sqrt{\dfrac{\partial y_p}{\partial \chi_{pq}}\dfrac{\partial y_p}{\partial \chi_{pq}}}}\right]\frac{\partial y_p}{\partial \chi_{ij}} \tag{3.93}$$

Substitution of the above expression into (3.89) results in the expression relating the stress, strain and damage increments

$$\dot{\varepsilon}_{ij} = \frac{D_{ijkl}\dot{\sigma}_{kl}}{1-\alpha_d} + \frac{D_{ijkl}\sigma_{kl}}{(1-\alpha_d)^2}\dot{\alpha}_d - \left[\frac{\dfrac{\partial y_p^*}{\partial \sigma_{kl}}\dot{\sigma}_{kl} + \dfrac{\partial y_p^*}{\partial \alpha_d}\dot{\alpha}_d}{c\dfrac{\partial y_p^*}{\partial \varepsilon_p}\sqrt{\dfrac{\partial y_p}{\partial \chi_{pq}}\dfrac{\partial y_p}{\partial \chi_{pq}}}}\right]\frac{\partial y_p}{\partial \chi_{ij}} \tag{3.94}$$

The stress increment can be obtained from the above expression

$$\dot{\sigma}_{kl} = \left\{\dot{\varepsilon}_{mn} - \left[\frac{D_{mnpq}\sigma_{pq}}{(1-\alpha_d)^2} - \frac{\dfrac{\partial y_p}{\partial \chi_{mn}}\dfrac{\partial y_p^*}{\partial \alpha_d}}{c\dfrac{\partial y_p^*}{\partial \varepsilon_p}\sqrt{\dfrac{\partial y_p}{\partial \chi_{pq}}\dfrac{\partial y_p}{\partial \chi_{pq}}}}\right]\dot{\alpha}_d\right\}\left[D^{st}_{mnkl}\right]^{-1} \tag{3.95}$$

where D^{st}_{ijkl} is the compliance tensor which is secant with respect to damage and tangent with respect to plasticity.

$$D_{ijkl}^{st} = \frac{D_{ijkl}}{1-\alpha_d} - \frac{\dfrac{\partial y_p}{\partial \chi_{ij}} \dfrac{\partial y_p^*}{\partial \sigma_{kl}}}{c \dfrac{\partial y_p^*}{\partial \varepsilon_p} \sqrt{\dfrac{\partial y_p}{\partial \chi_{pq}} \dfrac{\partial y_p}{\partial \chi_{pq}}}} \tag{3.96}$$

Substitute (3.95) into (3.91), we obtain an equation for the damage increment $\dot{\alpha}_d$

$$\frac{D_{ijkl}\sigma_{ij}\dot{\varepsilon}_{mn}\left[D_{mnkl}^{edp}\right]^{-1}}{(1-\alpha_d)^2} - \frac{D_{ijkl}\sigma_{ij}}{(1-\alpha_d)^2}\left[\frac{D_{mnpq}\sigma_{pq}}{(1-\alpha_d)^2} - \frac{\dfrac{\partial y_p}{\partial \chi_{mn}} \dfrac{\partial y_p^*}{\partial \alpha_d}}{c \dfrac{\partial y_p^*}{\partial \varepsilon_p} \sqrt{\dfrac{\partial y_p}{\partial \chi_{rs}} \dfrac{\partial y_p}{\partial \chi_{rs}}}}\right]\left[D_{mnkl}^{st}\right]^{-1}\dot{\alpha}_d \tag{3.97}$$
$$+ \frac{D_{ijkl}\sigma_{ij}\sigma_{kl}}{(1-\alpha_d)^3}\dot{\alpha}_d - \frac{\partial F_1}{\partial \alpha_d}\dot{\alpha}_d = 0$$

The damage evolution is directly obtained from the above equation

$$\dot{\alpha}_d = \frac{N_{mn}\dot{\varepsilon}_{mn}}{P} \tag{3.98}$$

where N_{mn} and P are defined as follows

$$N_{mn} = \frac{D_{ijkl}\sigma_{ij}\left[D_{mnkl}^{st}\right]^{-1}}{(1-\alpha_d)^2} \tag{3.99}$$

$$P = \frac{D_{ijkl}\sigma_{ij}}{(1-\alpha_d)^2}\left[\frac{D_{mnpq}\sigma_{pq}}{(1-\alpha_d)^2} - \frac{\dfrac{\partial y_p}{\partial \chi_{mn}} \dfrac{\partial y_p^*}{\partial \alpha_d}}{c \dfrac{\partial y_p^*}{\partial \varepsilon_p} \sqrt{\dfrac{\partial y_p}{\partial \chi_{rs}} \dfrac{\partial y_p}{\partial \chi_{rs}}}}\right]\left[D_{mnkl}^{st}\right]^{-1} - \frac{D_{ijkl}\sigma_{ij}\sigma_{kl}}{(1-\alpha_d)^3} + \frac{\partial F_1}{\partial \alpha_d} \tag{3.100}$$

The damage evolution can then be substituted into (3.94) to obtain the expression

$$\dot{\varepsilon}_{ij} = D_{ijkl}^{st}\dot{\sigma}_{kl} + \left[\frac{D_{ijpq}\sigma_{pq}}{(1-\alpha_d)^2} - \frac{\dfrac{\partial y_p}{\partial \chi_{ij}} \dfrac{\partial y_p^*}{\partial \alpha_d}}{c \dfrac{\partial y_p^*}{\partial \varepsilon_p} \sqrt{\dfrac{\partial y_p}{\partial \chi_{pq}} \dfrac{\partial y_p}{\partial \chi_{pq}}}}\right]\frac{N_{mn}\dot{\varepsilon}_{mn}}{P} \tag{3.101}$$

from which the stress increment $\dot{\sigma}_{kl}$ can be obtained

$$\dot{\sigma}_{kl} = \left[D^{st}_{ijkl}\right]^{-1}\left\{\delta_{im}\delta_{jn} - \left[\frac{D_{ijpq}\sigma_{pq}}{\left(1-\alpha_d\right)^2} - \frac{\dfrac{\partial y_p}{\partial \chi_{ij}}\dfrac{\partial y^*_p}{\partial \alpha_d}}{c\dfrac{\partial y^*_p}{\partial \varepsilon_p}\sqrt{\dfrac{\partial y_p}{\partial \chi_{rs}}\dfrac{\partial y_p}{\partial \chi_{rs}}}}\right]\frac{N_{mn}}{P}\right\}\dot{\varepsilon}_{mn} \tag{3.102}$$

The tangent stiffness tensor follows straightforwardly

$$C^{t}_{mnkl} = \left[D^{st}_{ijkl}\right]^{-1}\left\{\delta_{im}\delta_{jn} - \left[\frac{D_{ijpq}\sigma_{pq}}{\left(1-\alpha_d\right)^2} - \frac{\dfrac{\partial y_p}{\partial \chi_{ij}}\dfrac{\partial y^*_p}{\partial \alpha_d}}{c\dfrac{\partial y^*_p}{\partial \varepsilon_p}\sqrt{\dfrac{\partial y_p}{\partial \chi_{rs}}\dfrac{\partial y_p}{\partial \chi_{rs}}}}\right]\frac{N_{mn}}{P}\right\} \tag{3.103}$$

3.4 A comparison of two thermodynamic approaches

In this section a comparison between the thermodynamic framework by Houlsby and Puzrin (2000) and that proposed by Lemaitre (Lemaitre, 1992; Lemaitre and Chaboche, 1990) is carried out. The differences between the thermodynamic framework by Houlsby and Puzrin (2000) and the reference one by Lemaitre will be pointed out and discussed. To be convenient, the same terminology (Houlsby and Puzrin, 2000), as adopted and used in sections (3.2) and (3.3), is used here for both approaches. In addition, for the sake of simplicity, only a simple plasticity model based on these two frameworks is considered. In particular, the dissipation process here is assumed to be purely due to the plastic deformation process, with the Von Mises yield criterion and isotropic linear hardening. The flow rule is assumed to be associated, making the dissipation potential in the reference approach (Lemaitre, 1992) coincide with the yield function.

For the derivation of a Von Mises plasticity model based the adopted thermodynamic framework (by Houlsby and Puzrin, 2000), we omit the intermediate details and only present the necessary expressions. The two energy functions needed for the derivation of the model are

$$f = \frac{1}{2}a_{ijkl}\left(\varepsilon_{ij} - \alpha_{ij}\right)\left(\varepsilon_{kl} - \alpha_{kl}\right) \tag{3.104}$$

$$d = \left(\sigma_y + H\varepsilon_p\right)\sqrt{\frac{2}{3}\dot{\alpha}'_{kl}\dot{\alpha}'_{kl}} + \Lambda_1 C_1 + \Lambda_2 C_2 \tag{3.105}$$

where σ_y is defined as the initial yield threshold; the first constraint, $C_1 = \dot{\varepsilon}_p - \sqrt{2\dot{\alpha}_{ij}\dot{\alpha}_{ij}/3} = 0$, for the equivalent plastic strain has been defined in section (3.3); the second constraint, $C_2 = \dot{\alpha}_{kk} = 0$, is the plastic incompressibility condition for the derived Von Mises yield criterion; and Λ_1 and Λ_2 are simply two Lagrangian multipliers for the constraints C_1 and C_2 (see Houlsby and Puzrin, 2000). This simple model was in fact used as a typical example for the derivation of plasticity model from the thermodynamic framework presented in this study (Puzrin and Houlsby, 2001). The obtained relations governing the stress-strain behaviour of the model are

$$\sigma_{ij} = a_{ijkl}\left(\varepsilon_{kl} - \alpha_{kl}\right) \tag{3.106}$$

$$y_p = \sqrt{\frac{3}{2}\chi'_{ij}\chi'_{ij}} - \left(\sigma_y + H\varepsilon_p\right) = 0 \tag{3.107}$$

$$y_p^* = \sqrt{\frac{3}{2}\sigma'_{ij}\sigma'_{ij}} - \left(\sigma_y + H\varepsilon_p\right) = 0 \tag{3.108}$$

For Lemaitre's approach (Lemaitre and Chaboche, 1990; Lemaitre, 1992), without thermal effects, the dissipation expression (the Clausius-Duhem inequality) reads:

$$d = \sigma_{ij}\dot{\varepsilon}_{ij} - \dot{f} \geq 0 \tag{3.109}$$

which is exactly same in the two approaches compared here. The Helmholtz free energy function, following Lemaitre, is of the form

$$f = \frac{1}{2}a_{ijkl}\left(\varepsilon_{ij} - \alpha_{ij}\right)\left(\varepsilon_{kl} - \alpha_{kl}\right) + \frac{1}{2}Hr^2 \tag{3.110}$$

In the expression above, the first energy term is related to the elastic strain energy of the material while the second term is the energy associated with the plastic dissipation process. This decomposition of energy is in fact very common and has been adopted by several researchers in their thermodynamic approaches (Simo and Ju, 1987; Meschke *et al.*, 1998; Borino *et al.*, 1999; Salari *et al.*, 2004; Kratzig and Polling, 2004). Substituting the rate form of f into (3.109), after rearranging the obtained expression, one gets:

$$d = \sigma_{ij}\dot{\alpha}_{ij} - \frac{\partial f}{\partial r}\dot{r} \geq 0 \tag{3.111}$$

The stress and thermodynamic forces associated with the internal variables are derived as follows

$$\sigma_{ij} = \frac{\partial f}{\partial \varepsilon_{ij}^{e}} = a_{ijkl}\left(\varepsilon_{kl} - \alpha_{kl}\right) \tag{3.112}$$

$$\overline{\chi}_r = -\frac{\partial f}{\partial r} = -Hr \tag{3.113}$$

A loading function y_p, along with a potential of dissipation φ, is needed to define the plastic flow process. For the Von Mises yield criterion with associated flow rule, the following function was adopted (Lemaitre, 1992):

$$\varphi = y_p = \sqrt{\frac{3}{2}\sigma'_{ij}\sigma'_{ij}} + \overline{\chi}_r - \sigma_y = 0 \tag{3.114}$$

where $\overline{\chi}_r = -Hr$ is the hardening part of the evolving yield threshold $\sigma_y - \overline{\chi}_r$. The above function is similar to that in (3.108), with r in place of ε_p. It can readily be seen here that φ in fact acts as a plastic potential governing the plastic flow after yielding. Lemaitre and Chaboche (1990) also showed that φ must be convex, and contain the origin for any thermodynamically admissible process. The evolutions of internal variables (α_{ij} and r) are as follows:

$$\dot{\alpha}_{ij} = \lambda \frac{\partial \varphi}{\partial \sigma_{ij}} = \lambda \frac{\sqrt{\frac{3}{2}}\sigma'_{ij}}{\sqrt{\sigma'_{kl}\sigma'_{kl}}} \tag{3.115}$$

$$\dot{r} = \lambda \frac{\partial \varphi}{\partial \overline{\chi}_r} = \lambda \tag{3.116}$$

Using (3.115) and the definition of the equivalent plastic strain: $\dot{\varepsilon}_p = \sqrt{2\dot{\alpha}_{ij}\dot{\alpha}_{ij}/3}$, we obtain $\lambda = \dot{\varepsilon}_p$, resulting in the coincidence of $\dot{r}$ and $\dot{\varepsilon}_p$. The incremental stress-strain relationship can readily be derived following procedures illustrated in the preceding sections. However, that is not the purpose as the attention here is the difference of the two compared thermodynamic approaches rather than the computational aspects of the derived constitutive models.

The difference in the two energy functions (3.104) and (3.110) in the compared approaches results in two different dissipation functions. In Lemaitre's approach, the dissipation function can be obtained from the adopted yield function y_p and the dissipation potential φ. This process is in fact similar to that used by Houlsby and Puzrin (2000) based on the Legendre transformation of the yield and dissipation functions (Collins and Houlsby, 1998). From (3.115), it can be seen that $\dot{\alpha}_{ij} = \dot{\alpha}'_{ij}$ and

$\dot{\alpha}_{kk} = 0$, showing the incompressibility of the plastic deformation. The plasticity multiplier λ is obtained in terms of $\dot{\alpha}_{ij}$ either from (3.116), or by "squaring" both sides of (3.115), yielding:

$$\lambda = \sqrt{\frac{2}{3}\dot{\alpha}'_{ij}\dot{\alpha}'_{ij}} \tag{3.117}$$

Therefore, the dissipation (3.111) turns out to be:

$$d = \sigma_{ij}\dot{\alpha}_{ij} - \frac{\partial f}{\partial r}\dot{r} = \frac{\sigma'_{ij}\sigma'_{ij}\sqrt{\dot{\alpha}'_{kl}\dot{\alpha}'_{kl}}}{\sqrt{\sigma'_{mn}\sigma'_{mn}}} - Hr\sqrt{\frac{2}{3}\dot{\alpha}'_{kl}\dot{\alpha}'_{kl}} \tag{3.118}$$

After some mathematical manipulations, using the yield function (3.114), we obtain the dissipation function d:

$$d = \sigma_y\sqrt{\frac{2}{3}\dot{\alpha}'_{kl}\dot{\alpha}'_{kl}} \tag{3.119}$$

The table overleaf summarizes the above comparisons

At the first glance, the two approaches are slightly different from each other in the choice of the Helmholtz free energy function f. In Lemaitre's approach, part of the energy which should have dissipated during the plastic flow process goes to the second term of the energy function (the term $Hr^2/2$). This results in the difference in the derived dissipation function (3.119), compared to that in the approach by Houlsby and Puzrin (2000). However, the main distinction of the adopted approach with respect to that of Lemaitre is the use of standard procedures within a well-defined thermodynamic framework (Houlsby and Puzrin, 2000) to formulate a constitutive model. The Legendre transformation to interchange the yield function and the dissipation function is used in these standard procedures. In addition, for the use of the Legendre transformation, the generalized stress $\overline{\chi}_{ij}$ and the dissipative generalized stress χ_{ij} are kept as separate variables. Enforcement of the condition $\overline{\chi}_{ij} = \chi_{ij}$ (and/or $\overline{\chi}_r = \chi_r$) is made later in the formulation, and is part of the standard procedures for the derivation of a constitutive model.

Lemaitre's approach	Present approach
Energy function and dissipation expression/function	
$f = \frac{1}{2} a_{ijkl}(\varepsilon_{ij} - \alpha_{ij})(\varepsilon_{kl} - \alpha_{kl}) + \frac{1}{2} Hr^2$ $d = \sigma_{ij}\dot{\alpha}_{ij} - \frac{\partial f}{\partial r}\dot{r} \geq 0$	$f = \frac{1}{2} a_{ijkl}(\varepsilon_{ij} - \alpha_{ij})(\varepsilon_{kl} - \alpha_{kl})$ $d = (\sigma_y + H\varepsilon_p)\sqrt{\frac{2}{3}\dot{\alpha}'_{kl}\dot{\alpha}'_{kl}} + \Lambda_1 C_1 + \Lambda_2 C_2$ $C_1 = \dot{\varepsilon}_p - \sqrt{2\dot{\alpha}_{ij}\dot{\alpha}_{ij}/3} = 0\ ;\ C_2 = \dot{\alpha}_{kk} = 0$
Thermodynamic forces	
$\sigma_{ij} = \frac{\partial f}{\partial \varepsilon^e_{ij}} = a_{ijkl}(\varepsilon_{kl} - \alpha_{kl})$ $\overline{\chi}_{ij} = -\frac{\partial f}{\partial \alpha_{ij}} = \sigma_{ij}\ ;\ \chi_{ij} = \frac{\partial d}{\partial \dot{\alpha}_{ij}} = \sigma_{ij}$ $\overline{\chi}_r = -\frac{\partial f}{\partial r} = -Hr\ ;\ \chi_r = \frac{\partial d}{\partial \dot{r}} = -\frac{\partial f}{\partial r} = \overline{\chi}_r$	$\sigma_{ij} = \frac{\partial f}{\partial \varepsilon_{ij}} = a_{ijkl}(\varepsilon_{kl} - \alpha_{kl})$ $\overline{\chi}_{ij} = -\frac{\partial f}{\partial \alpha_{ij}} = \sigma_{ij}$ $\chi_{ij} = \frac{\partial d}{\partial \dot{\alpha}_{ij}} = (\sigma_y + H\varepsilon_p)\sqrt{\frac{2}{3}}\frac{\dot{\alpha}'_{ij}}{\sqrt{\dot{\alpha}'_{kl}\dot{\alpha}'_{kl}}}$
Yield function	
$y_p = \sqrt{\frac{3}{2}\sigma'_{ij}\sigma'_{ij}} + \overline{\chi}_r - \sigma_y = 0$	$y_p = \sqrt{\frac{3}{2}\chi'_{ij}\chi'_{ij}} - (\sigma_y + H\varepsilon_p) = 0$ $\chi_{ij} = \overline{\chi}_{ij} = \sigma_{ij}$
Flow rule	
$\dot{\alpha}_{ij} = \lambda \frac{\partial y_p}{\partial \sigma_{ij}}$	$\dot{\alpha}_{ij} = \lambda \frac{\partial y_p}{\partial \chi_{ij}}$
Rate of dissipation (dissipation function)	
$d = \sigma_y \sqrt{\frac{2}{3}\dot{\alpha}'_{kl}\dot{\alpha}'_{kl}}$	$d = (\sigma_y + H\varepsilon_p)\sqrt{\frac{2}{3}\dot{\alpha}'_{kl}\dot{\alpha}'_{kl}}$

Table 3.1: Comparison of two thermodynamic approaches

In contrast with this, Lemaitre's approach provides thermodynamic restrictions on the proposed constitutive models through the non-negativeness of the dissipation expression (or the Clausius-Duhem inequality). In other words, the dissipation inequality (3.111) is used as a condition for the thermodynamic admissibility of a constitutive model, rather than being explicitly specified as one of the two energy functions needed for the model formulation. As illustrated through the above comparison, the conditions $\overline{\chi}_{ij} = \chi_{ij}$ and $\overline{\chi}_r = \chi_r$ are automatically satisfied in Lemaitre's framework. The yield function y_p and dissipation potential φ are necessarily specified for the definition of a plasticity-based constitutive model within Lemaitre's thermodynamic framework. Restrictions on the shape of the dissipation potential are also required for the thermodynamic admissibility of the defined constitutive model.

3.5 Summary

In this chapter, the extension of the thermodynamic framework proposed by Houlsby and Puzrin (2000) has been completed. This includes the introduction of a new internal variable representing the material deterioration, along with the modification of the energy and dissipation functions for the accommodation of damage dissipation processes. A simple formulation for coupled damage-plasticity constitutive models has also been presented. The whole formulation is based on the above-mentioned thermodynamic framework and therefore inherits advantages of the approach, realized through the simplicity and rigorousness of the derivation procedures and the resulting thermodynamic admissibility of the obtained constitutive models. Both strain- and stress-based models can be accommodated in this framework and formulated following established procedures. The computational aspect of the proposed damage-plasticity models has also been preliminarily addressed, with the derivation of the tangent stiffness tensors for both stress- and strain-based constitutive models.

The adopted approach makes use of the Legendre transformation of the dissipation function and, in a more rigorous way, leads to a natural occurrence of the yield and damage loading functions. There is no need to have any assumption on the form of a dissipation potential, as usually encountered in several thermomechanical approaches (Lemaitre and Chaboche, 1990; Lemaitre, 1992; Maugin, 1992). Coupling between damage and non-associated plasticity in both stress- and strain-based models is

implicitly embedded in the governing constitutive relations; and the evolution laws of internal variables can be straightforwardly derived from those relations. In particular, in the proposed damage-plasticity models, the parameters k (3.34) and β (3.35) of the yield function are decreasing functions with respect to the damage indicator α_d, characterizing the reduction of the plasticity threshold due to microcracking processes (Nguyen, 2002; Nguyen and Houlsby, 2004; Salari *et al*, 2004). This is equivalent to introducing effective instead of nominal stress to the yield function (e.g. in Lemaitre and Chaboche, 1990; Lemaitre, 1992).

This chapter merely addresses the thermodynamic aspects of the proposed constitutive models. Without experimental- and micromechanical-based details, the simple models described in this chapter are not yet ready for use in the constitutive modelling of cement-based materials. This specification of the proposed models will therefore be carried out and presented in the subsequent chapter. The stress-based model described in section 3.3.2, enhanced by the decomposition of the total stress tensor to capture the different responses of the concrete in tension and compression, will be used.

Chapter 4:

Constitutive Models of Concrete for 2D Applications

4.1 Introduction

It has been experimentally found that the response of concrete is different in tension and in compression, primarily due to the much lower tensile strength of the aggregate-mortar interface compared to that of the mortar. The mechanism of stiffness degradation, which is experimentally observed in both compressive and tensile loading, becomes more complicated during elastic unloading from a tensile state to a compressive state, and vice versa, because of the opening and closing of microcracks.

Many attempts have been paid to model this phenomenon (Mazars and Pijaudier-Cabot, 1989; Fremond and Nejdar, 1995; Murakami and Kamiya, 1997; Lee and Fenves, 1998; Ragueneau *et al.*, 2000). As has been addressed in the literature, the anisotropic nature of damage, even for initially isotropic materials, requires a tensorial representation of the damage variable. Generally this unilateral character of damage can be integrated in the modelling using damage variable as a tensor (Murakami and Kamiya, 1996; Ju, 1989). However, in a much simplified way, this can also be done with isotropic damage models by using two separate scalar damage variables for tensile and compressive loadings (Mazars and Pijaudier-Cabot, 1989; Fremond and Nejdar, 1995; Lee and Fenves, 1998). In such cases, in order to distinguish the damage due to tension from that due to compression, the decomposition of stress and strain tensors into positive and negative parts is necessary (Mazars and Pijaudier-Cabot, 1989; Ju, 1989; Fremond and Nejdar, 1995).

The detailed specification of the models proposed in the previous chapter is conducted in this section. However, only the stress-based model is considered, due to the difficulties in dealing with the decomposition of both total and plastic strains in strain-based elasto-plastic damage models. For the use of the Drucker-Prager yield criterion, with the lack of dependence on the Lode angle θ, application of the proposed models is appropriate to two-dimensional problems only. Further extension of the approach to general stress states is therefore still needed.

4.2 Constitutive model for concrete in 2D

4.2.1 Stress decomposition

In uniaxial cases, the crack closing/opening takes place during unloading/reloading when $\sigma = 0$. However, for multi-axial stress states the mechanism of crack closing/opening is much more complex and an appropriate criterion must be used to distinguish the tensile and compressive stress states inside the material body. The eigenvalue decomposition method, which is in accordance with the basic features of damage mechanics (Lemaitre, 1992), is used here to decompose the stress/strain tensor into positive and negative parts. Following the method, the positive stress tensor σ_{ij}^{+} is expressed as (Ortiz, 1985)

$$\sigma_{ij}^{+} = \sum_{m=1}^{3} \left\langle \sigma^{m} \right\rangle p_i^m p_j^m \tag{4.1}$$

where $\mathbf{p}^m$ is the unit vector of the m^{th} principal direction, σ^m is the m^{th} principal stress, and $\langle\ \rangle$ denotes the Macaulay bracket. The negative stress tensor σ_{ij}^{-} is then

$$\sigma_{ij}^{-} = \sigma_{ij} - \sigma_{ij}^{+} \tag{4.2}$$

As the decomposition here is based on the eigenvalue decomposition, the following properties are needed and have been analytically proved by Ladeveze (1983) (care with the order of operations is needed in the following):

$$\sigma_{ij}^{+}\sigma_{ij}^{-} = 0 \tag{4.3}$$

$$\sigma_{kk} = (\sigma_{kk})^{+} + (\sigma_{kk})^{-} \tag{4.4}$$

$$\sigma_{ij}\sigma_{ij} = \sigma_{ij}^{+}\sigma_{ij}^{+} + \sigma_{ij}^{-}\sigma_{ij}^{-} \tag{4.5a}$$

$$\sigma_{kk}\sigma_{ll} = (\sigma_{kk})^{+}(\sigma_{ll})^{+} + (\sigma_{kk})^{-}(\sigma_{ll})^{-} \tag{4.5b}$$

$$\frac{\partial}{\partial \sigma_{ij}}\left(\frac{1}{2}\sigma_{ij}^{+}\sigma_{ij}^{+}\right) = \frac{\partial}{\partial \sigma_{ij}}\left(\frac{1}{2}\sigma_{ik}^{+}\sigma_{kj}^{+}\delta_{ij}\right) = \sigma_{ij}^{+} \tag{4.6}$$

$$\frac{\partial}{\partial \sigma_{ij}}\left[\frac{1}{2}(\sigma_{kk})^{+}(\sigma_{ll})^{+}\right] = (\sigma_{kk})^{+}\delta_{ij} \tag{4.7}$$

In addition, it can be readily proved that σ_{ij}^{+} and σ_{ij}^{-} are piecewise continuous and first order homogeneous functions of σ_{ij}. These two functions are discontinuous only at specific points where the principal stresses change signs. As a consequence, Euler's theorem of homogeneous function gives.

$$\sigma_{ij}^{+} = \frac{\partial \sigma_{ij}^{+}}{\partial \sigma_{kl}} \sigma_{kl} \tag{4.8}$$

and

$$\sigma_{ij}^{-} = \frac{\partial \sigma_{ij}^{-}}{\partial \sigma_{kl}} \sigma_{kl} \tag{4.9}$$

4.2.2 Choice of energy function

Making use of the tensor decomposition, the energy potential can be considered to consist of two parts, representing the energies due to negative and positive stress tensors respectively. For linear elasticity without damage and plasticity, the Gibbs free energy function reads

$$g = g\left(\sigma_{ij}\right) = \frac{1}{2E}\left[-(1+\nu)\sigma_{ij}\sigma_{ij} + \nu\sigma_{kk}\sigma_{ll}\right] \tag{4.10}$$

Using the above stress decomposition, noting that $(\sigma_{kk})^{+} = \langle \sigma_{kk} \rangle \neq \sigma_{kk}^{+}$ (where $\langle\ \rangle$ is the Macaulay bracket), we can rewrite g as

$$\begin{aligned} g = g\left(\sigma_{ij}\right) = & \frac{1}{2E}\left[-(1+\nu)\sigma_{ij}^{+}\sigma_{ij}^{+} + \nu(\sigma_{kk})^{+}(\sigma_{ll})^{+}\right] \\ & + \frac{1}{2E}\left[-(1+\nu)\sigma_{ij}^{-}\sigma_{ij}^{-} + \nu(\sigma_{kk})^{-}(\sigma_{ll})^{-}\right] \end{aligned} \tag{4.11}$$

After introducing the internal variables characterizing the plasticity and damage processes, one gets

$$\begin{aligned} g &= g\left(\sigma_{ij}, \alpha_{ij}, \alpha_d^t, \alpha_d^c\right) \\ &= \frac{1}{2E\left(1-\alpha_d^t\right)}\left[-(1+\nu)\sigma_{ij}^{+}\sigma_{ij}^{+} + \nu(\sigma_{kk})^{+}(\sigma_{ll})^{+}\right] \\ &+ \frac{1}{2E\left(1-\alpha_d^c\right)}\left[-(1+\nu)\sigma_{ij}^{-}\sigma_{ij}^{-} + \nu(\sigma_{kk})^{-}(\sigma_{ll})^{-}\right] - \sigma_{ij}\alpha_{ij} \end{aligned} \tag{4.12}$$

where α_d^t and α_d^c are respectively the scalar damage indicator for tensile and compressive damage mechanisms. In the absence of damage, the above function

reduces to the usual form of the elastic Gibbs free energy function, thus fulfilling basic thermodynamic requirements.

Important remarks should be made here on the above energy function. Separation of energy terms in the energy potential leads to the separation of the elastic strain into two corresponding parts expressed in terms of positive and negative stress tensors respectively.

$$\begin{aligned}\varepsilon_{ij}^{e} = \varepsilon_{ij} - \alpha_{ij} = -\frac{\partial g}{\partial \sigma_{ij}} - \alpha_{ij} = &\frac{1}{E\left(1-\alpha_d^t\right)}\left[(1+\nu)\sigma_{ij}^{+} - \nu\left(\sigma_{kk}\right)^{+}\delta_{ij}\right] \\ &+ \frac{1}{E\left(1-\alpha_d^c\right)}\left[(1+\nu)\sigma_{ij}^{-} - \nu\left(\sigma_{kk}\right)^{-}\delta_{ij}\right]\end{aligned} \tag{4.13}$$

As a consequence, using the properties (4.8) and (4.9), the secant compliance tensor can be proved to be symmetric and stress-dependent. The model in this case exhibits stress-induced anisotropy.

$$\begin{aligned}C_{ijkl} = &\frac{1}{E\left(1-\alpha_d^t\right)}\left[(1+\nu)\frac{\partial \sigma_{ij}^{+}}{\partial \sigma_{kl}} - \nu H\left(\sigma_{kk}\right)\delta_{ij}\delta_{kl}\right] \\ &+ \frac{1}{E\left(1-\alpha_d^c\right)}\left[(1+\nu)\frac{\partial \sigma_{ij}^{-}}{\partial \sigma_{kl}} - \nu H\left(-\sigma_{kk}\right)\delta_{ij}\delta_{kl}\right]\end{aligned} \tag{4.14}$$

in which $H(x)$ is the Heaviside function equal to unity if $x > 0$ and zero otherwise. As can be seen, the tensor differential in (4.14) requires a reliable algorithm for the numerical differentiation. Moreover, it has been experienced in this study that this stress-induced anisotropy can introduce instability to the numerical analysis. In the 2D tension-compression quadrant with dominating tensile stress, the instability comes from the scaling of the compliance tensor (4.14) only in the direction of the principal tensile stress, as the material is deteriorated in tension only. Inversion of the compliance tensor for the formulation of the stiffness matrix in finite element analysis will result in a "poor" stiffness tensor once tensile damage measure reaches values in the range of 0.7~0.8. The term "poor" here refers to increasingly stiff response of the material model after this value of damage has been reached, while the material is expected to soften continuously due to damage.

In the following alternative formulation, isotropic damage is adopted for the constitutive model. The stress decomposition is used in the dissipation function and

does not have any effect on the isotropic response of the constitutive model. The energy function is of the form

$$g = g(\sigma_{ij}) = \frac{-(1+\nu)\sigma_{ij}\sigma_{ij} + \nu\sigma_{kk}\sigma_{ll}}{2E\left[1 - H(\sigma_{kk})\alpha_d^t\right]\left(1 - \alpha_d^c\right)} - \sigma_{ij}\alpha_{ij} \tag{4.15}$$

with the corresponding elastic strain

$$\varepsilon_{ij}^e = \varepsilon_{ij} - \alpha_{ij} = -\frac{\partial g}{\partial \sigma_{ij}} - \alpha_{ij} = \frac{(1+\nu)\sigma_{ij} - \nu\sigma_{kk}\delta_{ij}}{E\left[1 - H(\sigma_{kk})\alpha_d^t\right]\left(1 - \alpha_d^c\right)} \tag{4.16}$$

The Heaviside step function H is used in the expression of the energy function to take into account the unilateral behaviour of the material, in which compressive damage results in the stiffness reduction in tension while its tensile counterpart can be considered to have no effect on the compressive behaviour of the material. This phenomenological feature has been confirmed by several experiments on concrete (e.g. in Reinhardt *et al.*, 1986; see also Chapter 2) and widely accepted in the research community (Lemaitre, 1992; Lee and Fenves, 1998; Ung-Quoc, 2003).

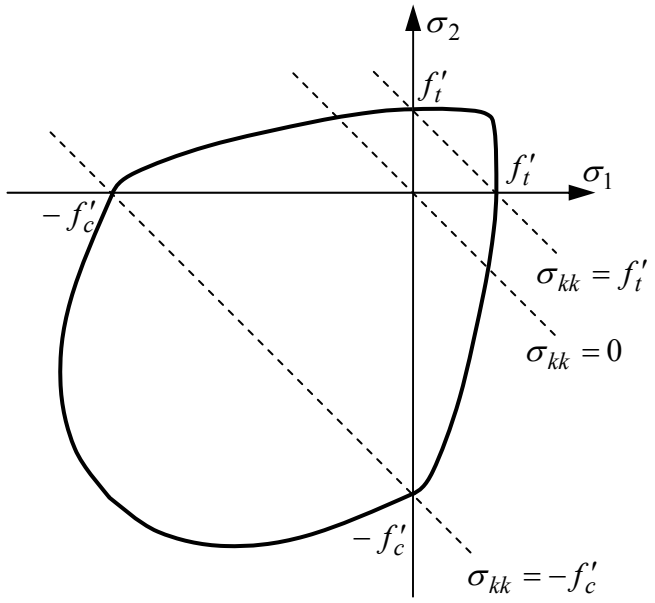

Figure 4.1: Schematic view of the desired damage surface in 2D principal stress space

Tensile damage in this case can only have an impact on the constitutive behaviour if the stress state is tensile-dominant, represented by the positiveness of the first invariant of the stress tensor: $I_1 = \sigma_{kk} > 0$. In a uniaxial test this type of tension switch works fairly well as the energy potential takes zero value when the uniaxial stress vanishes, followed by the stiffness recovery from tension to compression, thus making the energy change

not abrupt. Nevertheless, the switch is rather crude as it does not guarantee the smooth transition in the tension-compression regions in multi-axial stress states. In other words, a discontinuity occurs in the energy function when the stress state passes through the plane $\sigma_{kk}=0$ in the principal stress space (see figure 4.1).

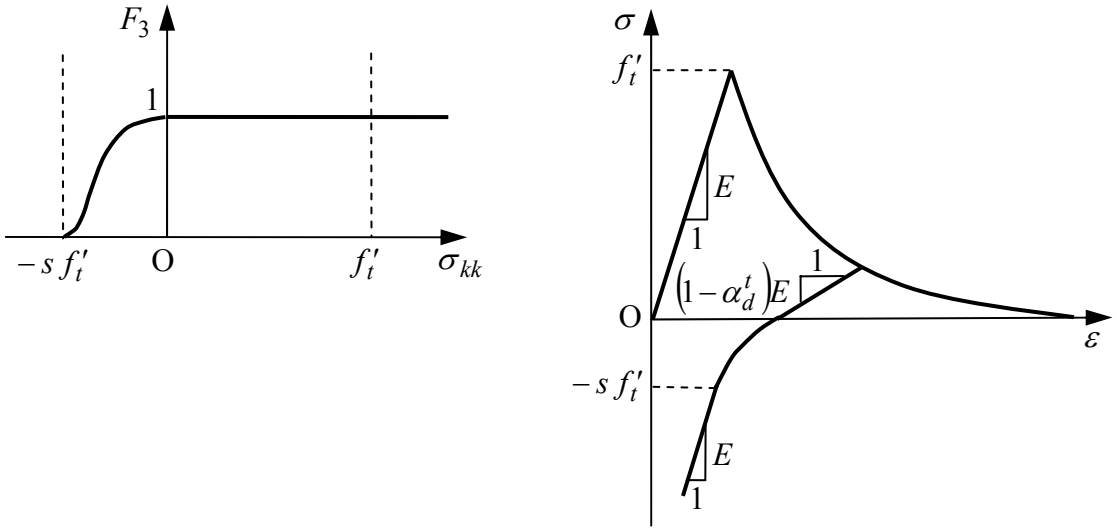

Figure 4.2: Function $F_3(\sigma_{kk})$ and its corresponding effect on the unilateral behaviour

Full remedy of the above-discussed problems is in principle straightforward, but is left to future work. It is only briefly discussed here. This treatment can make the formulation unnecessarily cumbersome and much more complicated, as the above problem of state transition just occurs during load reversal from tension to compression, and vice versa, e.g. in cyclic loading or non-proportional loading. As an example, one possible way to remedy the problem is to use, instead of the Heaviside step function, a continuous stress-dependent function being able to smooth out this transition (figure 4.2). In this case, the energy function reads

$$g = g(\sigma_{ij}) = \frac{-(1+\nu)\sigma_{ij}\sigma_{ij} + \nu\sigma_{kk}\sigma_{ll}}{2E\left[1-F_3(\sigma_{kk})\alpha_d^t\right]\left(1-\alpha_d^c\right)} \tag{4.17}$$

The elastic strain derived from this energy function is

$$\begin{aligned}\varepsilon_{ij}^e &= \varepsilon_{ij} - \alpha_{ij} = -\frac{\partial g}{\partial \sigma_{ij}} - \alpha_{ij} \\ &= \frac{(1+\nu)\sigma_{ij} - \nu\sigma_{kk}\delta_{ij}}{E\left[1-F_3(\sigma_{kk})\alpha_d^t\right]\left(1-\alpha_d^c\right)} + \frac{\left[(1+\nu)\sigma_{kl}\sigma_{kl} - \nu\sigma_{kk}\sigma_{ll}\right]\dfrac{\partial F_3}{\partial \sigma_{pp}}\delta_{ij}\alpha_d^t}{2E\left[1-F_3(\sigma_{kk})\alpha_d^t\right]^2\left(1-\alpha_d^c\right)}\end{aligned} \tag{4.18}$$

Compared to (4.16), the model can be seen to exhibit stress-induced anisotropy property due to the appearance of the second term in the expression of elastic strain. However, with relevant choices of function $F_3(\sigma_{kk})$, the effect of this extra term can be limited to cases in which the material is first loaded in tension and then unloaded to the compression regime. This is simply depicted for uniaxial case in figure (4.2). In that figure, function $F_3(\sigma_{kk})$ has a non-zero derivative only in the range $[-s f_t', 0]$ where $s<1$ can be considered as a material parameter, determined from a cyclic uniaxial test. As a consequence, the effect on the constitutive behaviour of the model only takes place in the specified range, thus rendering the possibility of simplifying the formulation by use of the Heaviside function $H(\sigma_{kk})$ in place of function $F_3(\sigma_{kk})$. However, in nonlinear numerical analysis, the stress state of a certain point can change from tension-dominance (above the plane $\sigma_{kk}=0$) to compressive-dominance (just below the plane $\sigma_{kk}=0$) and vice versa, resulting in sudden change in the stiffness matrix of that point, which is the source of numerical instability. To avoid this, the trace of tensile stress tensor, denoted here as σ_{kk}^{+} will be used in the Heaviside step function. A change in the stress-strain relationship only takes place when crossing the planes $\sigma_1=0$ or $\sigma_2=0$ to compression-compression quadrant.

4.2.3 Formulation

Neglecting the discontinuity of the energy function, we can use its simple form with the Heaviside step function employed to model the stiffness recovery in tensile loading – compressive unloading.

$$g = g(\sigma_{ij}) = \frac{-(1+\nu)\sigma_{ij}\sigma_{ij} + \nu\sigma_{kk}\sigma_{ll}}{2E\left[1-H(\sigma_{kk}^{+})\alpha_d^t\right](1-\alpha_d^c)} - \sigma_{ij}\alpha_{ij} \tag{4.19}$$

The parabolic Drucker-Prager yield criterion is used here along with two damage criteria for tensile and compressive behaviour. The corresponding dissipation function, which is homogeneous first order in the rate of internal variables, reads

$$\begin{aligned} d = {} & F_1^{t\,*}(\sigma_{ij}, \alpha_d^t, \alpha_d^c)\dot{\alpha}_d^t + F_1^{c\,*}(\sigma_{ij}, \alpha_d^c)\dot{\alpha}_d^c \\ & + \left[\frac{k}{\beta} - (1-r)\sigma_{kk}\right]\frac{\dot{\alpha}_{kk}}{3r} + \frac{3\beta r\dot{\alpha}_{ij}'\dot{\alpha}_{ij}'}{2\dot{\alpha}_{kk}} + \Lambda_t C_t + \Lambda_c C_c \end{aligned} \tag{4.20}$$

It can be seen that functions $F_1^{t\,*}$ and $F_1^{c\,*}$ are stress-dependent, and this feature is different from that in chapter 3. The two damage-related functions are modified here to

account for the ductility of the material behaviour under confining pressure (see figure 4.1). The forms of the two functions will be specified later during the model derivation.

For the independence of the model in separately capturing the permanent deformations in tension and compression, two constraints for the accumulated plastic strains are required, resembling (3.36) in the preceding chapter:

$$C_t = \dot{\varepsilon}_p^t - cF_4^t(\sigma_{kk})\sqrt{\dot{\alpha}_{ij}\dot{\alpha}_{ij}} = 0 \tag{4.21}$$

$$C_c = \dot{\varepsilon}_p^c - cF_4^c(\sigma_{kk})\sqrt{\dot{\alpha}_{ij}\dot{\alpha}_{ij}} = 0 \tag{4.22}$$

in which c is a constant usually taken as $\sqrt{2/3}$. As mentioned in chapter 3, this value is in fact only suitable for the use of pressure-independent material with plastic incompressibility condition. In such cases the definitions (4.21) and (4.22) agree for the uniaxial case. For the parabolic Drucker-Prager criterion used here, other choices of c are not straightforward. For the sake of simplicity, $c = \sqrt{2/3}$ is used throughout this study.

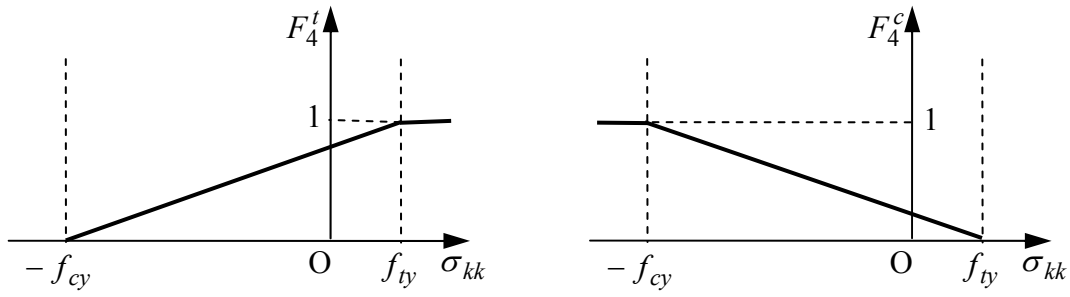

Figure 4.3: Definitions of function $F_4^t(\sigma_{kk})$ and $F_4^c(\sigma_{kk})$

Functions F_4^t and F_4^c in (4.21) and (4.22) are dependent on the first invariant of the stress tensor, aiming at producing a smooth transition between tension and compression in tension-compression quadrants in 2D principal stress space. In a similar way to the definition of function $F_3(\sigma_{kk})$, they are defined

$$F_4^t = \min\left(1, \left\langle \frac{\sigma_{kk} + f_{cy}}{f_{cy} + f_{ty}} \right\rangle\right) \tag{4.23}$$

$$F_4^c = \min\left(1, \left\langle \frac{f_{ty} - \sigma_{kk}}{f_{cy} + f_{ty}} \right\rangle\right) = 1 - F_4^t \tag{4.24}$$

where $\langle\ \rangle$ is the Macaulay bracket and f_{cy} and f_{ty} are the ultimate stresses in uniaxial compression and tension respectively. They are dependent on both hardening and damage dissipation processes, and their forms will be specified later. It can be noted that this is only a simple way to decompose the incremental accumulated plastic strain $\dot{\varepsilon}_p$ defined in (3.36) into tensile and compressive parts, by making use of the property $F_4^t + F_4^c = 1$. Nonlinear forms of F_4^t and F_4^c are of course applicable but intentionally not pursued here in order to preserve the simplicity of the proposed formulation.

From the Gibbs free energy function, the total strain is

$$\varepsilon_{ij} = -\frac{\partial g}{\partial \sigma_{ij}} = \frac{(1+\nu)\sigma_{ij} - \nu\sigma_{kk}\delta_{ij}}{E\left[1 - H\left(\sigma_{kk}^{+}\right)\alpha_d^t\right]\left(1-\alpha_d^c\right)} + \alpha_{ij} \tag{4.25}$$

The generalised stresses are derived following procedures established in the original framework (by Houlsby and Puzrin, 2000) and illustrated in Chapter 3.

$$\overline{\chi}_{ij} = -\frac{\partial g}{\partial \alpha_{ij}} = \sigma_{ij} \tag{4.26}$$

$$\overline{\chi}_d^t = -\frac{\partial g}{\partial \alpha_d^t} = \frac{\left[(1+\nu)\sigma_{ij}\sigma_{ij} - \nu\sigma_{kk}\sigma_{ll}\right]H\left(\sigma_{kk}^{+}\right)}{2E\left[1 - H\left(\sigma_{kk}^{+}\right)\alpha_d^t\right]^2\left(1-\alpha_d^c\right)} \tag{4.27}$$

$$\overline{\chi}_d^c = -\frac{\partial g}{\partial \alpha_d^c} = \frac{(1+\nu)\sigma_{ij}\sigma_{ij} - \nu\sigma_{kk}\sigma_{ll}}{2E\left[1 - H\left(\sigma_{kk}^{+}\right)\alpha_d^t\right]\left(1-\alpha_d^c\right)^2} \tag{4.28}$$

$$\overline{\chi}_p^t = -\frac{\partial g}{\partial \varepsilon_p^t} = 0 \tag{4.29}$$

$$\overline{\chi}_p^c = -\frac{\partial g}{\partial \varepsilon_p^c} = 0 \tag{4.30}$$

In the same way, we derive the dissipative generalized stresses from the dissipation function as:

$$\begin{aligned}\chi_{ij} = \frac{\partial d}{\partial \dot{\alpha}_{ij}} = &\left[\frac{k}{\beta} - (1-r)\sigma_{kk}\right]\frac{\delta_{ij}}{3r} + \frac{3\beta r\dot{\alpha}'_{ij}}{\dot{\alpha}_{kk}} - \frac{3\beta r\dot{\alpha}'_{mn}\dot{\alpha}'_{mn}}{2}\frac{\delta_{ij}}{\dot{\alpha}_{kk}\dot{\alpha}_{ll}} \\ &- \frac{c\Lambda_t F_4^t\dot{\alpha}_{ij}}{\sqrt{\dot{\alpha}_{kl}\dot{\alpha}_{kl}}} - \frac{c\Lambda_c F_4^c\dot{\alpha}_{ij}}{\sqrt{\dot{\alpha}_{kl}\dot{\alpha}_{kl}}}\end{aligned} \tag{4.31}$$

$$\chi_d^t = \frac{\partial d}{\partial \dot{\alpha}_d^t} = F_1^{t^*}\left(\sigma_{ij}, \alpha_d^t, \alpha_d^c\right) \tag{4.32}$$

$$\chi_d^c = \frac{\partial d}{\partial \dot{\alpha}_d^c} = F_1^{c^*}\left(\sigma_{ij}, \alpha_d^c\right) \tag{4.33}$$

$$\chi_p^t = \frac{\partial d}{\partial \dot{\varepsilon}_p^t} = \Lambda_t \tag{4.34}$$

$$\chi_p^c = \frac{\partial d}{\partial \dot{\varepsilon}_p^c} = \Lambda_c \tag{4.35}$$

Using the conditions $\overline{\chi}_p^t = \chi_p^t$ and $\overline{\chi}_p^c = \chi_p^c$ it can be immediately deduced that $\Lambda_t = \Lambda_c = 0$, thus making the formulation much simpler. The derivation of yield and damage loading functions follows procedures established in the original framework and illustrated in chapter 3. Therefore, all unnecessary intermediate details are omitted here. The yield function still has the same form in generalized and true stress spaces

$$y_p = \beta\left[r\chi_{kk} + (1-r)\sigma_{kk}\right] + \frac{\chi'_{ij}\chi'_{ij}}{2} - k = 0 \tag{4.36}$$

$$y_p^* = \beta\,\sigma_{kk} + \frac{\sigma'_{ij}\sigma'_{ij}}{2} - k = 0 \tag{4.37}$$

However, their parameters k and β are now

$$k\left(\alpha_d^t, \alpha_d^c, \varepsilon_p\right) = \frac{f_{cy} f_{ty}}{3} \tag{4.38}$$

$$\beta\left(\alpha_d^t, \alpha_d^c, \varepsilon_p\right) = \frac{f_{cy} - f_{ty}}{3} \tag{4.39}$$

For the sake of simplicity, a linear hardening law in both tension and compression is assumed. We then have f_{cy} and f_{ty} as

$$f_{cy} = \left(f_{c0} + H_c \varepsilon_p^c\right)\left(1 - \alpha_d^c\right) \tag{4.40}$$

$$f_{ty} = \left(f_{t0} + H_t \varepsilon_p^t\right)\left(1 - \alpha_d^t\right)\left(1 - \alpha_d^c\right) \tag{4.41}$$

In the above expressions, the two initial yield thresholds are denoted as f_{c0} and f_{t0} for uniaxial compression and tension respectively. Figure (4.4) depicts the parabolic Drucker-Prager yield surface in 2D principal stress space. As yielding in uniaxial compression takes place at a stress level much lower than the ultimate compressive

strength f_c', f_{c0} can be taken as only 30% of this ultimate compressive strength (Chen and Han, 1988). However, this is not the case in tension, when the material behaviour is almost linear before peak stress f_t'. The initial value $f_{c0} = f_t'$ is therefore adopted here. As can be seen in (4.41), compressive damage in this case has the effect on the tensile strength of the material. This is realized through the presence of the compressive damage indicator α_d^c in the expression of the tensile yield threshold.

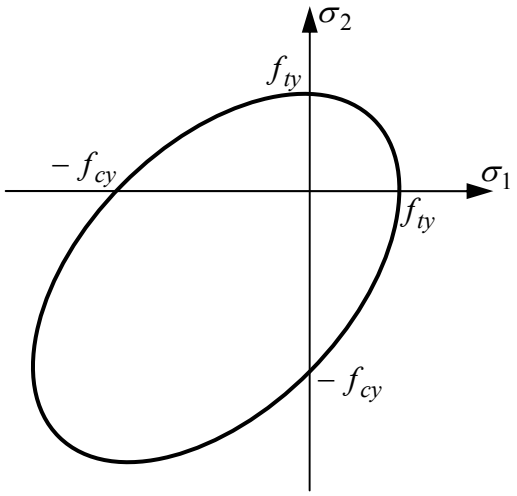

Figure 4.4: The parabolic Drucker-Prager yield criterion in 2D principal stress space

The procedures demonstrated in chapter 3 leads to two separate tensile and compressive damage criteria.

$$y_d^{t\,*} = \frac{\left[(1+\nu)\sigma_{ij}\sigma_{ij} - \nu\sigma_{kk}\sigma_{ll}\right]H\left(\sigma_{kk}^{+}\right)}{2E\left[1-H\left(\sigma_{kk}^{+}\right)\alpha_d^t\right]^2\left(1-\alpha_d^c\right)} - F_1^{t\,*}\left(\sigma_{ij},\alpha_d^t,\alpha_d^c\right) = 0 \tag{4.42}$$

$$y_d^{c\,*} = \frac{(1+\nu)\sigma_{ij}\sigma_{ij} - \nu\sigma_{kk}\sigma_{ll}}{2E\left[1-H\left(\sigma_{kk}^{+}\right)\alpha_d^t\right]\left(1-\alpha_d^c\right)^2} - F_1^{c\,*}\left(\sigma_{ij},\alpha_d^c\right) = 0 \tag{4.43}$$

in which, functions $F_1^{t\,*}\left(\sigma_{ij},\alpha_d^t,\alpha_d^c\right)$ and $F_1^{c\,*}\left(\sigma_{ij},\alpha_d^c\right)$ take the following forms

$$F_1^{t\,*}\left(\sigma_{ij},\alpha_d^t,\alpha_d^c\right) = \frac{\dfrac{(1+\nu)\sigma_{ij}\sigma_{ij} - \nu\sigma_{kk}\sigma_{ll}}{2E\left[1-H\left(\sigma_{kk}^{+}\right)\alpha_d^t\right]^2\left(1-\alpha_d^c\right)}}{\dfrac{(1+p_t)\sigma_{ij}^{+}\sigma_{ij}^{+} - p_t\left(\sigma_{kk}\right)^{+}\left(\sigma_{ll}\right)^{+}}{2E\left(1-\alpha_d^t\right)^2}} F_1^t\left(\alpha_d^t,\alpha_d^c\right) \tag{4.44}$$

and

$$F_1^{c^*}\left(\sigma_{ij},\alpha_d^c\right)=\frac{\dfrac{(1+\nu)\sigma_{ij}\sigma_{ij}-\nu\sigma_{kk}\sigma_{ll}}{2E\left[1-H\left(\sigma_{kk}^+\right)\alpha_d^t\right]\left(1-\alpha_d^c\right)^2}}{\dfrac{(1+p_c)\sigma_{ij}^-\sigma_{ij}^- - q_c\left(\sigma_{kk}\right)^-\left(\sigma_{ll}\right)^- + r_c f_c'(1-\alpha_d^c)\left(\sigma_{kk}\right)^-}{2E\left(1-\alpha_d^c\right)^2}} F_1^c\left(\alpha_d^c\right) \quad (4.45)$$

The decomposition of total stress tensor into tensile and compression parts is applied in the above expression to distinguish the failure in tension and compression. As the numerators in the above expressions are non-negative and immediately become positive when loading takes place, their elimination in (4.42) and (4.43) is straightforward. We can now rewrite the damage criteria in their final forms, which bear a resemblance to the damage criterion in the preceding chapter.

$$y_d^t=\frac{(1+p_t)\sigma_{ij}^+\sigma_{ij}^+ - p_t\left(\sigma_{kk}\right)^+\left(\sigma_{ll}\right)^+}{2E\left(1-\alpha_d^t\right)^2}H\left(\sigma_{kk}^+\right)-F_1^t\left(\alpha_d^t,\alpha_d^c\right)=0 \quad (4.46)$$

$$y_d^c=\frac{(1+p_c)\sigma_{ij}^-\sigma_{ij}^- - q_c\left(\sigma_{kk}\right)^-\left(\sigma_{ll}\right)^- + \left(1-\alpha_d^c\right)r_c f_c'\left(\sigma_{kk}\right)^-}{2E\left(1-\alpha_d^c\right)^2}-F_1^c\left(\alpha_d^c\right)=0 \quad (4.47)$$

in which p_t, p_c, q_c and r_c are model parameters, the roles of which will be discussed in the next section.

With stress-strain relationship (4.25), yield criterion (4.37) and damage criteria (4.46, 4.47) available, the constitutive behaviour of the proposed concrete model is now ready. A closer look at the behaviour of the model will be made in the following section.

4.2.4 Composite loading-failure surface

There have been several damage models developed for the analysis of concrete structures, and many of them (Yazdani and Schreyer, 1990; Lee and Fenves, 1998; Meschke *et al.*, 1998; Comi, 2001; Comi and Perego, 2001; Salari *et al.*, 2004) carefully took into account both the tensile and compressive behaviour of the material. In fact, the neglect of compressive response in the modelling is acceptable only in direct or indirect tensile tests, where the material shows its brittle behaviour beyond the peak stress. However, this is not the case in compressive tests, especially under confining pressure, where ductility is observed. All the above features have been mentioned in chapter 1. They will be illustrated here using the proposed coupled damage-plasticity models.

The damage criteria (4.46) and (4.47) will be explored in detail hereafter. It is noted that both the initial damage and yield surfaces, which can all be expressed in terms of stress, can be plotted in the same graph, thus making it easy for interpretation. The damage and yield criteria here are coupled with each other, and hence can also be regarded as an integrated yield-failure criterion characterizing the behaviour of the material. The term failure surface (Chen and Han, 1988) here should be distinguished with the concept of yield surface widely used in literature, as it refers to the failure stage of the material, at which softening begins to occur.

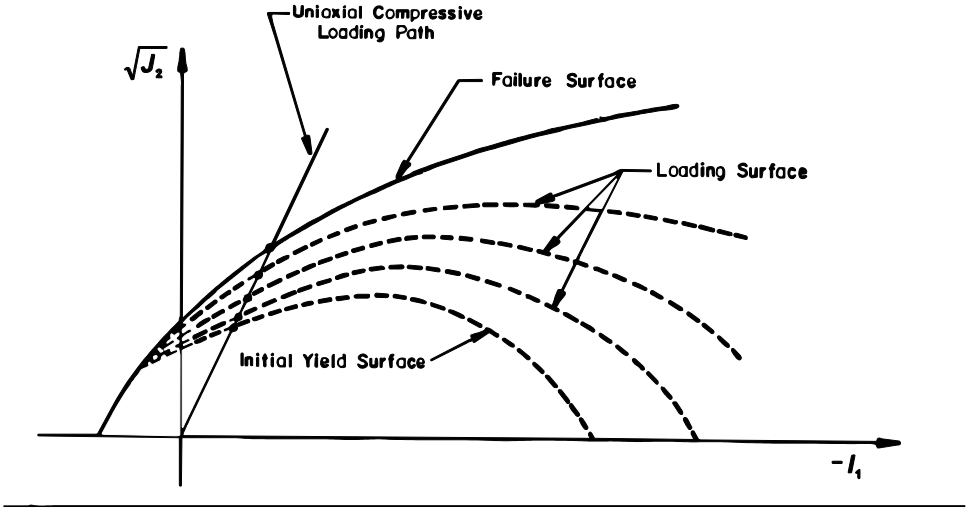

Figure 4.5: Evolution of loading surface (after Chen and Han, 1988)

The explicit expressions for initial damage surfaces in principal stress space can be derived here, noting that $\alpha_d^t = \alpha_d^c = 0$ at the beginning of the damage process. Experiments (Kotsovos and Newman, 1977; Chen and Han 1988) have shown that bond cracks start to develop very early at a stress level just above the elastic limit of about $0.3 f_c'$ in uniaxial compression. This can be captured by choosing an appropriate expression for function F_1^c, with an initial threshold below the ultimate stress f_c' in uniaxial compression. The so-called cap behaviour in compression, as depicted in Figure (4.5), can also be modelled using capped damage surface. During the pre-peak stage, the initial capped damage surface gradually evolves to become an open-shaped failure surface (figure 4.5). For a capped damage loading function in compression, modification must be taken in the expression of the compressive damage criterion

$$y_d^c = \frac{(1+p_c)\bar{\sigma}_{ij}\bar{\sigma}_{ij} - q_c\left(\alpha_d^c\right)\langle\sigma_{kk}\rangle^-\langle\sigma_{ll}\rangle^- + r_c\left(\alpha_d^c\right)f_c'\langle\sigma_{kk}\rangle^-}{2E\left(1-\alpha_d^c\right)^2} - F_1^c\left(\alpha_d^c\right) = 0 \qquad (4.48)$$

in which q_c and r_c now turn out to be functions of the compressive damage indicator α_d^c. Along with function F_1^c, they must be also chosen to account for the fact that in 3D principal stress space, the initial damage ellipsoid transforms to a paraboloid when peak stress is reached, and then gradually contracts with progressive loading. The failure surface finally reduces to a single straight line, coinciding with the hydrostatic axis, when the material is totally damaged, represented by $\alpha_d^c = 1$. Although the above-mentioned approach significantly improves the performance of the proposed model in hydrostatic compression (e.g. in the model by Comi and Perego, 2001), it is left here as further extension to the 3D formulation, in which further modifications are also needed to take into account the different responses of the material in the deviatoric plane. In particular, lack of Lode angle dependency in the deviatoric section will also need to be remedied in the future by adding the third stress invariant to the damage functions.

In the present study, the initial values of F_1^t and F_1^c are taken such that damage in uniaxial tension and compression test take place at $\sigma_1 = f_t'$ and $\sigma_1 = f_c'$ respectively. The damage surfaces therefore act as failure surfaces. For the open shape of the compressive damage loading surface, only one parameter is needed, and the function can be rewritten as

$$y_d^c = \frac{(1+p_c)\bar{\sigma}_{ij}\bar{\sigma}_{ij} - p_c\langle\sigma_{kk}\rangle^-\langle\sigma_{ll}\rangle^-}{2E\left(1-\alpha_d^c\right)^2} - F_1^c\left(\alpha_d^c\right) = 0 \qquad (4.49)$$

which resembles that in tension. The resulting damage thresholds in tension and compression are:

$$F_1^t(0,0) = \frac{f_t'^2}{2E} \qquad (4.50)$$

$$F_1^c(0) = \frac{f_c'^2}{2E} \qquad (4.51)$$

As a consequence, below the ultimate stress in compression, it has been assumed here that plastic deformation is the only dissipation mechanism governing the constitutive behaviour of the model. Therefore, the failure surface opens towards the negative direction of the hydrostatic axis, and it only undergoes contraction during the

deformation process, resulting in pure elastic behaviour in hydrostatic compression. This is accepted as a deficiency of the present model in capturing the ductility of the material in hydrostatic compression.

In 2D principal stress space, the composite failure surface consists of four parts corresponding to four quadrants of the space. However, further divisions of the surface are also encountered in tension-compression and compression-tension quadrants, as the first invariant of stress tensor changes sign in crossing the plane $I_1 = \sigma_{kk} = 0$, which divides those quadrants. The equations can be derived as shown below:

For $\sigma_1 \geq 0$, $\sigma_2 \geq 0$:

$$y_d^t = \frac{(1+p_t)\left(\sigma_1{}^2 + \sigma_2{}^2\right) - p_t(\sigma_1+\sigma_2)^2}{2E} - \frac{f_t'^2}{2E} = 0 \tag{4.52}$$

$$y_d^c = -\frac{f_c'^2}{2E} < 0 \tag{4.53}$$

For $\sigma_1 \geq 0$, $\sigma_2 < 0$, $\sigma_1 + \sigma_2 \geq 0$:

$$y_d^t = \frac{(1+p_t)\sigma_1{}^2 - p_t(\sigma_1+\sigma_2)^2}{2E} - \frac{f_t'^2}{2E} = 0 \tag{4.54}$$

$$y_d^c = \frac{(1+p_c)\sigma_2{}^2}{2E} - \frac{f_c'^2}{2E} = 0 \tag{4.55}$$

For $\sigma_1 \geq 0$, $\sigma_2 < 0$, $\sigma_1 + \sigma_2 < 0$:

$$y_d^t = \frac{(1+p_t)\sigma_1{}^2}{2E} - \frac{f_t'^2}{2E} = 0 \tag{4.56}$$

$$y_d^c = \frac{(1+p_c)\sigma_2{}^2 - p_c(\sigma_1+\sigma_2)^2}{2E} - \frac{f_c'^2}{2E} = 0 \tag{4.57}$$

For $\sigma_1 < 0$, $\sigma_2 \geq 0$, $\sigma_1 + \sigma_2 \geq 0$:

$$y_d^t = \frac{(1+p_t)\sigma_2{}^2 - p_t(\sigma_1+\sigma_2)^2}{2E} - \frac{f_t'^2}{2E} = 0 \tag{4.58}$$

$$y_d^c = \frac{(1+p_c)\sigma_1{}^2}{2E} - \frac{f_c'^2}{2E} = 0 \tag{4.59}$$

For $\sigma_1 < 0$, $\sigma_2 \geq 0$, $\sigma_1 + \sigma_2 < 0$:

$$y_d^t = \frac{(1+p_t)\sigma_2{}^2}{2E} - \frac{f_t'^2}{2E} = 0 \tag{4.60}$$

$$y_d^c = \frac{(1+p_c)\sigma_1{}^2 - p_c(\sigma_1+\sigma_2)^2}{2E} - \frac{f_c'^2}{2E} = 0 \tag{4.61}$$

For $\sigma_1 < 0$, $\sigma_2 < 0$:

$$y_d^t = -f_t'^2 < 0 \tag{4.62}$$

$$y_d^c = \frac{(1+p_c)\left(\sigma_1{}^2 + \sigma_2{}^2\right) - p_c(\sigma_1+\sigma_2)^2}{2E} - \frac{f_c'^2}{2E} = 0 \tag{4.63}$$

It is worth noting here that using the concept of effective stress, the composite failure surface can be always proved to expand in the effective stress space during the deformation process. The contraction of the yield surface in this case is due to the effect of damage, through the progressive reduction of the yield thresholds during the fracture process.

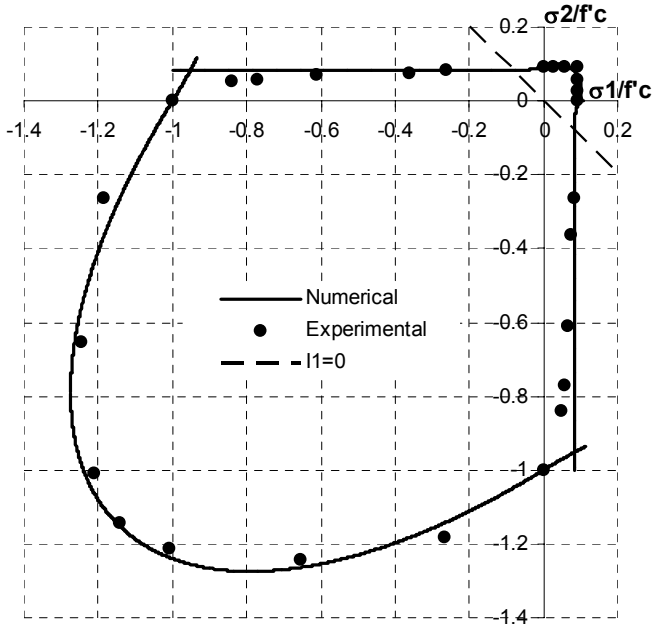

Figure 4.6: Damage failure surface in 2D principal stress space

Figure (4.6) shows the numerical and experimental failure surfaces of the material in biaxial test. Solid lines in the figure represent the composite failure surface generated by the tension and compression damage loading functions, with $f_c' = 311\text{kp/cm}^2$, $f_t' = 0.64\sqrt[3]{f_c'^2}$ (Kupfer and Gerstle, 1973), $p_t = 0.33$, $p_c = 0.62$. Experimental points in this case are taken from the biaxial tests on concrete by Kupfer and Gerstle (1973).

A detail of the graph showing the tensile behaviour is depicted in figure (4.7). This clearly shows the C_1 continuity (continuous up to the first derivative) of the damage loading functions in the transition across the plane $I_1 = 0$, which can also be proved analytically. Similarly to this, the composite failure surface can also be proved to be C_1 continuous at its intersection points with the coordinate axes $\sigma_1 = 0$ and $\sigma_2 = 0$, while discontinuities in the first derivatives are encountered only at the intersections between the two damage surfaces.

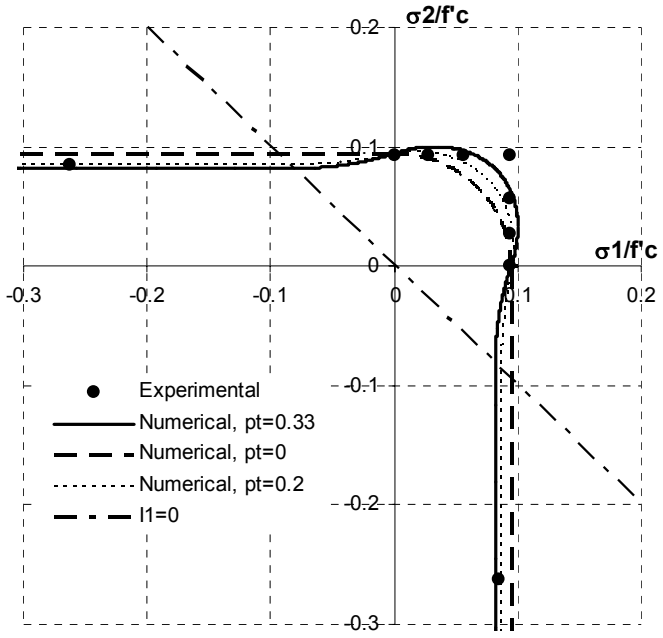

Figure 4.7: Damage failure surface, tensile behaviour

The effect of the parameter p_t on the shape of the failure surface in tension quadrant can also be seen in figure (4.7). For smaller values of p_t, the constitutive model tends to underestimate the material strength in biaxial tension, and vice versa. However, for $p_t \geq 0.5$, we obtain a damage surface opening to the positive side of the hydrostatic axis, which is unacceptable. By varying p_t, it can be concluded that its appropriate values should be in the range $0 \leq p_t \leq 0.4$, where $p_t = \nu$ is the special case with the energy term in y_d^t coinciding with the damage energy release rate $\bar{\chi}_d^t$

Obviously, a set of parameters which yields a better fit can be obtained using least-square fitting. However, this identification of parameters should be carried out based on a sufficient number of experimental sets of data to give convincing results. This model calibration is unfortunately out of the scope of the study. Therefore, for the sake of simplicity only an estimate ($p_t = 0.33$, $p_c = 0.62$) is used here to obtain the parameters

governing the shape of the damage surfaces. From the graphs (figures 4.6 and 4.7), the experimental and numerical curves match rather well in pure tension ($\sigma_1 \geq 0$, $\sigma_2 \geq 0$) or pure compression ($\sigma_1 < 0$, $\sigma_2 < 0$), while this is not the case in tension/compression quadrants. However, neglecting those slight differences, it can be preliminarily concluded that the overall behaviour of the material at failure in biaxial test can be well represented by the proposed unilateral damage model. The ductility of the material in biaxial loading ($\sigma_1 = \sigma_2 < 0$) has been accounted for, with compressive damage only being activated at stress level higher than the uniaxial compressive strength f_c'.

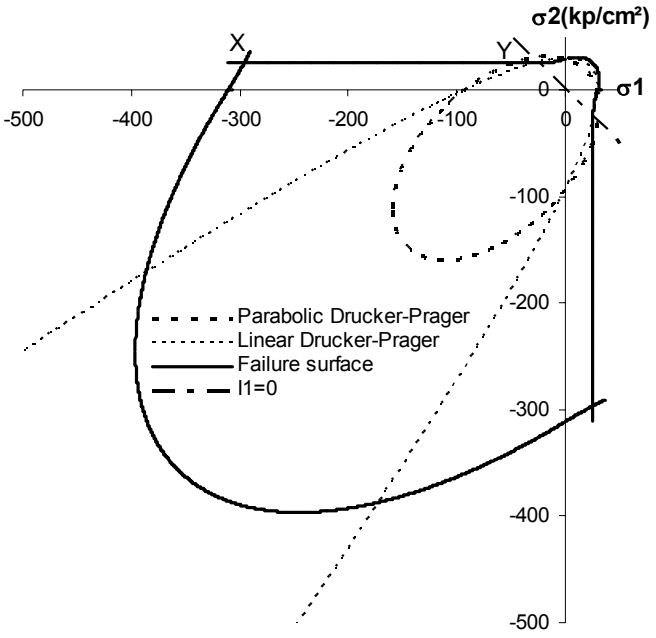

Figure 4.8: Yield and failure surfaces in principal stress space σ_1-σ_2

As the failure surface here comprises several segments in four quadrants of the plane $\sigma_3 = 0$, convexity of the damage loading surfaces in stress space is not preserved in this case. Although this concavity of the failure surface in stress space is unacceptable in conventional plasticity, here it does not violate any thermodynamic restrictions. Unlike the thermodynamic requirements for the yield surface, one consequence of which is the convexity of the yield surface, though not necessarily to be strictly satisfied (Houlsby and Puzrin, 2000), it is however not the case for damage processes with scalar damage variables. In such cases, the damage indicators and their associated variables are all scalars, automatically satisfying the thermodynamic restrictions as long as the products $\chi_d^t \dot{\alpha}_d^t$ and $\chi_d^c \dot{\alpha}_d^c$ are non-negative.

Figure (4.8) plots both the composite failure surface and the yield surface in the coordinate plane $\sigma_3 = 0$, with f_t' and $0.3f_c'$ being used as initial yield thresholds in uniaxial tension and compression respectively. For the comparison, the linear Drucker-Prager yield surface is also plotted, using f_t' and $0.3f_c'$. It is clearly seen from the figure that use of this linear Drucker-Prager surface is not appropriate for the constitutive modelling of concrete material, as it obviously does not produce plastic strains in the neighbourhood of the straight line $\sigma_1 = \sigma_2$ in biaxial tests.

From the figures (4.6, 4.7 and 4.8), the behaviour of the constitutive model can be observed. In the tension/tension quadrant the inner surface is the yield surface, but there is not much difference between yield and failure surface. In other words, plasticity is activated first but only little plastic strain occurs up to failure. However, both dissipation mechanisms are activated at the same time in uniaxial tension. The material behaviour beyond peak stress is governed by both tensile damage and plastic deformational mechanisms, which agrees well with experimental observation.

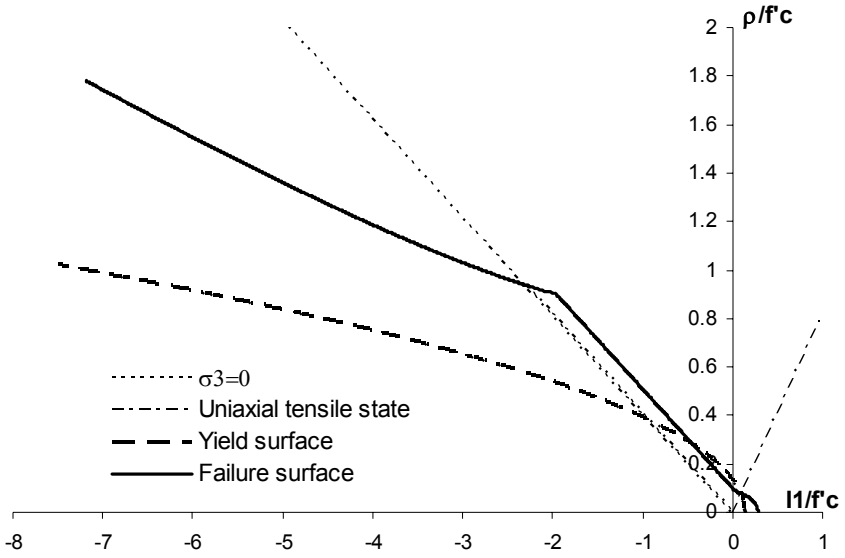

Figure 4.9: Yield and failure surfaces in the meridian plane

In tension/compression regions, tensile damage is the governing dissipation mechanism as far as the intersection of the yield surface and tensile damage surface (point Y, figure 4.8), where coupling behaviour occurs. Beyond this intersection point, from Y to X (figure 4.8), plasticity is the first dissipation mechanism to take place, followed by the coupling between damage and plasticity when the yield surface expands and hits the failure surface. A similar kind of response happens in the

compression/compression quadrant where plasticity first controls the deformation process, and then the yield surface expands until the failure surface is reached.

Use of a yield surface in conjunction with a composite failure surface also brings here some advantages of nonuniform hardening plasticity (Chen and Han, 1988) in constitutive modelling of concrete. As it is bounded by the failure surface, the yield surface cannot uniformly expand in any direction. All expansions in the tension/tension and tension/compression regions are strictly restrained by the failure surface. The yield surface can expand mostly in the compression/compression quadrant. Therefore, overestimation of plastic deformations in tension and underestimation in confined compression loading can be avoided.

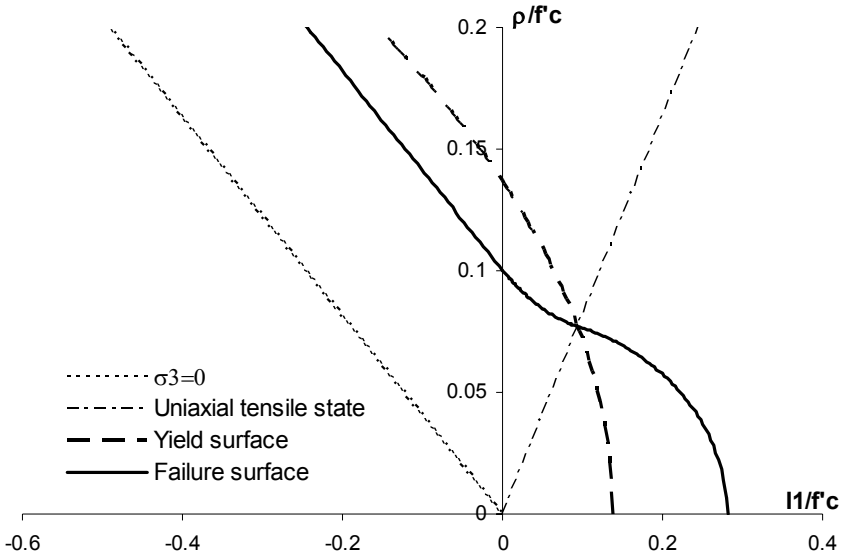

Figure 4.10: A close-up view of the yield and damage surfaces in the meridian plane

In figures (4.9) and (4.10), the yield and failure surfaces are also shown in the meridian plane. Again, the parabolic Drucker-Prager yield surface is plotted using $0.3f_c'$ as the initial yield stress in uniaxial compression. In pure tension and pure compression, the adopted yield surface represents the elastic region of the material. As can be seen, the model also exhibits "cap-behaviour" in hydrostatic tensile loading, which is physically reasonable.

4.3 Parameter identification

4.3.1 Background information

The identification and calibration of model parameters plays a crucial part in the development of constitutive models for concrete. The identification of model parameters is carried out based on either one or a series of standard experimental tests, while the calibration can be performed on a specific simulation. In other words, the parameter identification process provides us with relationships from which values of the model parameters can be obtained from input material properties and then used in the numerical analyses. This helps to relate model parameters with the material properties measured in experiments. Based on the established relationships between experimental data and model parameters, the optimal calibration can then be performed on a series of similar experimental tests to yield the best set of model parameters.

However, in practice, parameter identification is not an easy and straightforward process, especially for complicated constitutive models such as the nonlocal or gradient enhanced damage models. In particular, for smeared crack models the material data provided by experimental standard tests do not always suffice to identify all model parameters. In the case of concrete in tension, besides some properties for the elastic behaviour of the material, the additional data should include the fracture energy G_F, with the physical meaning of energy dissipated per unit cracked area, a length related to the width of the damage zone, and data on the unloading responses of the material. Difficulties in carrying out experimental tests to measure those properties, especially the material characteristic length, make the identification extremely difficult, even impossible. In addition, data on the unloading paths are not always available from standard tests. All these cause the difficulties in parameter identification, especially for complicated models with multiple dissipation mechanisms.

In this section, the identification of model parameters will be carried out independently in tension and compression, thanks to the capability of the proposed coupled damage-plasticity model (represented by equations 4.25, 4.37, 4.46 and 4.49) in distinguishing tensile and compressive responses. Some model parameters (p_t and p_c) have been directly determined from biaxial tests and presented in preceding section. However, they are only used to determine the initial shape of the failure envelope and

have no relation with the evolution of the yield and damage surfaces. The contraction of the composite failure surface in stress space is in fact governed by functions F_1^t and F_1^c, the forms and parameter identification of which will be detailed in this section. The whole process is based on uniaxial tensile and compressive tests. As a consequence, the evolution patterns of internal variables in dissipation processes are only relevant to the uniaxial behaviour of the material; however they can also be tentatively generalised to mutiaxial loading cases for practical purposes. Of course, this generalization cannot always be appropriate, but is still widely accepted and adopted in the research community for its simplicity (Meschke *et al.*, 1998; Comi, 2001; Comi and Perego, 2001; Jirasek and Patzak, 2002; Jirasek *et al.*, 2004; Salari *et al.*, 2004).

For softening materials, the explicit uniaxial stress-strain relationship cannot be obtained from experiments, causing difficulties for the identification. Therefore, to define the stress-strain law, an approximation based on quantities related to the fracture process is used. Besides the elastic properties of the material, standard tests (e.g. the three-point bending test; see section 5.2.4, Chapter 5) normally provide the fracture energy G_F in tension and possibly G_c in compression, which is insufficient for the identification. Other vital properties such as the characteristic lengths l_t and l_c in tension and compression, which are believed to be related and proportional to the widths w_t and w_c of the localization zones, are not always available from those tests.

For simple isotropic pure damage models dedicated to tensile behaviour, at least two additional material properties related to the damage process are required: the tensile fracture energy G_F and the width w_t of the fracture process zone (or alternatively the characteristic length l_t along with the ratio between w_t and l_t). The width w_t here is defined as that of an imaginary and uniformly damaged crack band (Ferrara and di Prisco, 2001; see figure 4.11). Details on w_t and the relationship between w_t and l_t will be presented in the next Chapter. The fracture energy G_F here is associated with the cohesive crack model, the correspondence of which with smeared crack model is shown in figure (4.11). It should be noted here that G_F, as the area under the stress – opening displacement curve in cohesive crack model (see section 5.2.1, Chapter 5), is not the only fracture property needed. Ideally, the stress – opening displacement curve (or stress – separation law) in cohesive crack model should be provided from experiments for the determination of model parameters. This stress-separation law can

be in principle obtained based on either fully experimental method (e.g. work of fracture method by Petersson, 1981; Bazant, 1996) or indirect method (Tin-Loi and Que, 2001; Que and Tin-Loi, 2002) using both numerical procedures and experimental data. Correspondence between the stress-separation law and stress-strain relation in continuum model is depicted in figure (4.11). As this stress-separation law is not always available from experiments, used of the fracture energy G_F along with a bilinear stress-separation law (proposed by Bazant and Becq-Giraudon, 2002; Bazant *et al.*, 2002) is adopted in this study. Similar fracture properties of the material, e.g. the compressive fracture energy G_c and the width w_c, for concrete under compression are also needed for compressive damage models. Although there have been research works on the compressive fracture energy G_c (Vonk, 1992; Jansen and Shah, 1997), the lack of experimental results still limits its frequent use in practice.

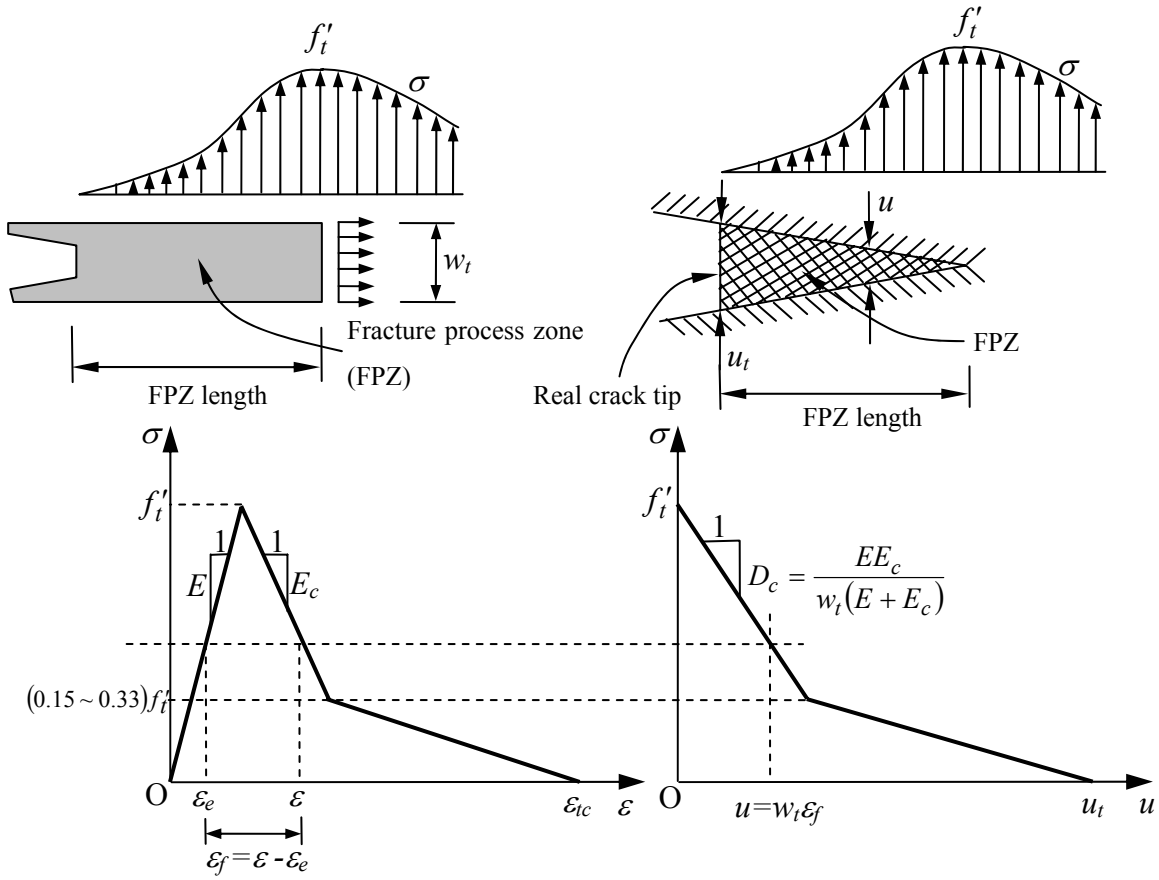

Figure 4.11: Correspondence between stress-separation law in cohesive crack model (right) and stress-strain relation in continuum model (left);
after Bazant (2002); and Elices *et al.*, 2002.

To avoid any possible confusion at this stage, it is wise just to consider the point-wise behaviour of the model. Anything related to the treatment of softening and localization will be left to Chapter 5, after sufficient details on the aspects of softening have been discussed. Therefore, from standard tests, what is vitally needed for a pure damage model in this study is the local (or specific) fracture energies g_F and g_c, represented by the area under the stress-strain curve and obtained from G_F, G_c, w_t and w_c by

$$g_F = \frac{G_F}{w_t} \text{ and } g_c = \frac{G_c}{w_c} \tag{4.64}$$

In tension, the shape of the stress-separation curve can be determined based on experimental observation (Bazant, 2002), in which the fracture energy G_F can be considered to consist of two parts corresponding to the peak and tail responses of the material (Bazant, 2002). This in fact stems from a rough estimation of the initial fracture energy G_f, which is represented by the area under the initial tangent of the stress-separation curve in the cohesive crack model (figure 4.12, right).

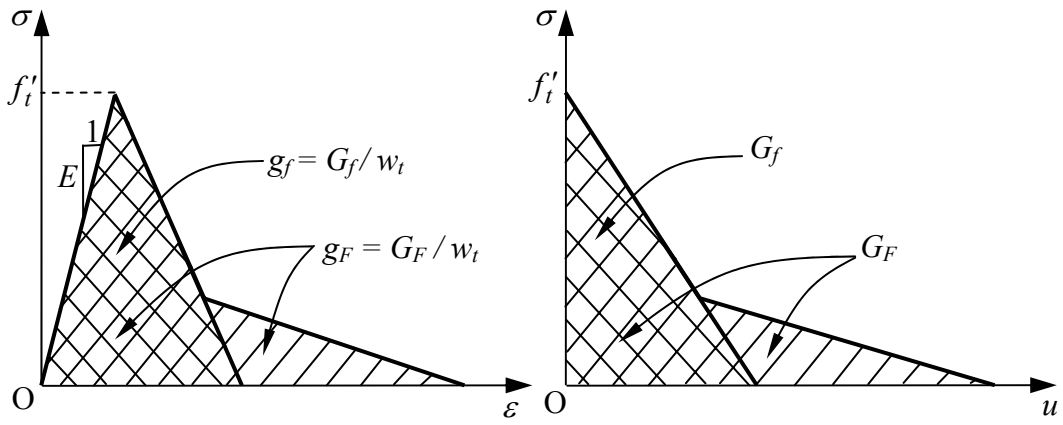

Figure 4.12: Fracture energies in cohesive crack model (right; after Bazant, 2002) and corresponding local fracture energies in continuum models (left)

Unlike G_F, which is associated with the cohesive crack model, the size-independent fracture energy G_f is determined by the size effect method (SEM, Bazant, 2002) and is related to the fracture toughness of the material. A detailed discussion on the relationship between the two fracture energies and the methods of obtaining them would give an insight into the size effect in quasi-brittle materials, but falls beyond the scope of this study. For our application, it is practical to adopt the estimation $G_F / G_f = 2.5$ proposed and confirmed by several researchers (Planas and Elices, 1990; Bazant and

Becq-Giraudon, 2002; Bazant *et al.*, 2002). Although rather scattered data on this relationship have been reported (Bazant and Becq-Giraudon, 2002), it can be used here with success in the numerical simulation, which will be shown in the coming chapters.

The above is only what has been generally observed experimentally on the behaviour of concrete and characterized in theory using a simple stress-separation law of cohesive crack models (see section 5.2.1, Chapter 5). In practice, with only G_F and G_f supplied and calculated from standard tests (e.g. the three-point bending test), the stress-separation law is usually assumed to be bilinear. As a consequence, the experimental stress-strain curve therefore can only be derived in bilinear form, with slope change at $0.15f_t'$ to $0.33f_t'$ (CEB-FIB code, 1993; Bazant, 2002). The correspondence of this curve with the stress-separation curve has been given in the literature (figure 4.11) and will be used here in this study. Following this, the stress-strain curve of the proposed model should be calibrated so as to be in accordance with this bilinear stress-strain law.

CEB-FIB model code (1993) also provided a bilinear stress-separation law for concrete, the form of which is determined based on G_F, f_t' and the maximum aggregate size $d_{\max}$. However, compared to the relation $G_F/G_f = 2.5$ (Bazant and Becq-Giraudon, 2002, Bazant *et al.*, 2002), the CEB-FIB law looks very different: $G_F/G_f = 1.36 - 2.13$ for $d_{\max} = 8 - 32\text{mm}$. Justifying those relations is not an easy task and requires further research on the fracture properties of the material, which is obviously outside the scope of this study. Meanwhile, we use here that having been proposed and recently confirmed by several authors: $G_F/G_f = 2.5$, although the maximum aggregate size in the determination of G_f is only implicitly present in G_F. Therefore the behaviour of the proposed models in this study only shows a weak link to $d_{\max}$ through the determination of model parameters based on G_F. More on the relationship between the model parameters and material properties will be presented in the coming Chapter on nonlocal regularization.

In compression, in a similar way, we also assume here that the local fracture energy g_c and the stress-strain curve can be derived from the experimentally-provided fracture energy G_c (see 4.64). However, due to the lack of experimental evidence no further assumption on the stress-strain curve can be made, resulting in a rather arbitrary way of choosing model parameters for compressive behaviour. This is obviously a

deficiency of the proposed model, which can only be resolved in combination with further experimental research on the compression behaviour of the material.

4.3.2 Coupling between damage and plasticity

The above issues are only applicable to pure damage models. To take into account the combined effects of both damage and plasticity dissipation mechanisms on the model behaviour, additional information on the loading-unloading cycles is needed. Those experimental data unfortunately cannot be obtained from standard tests. In this section, we address the coupling between damage and plasticity, and its realization in the parameter identification.

There have been several coupled damage-plasticity models proposed in the literature (see chapter 2). While most of them are truly coupled models, the some are merely pure damage models with *ad hoc* modifications on the unloading behaviour of the models (Reinhardt *et al.*, 1986; Hordijk, 1992; Hatzigeorgiou and Beskos, 2002). Although these modified damage models can produce residual strains upon unloading, which fit fairly well the experimental unloading paths in some cases, the dissipation energy in the model is solely due to damage mechanisms. Despite the simplicity and success in some cases, those *ad hoc* approaches exhibit inconsistency in the modelling and should be avoided.

In this study, coupling between damage and plasticity is implicitly contained in the system defined by (4.25), (4.37), (4.46) and (4.49), which governs the behaviour of the model. In this case, the energy dissipated per unit volume g_F, represented by the area under the stress-strain curve, is contributed from both failure mechanisms: damage and plasticity. On the other hand, it has also been shown (Bazant, 1996) that the fracture energy G_F determined by the work-of-fracture method (RILEM, 1985), assuming that the material behaviour follows that of cohesive crack model, always contains plastic-frictional energy dissipation. This evidence can be confirmed by cyclic tests on tensile-dominant behaviour of concrete (Reinhardt *et al.*, 1986; Hordijk, 1992; Perdikaris and Romeo, 1995). However, the fact that G_F is not a pure damage fracture energy has been sometimes disregarded in continuum damage models developed for the constitutive modelling of concrete.

In those pure damage models, the fracture energy G_F was used as a material property governing the post-peak behaviour of the material, regardless of the fact that a significant part of G_F is contributed from plastic-frictional dissipation mechanisms, e.g. aggregate interlock or interfacial frictions between the constituents. This is in fact acceptable, as the sole damage dissipation mechanism in such cases must produce same dissipation energy at a structural level. However, it is not the case in which a plastic deformation mechanism and damage mechanism are present in the constitutive model. The correct fracture energy that should be used for damage law in this case must be the pure fracture energy denoted here as G_{pF}, which in principle can be determined if the unloading stiffness is known for a sufficient number of points on the softening load-deflection curve (Bazant, 1996). It is also worth making clear here that G_{pF} should also be used in case where the damage evolution law is explicitly defined in a coupled model, which is not the case with the models proposed in this study.

For the coupled damage-plasticity models in this study, the evolution laws of damage indicators and plastic strains as well as the coupling between the two dissipation mechanisms are implicitly defined through the constitutive relations (4.25), (4.37), (4.46) and (4.49). The stress-strain curve and hence the fracture energy are governed by all the parameters of the coupled model. As a consequence, the fracture energy G_F along with some other material properties in unloading should be used for the determination of model parameters. Separation of the energy dissipated during the failure process is needed, which is in fact based on the assumption that unloading data can be obtained from standard experiments (Bazant, 1996), e.g. the three-point bending test for fracture energy recommended by RILEM (1985). The adoption and realization of this assumption in testing practice are, however, still far from reality.

4.3.3 Tensile behaviour, identification of model parameters

The process here is based on a one-dimensional model and for coupled damage-plasticity models (represented by equations 4.25, 4.37, 4.46 and 4.49). In one-dimensional tension, functions $F_1^{t^*}$ and F_1^t coincide, the energy function and dissipation function are of simplified forms:

$$f = \frac{1}{2}\left(1-\alpha_d^t\right)E\left(\varepsilon-\alpha_p\right)^2 \tag{4.64a}$$

$$d = F_1^t\left(\alpha_d^t, \alpha_d^c\right)\dot{\alpha}_d^t + \left(1-\alpha_d^t\right)\left(f_t' + H_t\alpha_p\right)\dot{\alpha}_p \tag{4.64b}$$

and the governing constitutive relations (4.25, 4.37, 4.46) reduce to

$$\sigma = \left(1-\alpha_d^t\right)E\left(\varepsilon - \alpha_p\right) \tag{4.65}$$

$$y_p = \sigma - \left(1-\alpha_d^t\right)\left(f_t' + H_t\alpha_p\right) = 0 \tag{4.66}$$

$$y_d^t = \frac{E\left(\varepsilon-\alpha_p\right)^2}{2} - F_1^t\left(\alpha_d^t, \alpha_d^c\right) = 0 \tag{4.67}$$

in which the accumulated plastic strain ε_p^t in (4.21) has been assumed to reduce to α_p in uniaxial tension. As mentioned in the model formulation (section 4.2.3), this assumption is in fact valid only in case where a pressure-independent yield function is used. It is adopted here only for simplicity. A strain-based damage model is used in this case; but in uniaxial tension, switching between strain- and stress-based models is straightforward. As the material behaviour is only in the tensile regime, the compressive damage indicator α_d^c is zero throughout the dissipation process and can be considered as a parameter of the function F_1^t.

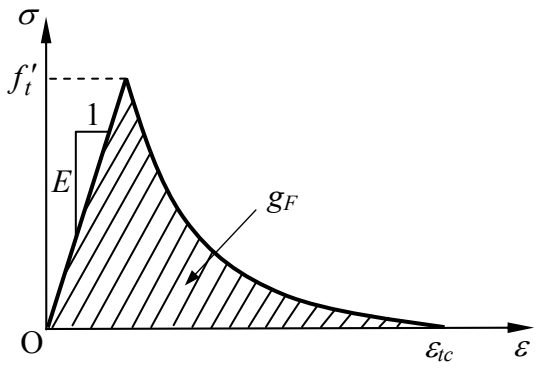

Figure 4.13: Local fracture energy g_F in uniaxial tension

The determination of the local (or specific, or volumetric) fracture energy g_F is the backbone of this parameter identification. From its definition (figure 4.13), g_F can be written

$$g_F = \int_0^\infty \sigma \, d\varepsilon \tag{4.68}$$

In principle, the stress σ, tensile damage indicator α_d^t and plastic strain α_p can be obtained analytically from the system (4.65-4.67), and can all be expressed in terms of

the total strain ε. Unfortunately, this is not always the case in practice as the solution of the system (4.65-4.67) strongly depends on the type of function F_1^t. As a remedy for the problem, it is much easier to perform all necessary mathematical manipulations with respect to the damage indicator α_d^t, as the only variable. As a consequence, in the integral (4.68), a change of variable is needed, with the damage indicator α_d^t replacing the total strain ε. Bypassing intermediate details of mathematical manipulations, we can obtain from (4.65-4.67) the stress σ, plastic strain α_p and total strain ε, all in terms of the damage indicator α_d^t as follows

$$\sigma = \left(1-\alpha_d^t\right)\sqrt{2EF_1^t\left(\alpha_d^t,\alpha_d^c\right)} \tag{4.69}$$

$$\alpha_p = \frac{1}{H_t}\sqrt{2EF_1^t\left(\alpha_d^t,\alpha_d^c\right)} - \frac{f_t'}{H_t} \tag{4.70}$$

$$\varepsilon = \frac{E+H_t}{H_t}\sqrt{\frac{2F_1^t\left(\alpha_d^t,\alpha_d^c\right)}{E}} - \frac{f_t'}{H_t} \tag{4.71}$$

Noting that $\alpha_d^t = 0$ at $\varepsilon \le f_t'/E$, the integral (4.68) becomes

$$\begin{aligned} g_F &= \frac{f_t'^2}{2E} + \int_0^1 \sigma\left(\alpha_d^t\right)\frac{\partial\varepsilon}{\partial\alpha_d^t}d\alpha_d^t \\ &= \frac{f_t'^2}{2E} + \frac{E+H_t}{H_t}\int_0^1\left(1-\alpha_d^t\right)\frac{\partial F_1^t}{\partial\alpha_d^t}\,d\alpha_d^t \end{aligned} \tag{4.72}$$

It is interesting to note here that the above local fracture energy can also be obtained from direct integration of the dissipation function d in (4.64b) (d is actually the rate of dissipation) in one dimensional tension. This is one of the advantages, although not very apparent here, of building constitutive models based on thermodynamic principles. From (4.72), it is essential that the integral in the second term is bounded, which can for instance be satisfied with the following choice of function F_1^t:

$$F_1^t = \left(1-\alpha_d^c\right)\frac{f_t'^2}{2E}\left[\frac{E+E_{pt}\left(1-\alpha_d^t\right)^{n_t}}{E\left(1-\alpha_d^t\right)+E_{pt}\left(1-\alpha_d^t\right)^{n_t}}\right]^2 \tag{4.73}$$

with initial values

$$F_1^t\Big|_{\alpha_d^t=0} = \frac{f_t'^2}{2E} \text{ and } \frac{\partial F_1^t}{\partial\alpha_d^t}\Big|_{\alpha_d^t=0} = \frac{f_t'^2}{E+E_{pt}} \tag{4.74}$$

in which E_{pt} and n_t are two model parameters controlling the damage process. In a pure damage model, $-E_{pt}$ is exactly the initial tangent modulus at peak stress and n_t is used to control the rate of change of this modulus during the deformation process. The above choice of function F_1^t also guarantees the asymptotic vanishing of stress σ for strain $\varepsilon \to \infty$, avoiding *ad hoc* procedures for the treatment of zero strength finite elements in the numerical implementation.

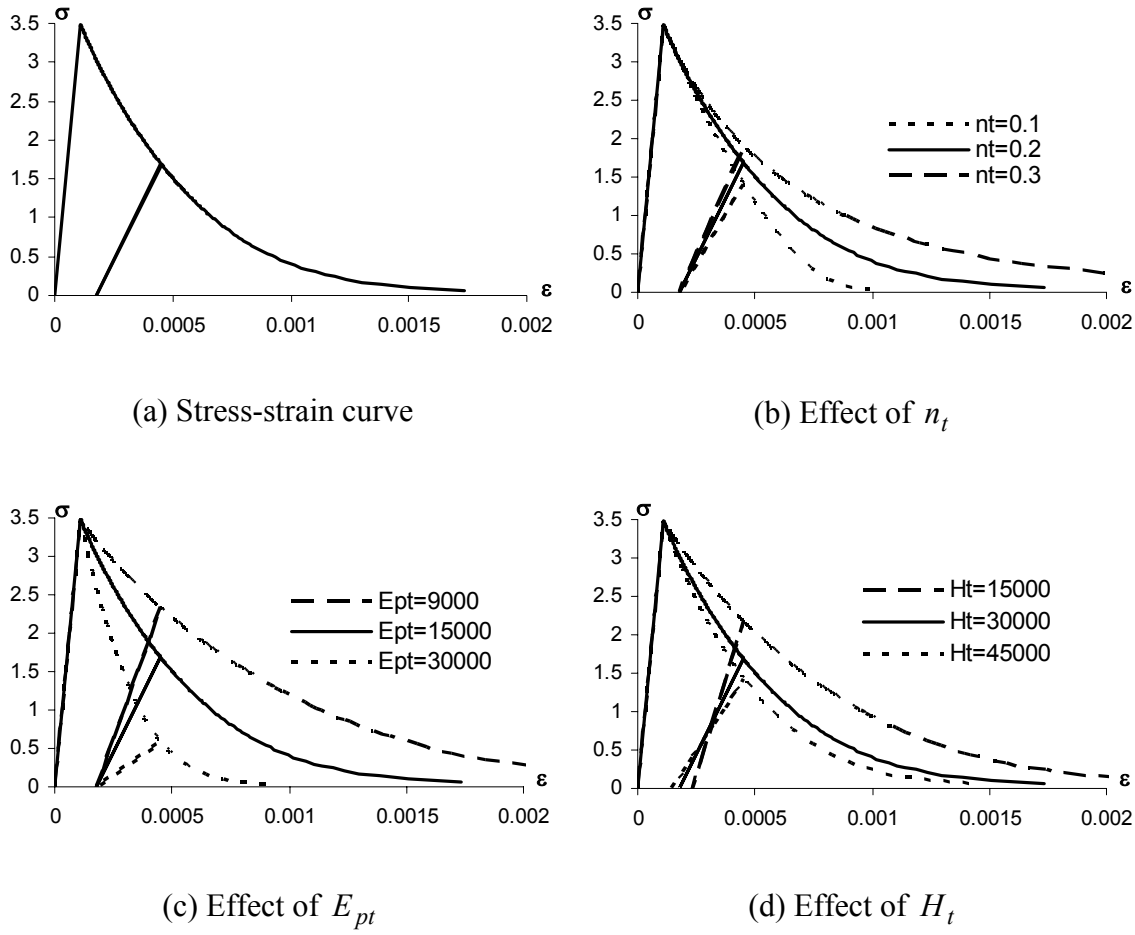

(a) Stress-strain curve

(b) Effect of n_t

(c) Effect of E_{pt}

(d) Effect of H_t

Figure 4.14: Effect of parameters on the model response in tension

The effect of model parameters on the stress-strain response is shown in figure (4.14), using the following material properties and model parameters: $E = 31700\text{Mpa}$, $f_t' = 3.48\text{Mpa}$, $E_{pt} = 15000\text{MPa}$, $n_t = 0.2$ and $H_t = 30000\text{MPa}$. The stress-strain curve corresponding to the above properties is plotted in figure (4.14a). In figures (4.14b), (4.14c) and (4.14d) each model parameter in turn is varied, while others are kept fixed, to show corresponding effect on the stress-strain curve. It can be clearly seen in these figures that the plastic strain α_p is governed solely by the hardening modulus H_t, while the stress-strain curve is controlled by all the parameters of the model.

In a similar way, for a pure damage model, we obtain, either from (4.69 and 4.71) or from direct integration of the dissipation function d with respect to the only active internal variable α_d^t

$$g_F = \int_0^1 F_1^t \, d\alpha_d^t = \frac{f_t'^2}{2E} + \int_0^1 \left(1 - \alpha_d^t\right) \frac{\partial F_1^t}{\partial \alpha_d^t} \, d\alpha_d^t \tag{4.75}$$

The only difference compared to (4.72) is the factor in front of the integral in g_F, which indicates that the pure damage model is an extreme case of a coupled one when $H_t \to \infty$.

All model parameters governing the evolution of the dissipation processes are to be determined based on equation (4.72). This is obviously impossible as in general, besides the hardening parameter H_t there are also other parameters appearing in function F_1^t and controlling the damage dissipation. The expression above can only be considered as a relationship between model parameters rather than an equation helping to explicitly determine those parameters. The proposed parameter identification therefore becomes ill-posed unless some constraints are imposed.

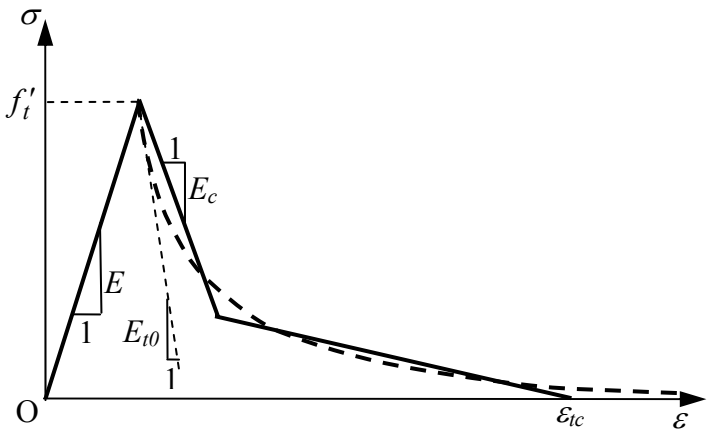

Figure 4.15: Nonlinear stress-strain curve based on the experimentally derived bilinear stress-strain relation

Ideally, the nonlinear softening curve used in this study should be calibrated based on a nonlinear stress-separation curve in cohesive crack model, which in turn is obtained from indirect experimental methods (see Tin-Loi and Que, 2001; Que and Tin-Loi, 2002). However, a stopgap based on the fracture energies G_F and G_f, and a bilinear softening law (see section 4.3.1), is used here due to the lack of experimental data on the nonlinear softening behaviour of the material. From the observation on the

shape of the softening curve (figure 4.15), the nonlinear stress-strain relation in the proposed model should yield a close fit to at least the first part of the bilinear softening law (see figure 4.15), determined by the local specific fracture energy g_f and realized through the initial tangent modulus E_c at peak stress. This modulus in turn is related to the slope D_c at peak stress in the cohesive crack model, through the relation

$$D_c = \frac{EE_c}{w_t\left(E + E_c\right)} \tag{4.76}$$

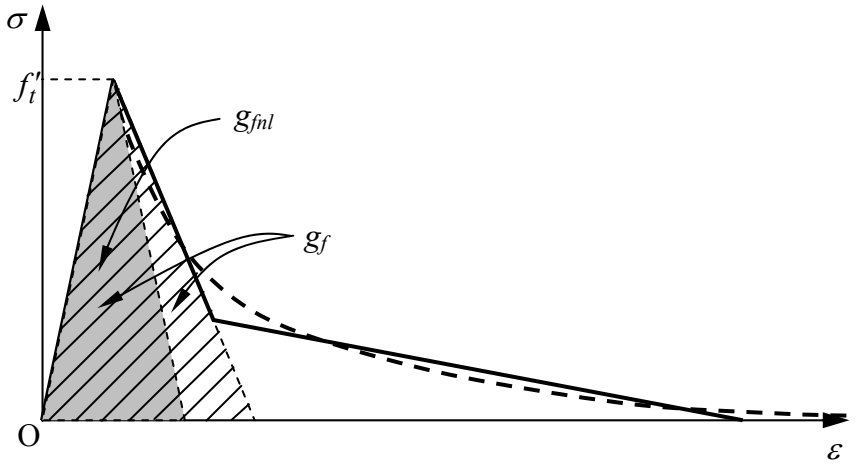

Figure 4.16: Definition of the local fracture energy g_{fnl} for nonlinear softening behaviour

Those slopes (E_c and D_c) decide the ultimate load of the analyzed structure (Bazant, 2002). Therefore, if one does not care about the tail response of the structure, the initial softening modulus E_{t0} (see figure 4.15) of the nonlinear stress-strain relation of the proposed model here can be taken as E_c, and directly derived from the input material properties (G_F, f_t' and the width w_t of the localization band). In such cases n_t should be kept small enough (less than 0.1 for function F_1^t in (4.73)) so as to minimize the effect of the gradual slope change in the stress-strain curve (see figure 4.14b) on the structural peak load. However, this neglect of tail response is not the case here and, to some extent, we will consider both peak and, though only roughly, tail responses of the overall load-displacement curve. If this is the case, optimal fitting for the proposed nonlinear stress-strain relation and the experimentally derived counterpart could be useful in the parameter identification. In this study, only simple fitting based on the ratio $t = g_{fnl}/g_F$ between the facture energies g_{fnl} and g_F (figure 4.16) is adopted.

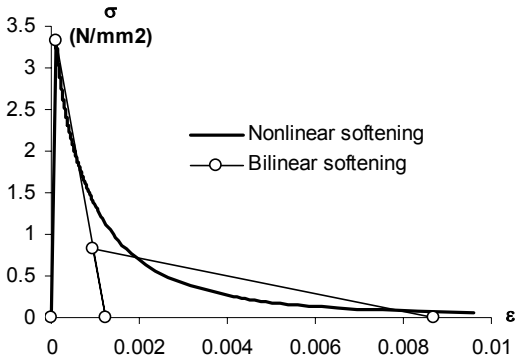

(a) w_t=24mm; t=g_{fnl}/g_F=0.2

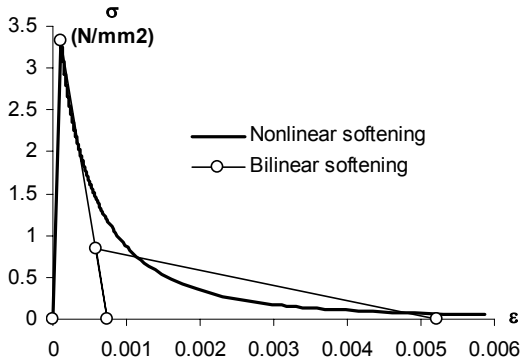

(b) w_t =40mm; t=g_{fnl}/g_F=0.25

($E = 30000\text{N/mm}^2$; $f_t' = 3.33\text{N/mm}^2$; $G_F = 0.124\text{N/mm}$; $d_{\max} = 8\text{mm}$)

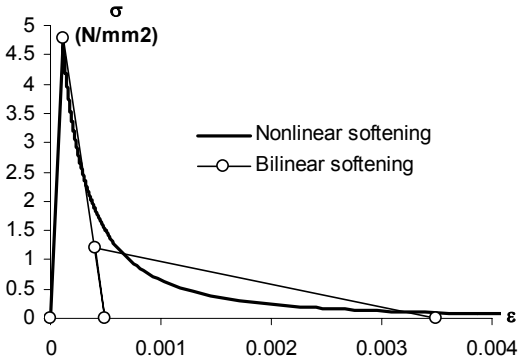

(c) w_t =30mm; t=g_{fnl}/g_F=0.25

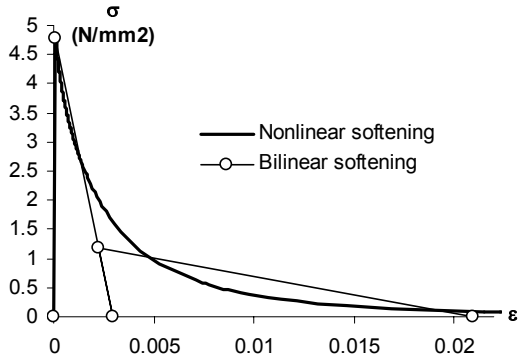

(d) w_t =5mm; t=g_{fnl}/g_F=0.15

($E = 43600\text{N/mm}^2$; $f_t' = 4.77\text{N/mm}^2$; $G_F = 0.08917\text{N/mm}$; $d_{\max} = 6\text{mm}$)

Figure 4.17: Determining the nonlinear stress-strain relation from the experimentally derived bilinear softening law

As can be seen in (4.76), the width w_t of the localization band also plays an important role in the derivation of the bilinear stress-strain relation from the corresponding stress-separation law. In other words, this width has a crucial effect on the initial softening modulus E_{t0} of the uniaxial bilinear stress-strain relation. As a consequence, the curve fitting heavily depends on w_t (see figure 4.17), and in turn on the element size (crack band models) or the nonlocal interaction radius R (for nonlocal models). The determination of w_t, which, in this study, is related to the nonlocal behaviour of the model adopted, will be presented in the next Chapter. Therefore, for the sake of simplicity, it is wise to assume here that w_t is known in advance.

From the suggested curve fitting (figures 4.15, 4.16 and 4.17), it is seen that the ratio $g_F/g_f = 2.5$ (or $G_F/G_f = 2.5$), which applies to the bilinear softening law, has to be appropriately adapted to the nonlinear softening law adopted here. In particular, the shaded area in figure (4.16), determined from the tangent of the nonlinear stress-strain curve at peak stress, should be smaller than g_f (striped area in figure 4.16) to yield a good fit. This shaded area is denoted here as g_{fnl} and for simplicity will be taken as $t\,g_F$ in this study, where t has value from 0.1 to 0.3, depending on the tensile strength f_t', fracture energy G_F of the material and width w_t of an imaginary and uniformly damaged crack band. This is only a rough estimation for practical application, as a better fit can generally be achieved by use of more advanced mathematical procedures. However, use of those advanced fitting techniques would become unnecessary on the basis of the rather crude bilinear approximation of the material behaviour. They are therefore not pursued here. In practice, it has been experienced in this study that $t = 0.2 \sim 0.3$ is adequate for nonlocal models, whereas in some cases $t = 0.1 \sim 0.2$ must be adopted for some rather small value of width w_t (see figure 4.17). However, this is only a rough estimation based on only very few experimental data and used here with some success in the numerical analysis. Choice of this ratio should therefore be further confirmed.

With an additional property (g_{fnl}) in hand, we can now derive another relationship between the model parameters and material properties. An explicit expression for the initial tangent modulus in uniaxial tension is required for this relationship, which can be obtained using the rate form of the system (4.65-4.67) or directly from (4.69 and 4.71). From (4.69) and (4.71), the tangent modulus E_t is derived as

$$E_t = \frac{d\sigma}{d\varepsilon} = \frac{-\sqrt{2EF_1^t\left(\alpha_d^t,\alpha_d^c\right)} + \left(1-\alpha_d^t\right)\dfrac{\partial F_1^t}{\partial \alpha_d^t}\dfrac{\sqrt{E}}{\sqrt{2F_1^t\left(\alpha_d^t,\alpha_d^c\right)}}}{\dfrac{E+H_t}{H_t}\dfrac{\partial F_1^t}{\partial \alpha_d^t}\dfrac{1}{\sqrt{2EF_1^t\left(\alpha_d^t,\alpha_d^c\right)}}} \tag{4.77}$$

Substitution of the initial values of function F_1^t and its derivative into (4.77) yields the initial tangent modulus E_{t0} (figure 4.15)

$$E_{t0} = -\frac{E_{pt}H_t}{E+H_t} \tag{4.78}$$

It is readily seen from (4.78) that $E_{t0} = -E_{pt}$ when $H_t \to \infty$, which is the case of a pure damage model. The initial local fracture energy g_{fnl} is now

$$g_{fnl} = \frac{f_t'^2}{2E} - \frac{f_t'^2}{2E_{t0}} = \frac{f_t'^2}{2}\left(\frac{1}{E} + \frac{E + H_t}{E_{pt}H_t}\right) \tag{4.79}$$

Using (4.72) and (4.79), two parameters E_{pt} and n_t in a pure damage model are now ready to be determined. However, for coupled damage-plasticity models, more material properties are still needed, which should be based on the unloading paths at several points on the stress-strain relationship (see figure 4.18).

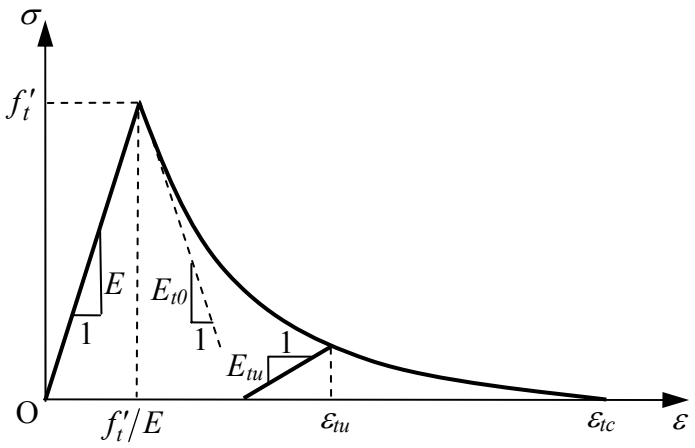

Figure 4.18: Assumed uniaxial stress-strain relationship with an unloading path

Those data can be obtained from the standard three-point bending test by measuring the unloading slopes at a sufficient number of points on the load-separation curve. These slopes are then transformed to unloading slopes in the stress-strain relationship. Alternatively, experiments on cyclic loading of a double edge notched specimen can be proposed to obtain the load-displacement response, through which the fracture energy G_F as well as unloading slopes can be derived. This proposal is based on the separation of energy dissipated during the deformation process (Bazant, 1996), in which energy dissipated through the damage and plasticity dissipation processes can be obtained and assigned to the corresponding mechanisms in the constitutive modelling. As it concerns both theoretical and experimental studies, the realization of this proposal is, however, left here for the future research. Therefore it can be simplified here assuming that unloading slopes at several points on the stress-strain curve have been obtained from experiments. In particular, the uniaxial strain ε_{tu} at which load reversal takes place and

the corresponding unloading modulus E_{tu} are assumed to be available (figure 4.18). Only one pair of ε_{tu} and E_{tu} is needed for the proposed model, as there is only one hardening parameter associated with the plasticity part of the model. Adoption of more advanced plasticity models, such as the continuous kinematic hardening hyperplasticity (Puzrin and Houlsby, 2001) is in principle possible, but obviously requires more data on the unloading paths.

All the model parameters are now ready to be derived, with the following nonlinear system of equations having to be solved for H_t, E_{pt} and n_t:

$$g_F = \frac{f_t'^2}{2E} + \frac{E + H_t}{H_t} \int_0^1 \left(1 - \alpha_d^t\right) \frac{\partial F_1^t}{\partial \alpha_d^t} \, d\alpha_d^t \tag{4.80}$$

$$g_{fnl} = \frac{f_t'^2}{2} \left(\frac{1}{E} + \frac{E + H_t}{E_{pt} H_t} \right) \tag{4.81}$$

$$\varepsilon_{tu} = \frac{E + H_t}{H_t} \sqrt{\frac{2F_1^t\left(\alpha_{du}^t, 0\right)}{E}} - \frac{f_t'}{H_t}; \text{ with } \alpha_{du}^t = 1 - \frac{E_{tu}}{E} \tag{4.82}$$

The input material properties are: elasticity modulus E; ultimate tensile stress f_t'; strain ε_{tu} at which unloading takes place and its corresponding unloading stiffness modulus E_{tu}; and the specific fracture energies g_F and g_{fnl}, where $g_{fnl} = (0.1 - 0.3) g_F$. Although the integration in (4.80) cannot be computed analytically, it can be shown to be bounded. A simplified version of the model with only damage mechanism activated can be directly derived from the above system by dropping out the last equation (4.82) and setting $H_t = \infty$ in equations (4.80) and (4.81). A Matlab code has been written to solve the above system of nonlinear equations.

4.3.4 Compressive behaviour, identification of model parameters

In a similar way, based on the specific fracture energy g_c (see figure 4.20) and unloading data at points on the stress-strain curve, we can also obtain the relationships between parameters of the proposed model (represented by equations 4.25, 4.37, 4.46 and 4.49) and the experimentally-provided material properties in compression. The governing constitutive relationships in uniaxial compression are:

In the pre-peak hardening region

$$\sigma = E\left(\varepsilon - \alpha_p\right) \tag{4.83}$$

$$y_p = \sigma - \left(f_{c0} + H_c \alpha_p\right) = 0 \tag{4.84}$$

In the post-peak softening region

$$\sigma = \left(1 - \alpha_d^c\right) E\left(\varepsilon - \alpha_p\right) \tag{4.85}$$

$$y_p = \sigma - \left(1 - \alpha_d^c\right)\left(f_{c0} + H_c \alpha_p\right) = 0 \tag{4.86}$$

$$y_d^c = \frac{E\left(\varepsilon - \alpha_p\right)^2}{2} - F_1^c\left(\alpha_d^c\right) = 0 \tag{4.87}$$

in which the equations have been simplified here because the stress σ and total strain ε are always positive. The accumulated plastic strain ε_p^c is always positive and assumed to reduce to the uniaxial plastic strain α_p which also takes positive value. No loss of generality occurs from the above simplification on the signs of stress and strain, as g_c is the product of stress and strain and is always non-negative, making it useful to consider both stress σ and strain ε either positive or negative.

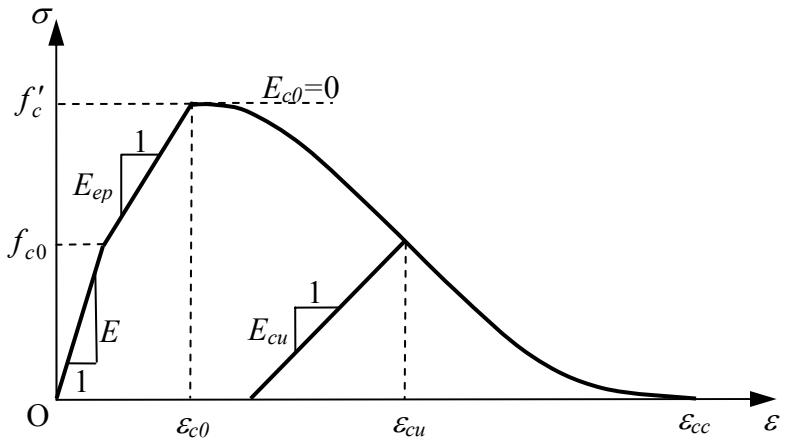

Figure 4.19: Assumed stress-strain relationship in uniaxial compression

Depicted in figure (4.19) is the constitutive behaviour of the model in uniaxial compression, in which plasticity is supposed to take place at $\sigma = f_{c0}$. From experiments, f_{c0} is found to be about 30% of the ultimate compressive stress f_c' (Chen and Han, 1988). For the adopted linear hardening plasticity in compression, only one hardening parameter (H_c) is needed, and can be directly determined from f_{c0}, f_c' and E. However, H_c also takes part in the post-peak behaviour of the model, along with other parameters of function F_1^c, and can also be determined based on the fracture energy g_c and unloading properties in figure (4.19). The contradiction can be avoided if more than one hardening parameter is used, for example one hardening parameter for

the ascending part and another for the descending branch of the stress-strain curve. Here, for simplicity, f_{c0} and H_c are treated as two dependent model parameters to be determined, provided that they satisfy the condition $0 < f_{c0} < f_c'$. This simplification is acceptable because of the path-independent nature of the plastic dissipation. The relationship between f_{c0} and H_c can be derived from figure (4.19)

$$f_{c0} = \frac{f_c'(E + H_c)}{E} - H_c \varepsilon_{c0} \tag{4.88}$$

with E_{ep} in the figure being the elasto-plastic tangent stiffness, defined by

$$\frac{1}{E_{ep}} = \frac{1}{E} + \frac{1}{H_c} \tag{4.89}$$

For the stress σ, from (4.85-4.87), we obtain

$$\sigma = \left(1 - \alpha_d^c\right)\sqrt{2EF_1^c\left(\alpha_d^c\right)} \tag{4.90}$$

Similarly to (4.70), and (4.71), we have the total strain ε and plastic strain α_p

$$\alpha_p = \frac{1}{H_c}\sqrt{2EF_1^c\left(\alpha_d^c\right)} - \frac{f_{c0}}{H_c} \tag{4.91}$$

$$\varepsilon = \frac{E + H_c}{H_c}\sqrt{\frac{2F_1^c\left(\alpha_d^c\right)}{E}} - \frac{f_c}{H_c} \tag{4.92}$$

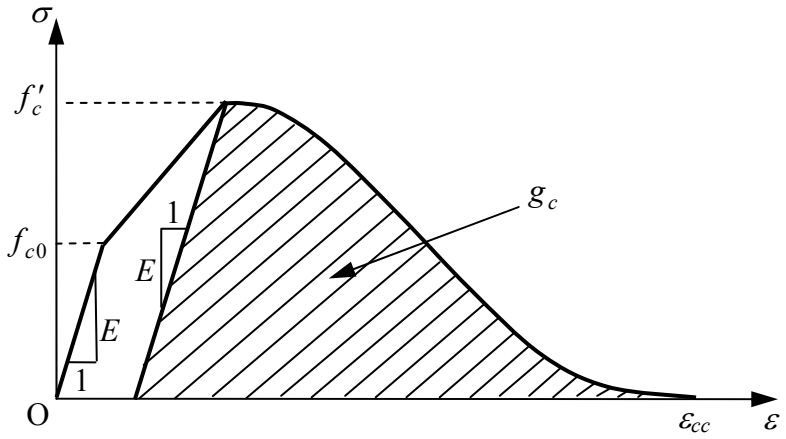

Figure 4.20: Local (specific or volumetric) fracture energy g_c in compression

The local fracture energy g_c in compression also resembles its tensile counterpart g_F in (4.72). One should note here that the local dissipation energy in compression comprises two parts corresponding to the pre-peak hardening and post-peak softening

regimes on the stress-strain curve. However, because of its localization nature only the second part (g_c in figure 4.20) is present in the measured fracture energy G_c provided by experiment (Krätzig and Pöling, 2004). This feature has in fact been proven and adopted for tensile softening with some hardening behaviour before peak load (Bazant, 1982; Bazant and Pijaudier-Cabot, 1989). We simply adopt it here without further discussion. Therefore, we have:

$$g_c = \frac{f_c'^2}{2E} + \int_0^1 \sigma\left(\alpha_d^c\right) \frac{\partial \varepsilon}{\partial \alpha_d^c} d\alpha_d^c = \frac{f_c'^2}{2E} + \frac{E + H_c}{H_c} \int_0^1 \left(1 - \alpha_d^c\right) \frac{\partial F_1^c}{\partial \alpha_d^c} d\alpha_d^c \tag{4.93}$$

in which function F_1^c is of the form

$$F_1^c = \frac{f_c'^2}{2E} \left\{ \frac{E + E_{pc}\left(1 - \alpha_d^c\right)^{n_c} \left[\ln\left(1 + \alpha_d^c\right)\right]^{m_c}}{E\left(1 - \alpha_d^c\right) + E_{pc}\left(1 - \alpha_d^c\right)^{n_c} \left[\ln\left(1 + \alpha_d^c\right)\right]^{m_c}} \right\}^2 \tag{4.94}$$

with initial values

$$F_1^c\Big|_{\alpha_d^c = 0} = \frac{f_c'^2}{2E} \tag{4.95}$$

$$\left.\frac{\partial F_1^c}{\partial \alpha_d^c}\right|_{\alpha_d^c = 0} = \frac{f_c'^2}{E} = 2F_1^c\Big|_{\alpha_d^c = 0} \tag{4.96}$$

In (4.94), there are three parameters controlling the damage process in compression: m_c controlling the ductility of the stress-strain curve, n_c governing the tail response of the model, and E_{pc} deciding the descending slope of the stress-strain curve. Like F_1^t, the similar function F_1^c also guarantees the asymptotic vanishing of stress σ for strain $\varepsilon \to \infty$. Moreover, the properties in (4.95-4.96) also result in zero tangent stiffness at peak stress ($E_{c0} = 0$). In addition, for relevant values of E_{pc}, m_c and n_c, the local compressive fracture energy g_c, represented by the striped area under the stress-strain curve in figure (4.20) and calculated using (4.93), can also be found to be bounded.

To illustrate the effect of the model parameters on the behaviour of the model, a simple uniaxial stress-strain curve in compression is used, with the following material properties and model parameters: $E = 30000\text{Mpa}$, $f_c' = 27.6\text{Mpa}$, $E_{pc} = 45000\text{MPa}$, $n_c = 0.15$, $m_c = 3$, $H_c = 15000\text{MPa}$ and $\varepsilon_{c0} = 2f_c'/E$. The stress-strain curve using the above properties and parameters are the solid lines in figure (4.21), in which the

results obtained from varying each parameter while keeping others fixed are also shown.

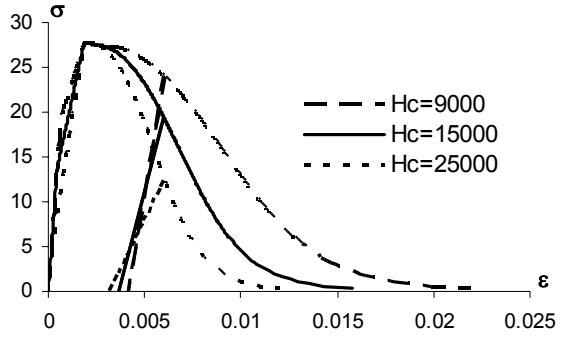

(a) Effect of H_c

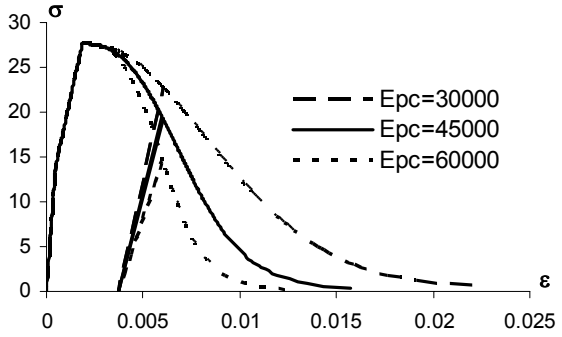

(b) Effect of E_{pc}

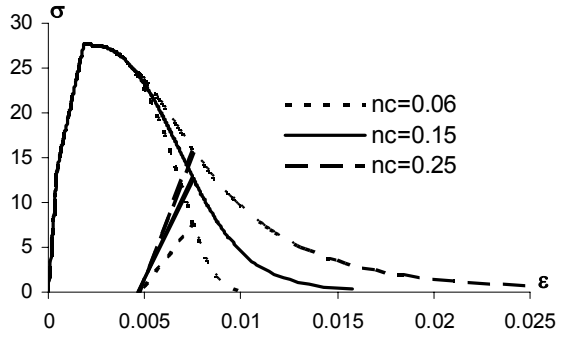

(c) Effect of n_c

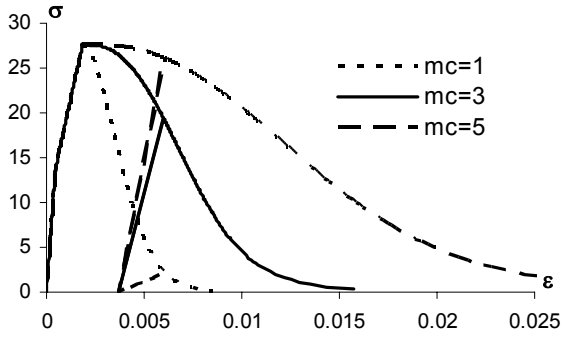

(d) Effect of m_c

Figure 4.21: Effect of parameters on the model response in compression

From (4.88), (4.93) and the unloading expression similar to (4.82), we have a set of equations established for the determination of model parameters in compression:

$$f_{c0} = \frac{f_c'\left(E + H_c\right)}{E} - H_c \varepsilon_{c0} \tag{4.97}$$

$$g_c = \frac{f_c'^2}{2E} + \frac{E + H_c}{H_c} \int_0^1 \left(1 - \alpha_d^c\right) \frac{\partial F_1^c}{\partial \alpha_d^c} \, d\alpha_d^c \tag{4.98}$$

$$\varepsilon_{cu} = \frac{E + H_c}{H_c} \sqrt{\frac{2F_1^c\left(\alpha_{du}^c\right)}{E}} - \frac{f_{c0}}{H_c}; \text{ with } \alpha_{du}^c = 1 - \frac{E_{cu}}{E} \tag{4.99}$$

It is noted here that equation (4.99) does not enter the calculation of model parameters, as H_c is directly obtained from (4.97), based on pre-assigned value of f_{c0} and ε_{c0}.

This equation (4.99) is only used to compute the permanent strain produced by the model in uniaxial compression. In a similar way to then tension case, a simplified model with only damage mechanism can be derived from the above system by dropping out equations (4.97) and (4.99), and setting $H_c = \infty$ in equation (4.98).

The input material properties in this case are the elasticity modulus E; initial yield stress f_{c0}, which, in practice, can be chosen in the range $0 < f_{c0} < f_c'$; uniaxial compressive strength f_c' and its corresponding strain ε_{c0}; and the local fracture energy g_c. With two equations (4.97 and 4.98) for four parameters to be determined, which are the hardening parameter H_c, and three parameters E_{pc}, m_c and n_c of function F_1^c, the system (4.97-4.98) is only solvable if there are two parameters being pre-assigned relevant values. The other parameters are then computed from the system (4.97-4.98). Normally, E_{pc} and either m_c or n_c, which control the shape of the post-peak uniaxial stress-strain curve, is chosen for this purpose. This is because (4.97) and (4.98) are independent and H_c can be directly obtained from (4.97). The residual strain at a given point on the stress-strain curve can then be computed (using 4.99) and compared with experimental value. As the values of H_c are bounded in the range $H_{c1} < H_c < H_{c2}$, with H_{c1} corresponding to $f_{c0} = 0$ and H_{c2} to $f_{c0} = f_c'$ (see 4.97), a compromised choice of H_c can be made in the specified range ($0 < f_{c0} < f_c'$) so as to yield closest fit to the given unloading path.

4.4 Numerical examples

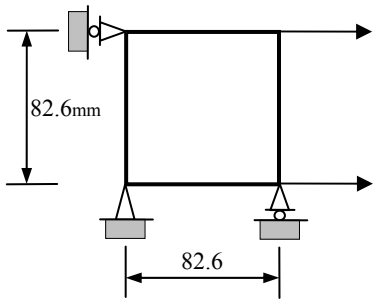

Figure 4.22: Single finite element used in the numerical examples

Simple numerical examples are provided in this section to demonstrate the capability of the proposed model (equations 4.25, 4.37, 4.46 and 4.49) in capturing the material behaviour in both tension and compression. These numerical examples are carried out based on the nonlocal damage-plasticity model described in Chapters 4 and 5, and implemented in Chapter 6. For a local numerical analysis in this section, the

nonlocal radius (see Chapter 5 for details) is simply set to zero. The examples were taken from the papers by Lee and Fenves (1998), with corresponding experimental data provided by Kupfer *et al.* (1969), Karsan and Jirsa (1969), and Gopalaratnam and Shah (1985). They will be carried out using a single quadrilateral finite element shown in figure 4.22. In some cases, one-dimensional results will also be illustrated for comparison purpose.

4.4.1 Cyclic uniaxial loading

In the first example of cyclic tension loading, the following material properties are used (Gopalaratnam and Shah, 1985): $E = 31700\text{MPa}$, $\nu = 0.18$, $f_t' = 3.48\text{MPa}$, $G_F = 0.04\text{N/mm}$. The stress-strain curve is obtained from the test by simply dividing the measured displacement in the stress-displacement curve by the gauge length ($l_g = 82.6\text{mm}$). This is obviously erroneous as there is no unique stress-strain relationship in the post-peak softening region (Gopalaratnam and Shah, 1985). However, in this section, it can be accepted (Lee and Fenves, 1998) just to transform the stress-displacement curve to a stress-strain curve for illustrating the capability of the proposed model. In a similar way, the specific fracture energy g_F is calculated by assuming that the localization bandwidth is $w_t = 45\text{mm}$, resulting in $g_F = 8.89 * 10^{-4}\,\text{N/mm}^2$. Obviously this choice of w_t is arbitrary, and different values of w_t will result in different responses of the model. However, it is left for detailed physical interpretation in the coming chapters; and this choice of w_t is used here only for the purpose of demonstrating the adopted identification procedure.

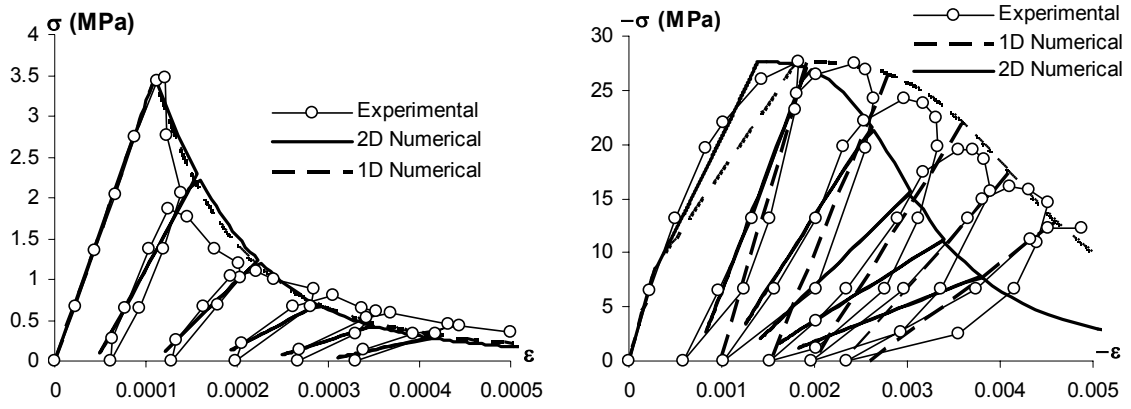

Figure 4.23: Behaviour of the proposed model in cyclic uniaxial tension (a) and cyclic uniaxial compression (b)

From the experimental stress-strain curve, we can obtain the properties of the material in unloading, which are: $\varepsilon_{tu} = 1.89 f_t'/E$ and $E_{tu} = 0.37E$. An associated flow rule, with the dilation factor $r = 1$, is assumed. The following model parameters are then obtained as solutions of the system (4.80-4.82): $E_{pt} = 1.0767 * 10^6$ Mpa, $n_t = 0.52$ and $H_t = 1.1218 * 10^3$ MPa. The stress-strain response is plotted in figure (4.23a).

The same assumption is applied to the case of cyclic compressive loading, with experimental data taken from Karsan and Jirsa (1969): $E = 31000$MPa, $\nu = 0.18$, $f_c' = 27.6$MPa. The required fracture energy $G_c = 5.69$N/mm is in fact taken from the same example in a paper by Lee and Fenves (1998). As in that paper the authors did not mention about how G_c was obtained, its value can only be used here for the sake of illustration only. In a similar way to the example on cyclic tension above, with the width of the localization zone in compression being assumed to be $w_c = 54$mm, the following specific fracture energy is derived: $g_c = 0.11$N/mm^2. We use here $f_{c0} = 0.3 f_c'$ as initial yield stress in compression, $\varepsilon_{c0} = 2.05 f_c'/E$ as the strain at peak stress, and get the value of H_c of 20743MPa from (4.97). Assuming that $E_{pc} = 90000$MPa and $n_c = 0.3$, the value of m_c is derived from equation (4.98): $m_c = 2.68$. The obtained stress-strain curve in compression is shown in figure (4.23b).

It can be clearly seen in the figures that the numerical responses using one- and two-dimension models are not identical, especially in compression. This is a predicted consequence of using the arbitrarily-chosen constant c to compute the accumulated plastic strain, using a pressure-dependent yield criterion. Use of deviatoric plastic strain increments instead of those of the total plastic strain helps to reduce this gap and also to avoid the dependency of the hardening process on the dilation factor r. However, the effect on reducing the difference is not significant for the adoption of deviatoric plastic strain in (4.21) and (4.22). In addition, for the pressure-dependent yield criterion, use of both types of plastic strain results in a nonlinear stress-strain relationship in the ascending part of the stress-strain curve (although not very apparent in figure 4.23b), as in both cases $\dot{\varepsilon}_p \neq \dot{\alpha}_p$ in uniaxial loading. Smaller values of c in (4.21) and (4.22) can yield a better fit, but so far no basis for the determination of those values has been derived in this study.

4.4.2 Unilateral behaviour

The unilateral behaviour of the proposed model is illustrated in this example, with the following material properties being used: $E = 31000\text{MPa}$, $\nu = 0.18$, $f_t' = 3.48\text{MPa}$, $f_c' = 27.6\text{MPa}$, $G_F = 0.04\text{N/mm}$, $G_c = 5.69\text{N/mm}$. For illustration purpose, all the model parameters from in the previous example are reused here, neglecting the slight difference in the elasticity modulus in tension and compression. The loading cycle is shown in figure (4.24). The stiffness recovery from tension to compression can be clearly seen in paths BCD and IJK, and the effect of compressive damage on tensile behaviour in path FGH.

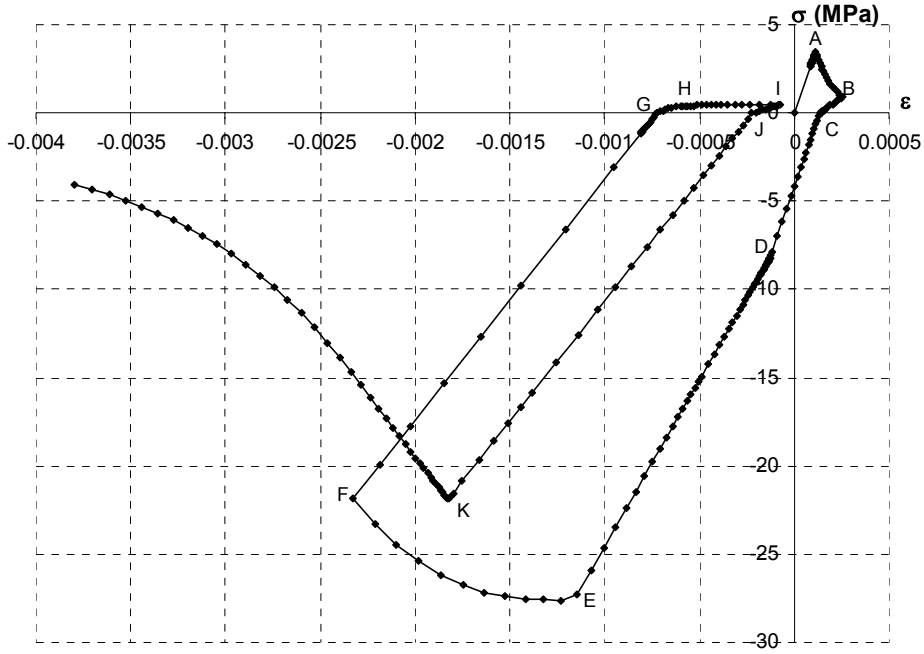

Figure 4.24: Cyclic loading under large tension and compression strains

Damage in compression results in the reduction of strength in tension, represented by lower tensile strength of the material at H, compared to the strength at B before load reversal takes place. In addition, compressive damage also makes a difference in yield and damage thresholds in tension, leading to plasticity taking place alone on path HI and the unloading slope IJ being parallel to GH. Tensile damage can possibly follow plasticity on path HI if a higher hardening parameter H_t is used. However, this is not very important here as the example only aims at demonstrating the model capability in capturing behaviour in cyclic loading under large tension and compression strains; this loading scheme rarely happens in practical situations.

4.4.3 Biaxial loading

This series of tests is to show the multiaxial behaviour of the proposed model in combined loadings. Comparison with experimental results (Kupfer *et al.*, 1969) was also made. We use here the following material properties: $E = 35000\text{MPa}$, $\nu = 0.18$, $f_c' = 2.4\text{MPa}$ and $f_c' = 32\text{MPa}$. No other needed material properties can be obtained from the test, and it is therefore adopted here that $f_{c0} = 0.3 f_c' = 9.6\text{MPa}$. In addition, with the experimental results available only in pre-peak regime, other model parameters can be assumed, to yield good fit in uniaxial compression: $H_c = 18968\text{MPa}$, $E_{pc} = 42000\text{MPa}$, $n_c = 0.2$, and $m_c = 1.0$. Again, the flow rule is assumed to be associated, with the dilation factor $r = 1$.

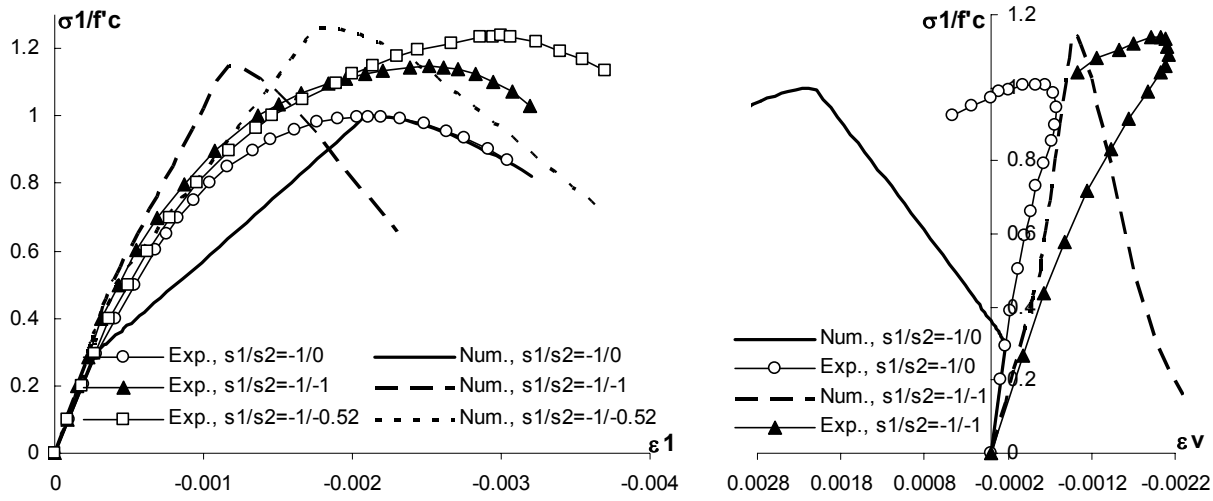

(a) Stress-strain behaviour (b) Volumetric strain

Figure 4.25: Biaxial compression-compression test

The numerical stress-strain curves shown in figures (4.25a) above, in both compression-compression and compression-tension biaxial loading, do not fit well the experimental ones (from Kupfer *et al.*, 1969). Only the peak stresses in uniaxial compression and biaxial compression-compression match their experimental counterparts well. It can be observed that the hardening law in this case is responsible for the mismatches, in which much stiffer numerical responses of the model come from the use of the adopted accumulated plastic strain in (4.22) in combination with a pressure-dependent yield criterion.

The volumetric behaviour of the material under compression can also be seen in figure (4.25b), in which the constitutive model overestimates the volumetric expansion

of the material in uniaxial compression, while that of the model prediction in biaxial compression does not exist. Clearly, this shows that a non-associated flow rule with $r < 1$ and a better hardening rule should be adopted to capture this feature of the material behaviour.

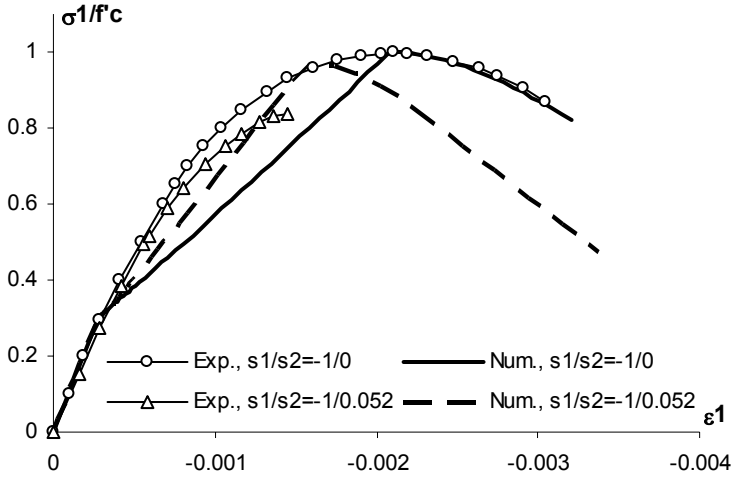

Figure 4.26: Biaxial compression-tension test

The model response in compression-tension loading (figure 4.26) shows another aspect of the proposed composite yield/failure surface in combined loading, with the overestimation of the material strength in the region far enough from the axis $\sigma_1 = 0$ (see figure 4.6) in the compression-tension quadrant (or far from $\sigma_2 = 0$ in tension-compression quadrant)

4.5 Summary and discussion

A combined damage-plasticity model (represented by equations 4.25, 4.37, 4.46 and 4.49) is presented in this chapter, aiming to apply to the numerical simulation of concrete structures under loading. However, attention at this stage is only paid to two-dimensional applications. Separate tensile and compressive responses of the material are fully captured using two separate damage criteria, along with a simple multiple hardening rule for the plasticity criterion. Calibration for the behaviour of the proposed model to real material behaviour in 2D was carried out, both in the shapes of the yield and failure envelopes, and the evolution rules of the composite damage-plasticity surfaces. A crucial part of this chapter was devoted to the identification of model parameters. Following the proposed identification procedures, all the model parameters have been shown to be identifiable and computable based on some standard tests on

concrete. Derivation of simpler pure damage models and their relations to the present coupled damage-plasticity model can also be clearly seen in the identification of parameters of the model.

Some drawbacks of the composite damage-plasticity loading surfaces can also be pointed out. In the meridian plane, the shape of the failure surface is in fact not very well in accordance with experimental observation (see Launay and Gachon, 1972). On the other hand, the deviatoric sections of both the yield and failure surfaces are independent of the Lode angle θ. Therefore, the model responses at tensile meridian $\theta = 0^\circ$, compressive meridian $\theta = 60^\circ$ and shear meridian $\theta = 30^\circ$ are identical, which is contrary to experimental observation. This independence of the model behaviour from θ can be neglected in 2D applications, but should be accounted for when moving to 3D.

Despite the enhancement by use of damage surfaces in combination with a plasticity yield surface, which helps to restrain the overestimation of plastic strain in tension, as encountered in plasticity models (Chen and Han, 1988), the hardening rule for the yield surface still requires further modification. Isotropic strain hardening cannot always appropriately reflect the anisotropic behaviour of the material. As a remedy, use of multiple hardening rules has been suggested (Ohtani and Chen, 1988) and is simply adopted in this study with the equivalent plastic strain increment $\dot{\varepsilon}_p$ being decomposed into two parts corresponding to tensile and compressive responses respectively. The resulting hardening behaviour is therefore different in every direction, depending on the value of the first invariant of the stress tensor. However, full incorporation of this multiple hardening feature into the constitutive modelling is not straightforward as it also concerns with the new model parameters, which can only be identified based on experimental observations. Moreover, on the thermodynamic aspects, convexity of the yield surface should be accounted for when it expands anisotropically under control of different evolving parameters. Separation of $\dot{\varepsilon}_p$ is only one simple way to deal with the different behaviour in tension and compression of the material.

An assumption on the maximum size of the failure envelope was made in the proposed model, with the initial damage threshold in compression being set to its maximum value corresponding to the ultimate compressive strength of the material. This helps simplify the coupling behaviour of the proposed model, but results in the

opening shape of the failure surface in triaxial compression. Nonlinear behaviour therefore cannot be encountered in hydrostatic loading. Modification to take into account this feature in hydrostatic loading has been briefly discussed in section 4.2.4.

In addition to the above shortcomings, the identification of model parameters should be studied further. The separation of energy dissipated during the failure process to parts due to damage and plasticity is only preliminarily proposed and no further details are presented in section 4.3 of this chapter. Therefore the material properties necessary for identifying parameters related to the unloading behaviour of the model have merely been assumed to exist, without any connection to the acquired standard tests. Proposal for the modification of standard concrete tests (e.g. the three-point bending test for G_F) and study on the separation of dissipated energy are necessary in future work.

The constitutive model (represented by equations 4.25, 4.37, 4.46 and 4.49) described in this chapter is only a local model and therefore cannot be used to capture properly the softening behaviour of concrete. In the next chapter, softening-related problems and the corresponding resolutions of those problems will be briefly discussed, followed by the modification of the local coupled damage-plasticity model proposed in this chapter. Enhancement of this local model using the nonlocal regularization technique will be adopted and presented.

Chapter 5: Nonlocal damage modelling

5.1 Introduction

Dealing with softening-related problems plays a crucial role in the development of constitutive models for strain softening materials in general and for concrete in particular. In the analysis of structures made of these materials, the strain localization can be triggered not only by strong local inhomogeneity such as cracks or flaws, which in some cases are large enough to have significant impact on the overall behaviour of the structures (Rice, 1976), but also by the softening behaviour of the constitutive models. However, from the aspect of constitutive laws, localization can be encountered even in case the materials feature a hardening behaviour, e.g. necking of a metallic bar in tension (geometric nonlinearity), or localization into a shear band due to nonassociate flow in frictional materials (Bazant and Cedolin, 1991).

In the constitutive modeling of concrete, localization due to softening is of great importance because strain softening and strength reduction are two of the most important features of the material behaviour. The use of damage mechanics, in combination with plasticity theory, enables us to derive appropriate models for the material. However, as the material exhibits significant post-peak softening, appropriate treatments, called regularization techniques, need to be applied to the constitutive modelling as well as the structural analysis. This is because conventional continuum mechanics is inadequate to capture correctly the softening behaviour of the material.

Mathematically speaking, quasi-static analysis of boundary value problems involving strain-softening material becomes ill-posed beyond a certain level of accumulated damage (Jirasek and Bazant, 2002). This is due to the local loss of ellipticity of the governing partial differential equations, if these are derived in the context of conventional continuum mechanics. From the numerical point of view, the strain in the damaged region tends to localize in a very narrow zone, called the fracture process zone (FPZ), which eventually leads to the formation of macro cracks. In the finite element analysis, this fracture process zone tends to narrow upon mesh refinement. As a consequence, the dissipation can asymptotically approach zero when the finite element mesh size is refined to zero, resulting in physically unreasonable

numerical solutions. The problem is similar in many numerical methods (e.g. finite element, boundary element, finite difference) employed for the solutions of the governing partial differential equations in continuum mechanics.

In fact, experimental work has proved that the strain softening zone in real tests does not vanish but concentrates in a very narrow zone, whose size is proportional to the so-called characteristic length of the material (Bazant and Oh, 1983; Bazant and Cedolin, 1991). In numerical analysis, the fact that this zone tends to vanish when refining the discretization is hence due to the inadequacy of conventional continuum mechanics to deal with such a kind of problems. Several remedies have been proposed, which range from the early work of Eringen (1972, 1981, 1983) on nonlocal elasticity and nonlocal plasticity, to recent work on nonlocal, gradient and rate-dependent models.

In this chapter, a brief introduction to regularization methods is represented in the first half in order to lay a background for the development of constitutive models based on nonlocal theory in the coming part of the chapter. This is then followed by the nonlocal thermodynamic formulation applied to the proposed damage-plasticity models in chapter 4. Connections between the parameters of nonlocal models and the material properties are also established. Simple numerical examples will be provided to show the consistency and effectiveness of the proposed approach.

5.2 A brief review on regularization methods

Obviously, the inadequacy of conventional continuum mechanics in modelling the behaviour of softening materials results in some unwanted aspects in the solutions of the boundary value problems. Details on those numerical and structural aspects can be found in several studies (Bazant and Cedolin, 1991; Peerlings, 1999; Jirasek and Bazant, 2002); and we only briefly present here the treatments for softening-related problems, which are vital in the constitutive modelling of softening materials. However, the remedies do not always necessarily lie directly in the governing partial differential equations but can be at a higher level, i.e. in the numerical discretization, such as crack band models with fixed localization bandwidth. In other words, it is desired but not necessary that the type of the governing partial differential equations be always unchanged and that the boundary value problem maintain the well-posedness during the deformation and damage processes. Physically reasonable solutions can be obtained

through various ways, with the key point being properly taking into account the necessary fracture properties of the materials in the constitutive modelling.

In the case of concrete constitutive modelling, besides the elastic properties including the Young modulus, Poisson's ratio and ultimate stresses, the material properties additionally needed are generally the characteristic lengths and fracture energies of the material in both tension and compression. Although the physical meanings and identification of those quantities, such as the existence of a material characteristic length and the use of the fracture energy as a material property, is sometimes controversial, they are generally and widely accepted in the research community. Therefore, properly taking into account the material micro-structural details characterized through the above-mentioned quantities can somehow ensure the success in the material modelling and numerical analysis of structures made of those materials. In the constitutive modelling of softening materials, the prevention of the localization of strains onto a surface through the introduction of the material characteristic lengths and fracture energies in the constitutive models is exploited. Different types of constitutive models, from simple (cohesive crack models, crack band models) to more advanced (nonlocal and gradient models, rate-dependent models), can be classified based on the way the characteristic length is introduced.

In this section, we will briefly examine some treatments applied to continuum mechanics in order to resolve the numerical difficulties in the constitutive modelling of strain softening materials. How the quantities characterizing the microstructural behaviour of the materials are taken into account in the theoretical and numerical analyses will also be presented. Here, by "treatment", we refer to a wide range of techniques applied to numerical analyses of structures made of strain softening materials. Those techniques help remove the mesh-dependency of the numerical solutions. Hence they enable the proper capturing of the softening behaviour of the materials and produce physically reasonable solutions, regardless of whether the well-posedness of the boundary value problem is strictly maintained.

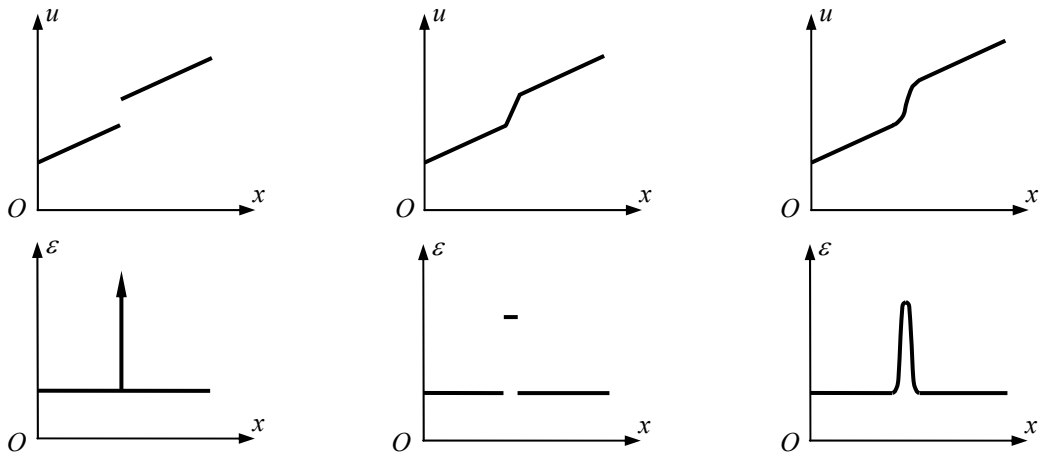

Strong discontinuity (a) Weak discontinuity (b) Continuity (c)

Figure 5.1: Displacement and strain fields in regularization methods

(after Jirasek and Patzak, 2001)

The classification of regularization methods by Jirasek and Patzak (2001) is adopted here. Based on the kinematic descriptions, which describe the one-dimensional displacement field across the boundary of the fracture process zone as strong discontinuity, weak discontinuity or continuity, three corresponding types of localization modelling can be classified. They are cohesive crack models, softening continuum models with partial regularization and fully regularized continuum models, the displacement and strain fields of which are depicted in one-dimensional case in figure 5.1. The above is only one typical classification for theoretical approaches to the solution of softening-related problems. Existing approaches, however, can also be classified in other ways, based on the constitutive models or numerical approximation techniques (Jirasek, 2001).

5.2.1 Cohesive crack models

In the first class of regularization methods, as can be seen in the figure (5.1a), the displacement field exhibits a jump across the surface of discontinuity, which is depicted as a single point in the one-dimensional case. In fact, the cohesive crack model, or fictitious crack model, here is a fracture model. It was first developed and applied to concrete modelling by Hillerborg *et al.* (1976) from a simpler model by Barenblatt (1962). To illustrate the idea, let us take an example of a structure with a stress free crack, shown in figure (5.2) below.

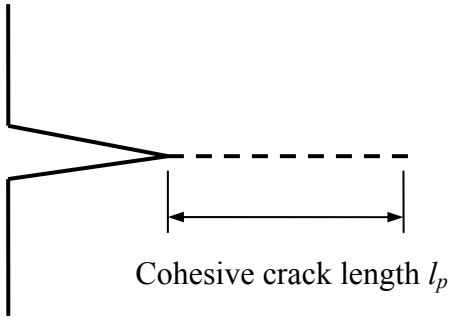

Figure 5.2: Cohesive crack zone

It is expected that the initiation and coalescence of new micro-cracks takes place in a small zone in front of the crack tip, determined by the cohesive crack length l_p. The relative size l_p of this FPZ with respect to that of the structure can be reflected through the appropriate numerical modelling of this zone. Linear elastic fracture mechanics can still be applied if this fracture process zone is sufficiently small compared to the dimensions of the structure. In such cases, the zone lumps into a single crack tip point, resulting in models without a material length. In contrast, a material length, defined by $l_{ch} = EG_F \big/ f_t'^2$, appears in the cohesive crack models and is proportional to the length l_p of the zero-thickness fracture process zone (Bazant and Pijaudier-Cabot, 1989). In several research papers (Petersson, 1981; Rocco *et al.*, 2001; Guinea *et al.*, 2002), the term "characteristic length" used for l_{ch} can be confused with that used in nonlocal or gradient models in the following section. In fact, they are entirely different in concept with l_{ch} defining the length of the fracture process zone and the characteristic length in nonlocal models being related to the minimum possible width of the softening zone in continuum models (Bazant and Pijaudier-Cabot, 1989).

In cohesive crack models, the softening behaviour is characterized through the stress-separation law of the cohesive crack line, in which the stress gradually decreases with increasing separation, and finally vanishes upon the crack opening exceeding a certain limit, resulting in a stress free crack. The dissipation energy in this case is guaranteed not to vanish and is always equal to the area under the stress-separation law, regardless of the mesh refinement, thus making the solutions physically acceptable. Obviously, a macro crack is formed, when the energy driving the development of this crack reaches the fracture energy G_F of the material:

$$G_F = \int_0^{u_t} \sigma \, du \tag{5.1}$$

in which σ and u are respectively the stress and displacement jump across the cohesive crack line; and u_t in this case is the critical crack opening at which the normal stress is zero (see figure 4.11 in the previous chapter). The above definition was the basis for the method of measuring the fracture energy G_F, recommended by RILEM (1985). However, to avoid any possible confusion about the model classification here, more details on the determination of G_F as well as its connections with regularization methods will be presented later in section 5.2.4.

Interface finite elements can be appropriate to model the cohesive crack line, with lines or surfaces of interface elements being inserted between continuum elements (Bocca *et al.*, 1991; Hordijk, 1992; Tijssens *et al.*, 2000; Galvez *et al.*, 2002; Yang and Chen, 2004). However, the requirement for the coincidence between the cohesive crack line and the element boundaries results in some problems and restrictions on the numerical discretization. On the other hand, the finite element mesh needs to be extremely fine in the region near crack tips in order to capture properly the crack propagation. Nevertheless, in some cases (e.g. mixed mode cracking with curved crack path) the orientation of the cracks is difficult to capture appropriately, even using a very fine mesh. Besides, as the crack trajectory is not known in advance, the same mesh density should be applied over the whole structure. Consequently, this makes the numerical analysis computationally costly. As a remedy, frequent remeshing during the nonlinear analysis can be used in the process zone in front of the crack tip of a coarse mesh (Bocca *et al.*, 1991; Yang and Chen, 2004). Alternatively, another promising approach is the use of finite elements with embedded discontinuities. These are special elements, in which the standard displacement interpolation functions are enriched so as to capture the jumps in the displacement field. This hence removes the need of continuous remeshing, which is encountered in the standard cohesive crack models. Reviews and details on this method are, however, beyond the scope of this study and can be found in several papers (Jirasek, 2000; Jirasek and Patzak, 2001; de Borst, 2001; de Borst, 2002; Alfaiate *et al.*, 2002; Alfaiate *et al.*, 2003).

5.2.2 Partially regularized continuum models

In softening continuum models with partial regularization, the displacement field is continuous, whereas the strain field is discontinuous across the boundary of the fracture process zone (figure 5.1). Unlike in models of the first class, this zone is no

longer lumped into a curve in two-dimensional cases (or a surface in three-dimensions) but smeared over a band with finite thickness. The condition on the smearing out process is that the energy dissipation produced by the two models of the first and second classes must have the same value. This can be maintained by either fixing the width of the localization band (Bazant, 1976) or adjusting the softening modulus of the material models used for finite elements in the FPZ, so that equal energy dissipation can be produced (Bazant, 1982; Bazant and Oh, 1983; Bazant and Cedolin 1991).

The softening region in this case extends over the smallest numerically resolved band, which is exactly over only one element in the one-dimensional case (for use of constant strain elements). However, fixing the thickness of the localization band to a prescribed value in the two-dimensional case is much more complicated and difficult. Indeed, the width of the numerically resolved band depends not only on the size, shape of the finite elements but also on the orientation of the band with respect to the mesh lines. In the simplest case, with structured finite element meshes aligned with the crack path (e.g. use of four-node quadrilateral elements above the notch in the three-point bending test), the strain localizes in a single layer of elements with the width w_t of the FPZ coinciding with or proportional to the element width. However, this is not always the case and in general the numerical discretization is subjected to some restrictions on the element size and mesh density, because the crack trajectory cannot be known in advance. In order to remedy this, finite elements with an embedded softening band have been proposed and employed (Larsson and Runesson, 1996; Jirasek, 2000). A more complete review on finite elements with embedded displacement and strain discontinuities can be found in some papers by Jirasek (2000), and de Borst (2001, 2002)

In this second kind of models of this class, the energy dissipation always takes a certain finite value through adjusting the softening modulus upon mesh refinement. In the literature, this is referred to as models with mesh-adjusted softening modulus (Simo, 1989). In addition, as it is aimed at properly reproducing the energy dissipation in the localization band, the approach is also called the fracture energy approach (Comi and Perego, 2001). Interestingly, this approach has a close relation with the cohesive crack models presented in the preceding section. In fact, the fracture energy approach has come from the idea of the cohesive crack model and was designated as the crack band

models by Bazant (Bazant, 1982; Bazant and Oh, 1983). The fracture energy G_F, which is equal to the area under the stress-separation curve in cohesive crack models, is now smeared out over the width of the localization band. We then have

$$G_F = \int_0^{u_t} \sigma\,\varepsilon(x)dx \tag{5.2}$$

where x is the coordinate in the direction normal to the localization band. In a similar way to this, the displacement discontinuity is also smeared out over this width and transformed into inelastic strain. In addition, it is usually assumed in numerical analyses that the strains are constant over the band width w_t (Bazant and Oh, 1983; de Borst, 2002), thus making the following expression hold

$$G_F = w_t g_F \tag{5.3}$$

in which the energy dissipated per unit area of totally damaged material (or local fracture energy) g_F is defined as

$$g_F = \int_0^{\varepsilon_{tc}} \sigma\, d\varepsilon \tag{5.4}$$

where $\varepsilon_{tc} = u_t / w_t$ is the critical strain normal to the crack direction (see figure 4.11 in chapter 4)

As the numerical resolved softening band always localizes in one layer of elements, from (5.3) and (5.4) it can readily be seen that if one adjusts the stress-strain curve so that the area under the curve is always equal to G_F / w_t with w_t in this case identical or proportional to the element size, the dissipated energy is then independent of the discretization and physically meaningful solutions can be obtained. This idea has been exploited by several researchers (Bazant and Oh, 1983; Meschke *et al.*, 1998; Comi and Perego, 2001; Feenstra and de Borst, 1996) in the context of both damage and softening plasticity. The partial regularization here is revealed through the asymptotic vanishing of the fracture process zone upon mesh refinement although the global response of the structure can be captured correctly and the dissipation energy converges to a finite value. It is also worth noting that the cohesive crack model can be interpreted as a simple version of the crack band model as the finite element mesh is refined (Bazant and Jirasek, 2002). Details and some relating aspects on the application of the

method can also be found in Comi and Perego (2001); de Borst (2001, 2002); Jirasek and Patzak (2001); Jirasek and Bazant (2002).

5.2.3 Fully regularized continuum models

The aim of the regularization techniques is to produce meaningful solutions, which are mesh-independent, with a physically reasonable amount of dissipated energy upon mesh refinement. For the first two classes of models, this is quite satisfactory from an engineering point of view. However, the fundamental difficulty encountered in the use of constitutive models for strain-softening materials cannot be completely resolved since the ill-posedness of the boundary value problem still exists, as a consequence of the local loss of ellipticity of the governing partial equations in the analysis using rate independent softening models. On the other hand, the beauty and simplicity of the ideas (5.2.1 and 5.2.2) introduced to the modelling of softening and localization are lost due to some limitations and constraints on the numerical discretization schemes as mentioned above.

Stronger regularization methods have been introduced based on the enrichment of conventional continuum mechanics using temporal or spatial terms. Models belonging to this third class are typically nonlocal, gradient, and rate-dependent models. Continuum damage mechanics, with nonlocal (Pijaudier-Cabot and Bazant, 1987; Bazant and Pijaudier-Cabot, 1988) or gradient enhancements (de Borst and Muhlhaus, 1992; Peerlings *et al.*, 1996) or rate-dependent regularization (Simo and Ju, 1987; Dube *et al.*, 1996), falls into the third type of this classification (see figure 5.1). Besides the main difference compared to other approaches, lying in the continuity of the displacement and strain fields (figure 5.1), the boundary value problem in this case always maintains its well-posedness because the governing partial differential equations do not locally change type during the deformation process (Bazant and Cedolin, 1991; Peerlings, 1999; Dube *et al.*, 1996). Mathematically, this is thanks to the introduction of temporal (rate-dependent models) or spatial terms (nonlocal and gradient models) to the governing partial differential equations.

From a physical point of view, a proper modelling of concrete fracture also requires the inclusion of rate effects (Sluys, 1992). This important feature seems to be natural under transient dynamics with high strain rates. In addition, high strain rates also

accompany final failure under quasi-static conditions (Sluys, 1992), showing the necessity of taking into account the rate-dependent properties of the materials. Moreover, a rate-dependent formulation can be interpreted as a numerical regularization technique employed in order to limit localization in quasi-static problems. However, as the rate of loading decreases, the regularizing effect also fades away (Jirasek and Bazant, 2002). For nonlocal and gradient models, from the physical point of view, the interpretation of the constitutive models can be based on the micromechanical analysis of microcrack interaction (Bazant, 1991; Bazant, 1994). In constitutive modelling the microcrack interactions are realized through the dependence of the constitutive behaviour of a material point not only on the state of the material at that point, but also on the state of the whole material body, or at least on a finite neighbourhood of that point.

In the rate-dependent case, the wave equation can be proved to be unconditionally hyperbolic (Sluys, 1992; Dube *et al.*, 1996), resulting in stable and well-posed wave problem. In addition, based on the work of Valanis (1985) the uniqueness of solutions in the rate-dependent case can also be obtained, as has been shown by Ju (1989), and Simo and Ju (1987). In the gradient and nonlocal models, spatial terms introduced to the partial differential equations can also regularize the boundary value problem. The proofs for the well-posedness of the boundary value problem have been given by several researchers, for a variety of nonlocal and gradient models (Peerlings, 1999; Comi, 2001; Borino *et al.*, 2003). In fact, a gradient formulation can be derived from nonlocal formulation (Bazant and Cedolin, 1991; Peerlings, 1999) and consists of two kinds of models: implicit and explicit gradient models, which are also respectively categorized as weakly and strongly nonlocal models. The term “weakly” here refers to the fact that the constitutive response of each material point depends only on an infinitesimal neighbourhood of that point (Jirasek and Bazant, 2002), which comes from the calculation of the gradients from the distribution of the function in an arbitrarily small neighbourhood. However, this is not the case in strongly nonlocal models, which consist of integral type and implicit gradient models, and in which the constitutive response of a material point is dependent on the whole material body or at least a finite neighbourhood within a certain interaction radius. The interaction radius here is in fact proportional to the characteristic length of the material (Bazant and Pijaudier-Cabot, 1989; Bazant and Cedolin, 1991) and controls the size of the softening zone.

Taking into account the nonlocality of the material behaviour through the introduction of the characteristic length of the material, we have regularized the conventional continuum models and prevented the energy dissipation from vanishing upon mesh refinement. However, this kind of "continuum regularization" also has a restriction on the finite element mesh. The width of the localization zone is in general small compared to the dimension of the structure. Moreover, in order to capture properly the structural behaviour and the fracture process zone, the size of finite elements in that zone must be considerably smaller than the width of the localization zone. This hence requires fine mesh density inside the fracture process zone, thus significantly increasing the computational cost.

5.2.4 Regularization methods and the fracture properties of the material

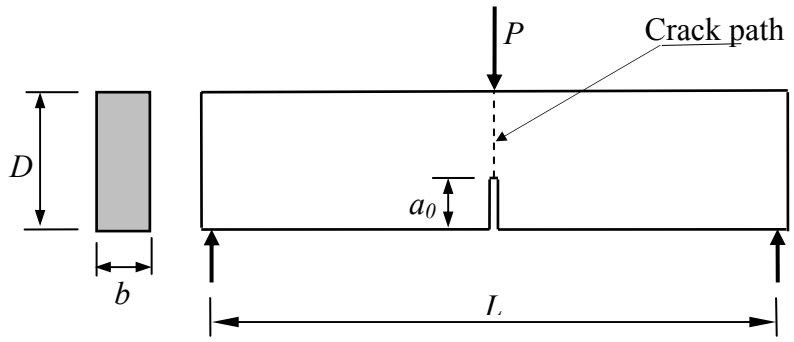

Figure 5.3: Three-point bending test

As has been briefly discussed in the previous chapters and preceding sections, the softening behaviour of concrete makes it impossible to properly determine the uniaxial stress-strain behaviour of the material from experiments. Therefore, the fracture energy, defined by the energy dissipated during the crack formation and propagation, must be used as a material property characterizing the material behaviour. The three-point bending test is usually recommended and adopted (RILEM, 1985) for this purpose, in conjunction with the cohesive crack model. Following the test, the apparent fracture energy G_{Fa} (Bazant, 1996) can be measured through the area under the load-deflection curves.

$$G_{Fa} = \frac{\int_0^\infty P(\delta)d\delta}{b(D-a_0)} \tag{5.5}$$

where b and D are respectively the beam thickness and depth, a_0 is the length of initial traction-free crack at mid-span; $b(D-a_0)$ is the total cracked area; P and δ are respectively the load and deflection at the load point; and the integral in the numerator is the energy required to completely break the specimen. The definition of the fracture energy in cohesive crack models (Hillerborg *et al.*, 1976) is rewritten here as

$$G_F = \int_0^{u_t} \sigma \, du \tag{5.6}$$

in which σ and u are respectively the stress and displacement jump across the cohesive crack line; and u_t in this case is the critical crack opening, at which the normal stress is zero. If the fracture energy G_{Fa} is totally dissipated by the cohesive crack, we have the equality between (5.6) and (5.7):

$$G_F = G_{Fa} \tag{5.7}$$

As can be seen, the above definition of G_F is most relevant to the cohesive crack model, with all dissipated energy lumped onto a fracture surface of zero thickness. To avoid confusion, from now on we use G_F to refer to the fracture energy of the material, regardless of the fact that G_F should be thought of being in association with the cohesive crack model. Using the equality (5.7), the stress-separation relationship $\sigma - u$ in cohesive crack models can be determined from the experimental $P-\delta$ curve. However, the above definition of the material fracture energy obviously contains errors due to the simplification in the assumption $G_F = G_{Fa}$ and the averaging of G_{Fa} over the crack length (Bazant, 1996; Hu and Duan, 2004).

The first source of error is that a considerable part (up to 50~80% of G_F; after Bazant, 2002) of the work done by the external load is in fact dissipated through a plastic-frictional mechanism (Bazant, 1996). In the experiment, it is due to pulling out of aggregates and fragments in the fracture process zone and is realized through the residual strains at zero stress state upon unloading.

The second source of error comes from the averaging of G_F over the length of the crack path, assuming that its distribution over the entire crack length is uniform. This assumption is in fact only relevant at the beginning of the fracture process, with the crack front far enough from the upper boundary of the specimen, due to the boundary effect (Hu and Wittman, 2000; Karihaloo *et al.*, 2003; Hu and Duan, 2004). Figure (5.4)

schematically shows the difference between the averaged fracture energy G_F (RILEM, 1985) and that being experimentally observed.

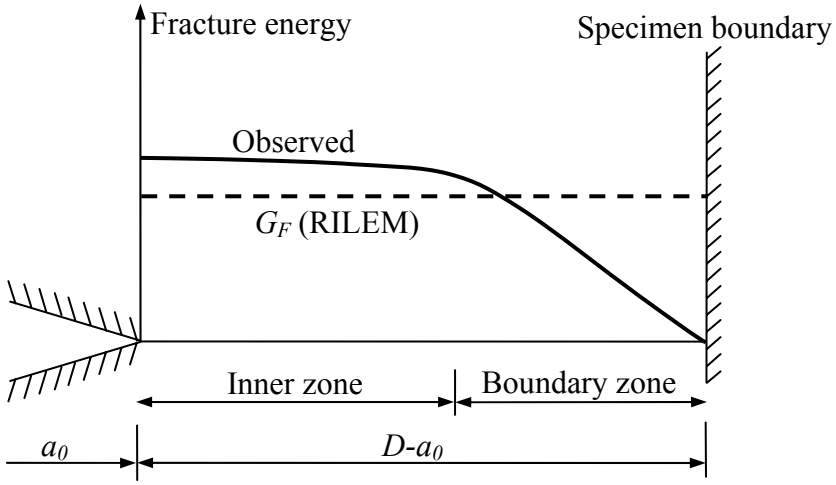

Figure 5.4: Boundary effect on the distribution of the fracture energy G_F

(after Karihaloo *et al.*, 2003; Hu and Duan, 2004)

A unique stress-separation relationship in cohesive crack model does not exist due to the specimen-dependent property of the defined fracture energy (Bazant, 1996). In addition, the actual fracture process zone, where the dissipation process takes place, in fact has a finite width, which gradually changes when the crack front moves towards the specimen boundary. This width reaches its maximum value when the crack tip is in the middle of the specimen and gradually reduces to nearly zero when the crack tip is close to the specimen boundary (Hu and Duan, 2004). However, in cohesive crack models, as it does not enter the calculation, this width is simply assumed to be zero. Neglect of changes in the width of the fracture process zone during the crack propagation therefore results in the error in the averaged fracture energy G_F (Bazant, 1996; Hu and Duan, 2004).

The above is merely a brief presentation of the definition of the fracture energy G_F used in the constitutive modelling of concrete. In conjunction with the regularization methods briefly presented in the preceding sections, it serves as a basis for the development of constitutive models for quasi-brittle materials. A closer look at the mentioned issues in the definition and measurement of G_F is, however, beyond the scope of this study, but can be found in several papers (Bazant, 1996; Bazant, 2002; Bazant and Becq-Giraudon, 2002; Karihaloo *et al.*, 2003; Hu and Duan, 2004).

A similar concept of characteristic length and fracture energy in compression will also be applied to the constitutive modelling in this study. The experimental test for the compressive fracture energy G_c was of course performed on totally different specimens (e.g. cylinder specimens under uniaxial compression in Jansen and Shah, 1997). However, lack of experimental research on this still prevents the wide use of G_c in practice. For that reason, we will have to tentatively apply the same concept of fracture energy in both tension and compression to the nonlocal regularization in this study. Further research on the compressive fracture energy and its corresponding characteristic length is hence worth pursuing.

5.3 Nonlocal damage modelling

Continuum mechanics and thermodynamics form the basis for the development of models for the analysis of deformation and fracture of structures. In these standard continuum theories, which can be regarded as local continuum theories, the physical state at a given point in the body is assumed to be completely determined by the material state at that mathematical point, where the quantities of these continuum theories are defined. In other words, it is assumed that there is no interaction between the material points of the structure. However from the physical point of view these continuum quantities should be thought of being averaged over a certain volume called a "representative volume element" whose size depends on every material and is proportional to the characteristic length of the material (Bazant and Oh, 1983). This volume must be of size large enough compared to the sizes of the material constituents (e.g. maximum aggregate size in concrete) so that continuum theories are still applicable and the material can be treated as being homogeneous. Details of the orders of magnitude of representative volume elements can be found in the book by Lemaitre and Chaboche (1990). The application of these continuum theories, which are based on the assumption of homogeneous materials, to heterogeneous media is only meaningful at the level of the size of the representative volume element. In this case, the stresses, strains and other internal variables are interpreted as the mean values averaged over this volume element.

The fact that all materials are generally heterogeneous requires some special treatments or assumptions in order to make use of the non-standard nonlocal continuum theories. Moreover from the micromechanical point of view, the interactions of a point

with other material points should be accounted for. This means that the state at a given point depends on the material state of the whole body. This is the basic assumption of nonlocal theories. In fact such concept of nonlocality has been developed for elasticity and then plasticity theory by Eringen (1972, 1981, 1983). This helps to explain some critical phenomena (e.g. the non-existence of a stress singularity at crack tip), which cannot be explained and predicted by local theories. The predictions by nonlocal theories in such cases are in accordance with the results from experiments (Eringen, 1983). However in practice, models based on standard continuum theories have been very successful in describing the macroscopic stress and strain fields in many engineering problems. In those models, the influence of the material substructures such as pre-existing microcracks, molecules, grains, or pores is totally neglected. This neglect can be appropriate in some cases, e.g. in elasticity or hardening plasticity materials with associative flow rules, where softening and localization do not occur. In the case of softening-induced localization, this leads to stability problems and to the discretization-dependency in the numerical analysis, which are (for rate-independent material model) the results of the loss of ellipticity of the governing differential equations. In order to remedy these deficiencies, the details of the heterogeneity of the materials should be taken into account. However, direct consideration of those details will inevitably lead to considerable amount of computational cost. This is the case of microscopic approaches. Besides, one of the great difficulties of microscopic approaches is that the microscopic variables are very difficult to measure and moreover difficult to use in practical computations (Lemaitre and Chaboche, 1990).

In the so-called nonlocal macroscopic approach, the state variables are defined as the mean over the representative volume element, and treated as nonlocal quantities. In other words, the effects of the whole body on a material point are taken into account. In a similar way to this, the enrichment of the constitutive relations with higher order deformation gradients results in the so-called gradient dependent models (Peerlings *et al.*, 1996; Peerlings, 1999). In fact gradient dependent models are strongly related to the nonlocal models since the gradients of the variable can be calculated from the distribution of the variable in a neighbourhood of the point under consideration (Bazant and Cedolin, 1991; Jirasek and Bazant, 2002). These models are also considered as special cases of the nonlocal formulation by a Taylor series expansion of the nonlocal spatial integral (Bazant and Cedolin, 1991; Peerling, 1999). However, as argued by

Bazant (1994), the physical explanation of gradient models from micromechanics is still lacking or unconvincing.

In earlier work (Eringen, 1981; Eringen, 1983; Bazant, 1984; Bazant *et al.*, 1984) on nonlocal approaches, the nonlocal treatments are generally applied to all variables, including stress and total strain. This results in the appearance of the spatial integrals in the equilibrium equations and the boundary conditions. Therefore, the governing partial differential equations along with the boundary conditions and constitutive equations all must be rewritten in nonlocal forms. As a consequence, both the formulation and the numerical implementation become difficult and cumbersome (Bazant, 1991). To overcome this shortcoming, it has been found that it is necessary to apply nonlocal treatment only to variables controlling the softening process (Pijaudier-Cabot and Bazant, 1987). In concrete, a quasi-brittle material, the softening behaviour is the result of damage in the material and hence requires appropriate nonlocal treatment for the damage variable, damage energy or strain, which directly or indirectly governs the softening behaviour of the constitutive models.

A simple modification of the thermodynamic formulation for coupled damage-plasticity will be carried out in the following section, backed by some preliminary micromechanical analyses of concrete material by Bazant (1991, 1994). The nonlocal nature of damage in this case is mostly due to the interactions of microcracks within a certain volume element, whose size is proportional to the characteristic length of the material (Bazant, 1991, 1994). As a result of this nonlocal nature, the spatial integral of some variables controlling the strain softening must appear in the constitutive equations. However, in this study, we do not go further into details of the micromechanical analysis of crack interactions, which can be found in some relevant research papers (Bazant, 1991; Bazant and Tabbara, 1992; Bazant, 1994). Instead, the concept of nonlocality will be used for the thermodynamic approach, which places much emphasis on the energy exchange in the material due to the nonlocality of damage. This just gives a physical background for the nonlocal approach, instead of thinking of it as a pure mathematical way to regularize the ill-posed boundary problem due to softening. The force of the argument is unfortunately still, however, far from being widely accepted.

5.3.1 Nonlocal thermodynamic approach

In the case of damage-induced softening, the damage variables or the associated damage energies should be treated as nonlocal quantities (Bazant, 1991). Of course, generally one can choose other variables, which are indirectly related to the strain softening behaviour of the materials (e.g. the elastic strain, which is in fact related to the damage energy) for nonlocal treatment. However, these treatments can lead to models producing high residual stresses even at very late stages of the deformation process (Jirasek, 1998). These models are hence not capable of modelling the macroscopic cracks, which are widely open in a complete separation mode. Therefore the choice of nonlocal internal variables and the corresponding nonlocal models should be carefully considered and examined in order to avoid these pathologies. Among nonlocal damage approaches, that are based on the nonlocality of the damage energy has been proved to be appropriate and can give reasonably low residual stress when the damage measure is close to unity (Jirasek, 1998). We adopt this kind of damage energy nonlocality in this study.

Since our attempt in this study is to formulate models based on thermodynamics, the problem here is the possibility of adapting the adopted thermodynamic framework to a nonlocal approach. The energy potential can be modified by introducing the damage gradient as a new internal variable (Maugin, 1990; Santaoja, 2000; Nedjar, 2001) in order to account for the energy exchange due to nonlocality. An alternative to introduce nonlocality is to express the first law of thermodynamics in a more general form in order to account for the energy redistribution in a certain volume element, where damage occurs, due to the microcrack interactions. The size of this volume element, where the energy redistribution takes place, is proportional to the material characteristic length. Originally proposed by Edelen and Law (1971) with the concept of the nonlocality residual, this is the approach adopted by several Italian researchers (Polizzotto *et al.*, 1998; Polizzotto and Borino, 1998; Borino *et al.*, 1999; Benvenuti *et al.*, 2002).

This approach is based on the assumption that there is energy exchange between points within a certain volume element, whose size is proportional to the material internal length scale. In this case, the nonlocality of damage, which can be explained through micromechanics analysis of microcrack interactions in a volume element

(Bazant, 1994), is accounted for based on the thermodynamic analysis of that volume. The interactions of microcracks are represented through the energy exchange at points inside that volume element. Following the approach, the first law of thermodynamics, which is usually derived in its local form, is now stated in the nonlocal form over that volume of the material.

$$\int_{V_p} \dot{W} dV + \int_{V_p} \dot{Q} dV = \int_{V_p} \dot{u} dV \tag{5.8}$$

where V_p is any region where the dissipation processes takes place. However, the size of this region cannot be infinitesimal but is restricted by the material characteristic length (Polizzottto *et al.*, 1998). As V_p is of finite size and cannot be arbitrarily small, the local form of energy balance can only be withdrawn from (5.8) by using a nonlocality residual P accounting for the energy exchange in the region V_p.

$$\dot{W} + \dot{Q} + P = \dot{u} \tag{5.9}$$

In this case, the insulation condition (Polizzottto and Borino, 1998)

$$\int_{V_p} P dV = 0 \tag{5.10}$$

must be satisfied, restricting the energy exchange only within the volume V_p. It should also be noted here that P is non zero at points inside the volume V_p and equal to zero everywhere outside V_p, where there are no irreversible processes. The insulation condition therefore also holds in the whole material body.

The assumption on the nonlocality of energy exchange seems reasonable as damage in this case produces effects not only where it occurs but also at neighbouring points within the defined volume element. As a result of this, the energy redistribution of points inside that volume results in the global satisfaction of the first law of thermodynamics in this volume element (Polizzotto *et al.*, 1998). The second law of thermodynamics in this case is still cast in its local form (3.2), but the dissipation (we consider here isothermal processes only) turns out to be nonlocal due to the appearance of the nonlocality residual P.

$$d = \sigma_{ij} \dot{\varepsilon}_{ij} - \dot{f} + P \geq 0 \tag{5.11}$$

In this case, the Clausius-Duhem inequality does not hold pointwise, as it does in the local approach (see 3.9, chapter 3). Instead, due to the insulation condition (5.10), the Clausius-Duhem inequality now takes the following nonlocal form

$$\int_{V_p} \left(\sigma_{ij}\dot{\varepsilon}_{ij} - \dot{f}\right) dV \geq 0 \tag{5.12}$$

This means local violation of the inequality is allowed to occur during the irreversible processes. Nevertheless, the local dissipation (5.11) is always non-zero though in this case of nonlocality it does not coincide with the local form (3.9) of the Clausius-Duhem inequality.

In a similar way, one can also introduce nonlocality into the existing thermodynamic approach by casting the second law in a nonlocal form, while retaining the local form (3.1) of the first law of thermodynamics. The nonlocal second law now reads

$$\int_{V_p} \left(\theta \dot{s} + q_{k,k} - \frac{q_k \theta_{,k}}{\theta} \right) dV \geq 0 \tag{5.13}$$

Using the nonlocality residual P, we can transform the above law to a local form.

$$\theta \dot{s} + q_{k,k} - \frac{q_k \theta_{,k}}{\theta} + P \geq 0 \tag{5.14}$$

Neglecting the thermal term (see chapter 3), the mechanical dissipation now becomes

$$d = \theta \dot{s} + q_{k,k} + P \geq 0 \tag{5.15}$$

which, after being substituted into the expression of the local first law of thermodynamics, turns out to be exactly same as (5.11) in the previous case (for isothermal processes). As a result, the Clausius-Duhem inequality in this case is also satisfied in a global sense (see 5.12).

As can be seen from (5.13), the global satisfaction of the second law of thermodynamics can lead to processes in which (5.13) are satisfied as an equality at global level. These processes are therefore interpreted as reversible at global level. Since the inequality (5.13) does not guarantee the pointwise satisfaction of (5.13), Polizzotto (2003) argued that these processes could be physically meaningless. However, in both cases of nonlocality (nonlocality introduced to the first and the second laws of thermodynamics), that mentioned problem also occurs with the Clausius-Duhem

inequality (5.12), which is generally used as a condition for any thermodynamically admissible processes. The physical interpretation here could be the exchange of energies, which must have been dissipated by heat, at points in the defined representative volume element. In other words, in the irreversible processes, energy at point-wise level within each volume element can be either dissipated by heat or transferred to neighbouring points within that volume element. The latter case here represents the local violation of the second law of thermodynamics (or violation of the local Clausius-Duhem inequality), which can be directly predicted as a consequence of the global satisfaction of the second law. Therefore, in the author's view, the introductions of nonlocality to the first and the second law of thermodynamics have equal physical meaning and can be treated as equivalent.

The above-presented approaches have introduced a way of incorporating nonlocality into an existing thermodynamic framework, based on the concept of nonlocality residual. The idea can be adapted to any existing thermodynamic approach without any difficulty. However, the main difficulty and drawback of that kind of approach lies in the choice of an appropriate expression for the nonlicality residual P, which helps to bring the dissipation function (3.20) to its usual form but with the dissipative generalized stresses being replaced with their nonlocal counterparts. Various choices have been adopted (Polizzotto and Borino, 1998; Polizzotto *et al.*, 1998) based on the introduction of the regularization operator R and its adjoint R^* defined on the internal variables to be made nonlocal.

For concrete damage, there should be two different internal variables to be treated as nonlocal quantities, which are the tensile and compressive damage measures α_d^t and α_d^c respectively. In addition to the tensile characteristic length, the same concept of compressive fracture energy and material characteristic length should also be applied to the modelling of the material compressive behaviour (Feenstra and de Borst, 1996; Jansen and Shah, 1997). However, the characteristic length related to the compressive fracture energy is in general different from its tensile counterpart (Comi, 2001), due to different failure mechanisms in tension and compression. For that reason, the volume V_p must be defined so as to take into account two possible dissipation processes due to damage in tension and compression respectively. The elegance and physical significance of the theory is lost. More physical interpretation for the material nonlocal

responses in both tensile and compressive softening should therefore be provided. This, however, is left to future study.

A simple nonlocal thermodynamic approach is proposed in this section based on the framework (by Houlsby and Puzrin, 2000) presented in chapter 3. Using the advantages and consistency of the adopted framework in linking the specified energy functions with the derived constitutive models, nonlocality can be incorporated in the approach by simply introducing nonlocal terms into the expression of the dissipation functions. For the coupled damage-plasticity models presented in chapter 4, the incorporation of nonlocal regularization into the proposed approach and the derived constitutive model, the local version of which is represented by equations (4.25), (4.37), (4.46) and (4.49), is rather straightforward. The procedures in section 4.3 of the previous chapter can be repeated here, with some minor modifications to introduce nonlocality to the dissipation function, through two component functions $F_1^{t^*}$ and $F_1^{c^*}$.

In this case, nonlocality occurs in both the tensile and compressive damage criteria. The dissipation function (4.20) now takes the following nonlocal form:

$$d = F_1^{t^*}\left(\sigma_{ij},\alpha_d^t,\alpha_d^c\right)\dot{\alpha}_d^t + F_1^{c^*}\left(\sigma_{ij},\alpha_d^c\right)\dot{\alpha}_d^c + \left[\frac{k}{\beta}-(1-r)\sigma_{kk}\right]\frac{\dot{\alpha}_{kk}}{3r} + \frac{3\beta r\dot{\alpha}'_{ij}\dot{\alpha}'_{ij}}{2\dot{\alpha}_{kk}} \qquad (5.16)$$

Referring to Chapter 4 on the local approach, we see that functions $F_1^{t^*}\left(\sigma_{ij},\alpha_d^t,\alpha_d^c\right)$ and $F_1^{c^*}\left(\sigma_{ij},\alpha_d^c\right)$ have been defined in local forms as

$$F_1^{t^*}\left(\sigma_{ij},\alpha_d^t,\alpha_d^c\right) = \frac{\dfrac{(1+\nu)\sigma_{ij}\sigma_{ij}-\nu\sigma_{kk}\sigma_{ll}}{2E\left[1-H\left(\sigma_{kk}^+\right)\alpha_d^t\right]^2\left(1-\alpha_d^c\right)}}{\dfrac{(1+p_t)\sigma_{ij}^+\sigma_{ij}^+ - p_t\left(\sigma_{kk}\right)^+\left(\sigma_{ll}\right)^+}{2E\left(1-\alpha_d^t\right)^2}} F_1^t\left(\alpha_d^t,\alpha_d^c\right) \qquad (5.17a)$$

and

$$F_1^{c^*}\left(\sigma_{ij},\alpha_d^c\right) = \frac{\dfrac{(1+\nu)\sigma_{ij}\sigma_{ij}-\nu\sigma_{kk}\sigma_{ll}}{2E\left[1-H\left(\sigma_{kk}^+\right)\alpha_d^t\right]\left(1-\alpha_d^c\right)^2}}{\dfrac{(1+p_c)\sigma_{ij}^-\sigma_{ij}^- - p_c\left(\sigma_{kk}\right)^-\left(\sigma_{ll}\right)^-}{2E\left(1-\alpha_d^c\right)^2}} F_1^c\left(\alpha_d^c\right) \qquad (5.18a)$$

For a nonlocal approach here, $F_1^{t\,*}$ and $F_1^{c\,*}$ are now of nonlocal forms

$$F_1^{t\,*} = \frac{\dfrac{(1+\nu)\sigma_{ij}\sigma_{ij} - \nu\sigma_{kk}\sigma_{ll}}{2E\left[1-H\left(\sigma_{kk}^{+}\right)\alpha_d^t\right]^2\left(1-\alpha_d^c\right)}}{\dfrac{1}{G_t(\mathbf{x})}\displaystyle\int_{V_t} g\left(\|\mathbf{y}-\mathbf{x}\|\right)\frac{(1+p_t)\sigma_{ij}^{+}\sigma_{ij}^{+} - p_t\left(\sigma_{kk}\right)^{+}\left(\sigma_{ll}\right)^{+}}{2E\left(1-\alpha_d^t\right)^2}dV_y} F_1^t\left(\alpha_d^t,\alpha_d^c\right) \tag{5.17b}$$

and

$$F_1^{c\,*} = \frac{\dfrac{(1+\nu)\sigma_{ij}\sigma_{ij} - \nu\sigma_{kk}\sigma_{ll}}{2E\left[1-H\left(\sigma_{kk}^{+}\right)\alpha_d^t\right]\left(1-\alpha_d^c\right)^2}}{\dfrac{1}{G_c(\mathbf{x})}\displaystyle\int_{V_c} g\left(\|\mathbf{y}-\mathbf{x}\|\right)\frac{(1+p_c)\sigma_{ij}^{-}\sigma_{ij}^{-} - p_c\left(\sigma_{kk}\right)^{-}\left(\sigma_{ll}\right)^{-}}{2E\left(1-\alpha_d^c\right)^2}dV_y} F_1^c\left(\alpha_d^c\right) \tag{5.18b}$$

As can be seen, nonlocality is introduced directly to the dissipation function (5.16). The above expressions (5.17b and 5.18b) only differ from their counterparts (5.17a and 5.18a) in the appearance of spatial integrals in the denominators. In a similar way to the derivation of the damage loading functions (4.46) and (4.49) in Chapter 4, we obtain here two nonlocal damage loading functions

$$y_d^t = \frac{H\left(\sigma_{kk}^{+}\right)}{G_t(\mathbf{x})}\int_{V_t} g\left(\|\mathbf{y}-\mathbf{x}\|\right)\frac{(1+p_t)\sigma_{ij}^{+}\sigma_{ij}^{+} - p_t\left(\sigma_{kk}\right)^{+}\left(\sigma_{ll}\right)^{+}}{2E\left(1-\alpha_d^t\right)^2}dV - F_1^t\left(\alpha_d^t,\alpha_d^c\right) = 0 \tag{5.19}$$

and

$$y_d^c = \frac{1}{G_c(\mathbf{x})}\int_{V_c} g\left(\|\mathbf{y}-\mathbf{x}\|\right)\frac{(1+p_c)\sigma_{ij}^{-}\sigma_{ij}^{-} - p_c\left(\sigma_{kk}\right)^{-}\left(\sigma_{ll}\right)^{-}}{2E\left(1-\alpha_d^c\right)^2}dV - F_1^c\left(\alpha_d^c\right) = 0 \tag{5.20}$$

In the above expressions, V_t and V_c respectively represent the volume elements where the dissipation processes due to tensile and compressive damage take place. These volumes should be distinguished due to different natures of the two failure mechanisms, characterized through two different characteristic lengths and two different fracture energies in tension and compression. This difference unfortunately can cause difficulties in the numerical implementation, and therefore will be overcome by the proposal of appropriate procedures for the determination of model parameters. Those procedures are the main subject of the next sections.

The use of spatial integrals for energy-like terms in the denominators of (5.17b) and (5.18b) results in two energy-based nonlocal damage criteria (5.19 and 5.20). As mentioned at the beginning of section 5.3.1, in the numerical failure simulations these energy-based damage functions help avoid the unrealistically high residual stresses at very late stages of the damage process, when macro cracks begin to occur (Jirasek, 1998). The integrals in the denominators of (5.19) and (5.20) represent the nonlocality of energy-like quantities, which can in general be expressed as

$$\tilde{\omega}_i(\mathbf{x}) = \frac{1}{G_i(\mathbf{x})} \int_{V_i} g_i(\|\mathbf{y}-\mathbf{x}\|)\omega_i(\mathbf{y})dV \tag{5.21}$$

in which $\tilde{\omega}_i$ (i stands for t or c) is the nonlocal counterpart of the energy-like quantity ω_i; $\mathbf{x}$ and $\mathbf{y}$ are coordinate vectors of points within the defined volume element V_i; $g_i(\|\mathbf{y}-\mathbf{x}\|)$ is the weighting function; and $G_i(\mathbf{x})$ is the weight associated with point $\mathbf{x}$, aiming to normalize the weighting scheme applied to ω_i.

$$G_i(\mathbf{x}) = \int_{V_i} g_i(\|\mathbf{y}-\mathbf{x}\|)dV \tag{5.22}$$

Therefore the normalization condition of the weighting scheme is satisfied:

$$\frac{1}{G_i(\mathbf{x})} \int_{V_i} g_i(\|\mathbf{y}-\mathbf{x}\|)dV = 1 \tag{5.23}$$

The weighting function g can be in the form of either a Gauss weight function

$$g_i(r) = g_i(\|\mathbf{y}-\mathbf{x}\|) = \exp\left(\frac{r^2}{2l_i^2}\right) \tag{5.24}$$

or a bell-shaped function

$$g_i(r) = g_i(\|\mathbf{y}-\mathbf{x}\|) = \begin{cases} 0 & \text{if } r > R_i \\ \left(1-\dfrac{r^2}{R_i^2}\right)^2 & \text{if } r \le R_i \end{cases} \tag{5.25}$$

where $r = \|\mathbf{y}-\mathbf{x}\|$ is the distance between the considered points; l_i and R_i are the length parameters of nonlocal continuum, governing the nonlocal spread of the damage. These lengths (l_i and R_i) in nonlocal models defines a finite volume characterizing the constitutive behaviour of the material (Ferrara and di Prisco, 2001). They are parameters associated with nonlocal model and their relationships with the width w_i of

the fracture process zone are dependent on the material properties and the constitutive behaviour of the nonlocal model. These relationships will be explored in the next section. In the literature (Jirasek, 1998a; Ferrara and di Prisco, 2001), the term internal length is usually used to refer to the length parameter l_i in the Gauss weight function (5.24). For an arbitrary weighting function $g(r)$, a definition of the internal length l_i is (Jirasek, 1998a):

$$l_i = \sqrt{\frac{\int_0^\infty r^2 g_i(r) dr}{\int_0^\infty g_i(r) dr}} \tag{5.25a}$$

For the bell-shaped function in (5.25), the above equation gives $l_i = R_i / \sqrt{7}$. It is also noted here that the term "characteristic length" in the literature can be used to refer to a length parameter in nonlocal continuum (Bazant and Pijaudier-Cabot, 1989; Bazant and Cedolin, 1991), or the width w_i of an imaginary and uniformly damaged crack band (Ferrara and di Prisco, 2001). In this study, we use both terms "characteristic length" and "internal length" for a length parameter of the nonlocal continuum, and refer to w_i as the width of an imaginary and uniformly damaged crack band.

Use of the above nonlocal averaging leads to a non-symmetric structural stiffness matrix in the finite element analysis, due to the effect of the boundary of the analyzed structure on the weighting scheme (Jirasek and Patzak, 2002; Bazant and Jirasek, 2002; Borino *et al.*, 2003). This effect, however, merely matters at the structure boundary, where $G_i(\mathbf{x})$ varies at points within a certain distance (less than the nonlocal interaction radius R_i) from the boundary and is different from its maximum value obtained when the structure is unbounded. A modified weighting scheme was also proposed by Borino *et al.* (2003) to remedy the problems of a non-symmetric stiffness matrix. It is, however, not yet adopted in this study.

The advantage of this proposed introduction of nonlocality is the simplicity over the approach adopted by the Italian researchers (Polizzotto *et al.*, 1998; Polizzotto and Borino, 1998; Borino *et al.*, 1999; Benvenuti *et al.*, 2002). Nonlocality occurs in the dissipation function and helps redistribute the dissipated energy over the regions where the irreversible processes take place. The nonlocal rates of dissipation are therefore significantly controlled by the two expressions under the spatial integrals and obviously

affect the damage process. On the other hand, the connection between the dissipation function and the obtained yield/damage criteria has been examined in chapter 3, and here helps obtain the physical interpretation of the proposed nonlocal regularization. This connection, through the use of the Legendre transformation, guarantees the consistency of the adopted thermodynamic approach, represented through the possibility of obtaining the total dissipated energy directly from the specified dissipation function. As a consequence, casting the dissipation function in nonlocal form directly results in the regularization effects on the derived constitutive model, realized through the nonlocal damage criteria (5.19) and (5.20). This is one of the great advantages of the thermodynamic framework adopted in this study.

5.3.2 Parameter identification for nonlocal damage models

5.3.2.1 Background and a brief review

The relationship between the width of the fracture process zone w_t and the tensile internal length l_t was established by Bazant and Pijaudier-Cabot (1989), in which $w_t \approx l_t$ was found along with the relationship $l_t = 3d_{\max}$ between l_t and the maximum aggregate size $d_{\max}$. In addition, $w_t = 3d_{\max}$ was also found by Bazant and Oh (1983) as an optimal fit for various experimental tests, based on their proposed crack band model. However, those relationships cannot be generalized as their derivations were carried out merely based on specific conditions of the adopted experimental test (Bazant and Pijaudier-Cabot, 1989) and assumptions on the adopted constitutive models [e.g. linear softening with constant strain across the width in crack band model (in Bazant and Oh, 1983), and use of a specific expression for the damage evolution (in Bazant and Cedolin, 1991 and Bazant and Pijaudier-Cabot, 1988)]. Moreover, w_t in continuum models does not mean the actual width of the micro-cracked zone, but the minimum admissible dimension of the representative volume element (Bazant and Oh, 1983). From that viewpoint, $w_t = 3d_{\max}$ is merely an approximation and can vary with the material properties, e.g. smaller ratio $w_t/d_{\max}$ for high strength concrete with less difference between the elastic modulus of mortar and aggregate (Bazant and Oh, 1983). Therefore, from the viewpoint of data fitting, a different ratio, e.g. $w_t = 1.5d_{\max}$, could be acceptable, provided that the tensile fracture energy G_F of the material is invariant with respect to any change of w_t (Bazant and Oh, 1983).

The above is merely a very brief review on the relationship between the width of the tensile fracture process zone w_t, the tensile internal length l_t, and the maximum aggregate size $d_{\max}$, which will serve as a basis for the identification of parameters of the proposed nonlocal model in this study. However, that is not enough for our proposed model with two separate modes of tensile and compressive damage-induced softening. Relationships between w_c, l_c and $d_{\max}$ in compression are additionally needed for the compressive behaviour of the model. Unfortunately they cannot be obtained from available experimental research, which mostly deal with the tensile fracture properties of the material. Besides, the ratio $w_c/d_{\max}$ is also expected to differ significantly from that in tension, due to different mechanisms of failure in tension and compression. As a consequence, the nonlocal interaction radiuses R_t and R_c should be different in tension and compression respectively. This causes difficulties in the implementation of the proposed models as well as the numerical analysis, especially in the case that two modes of damage are activated in the same part of the analyzed structure (e.g. in the splitting test of a concrete prism). Comi (2001) also addressed the necessity of adopting different tensile and compressive internal lengths in the nonlocal constitutive modelling of concrete, but still used the same value for both lengths in her relevant numerical example.

Bearing in mind the mentioned problems, we should seek an alternative way to determine the relationships between the nonlocal interaction radiuses R_t and R_c (or alternatively between the internal lengths l_t and l_c) used in the numerical analysis and the corresponding widths w_t and w_c of the fracture process zones. In this study, the balance of the dissipated energy in an equivalent crack band model and our adopted nonlocal model is used as a basis for determining the mentioned relationships. To lessen the difficulties and complication in the numerical implementation, R_t and R_c are taken identical in this study; and we use R as the nonlocal interaction radius in both tension and compression. This simplification, however, causes almost no loss of generality thanks to the adoption of an appropriate procedure for the parameter identification. The procedure is, however, presented for tensile behaviour only. Its adaptation to compression is straightforward.

Mathematically, the incorporation of nonlocality into the model will prevent the governing differential equations changing type at the onset of damage and help to

maintain the well-posedness of the boundary value problem. From the structural point of view, nonlocal regularization will prevent the dependence of the solutions on the discretization in the finite element analysis. The dissipation in nonlocal analysis in fact spreads over a band with a finite thickness dependent on the nonlocal interaction radius R and other parameters of the model. This bandwidth, denoted here as z_t, is different from the width w_t (w_t is also termed the dissipation length in Jirasek (1998a); and Bazant and Jirasek (2002)) of the fracture process zone in an equivalent crack band model (see figure 5.4a). In addition, due to the averaging process in nonlocal models, the stress-strain relations are not the same for all material points in the FPZ. This is totally different from those in crack band models, where a unique stress-strain relation is maintained at every material point undergoing damage. As a consequence, in the structural analysis with nonlocal softening models, the local dissipation is different at every material point in the FPZ. Nevertheless, the total energy dissipated in the zone z_t in the nonlocal model should be equal to that within the width w_t in the equivalent crack band model. Therefore, the parameters of the local stress-strain relations in nonlocal models should be determined so as to guarantee the right amount of total dissipated energy per unit area imposed by the fracture energy G_F.

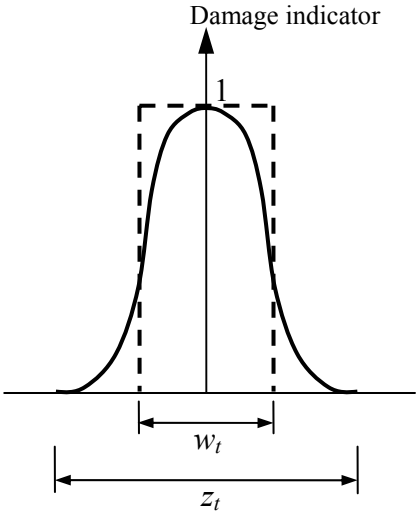

Figure 5.4a: Damage profile in uniaxial test using nonlocal model,
and definition of w_t and z_t (adapted from Bazant and Pijaudier-Cabot, 1989)

The above observation is the basis for the determination of parameters for nonlocal damage models. Based on the equivalence of dissipated energy, a relationship between the internal length l_t and the width w_t of an imaginary and uniformly damaged crack

band is needed for the determination of parameters for nonlocal models. However, the condition of preserving the right amount of dissipated energy has rarely been addressed or inappropriately used in numerical studies using nonlocal (or gradient) damage models [e.g. in de Borst and Pamin (1996), Meftah and Reynouard (1998); Di Prisco *et al.* (2000)]. De Borst and Pamin (1996) and Di Prisco *et al.* (2000) used the constant ratios $z_t/w_t = 2$ and $z_t/l_t = 2\pi$ to yield a linear relationship between w_t and l_t. The choice of the ratio $z_t/w_t = 2$ was in fact rather arbitrary as it was not accompanied by any theoretical or experimental basis. In addition, the ratio $z_t/l_t = 2\pi$ was obtained by de Borst and Muhlhaus (1992) based on a simple uniaxial model with linear softening law and therefore cannot be applied to models with nonlinear softening law. Similarities are also observed in Meftah and Reynouard (1998), with the use of $z_t/l_t = 2\pi$, which is derived from a gradient model with linear softening law, for a nonlinear softening constitutive equation.

Ferrara and di Prisco (2001) carried out numerical analyses for different types of concrete structures in mode I fracture to establish relationships between l_t (or alternatively the radius R) and w_t. In their analyses, all the parameters controlling the local behaviour of the model are kept fixed, realized through the constant value of the specific fracture energy g_F, while the internal length l_t is varied. Numerical failure analysis of the considered structure is carried out for each given value of l_t. The calculated dissipated energy, as the area under the load-displacement curve, is then divided by the fracture area to yield the fracture energy G_F. The width w_t corresponding to the given value of l_t is obtained as $w_t = G_F/g_F$. It was shown (Ferrara and di Prisco, 2001) that for each type of nonlinear softening curve, w_t was linearly dependent on l_t, which means $k = w_t/l_t$ is a constant. However, this numerical observation came from the use of parameters of the local constitutive model independent from the internal length l_t and hence also independent from the width w_t (see Ferrara and di Prisco, 2001). In other words, the correspondence between the stress-separation law in cohesive crack model and stress-strain relation in continuum model (see figure 4.11, Chapter 4) is not respected. Therefore, the obtained linear relationship between l_t and w_t cannot be considered appropriate for nonlocal constitutive model.

In fact, the parameters which govern the local behaviour of the continuum model should be related to the width w_t of the fracture process zone. In the crack band model of Bazant and Oh (1983), it is the dependence of the softening modulus of the post-peak uniaxial stress-strain curve on the crack bandwidth w_t. In research on gradient plasticity, Vardoulakis (1999) also pointed out the nonlinear dependence of the maximum shear band thickness on the internal length l_t, as a result of the determination of the softening rate of the model through inverse analysis of the shear band thickness. Similar relationship was also obtained in recent study by Zhao *et al.* (2005) on shear banding in geomaterials using gradient damage model. The authors (Zhao *et al.*, 2005) arrived at a ratio w_t/l_t expressed in terms of the Poisson's ratio and a parameter representing the shape of uniaxial stress-strain curve. Nevertheless, these analytical expressions describing the nonlinear relationship between l_t and w_t are obtained from specific models with simplifications, e.g. linear softening law (Zhao *et al.*, 2005), and therefore cannot be universally applicable in practice. A general numerical procedure for the establishment of a relationship between l_t and w_t accounting for the influence of other parameters of an arbitrary local constitutive model is hence needed.

Jirasek (1998a) addressed the nonlinear relationship between l_t and w_t, and proposed a simple iterative procedure for the determination of parameters of constitutive models based on nonlocal damage theory. In his research, different types of softening law (linear or nonlinear), nonlocal weight function (using Gauss function or bell-shaped function) and nonlocal formulation (using the nonlocality of damage energy, strain or damage variable) were used to derive different nonlinear relationships between $k = w_t/l_t$ and the ductility parameter $\eta = g_F/g_p$, with g_p being the elastic energy density at uniaxial peak stress ($g_p = f_t'^2/2E$; see figure 5.5). The established graphs are exploited for the selection of model parameters in an iterative manner (see Jirasek, 1998a). Despite the slight variation of k (for highly ductile softening law) with respect to the local constitutive law and the type of nonlocal formulation, use of pre-established graphs for the determination of model parameters is not always appropriate, as these graphs are implicitly dependent on the material properties used. In other words, these graphs should be established for every set of experimentally given material properties, softening curve and nonlocal weight function, instead of using pre-built graphs for all cases. In addition, a more effective procedure should be sought to replace the iterative procedure proposed by the author (Jirasek, 1998a).

5.3.2.2 A procedure for the determination of parameters for nonlocal models

In this section, a procedure to deal with the determination of parameters for nonlocal damage models is proposed. The method takes into account the dependence of the local constitutive equations and the length parameter R of the nonlocal model on the width w_t of the fracture zone. The key idea of the procedure is to assure the right amount of dissipation of a nonlocal damage model at the end of the damage process. In other words, the model should behave so that the damage process results in the averaged dissipated energy per unit area identical with that imposed by the material fracture energy G_F. For the sake of simplicity, only pure damage models and a uniaxial problem are considered. The proposed procedure is, however, also applicable to the general elasto-plastic-damageable models and not restricted by the uniaxial problems studied in this Chapter.

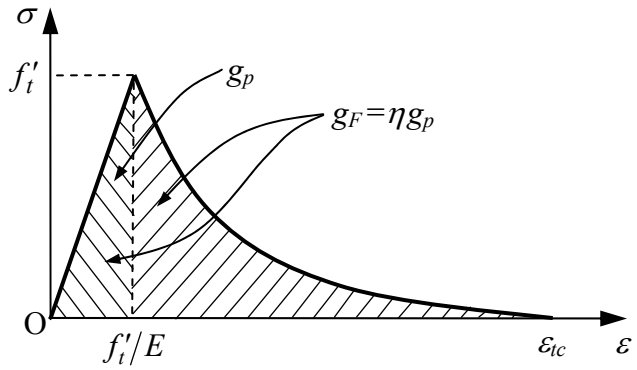

Figure 5.5: Definition of the ductility parameter η

From the specified nonlocal interaction radius R, the parameters to be determined is the width w_t of the FPZ in an equivalent crack band model, or alternatively the ratio $k = w_t / R$. They are related to the fracture energy G_F through the relationship

$$G_F = w_t \, g_F = k \, R \, g_F \tag{5.26}$$

in which g_F is termed the specific fracture energy (or local fracture energy), which has been essentially used for the determination of other model parameters in the previous chapter. As can be seen, all parameters of the nonlocal model (R and those in functions F_1^t) are strongly dependent on each other and need to be appropriately determined. For this reason, in a study by Jirasek (1998a), a simple iterative process based on a one-dimensional numerical analysis of a tensile bar was used. Following this process (in Jirasek, 1998a), the nonlocal interaction radius R need to be specified first based on the

maximum aggregate size of aggregate or the dimension of the structural members, while iterations are needed for the determination on of the ratio k between the width w_t of the equivalent FPZ and the nonlocal radius R.

The initial value of k can be chosen in the range $k = 1 \sim 3$, depending on the type of nonlocality (e.g. nonlocal strain, or nonlocal damage energy). For an assumed value of k, the specific fracture energy g_F can be determined from the relation (5.26), followed by the determination of all parameters of the model, as illustrated in Chapter 4. With all parameters in hand, we can then carry out the numerical failure analysis for a one-dimensional bar with a defect at its middle length to trigger damage (see figure 5.6), and obtain the total dissipation as the area under the load-displacement curve. In principle, the averaged dissipated energy obtained, after having been divided by the cross sectional area of the bar and denoted as G_F', should coincide with G_F, representing the right amount of energy dissipated per unit area during the fracture process. However, this is not always the case and the procedure should be repeated several times until the balance of dissipated energy is established.

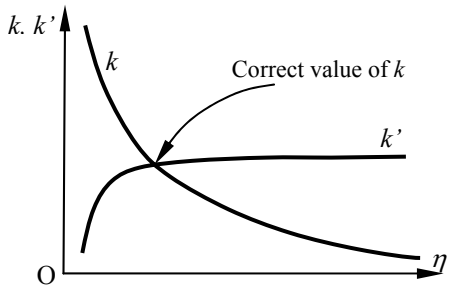

Figure 5.5a: Determination of the ratio $k = w_t'/R$

Relationships between non-dimensional quantities can be made use of for higher efficiency in the process of determining the ratio k. Jirasek (1998a) suggested using the relationships between the ductility parameter η, defined as the ratio of the local specific fracture energy g_F to the elastic energy density at peak stress (denoted here as $g_p = f_t'^2/2E$, figure 5.5), and the relative dissipation length as the ratio between w_t and the length parameter l_t used in the Gauss weight function. However, for use of the bell-shaped function in this study, $k = w_t/R$ is adopted as the relative dissipation length. The procedures proposed here, which help avoid the above iterative process, can be summarized as follow (see also figure 5.5a):

- Assume values of k_i's: $k_1 = 1.0, \ldots, k_n = 3.0$

- Calculate the fracture energies $g_{Fi} = G_F/(k_i R)$, ductility parameters $\eta_i = g_{Fi}/g_p$ and determine the corresponding sets of model parameters based on the procedures proposed in chapter 4
- Carry out the numerical analyses of a one-dimensional bar and calculate the corresponding total dissipated energies D_i as the areas under the load-displacement curves.
- From the dissipated energies obtained, calculate the corresponding fracture energies $G'_{Fi} = D_i/A$, where A is the cross-sectional area of the bar, and derive the ratios $k'_i = G'_{Fi}/Rg_{Fi}$
- The correct value of k will be found by plotting k_i and k'_i against $\eta_i = g_{Fi}/g_p$ and determining the intersection point of the two plotted curves (see figure 5.5a).

5.3.3 Numerical examples

The following examples demonstrate the above procedure. We use in the examples the following sets of material properties:

Set 1 (Perdikaris and Romeo, 1995)	Set 2 (Petersson, 1981)
$E = 43600\text{N/mm}^2$	$E = 30000\text{N/mm}^2$
$\nu = 0.2$	$\nu = 0.2$
$f'_t = 4.77\text{N/mm}^2$	$f'_t = 3.33\text{N/mm}^2$
$G_F = 0.08917\text{N/mm}$	$G_F = 0.124\text{N/mm}$
$d_{\max} = 6\text{mm}$	$d_{\max} = 8\text{mm}$

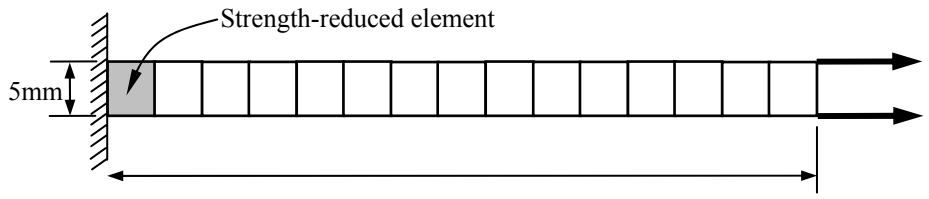

Figure 5.6: Finite element model used for the determination of parameter k

In the first material set, the nonlocal interaction radii are assumed to be: $R_1 = 2.5d_{\max} = 15\text{mm}$, $R_2 = 2.0d_{\max} = 12\text{mm}$ and $R_3 = 1.5d_{\max} = 9\text{mm}$. For the

second material set, we use: $R_1 = 2.5d_{\max} = 20\text{mm}$, $R_2 = 2.0d_{\max} = 16\text{mm}$ and $R_3 = 1.5d_{\max} = 12\text{mm}$.

A simple test (figure 5.6) is set up for the parameter identification. Because of symmetry, only half of the bar is modelled. To trigger damage, a one-percent reduction of the uniaxial tensile strength f_t' is applied to the blackened element in figure (5.6). As the energy dissipation is only affected by the area under the stress-strain curve regardless of the unloading path, a pure damage model can be adopted for simplicity. Choice of the parameter $t = g_{fnl}/g_F$ (section 4.3.3, chapter 4) may have effects on the procedures here. These effects are illustrated in figure (5.7).

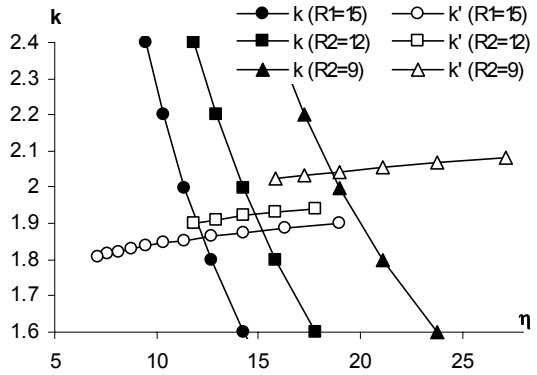

(a) Material set No. 1; $t = g_{fnl}/g_F = 0.4$

$k_{R_1} = 1.86$; $k_{R_2} = 1.92$; $k_{R_3} = 2.04$

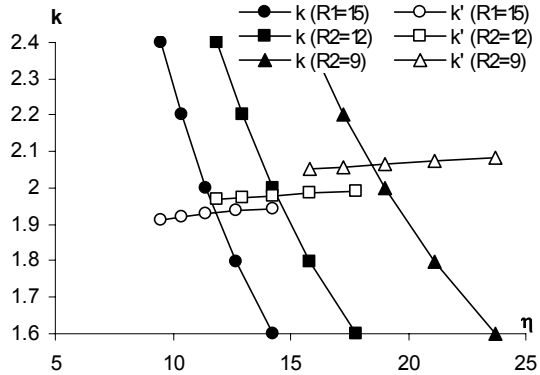

(b) Material set No. 1; $t = g_{fnl}/g_F = 0.25$

$k_{R_1} = 1.93$; $k_{R_2} = 1.98$; $k_{R_3} = 2.06$

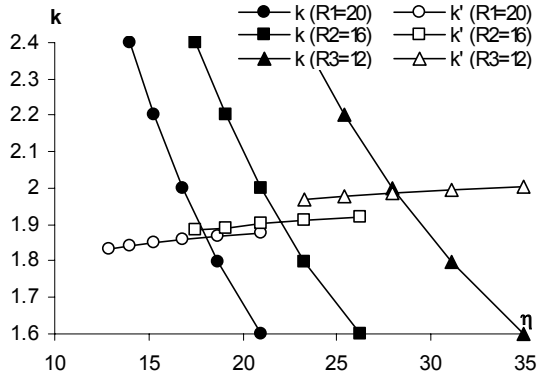

(c) Material set No. 2; $t = g_{fnl}/g_F = 0.4$

$k_{R_1} = 1.86$; $k_{R_2} = 1.91$; $k_{R_3} = 1.99$

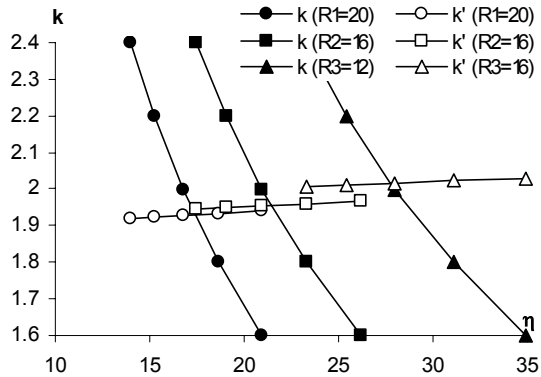

(d) Material set No. 2; $t = g_{fnl}/g_F = 0.25$

$k_{R_1} = 1.93$; $k_{R_2} = 1.96$; $k_{R_3} = 2.02$

Figure 5.7: Determination of parameter *k*

In addition, for the calculation of dissipated energy, one has to require the numerical analyses be carried out until failure (complete separation of the numerically-tested specimen in two pieces), characterized by damage measure α_d^t reaching unity. However, with the proposed nonlinear softening law, this is hardly achieved because the above-defined failure only happens at infinite strain. Therefore in the numerical example, the term failure refers to the states when $1-\alpha_d^t \le 10^{-9}$ and the uniaxial stress is normally below 10^{-5}N/mm^2. Linear interpolation is used to calculate the dissipated energy below this stress level.

The results are shown in figure (5.7), with the obtained values of k corresponding to the assumed values of the nonlocal interaction radius R. It can be seen that k tends to increase for decreasing value of R. In the above example, k can take values of 1.9~1.95 for R_1=2.5d_{max} or 2.0~2.1 for R_2=1.5d_{max}. This, however, is only a very rough suggestion and its effects on the results of the numerical simulations can be considered negligible taking into account many assumptions and simplifications of the adopted constitutive models.

Nonlocal radius	Set 1			Set 2		
	k	E_{pt} (MPa)	n_t	k	E_{pt} (MPa)	n_t
$R_1 = 2.5d_{\max}$	1.93	22345.90	0.38	1.93	8967.34	0.34
$R_2 = 2.0d_{\max}$	1.98	16800.07	0.36	1.96	6898.61	0.32
$R_3 = 1.5d_{\max}$	2.06	12083.68	0.34	2.02	5067.76	0.30

Table 5.1: Model parameters corresponding to the choice of nonlocal interaction radius

The above calculation of k can be readily confirmed by carrying out the numerical analysis of the corresponding three point bending tests (Perdikaris and Romeo, 1995; Petersson, 1981) corresponding to the material set numbers 1 and 2. Three different choices of nonlocal interaction radiuses: $R_1 = 2.5d_{\max}$, $R_2 = 2.0d_{\max}$ and $R_3 = 1.5d_{\max}$ are used in both tests, resulting in the corresponding values of k of 1.93, 1.98 and 2.06 (Perdikaris and Romeo, 1995), and 1.93, 1.96 and 2.02 (Petersson, 1981). The corresponding model parameters (E_{pt} and n_t) are obtained from equations (4.80) and (4.81) in Chapter 4 (with $H_t = \infty$ for pure damage behaviour). Their values are shown

in table (5.1). More details on the tests will come in Chapter 7 and only brief results are presented here to illustrate the effectiveness of the proposed parameter identification.

From the numerical results obtained (figure 5.8), it is seen that the numerical load-deflection curves match rather well the experimental ones, verifying the total dissipated energy in mode I fracture. The slight differences in the numerical responses come from the use of only one fitting parameter $t = g_{fnl} / g_F = 0.25$ for all three cases of different nonlocal radii. Nevertheless, all three different radii in the same bending test give very close numerical responses to the experimental load-deflection curves.

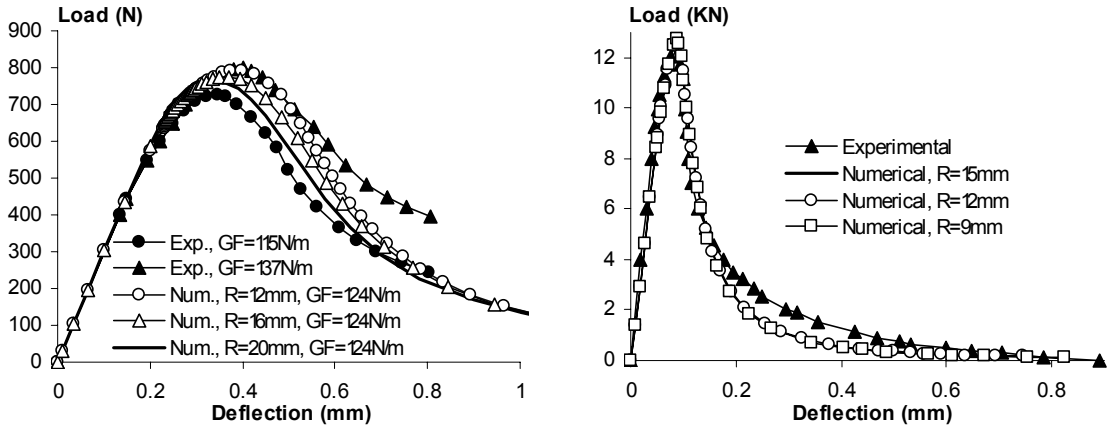

(a) Test of Petersson (1981) (b) Test of Perdikaris and Romeo (1995)

Figure 5.8: Verification of the choice of model parameters in three point bending test

In both numerical bending problems, the dissipated energies from the very long tail responses compensate for the difference in the dissipation over the range of deflections shown in the figures. Nevertheless, the tail behaviour of the numerical load-deflection curves can be improved by setting smaller value (e.g. $1.0\text{-}10^{-3}$) for the numerically-used critical damage ($1.0\text{-}10^{-13}$ in the examples here) in the evaluation of the local fracture energy g_F (see 4.72). In addition, better numerical responses can in principle be achieved through optimization procedures combined with size effect tests on specimens of different sizes, giving a better combination of fitting parameter t, nonlocal interaction radius R, and ratio k between R and the width w_t of the fracture process zone. This is, however, outside the scope of this study.

5.4 Summary and Discussion

The introduction of nonlocality to the proposed local constitutive model (equations 4.25, 4.37, 4.46 and 4.49) in the previous chapter has been presented in this chapter, backed by a brief review on regularization methods. Comparisons between the proposed approach and other nonlocal thermodynamic approaches have also been made, showing the simplicity yet the advantages and consistency of the developed approach. Although some physical interpretations for the nonlocal nature of concrete damage have been provided (Bazant, 1991, 1994) and realized in this study through the nonlocality of the energy of dissipation, generally they still need to be enriched with more evidence based on experiments and micromechanics. The proposed nonlocal damage-plasticity model (equations 4.25, 4.37, 5.19 and 5.20) therefore can only be considered as a mathematical approach towards the regularization of softening effects in the numerical modelling of concrete materials. This model and its derivatives (e.g. nonlocal tensile damage model, or nonlocal tensile damage-plasticity model,…) will be implemented into a finite element code (Chapter 6) and used for the numerical failure simulations of concrete structures (Chapter 7).

The connection between the parameters of the nonlocal model and the experimentally provided material properties has been established, through the identification of the parameter k relating the nonlocal interaction radius R with the width w_t of the fracture process zone in tension. In conjunction with the determination of model parameters in chapter 4, this newly-established connection helps provide a consistent and rigorous way of deriving the stress-strain behaviour in the proposed constitutive models from the stress-separation curve given by standard experiments. To some extent, in the numerical examples the structural responses can be seen to be unique regardless of the choice of different nonlocal interaction radiuses. This is an important point, which has rarely been discussed in the literature, about the nonlocal modelling of the materials.

The same procedures for the determination of nonlocal model parameters can be applied to the modelling of the compressive behaviour of the material, giving relevant value of the width w_c of the fracture process zone in compression, which in general differs from that in tension. However, those procedures can only be tentatively adopted here due to the lack of experimental data of concrete in compression, as well as the

requirements for more physical interpretation of the compressive fracture energy G_c and compressive internal length l_c. Much of research work is therefore still required to capture faithfully the complex behaviour of this quasi-brittle material.

Chapter 6: Numerical Implementation

6.1 Introduction

Numerical implementation plays an important part in the development of constitutive models for engineering materials. The implementation here comprises a method for the solutions of partial differential equations in solid mechanics, and the incorporation of the constitutive models into this system of governing differential equations. In our study, the finite element method is employed for solving the boundary value problems in continuum mechanics. However, as concrete exhibits highly nonlinear behaviour after peak stress, the incorporation of the nonlocal constitutive relationships into the system of governing differential equations in solid mechanics is not very easy. A suitable numerical scheme is needed for the integration of the nonlinear rate constitutive equations. For stability, implicit integration schemes like the backward and midpoint Euler schemes are preferred. In addition, due to the material nonlinearity, the system of linear algebraic equations arising from the finite element discretization also turns out to be nonlinear, with the stiffness matrix being dependent on the nodal displacements. Therefore, numerical solution methods, in which, the Newton methods are normally suitable and adequate for this purpose, will be used.

However, softening makes things complicated here, as the system of algebraic equations becomes singular at peak load and negative-definite beyond peak load. Snap-through and snap-back responses (see figure 6.1) on the equilibrium path represented by the load-displacement curves are typical when tracing the equilibrium paths in analysing structures made of softening materials. Displacement controlled Newton methods can handle snap-through behaviour, but fail when the equilibrium path exhibits snap-back. In the past, various arc-length control procedures have been proposed to deal with softening-related problems (Riks, 1979; de Borst, 1986; Crisfield and Wills, 1988; Crisfield, 1997; May and Duan, 1997). The key idea of the methods is the use of an additional constraint to the load and displacement vectors. The load multiplier in this case is not a constant, but acts as an additional variable to the unknown displacement vector. The new system of equations, augmented by this constraint, is always well-conditioned, even when the stiffness matrix is singular (Crisfield, 1997), enabling the

method to be used to tackle structural problems with an equilibrium path exhibiting snap-through and snap-back responses.

This chapter centres around the finite element implementation of the proposed nonlocal constitutive model, in which the nonlocal constitutive equations (4.25, 4.37, 5.19 and 5.20) in the previous chapters and an arc-length solution procedure are presented and implemented. A modified backward integration scheme, based on the algorithm proposed by Crisfield (1997, Vol. 1, Chap. 6) is employed for the integration of the rate constitutive equations. The arc-length control here is based on that proposed by May and Duan (1997), with a local, instead of global, constraint equation, and can be used in combination with either direct or indirect displacement controlled Newton methods. In addition, the indirect displacement controlled method can be seen to resemble this local arc-length procedure and can readily be incorporated into the existing finite element code OXFEM used in this study. Numerical examples showing the capability of the adopted arc-length control procedure in handling strong snap back behaviour will be presented in the next chapter.

6.2 Solution strategy

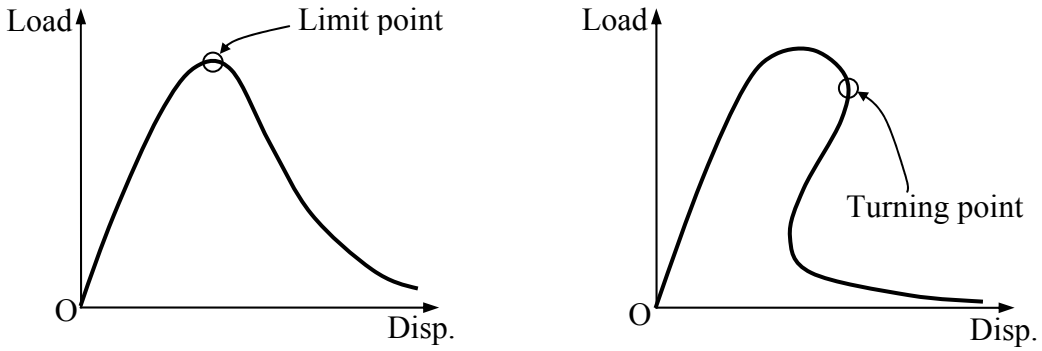

Figure 6.1: Snap-though (left) and snap-back (right)

The numerical techniques used in nonlinear finite element analysis are briefly introduced here, with the objective being tracing the nonlinear equilibrium paths of structures subjected to quasi-static loading. For this purpose, an incremental-iterative solution procedure is usually employed. The load is increased step by step, and within each step iterations are required to get to the equilibrium state. Therefore, two separate incremental and iterative procedures should be distinguished. Load control, displacement control and arc-length control are usually used for the incremental

analysis while Newton-like methods are the basis for iterative techniques. However, among the incremental procedures, only the arc-length control can tackle high nonlinearity, in which the equilibrium path usually represented by the load-displacement curves may show snap-though and snap-back responses (figure 6.1). Use of load control or displacement control in such cases is not appropriate as the former is not able to handle both snap-though and snap-back responses and the latter can merely overcome snap-though behaviour.

All the above numerical techniques have been well documented in text books (Chen and Han, 1988; Crisfield, 1997; Jirásek and Bazant, 2002). Therefore, they are not presented here. This section only concentrates on the presentation of relevant techniques for the nonlinear analysis of structures made of softening materials, in which snap-though and snap-back responses are often encountered. The arc-length control in combination with the Newton-Raphson iterative techniques is the basis for the implementation and will be briefly introduced hereafter. The presentation of the solution methods in this part of the chapter is merely a reproduction of the research work by several researchers (mainly that of de Borst, 1986; and May and Duan, 1997), aiming at setting a background for the implementation of the proposed constitutive models. Background and more details on the arc-length methods can be found in the cited references.

6.2.1 Arc-length methods

Arc-length methods are perhaps the most powerful and reliable control procedures to deal with softening-related problems in the finite element analysis. The methods originally stemmed from the proposal by Riks (1979) and have been adapted and developed by several researchers (de Borst, 1986; Crisfield and Wills, 1988; Crisfield, 1997; May and Duan, 1997). It has also been shown and proved by several researchers (de Borst, 1986; May and Duan, 1997; Yang and Proverbs, 2004) that the methods, especially when combined with the use of local or relative displacements in the constraint equation, can effectively handle snap back response in the equilibrium path.

The key idea of the method is the use of an additional constraint equation for the incremental load multiplier $\Delta\lambda$, which plays the role of an extra degree of freedom in the global linearized equilibrium equations. Although several types of constraints have

been proposed and employed, not all of them are able to deal with highly nonlinear behaviour of the material (e.g. strong snap-back behaviour). It has been documented (Yang and Proverbs, 2004; Yang and Chen, 2004) that the normal-plane and spherical arc-length methods may fail when encountering snap-back behaviour in dealing with problems involving softening materials. In addition, the spherical form of the method was also found to be more stable than the normal-plane arc-length (Crisfield, 1997), which has poor convergence or even divergence near a limit point. However, despite some enhancements to the choice of the appropriate root in the spherical arc-length (e.g. based on the minimum residual in Hellweg and Crisfield, 1998), that kind of arc-length control still suffers from the drawback of the parabolic constraint equation in having no real root in highly nonlinear cases (May and Duan, 1997; Yang and Proverbs, 2004).

A more rigorous form of arc-length control and its derivatives, which removes the drawback encountered in the spherical arc-length method, has been employed with success by several researchers (de Borst, 1986; May and Duan, 1997; Yang and Proverbs, 2004; Yang and Chen, 2004). That approach, termed updated normal plane control by De Borst (1986) and Yang and Proverbs (2004), is adopted in this study. The constraint equation in this case takes the modified form of the spherical arc-length

$$\Delta \mathbf{U}_1{}^T \Delta \mathbf{U}_i = \Delta L^2 \quad (i = 1, 2, 3, \dots) \tag{6.1}$$

in which ΔL is the arc-length; and the incremental displacement vector $\Delta \mathbf{U}_i$ at the i^{th} iteration is accumulated from the iterative ones as follows:

$$\Delta \mathbf{U}_i = \sum_{j=1}^{i} \delta \mathbf{U}_j \quad (i = 1, 2, 3, \dots) \tag{6.2}$$

Use of the above linearized constraints has been found to be superior to that used in the spherical arc-length as it yields a linear equation for the incremental load factor $\Delta \lambda_i$. Therefore, it is not necessary here to have any criterion for the choice of the appropriate root of the constraint equation, as required in the spherical arc-length method. In addition, May and Duan (1997) argued that the adopted constraint equation (6.1) also limits the iteration trajectory on a spherical surface, thus always yielding an intersection with the equilibrium path.

The iterative displacement vector $\delta \mathbf{U}_j$ in this case is split into two parts and can be expressed as (Crisfield, 1997)

$$\delta \mathbf{U}_i = \delta \mathbf{U}_i^F + \Delta\lambda_i \mathbf{U}_i^P \tag{6.3}$$

where $\delta \mathbf{U}_i^F$ is the displacement vector resulted from the out of balance force $\mathbf{F}_{i-1}$ at the end of the last iteration; and $\mathbf{U}_i^P$ is that from the total fixed load vector $\mathbf{P}$. They are expressed as follows:

$$\delta \mathbf{U}_i^F = -\mathbf{K}_i^{-1}\mathbf{F}_{i-1} \tag{6.4}$$

$$\mathbf{U}_i^P = \mathbf{K}_i^{-1}\mathbf{P} \tag{6.5}$$

In the above expressions, the residual force vector $\mathbf{F}_0$ needed at the first iteration is calculated from the last equilibrated state of the structure and the magnitude of its components normally depend on the convergence tolerance δ_f. As $\mathbf{F}_0$ is not accumulated during the incremental analysis, for small enough δ_f, the effects of $\mathbf{F}_0$ can be negligible and $\mathbf{F}_0$ is always assumed to be zero (Alfano and Crisfield, 2003).

During the iteration process, the global stiffness matrix $\mathbf{K}_i$ can be either sequentially updated or kept unchanged throughout the load increment, depending on the employed iterative techniques. However, the residual force $\mathbf{F}_i$ and the load applied on the structure $\lambda_i \mathbf{P}$ must be updated after every iteration to be in accordance with the updated load factor λ_i and updated displacement vector $\mathbf{U}_i$ of the iterative process. Therefore, we have here:

$$\lambda_i = \lambda_{i-1} + \Delta\lambda_i \quad (i = 1, 2, 3, \ldots) \tag{6.6}$$

$$\mathbf{U}_i = \mathbf{U}_{i-1} + \delta \mathbf{U}_i \tag{6.7}$$

$$\mathbf{F}_i = \mathbf{R}_i - \lambda_i \mathbf{P} \tag{6.8}$$

where λ_0 is the load factor at the last converged increment; $\mathbf{U}_0$ is the displacement vector corresponding to λ_0; and $\mathbf{R}_i$ is the internal force vector corresponding to the stresses at the end of the i^{th} iteration.

By substituting (6.2) and (6.3) into (6.1), after some mathematical manipulations we obtain the incremental load factor $\Delta\lambda_i$ as follows:

$$\Delta\lambda_1 = \frac{\Delta L}{\sqrt{\mathbf{U}_1^{P^T}\mathbf{U}_1^P}} \tag{6.9}$$

$$\Delta\lambda_i = \frac{\Delta L^2 - \Delta\mathbf{U}_1^T\left(\Delta\mathbf{U}_{i-1} + \delta\mathbf{U}_i^F\right)}{\Delta\mathbf{U}_1^T\mathbf{U}_i^P} \text{ for } i = 2, 3, 4, \ldots \tag{6.10}$$

In (6.9), the first iterative load factor $\Delta\lambda_1$ always takes positive value as the sign of the loading factor can be automatically changed during the iterative process (May and Duan, 1997; Yang and Proverbs, 2004). In addition, if the stiffness matrix $\mathbf{K}_i$ is kept unchanged within the load increment (for modified Newton-Raphson method), $\mathbf{U}_i^P$ will be constant during the iterations and (6.10) becomes

$$\Delta\lambda_i = \Delta\lambda_1 - \frac{\mathbf{U}_1^{P^T}\left(\Delta\mathbf{U}_{i-1} + \delta\mathbf{U}_i^F\right)}{\mathbf{U}_1^{P^T}\mathbf{U}_1^P} \text{ for } i = 2, 3, 4, \ldots \tag{6.11}$$

6.2.2 Local arc-length methods

In fact, for softening problems, the strains are highly localized in a narrow part of the structure and the arc-length controls using global constraint equations may fail in tracing the equilibrium paths. In such cases, only dominant degrees of freedom of nodes in or around the fracture process zone play an important role in the constraint equations. Therefore, some amendments on the constraint equations have been proposed (de Borst, 1986; Alfano and Crisfield, 2003). Instead of a global norm of displacements which contains all degrees of freedom of the analysed structure, only few degrees of freedom in the failure parts of the structure are taken into account. In particular, the crack mouth opening displacements (CMOD), crack mouth sliding displacements (CMSD) (de Borst, 1986) or relative displacements of the pairs of nodes of interface elements in cohesive crack models (Yang and Proverbs, 2004) can be directly chosen for this purpose. Alternatively, a weighting scheme can also be applied to bring only dominant degrees of freedom to the constraint equations (de Borst, 1986). However, those ways of choosing dominant degrees of freedom for the constraint equation can be readily seen to be problem-dependent and cannot be applied universally. The method therefore cannot preserve its elegance and generality.

Another way of choosing dominant degrees of freedom for the constraint equations has also been devised, which has also been proved to be very successful in the numerical simulations of structures made of softening materials (May and Duan, 1997; Yang and Proverbs, 2004; Yang and Chen, 2004). Following the approach, the dominant degrees of freedom in or surrounding the fracture process zone are picked up and updated sequentially during the numerical analysis. To remove the effect of rigid body movements on the success of the method, further enhancement to the constraint

equation can also be made (May and Duan, 1997), following which only relative displacements of nodal points of elements in the fracture process zone are taken in to account. In the numerical implementation, a selection criterion based on the positiveness of the damage variables and their increments at element Gauss points is used to select dominant elements in the fracture process zone. The degrees of freedom of nodal points of these elements, called dominant degrees of freedom, are then used in the constraint equations. Therefore, the whole process of choosing dominant degrees of freedom and relative nodal displacements can be carried out independently of the problems under consideration and therefore can be employed as a general method for the numerical simulations of softening processes in structural analysis. The advantage of this way of choosing dominant displacements is that very strong snap back behaviour can be captured successfully, even in cases where the incremental control using CMOD or CMSD fails. In other words, the local control using relative displacements does not suffer from the drawback that the CMODs or CMSDs must be always increasing through out the analysis, as a result of using the updated normal constraints (6.1).

The constraint equation (6.1) now takes its local form as

$$\sum_{e}\left[\nabla\left(\Delta\mathbf{U}_1\right)^T\nabla\left(\Delta\mathbf{U}_i\right)\right]=\Delta L^2\ \ (i=1,2,3,\ldots) \tag{6.12}$$

where e is the element considered and the symbol ∇ is used to denote the relative displacement vector of an n-node dominant element:

$$\nabla\left(\mathbf{U}\right)=\left[U_1-U_n\quad U_2-U_1\quad U_3-U_2\quad \ldots\quad U_{n-1}-U_{n-2}\quad U_n-U_{n-1}\right]^T \tag{6.13}$$

The incremental load factors (6.9) and (6.10) turn out to be (May and Duan, 1997)

$$\Delta\lambda_1=\frac{\Delta L}{\sqrt{\sum_{e}\left[\nabla\left(\mathbf{U}_1^P\right)^T\nabla\left(\mathbf{U}_1^P\right)\right]}} \tag{6.14}$$

$$\Delta\lambda_i=\frac{\Delta L^2-\sum_{e}\left\{\nabla\left(\Delta\mathbf{U}_1\right)^T\left[\nabla\left(\Delta\mathbf{U}_{i-1}\right)+\nabla\left(\delta\mathbf{U}_i^F\right)\right]\right\}}{\sum_{e}\left[\nabla\left(\Delta\mathbf{U}_1\right)^T\nabla\left(\mathbf{U}_i^P\right)\right]}\ \text{for}\ i=2,3,4,\ldots \tag{6.15}$$

6.3 Integrating the rate constitutive equations

This is a vital part in the numerical implementation, as it is directly concerned with the stability of the numerical solutions. For that reason, the implicit integration method is adopted in this study, based on the integration scheme proposed by several researchers (de Borst, 1986; Crisfield, 1997). The system of relations (4.25, 4.37, 5.19, 5.20) governing the constitutive behaviour of the model is rewritten here, with nonlocality incorporated in the two damage criteria.

$$\varepsilon_{ij} = \frac{(1+\nu)\sigma_{ij} - \nu\sigma_{kk}\delta_{ij}}{E\left[1 - H\left(\sigma_{kk}^{+}\right)\alpha_d^t\right]\left(1-\alpha_d^c\right)} + \alpha_{ij} \tag{6.16}$$

$$y_p^* = \beta\,\sigma_{kk} + \frac{\sigma'_{ij}\sigma'_{ij}}{2} - k = 0 \tag{6.17}$$

$$y_d^t = \frac{H\left(\sigma_{kk}^{+}\right)}{G(\mathbf{x})}\int_V g\left(\|\mathbf{y}-\mathbf{x}\|\right)\frac{(1+p_t)\sigma_{ij}^{+}\sigma_{ij}^{+} - p_t\left(\sigma_{kk}\right)^{+}\left(\sigma_{ll}\right)^{+}}{2E\left(1-\alpha_d^t\right)^2}dV - F_1^t\left(\alpha_d^t,\alpha_d^c\right) = 0 \tag{6.18}$$

$$y_d^c = \frac{1}{G(\mathbf{x})}\int_V g\left(\|\mathbf{y}-\mathbf{x}\|\right)\frac{(1+p_c)\sigma_{ij}^{-}\sigma_{ij}^{-} - p_c\left(\sigma_{kk}\right)^{-}\left(\sigma_{ll}\right)^{-}}{2E\left(1-\alpha_d^c\right)^2}dV - F_1^c\left(\alpha_d^c\right) = 0 \tag{6.19}$$

In the nonlocal damage criteria above, we have replaced the two different volumes V_t and V_c with V as the volume where both mechanisms of damage take place. This replacement is possible thanks to the introduction of the procedures for the determination of parameters of nonlocal models in chapter 5. In the above system, it is readily seen that the responses of every material point in the structure must satisfy entirely the system of equations (6.16-6.19), which in general can only be solved using numerical methods. The analysis is, however, more complex than in models where the evolution laws of damage are explicitly enforced (Peerlings *et al*., 1998; Peerlings, 1999; Jirasek and Patzak, 2002; Jirasek *et al.*, 2004). Because of the appearance of the spatial integral in equations (6.18 and 6.19), two spatial discretization schemes are necessary for solving the boundary value problem. The first discretization is required for the numerical solution of the partial differential equations. The second is an inner discretization, which deals with the integration of the rate constitutive equations along a loading path. Normally, for models based on local theory, only the outer discretization scheme is needed, as the integration of the rate constitutive equations can be carried out pointwise. In practice, the same discretization scheme can be used, resulting in the

nonlocal evaluation of energy-like quantities in the two damage criteria over the Gauss points used in the finite element discretization.

For the numerical analysis using finite elements, the integrals in (6.18) and (6.19) can be transformed to summations over Gauss points. Denoting by ω the energy-like quantity to be averaged, we can express its corresponding nonlocal counterpart as (see also section 5.1, Chapter 5):

$$\tilde{\omega}(\mathbf{x}) = \frac{1}{G(\mathbf{x})}\int_V g(\|\mathbf{y}-\mathbf{x}\|)\omega(\mathbf{y})dV \tag{6.20}$$

where

$$G(\mathbf{x}) = \int_V g(\|\mathbf{y}-\mathbf{x}\|)dV \tag{6.21}$$

The discretization using the finite element method leads to

$$\tilde{\omega}(\mathbf{x})\sum_{e=1}^{n}\int_{V_e} g(\|\mathbf{y}-\mathbf{x}\|)dV = \sum_{e=1}^{n}\int_{V_e} g(\|\mathbf{y}-\mathbf{x}\|)\omega(\mathbf{y})dV \tag{6.22}$$

in which e denotes the element index and n the total number of elements inside the interaction volume bounded by a sphere at centre $\mathbf{x}$ and of radius R; V_e is the corresponding volume of the finite element e. Numerical integration of both sides of the above equation results in

$$\tilde{\omega}(\mathbf{x})\sum_{e=1}^{n}\sum_{i=1}^{m_e} w_i^e\, g(\|\mathbf{y}_i^e-\mathbf{x}\|)\det J_i^e = \sum_{e=1}^{n}\sum_{i=1}^{m_e} w_i^e\, g(\|\mathbf{y}_i^e-\mathbf{x}\|)\det J_i^e\,\omega(\mathbf{y}_i^e) \tag{6.23}$$

where i is the i'th Gauss point of element e, and m_e is the number of Gauss points of this element inside the interaction volume; w_i^e and J_i^e are respectively the weight and Jacobian matrix at Gauss point i of element e. The expression of the nonlocal energy-like quantities in the damage criteria can now be rewritten in the following form

$$\tilde{\omega}(\mathbf{x}) = \frac{\sum_{e=1}^{n}\sum_{i=1}^{m_e} w_i^e\, g(\|\mathbf{y}_i^e-\mathbf{x}\|)\det J_i^e\,\omega(\mathbf{y}_i^e)}{\sum_{e=1}^{n}\sum_{i=1}^{m_e} w_i^e\, g(\|\mathbf{y}_i^e-\mathbf{x}\|)\det J_i^e} = \sum_{\gamma}^{n_\gamma} w_\gamma\omega_\gamma \tag{6.24}$$

where n_γ is the total number of Gauss points inside the interaction volume at point $\mathbf{x}$; w_γ and ω_γ are respectively the weight and energy-like quantity associated with the i'th Gauss point of element e, in which w_γ is defined by

$$w_\gamma = \frac{w_i^e g\left(\left\|\mathbf{y}_i^e - \mathbf{x}\right\|\right)\det J_i^e}{\sum_{e=1}^{n}\sum_{i=1}^{m_e} w_i^e g\left(\left\|\mathbf{y}_i^e - \mathbf{x}\right\|\right)\det J_i^e} \tag{6.25}$$

As mentioned in the introduction of this Chapter, an implicit Euler integration scheme is adopted for the integration of the rate constitutive equations. However, due to the presence of the spatial integrals in the damage criteria, the stress update procedure cannot be carried out point-wise as normally done in local models. Nonlocality in this case turns the pointwise-defined stress-strain constitutive equations to a system of nonlocal coupled equations, relating the stresses, strains and internal variables at several integration points in the failure region. This coupling makes the stress update routine more complicated, requiring considerable effort in the formulation and implementation as well as time cost in the numerical computation.

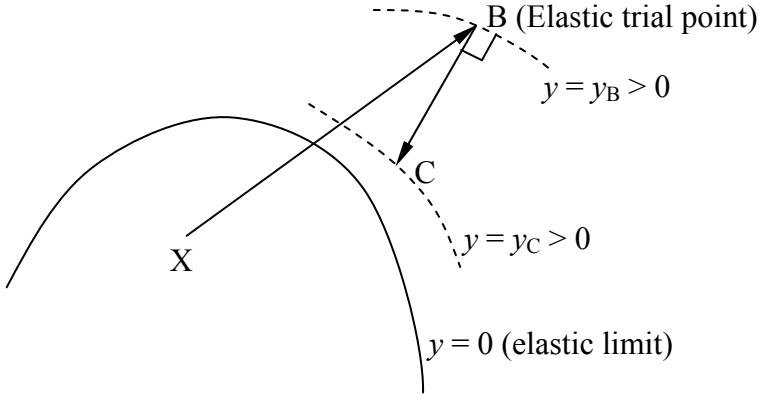

Figure 6.2: Pictorial presentation of the integration scheme

(after de Borst, 1986; and Crisfield, 1997)

As the constitutive relationships in this case contain coupled equations relating the stress and strain increments at several integration points, finding the intersection points between the stress path and the yield/damage surface is almost impossible. Instead, an elastic predictor – damage-plastic corrector integrating scheme is adopted here for the integration of the rate equations. This is based on the algorithm proposed by Crisfield (1997) and can be considered as a form of the backward Euler integration scheme (Crisfield, 1997). This algorithm makes use of the normal at the elastic trial point and hence avoids the necessity of computing the intersection between the elastically-assumed incremental stress vector (using secant elastic-damage behaviour) and the yield/damage surfaces. Furthermore, the method enforces the satisfaction of the yield

and damage criteria (6.17-6.19) at any stage of the loading process, thus removing the inaccuracies encountered when the consistency conditions of the yield and damage functions are used (de Borst, 1986).

At the starting point, the system of relations governing the constitutive behaviour of the material are rewritten in rate form by taking the first-order Taylor expansion of the yield and damage functions about the elastic trial point B (figure 6.2, with y representing either the yield or compressive/tensile damage surface). In this coupling case, it is assumed here that yielding and both mechanisms of damage take place at the same instant. Therefore, treatment for sharp corner (point X in figure 4.8, Chapter 4) on the composite damage surface is automatically accounted for. By dropping out appropriate terms we can straightforwardly work out simpler situations, in which only one or two failure mechanisms are activated. From (6.16 – 6.19), a system of rate equations governing the constitutive behaviour of the model can be written:

$$\begin{aligned} d\varepsilon_{ij} &= \frac{(1+\nu)d\sigma_{ij} - \nu\, d\sigma_{kk}\delta_{ij}}{E\left[1-H\left(\sigma_{kk}^{+}\right)\alpha_d^t\right]\left(1-\alpha_d^c\right)} + d\alpha_{ij} \\ &+ \frac{(1+\nu)\sigma_{ij} - \nu\sigma_{kk}\delta_{ij}}{E\left[1-H\left(\sigma_{kk}^{+}\right)\alpha_d^t\right]^2\left(1-\alpha_d^c\right)} H\left(\sigma_{kk}^{+}\right)d\alpha_d^t + \frac{(1+\nu)\sigma_{ij} - \nu\sigma_{kk}\delta_{ij}}{E\left[1-H\left(\sigma_{kk}^{+}\right)\alpha_d^t\right]\left(1-\alpha_d^c\right)^2} d\alpha_d^c \end{aligned} \tag{6.26}$$

$$y_p^* = y_p^*\Big|_B + \frac{\partial y_p^*}{\partial \sigma_{ij}} d\sigma_{ij} + \frac{\partial y_p^*}{\partial \alpha_d^t} d\alpha_d^t + \frac{\partial y_p^*}{\partial \alpha_d^c} d\alpha_d^c + \frac{\partial y_p^*}{\partial \varepsilon_p^t} d\varepsilon_p^t + \frac{\partial y_p^*}{\partial \varepsilon_p^c} d\varepsilon_p^c \tag{6.27}$$

$$y_d^t\Big|_C = y_d^t\Big|_B + H\left(\sigma_{kk}^{+}\right)\sum_\gamma w_\gamma \left[\begin{array}{l} \dfrac{(1+p_t)\sigma_{ij}^{+}d\sigma_{ij} - p_t\left(\sigma_{kk}\right)^{+}\delta_{ij}d\sigma_{ij}}{E\left(1-\alpha_d^t\right)^2} + \\ \dfrac{(1+p_t)\sigma_{ij}^{+}\sigma_{ij}^{+} - p_t\left(\sigma_{kk}\right)^{+}\left(\sigma_{ll}\right)^{+}}{E\left(1-\alpha_d^t\right)^3} d\alpha_d^t \end{array}\right] - \frac{\partial F_1^t}{\partial \alpha_d^t} d\alpha_d^t - \frac{\partial F_1^t}{\partial \alpha_d^c} d\alpha_d^c = 0 \tag{6.28}$$

$$y_d^c\Big|_C = y_d^c\Big|_B + \sum_\gamma w_\gamma \left[\begin{array}{l} \dfrac{(1+p_c)\sigma_{ij}^{-}d\sigma_{ij} - p_c\left(\sigma_{kk}\right)^{-}\delta_{ij}d\sigma_{ij}}{E\left(1-\alpha_d^c\right)^2} + \\ \dfrac{(1+p_c)\sigma_{ij}^{-}\sigma_{ij}^{-} - p_c\left(\sigma_{kk}\right)^{-}\left(\sigma_{ll}\right)^{-}}{E\left(1-\alpha_d^c\right)^3} d\alpha_d^c \end{array}\right] - \frac{\partial F_1^c}{\partial \alpha_d^c} d\alpha_d^c = 0 \tag{6.29}$$

The spatial integrals in the two damage criteria (6.28 and 6.29) have been replaced with the summations over integration points. The terms $y_p^*\Big|_B$, $y_d^t\Big|_B$ and $y_d^c\Big|_B$ in (6.27),

(6.28) and (6.29) are the values of the loading functions at the elastic trial point B. Furthermore, it is implied here that all the derivatives and terms in equations (6.27), (6.28) and (6.29) are evaluated at this stress point. Due to the appearance of the summations in (6.28) and (6.29), it should also be noted that B denotes several elastic trial points, from which y_d^t and y_d^c are evaluated, rather than a single point in the original scheme.

As mentioned above, the stresses at the elastic trial point B (figure 6.2) are obtained by adding elastically-assumed incremental stresses to the stresses at point X. Our aim is to compute the stress increments $\Delta\sigma_{ij}\big|_{BC}$, which is needed in going from B to C (figure 6.2), from the system (6.26) – (6.29). At first, from (6.27), using the flow rule

$$d\alpha_{ij} = \lambda_p \frac{\partial y_p}{\partial \chi_{ij}} \tag{6.30}$$

and two constraints C_1 and C_2 on the accumulated plastic strains (4.21 and 4.22 in chapter 4), the plastic strain rate $d\alpha_{ij}$ is obtained:

$$d\alpha_{ij} = \lambda_p \frac{\partial y_p}{\partial \chi_{ij}} = -\left[\frac{y_p^*\big|_B + \dfrac{\partial y_p^*}{\partial \sigma_{kl}} d\sigma_{kl} + \dfrac{\partial y_p^*}{\partial \alpha_d^t} d\alpha_d^t + \dfrac{\partial y_p^*}{\partial \alpha_d^c} d\alpha_d^c}{c\sqrt{\dfrac{\partial y_p}{\partial \chi_{mn}} \dfrac{\partial y_p}{\partial \chi_{mn}}} \left(F_4^t(\sigma_{kk}) \dfrac{\partial y_p^*}{\partial \varepsilon_p^t} + F_4^c(\sigma_{kk}) \dfrac{\partial y_p^*}{\partial \varepsilon_p^c} \right)} \right] \frac{\partial y_p}{\partial \chi_{ij}} \tag{6.31}$$

Secondly, back substituting the above plastic strain increment into (6.26), some mathematical manipulations lead to the relationship between the stress, strain and internal variables, written in incremental form as follows:

$$d\sigma_{mn} = \left\{ \begin{array}{l} d\varepsilon_{ij} + \dfrac{\left(y_p^*\big|_B + \dfrac{\partial y_p^*}{\partial \alpha_d^t} d\alpha_d^t + \dfrac{\partial y_p^*}{\partial \alpha_d^c} d\alpha_d^c \right) \dfrac{\partial y_p}{\partial \chi_{ij}}}{c\sqrt{\dfrac{\partial y_p}{\partial \chi_{kl}} \dfrac{\partial y_p}{\partial \chi_{kl}}} \left(F_4^t \dfrac{\partial y_p^*}{\partial \varepsilon_p^t} + F_4^c \dfrac{\partial y_p^*}{\partial \varepsilon_p^c} \right)} \\ - \dfrac{\left[(1+\nu)\sigma_{ij} - \nu\sigma_{kk}\delta_{ij} \right] H\left(\sigma_{ll}^+\right) d\alpha_d^t}{E\left[1 - H\left(\sigma_{kk}^+\right)\alpha_d^t\right]^2 \left(1 - \alpha_d^c\right)} - \dfrac{\left[(1+\nu)\sigma_{ij} - \nu\sigma_{kk}\delta_{ij} \right] d\alpha_d^c}{E\left[1 - H\left(\sigma_{kk}^+\right)\alpha_d^t\right] \left(1 - \alpha_d^c\right)^2} \end{array} \right\} \left[D_{ijmn}^{st} \right]^{-1} \tag{6.32}$$

where D_{ijmn}^{st} is the constitutive matrix which is tangent with respect to plasticity and secant with respect to damage (see section 6.4 for details):

$$D^{st}_{ijmn} = \frac{D_{ijmn}}{\left[1 - H\left(\sigma^{+}_{kk}\right)\alpha^{t}_{d}\right]\left(1 - \alpha^{c}_{d}\right)} - \frac{\dfrac{\partial y_p}{\partial \chi_{ij}} \dfrac{\partial y^{*}_{p}}{\partial \sigma_{mn}}}{c\sqrt{\dfrac{\partial y_p}{\partial \chi_{kl}} \dfrac{\partial y_p}{\partial \chi_{kl}}}\left(F^{t}_{4} \dfrac{\partial y^{*}_{p}}{\partial \varepsilon^{t}_{p}} + F^{c}_{4} \dfrac{\partial y^{*}_{p}}{\partial \varepsilon^{c}_{p}}\right)} \tag{6.33}$$

D_{ijmn} in the above expression is the elastic compliance matrix (see section 3.3.2). Finally, substituting (6.32) into (6.28) and (6.29), we obtain a system of linear equations in $d\alpha^{t}_{d}$ and $d\alpha^{c}_{d}$. This system is written for all integration points in the fracture process zone, each pair (tension and compression) of which has the following form:

$$y^{t}_{d} = H\left(\sigma^{+}_{pp}\right)\sum_{\gamma} w_{\gamma} Q_t - \frac{\partial F^{t}_{1}}{\partial \alpha^{t}_{d}} d\alpha^{t}_{d} - \frac{\partial F^{t}_{1}}{\partial \alpha^{c}_{d}} d\alpha^{c}_{d} + y^{t}_{d}\Big|_{B} = 0 \tag{6.34}$$

$$y^{c}_{d} = \sum_{\gamma} w_{\gamma} Q_c - \frac{\partial F^{c}_{1}}{\partial \alpha^{c}_{d}} d\alpha^{c}_{d} + y^{c}_{d}\Big|_{B} = 0 \tag{6.35}$$

where Q_t and Q_c are defined as follows:

$$Q_t = \left[\begin{array}{l}
\dfrac{\left(1+p_t\right)\sigma^{+}_{kl} - p_t\left(\sigma_{qq}\right)^{+}\delta_{kl}}{E\left(1-\alpha^{t}_{d}\right)^{2}}\left[D^{st}_{ijkl}\right]^{-1} \dfrac{\left(y^{*}_{p}\Big|_{B} + \dfrac{\partial y^{*}_{p}}{\partial \alpha^{t}_{d}} d\alpha^{t}_{d} + \dfrac{\partial y^{*}_{p}}{\partial \alpha^{c}_{d}} d\alpha^{c}_{d}\right)\dfrac{\partial y_p}{\partial \chi_{ij}}}{c\sqrt{\dfrac{\partial y_p}{\partial \chi_{mn}} \dfrac{\partial y_p}{\partial \chi_{mn}}}\left(F^{t}_{4} \dfrac{\partial y^{*}_{p}}{\partial \varepsilon^{t}_{p}} + F^{c}_{4} \dfrac{\partial y^{*}_{p}}{\partial \varepsilon^{c}_{p}}\right)} \\
-\dfrac{\left(1+p_t\right)\sigma^{+}_{kl} - p_t\left(\sigma_{qq}\right)^{+}\delta_{kl}}{E\left(1-\alpha^{t}_{d}\right)^{2}}\left[D^{st}_{ijkl}\right]^{-1} \dfrac{\left[(1+\nu)\sigma_{ij} - \nu\sigma_{qq}\delta_{ij}\right]H\left(\sigma^{+}_{mm}\right)d\alpha^{t}_{d}}{E\left[1 - H\left(\sigma^{+}_{nn}\right)\alpha^{t}_{d}\right]^{2}\left(1-\alpha^{c}_{d}\right)} \\
-\dfrac{\left(1+p_t\right)\sigma^{+}_{kl} - p_t\left(\sigma_{qq}\right)^{+}\delta_{kl}}{E\left(1-\alpha^{t}_{d}\right)^{2}}\left[D^{st}_{ijkl}\right]^{-1} \dfrac{\left[(1+\nu)\sigma_{ij} - \nu\sigma_{qq}\delta_{ij}\right]d\alpha^{c}_{d}}{E\left[1 - H\left(\sigma^{+}_{nn}\right)\alpha^{t}_{d}\right]\left(1-\alpha^{c}_{d}\right)^{2}} \\
+\dfrac{\left(1+p_t\right)\sigma^{+}_{ij}\sigma^{+}_{ij} - p_t\left(\sigma_{kk}\right)^{+}\left(\sigma_{ll}\right)^{+}}{E\left(1-\alpha^{t}_{d}\right)^{3}} d\alpha^{t}_{d}
\end{array}\right] \tag{6.36}$$

and

$$Q_c = \begin{bmatrix} \dfrac{(1+p_c)\bar{\sigma}_{kl} - p_c\left(\sigma_{pp}\right)^{-}\delta_{kl}}{E\left(1-\alpha_d^c\right)^2}\left[D_{ijkl}^{st}\right]^{-1}\dfrac{\left(y_p^*\big|_B + \dfrac{\partial y_p^*}{\partial \alpha_d^t}d\alpha_d^t + \dfrac{\partial y_p^*}{\partial \alpha_d^c}d\alpha_d^c\right)\dfrac{\partial y_p}{\partial \chi_{ij}}}{c\sqrt{\dfrac{\partial y_p}{\partial \chi_{mn}}\dfrac{\partial y_p}{\partial \chi_{mn}}}\left(F_4^t\dfrac{\partial y_p^*}{\partial \varepsilon_p^t} + F_4^c\dfrac{\partial y_p^*}{\partial \varepsilon_p^c}\right)} \\ -\dfrac{(1+p_c)\bar{\sigma}_{kl} - p_c\left(\sigma_{pp}\right)^{-}\delta_{kl}}{E\left(1-\alpha_d^c\right)^2}\left[D_{ijkl}^{st}\right]^{-1}\dfrac{\left[(1+\nu)\sigma_{ij} - \nu\sigma_{pp}\delta_{ij}\right]H\left(\sigma_{mm}^{+}\right)d\alpha_d^t}{E\left[1-H\left(\sigma_{nn}^{+}\right)\alpha_d^t\right]^2\left(1-\alpha_d^c\right)} \\ -\dfrac{(1+p_c)\bar{\sigma}_{kl} - p_c\left(\sigma_{pp}\right)^{-}\delta_{kl}}{E\left(1-\alpha_d^c\right)^2}\left[D_{ijkl}^{st}\right]^{-1}\dfrac{\left[(1+\nu)\sigma_{ij} - \nu\sigma_{pp}\delta_{ij}\right]d\alpha_d^c}{E\left[1-H\left(\sigma_{nn}^{+}\right)\alpha_d^t\right]\left(1-\alpha_d^c\right)^2} \\ +\dfrac{(1+p_c)\bar{\sigma}_{ij}\bar{\sigma}_{ij} - p_c\left(\sigma_{kk}\right)^{-}\left(\sigma_{ll}\right)^{-}}{E\left(1-\alpha_d^c\right)^3}d\alpha_d^c \end{bmatrix} \tag{6.37}$$

As can be seen, the strain increments disappear in (6.36) and (6.37) when substituting (6.32) into those equations, as they have been applied in moving from point X to the elastic trial point B (Crisfield, 1997). Solving the above system of equations will give the damage increments at all points in the damaged zone of the structure. Back substituting the damage increments into (6.32), noting that the strain increments have been applied in the predictor step (from X to B) and now must be removed from that expression, we obtain the stress increment $\Delta\sigma_{ij}\big|_{BC}$ in going from B to C. Finally, the stress at point C (see figure 6.2) is updated using (Crisfield, 1997)

$$\sigma_{ij}\big|_C = \sigma_{ij}\big|_B + \Delta\sigma_{ij}\big|_{BC} \tag{6.38}$$

in which $\Delta\sigma_{ij}\big|_{BC}$ is computed by

$$\Delta\sigma_{mn}\big|_{BC} = \left\{ \begin{array}{l} \dfrac{\left(y_p^*\big|_B + \dfrac{\partial y_p^*}{\partial \alpha_d^t}\Delta\alpha_d^t + \dfrac{\partial y_p^*}{\partial \alpha_d^c}\Delta\alpha_d^c\right)\dfrac{\partial y_p}{\partial \chi_{ij}}}{c\sqrt{\dfrac{\partial y_p}{\partial \chi_{kl}}\dfrac{\partial y_p}{\partial \chi_{kl}}}\left(F_4^t\dfrac{\partial y_p^*}{\partial \varepsilon_p^t} + F_4^c\dfrac{\partial y_p^*}{\partial \varepsilon_p^c}\right)} - \\ \dfrac{\left[(1+\nu)\sigma_{ij} - \nu\sigma_{kk}\delta_{ij}\right]H\left(\sigma_{ll}^{+}\right)\Delta\alpha_d^t}{E\left[1-H\left(\sigma_{kk}^{+}\right)\alpha_d^t\right]^2\left(1-\alpha_d^c\right)} - \dfrac{\left[(1+\nu)\sigma_{ij} - \nu\sigma_{kk}\delta_{ij}\right]\Delta\alpha_d^c}{E\left[1-H\left(\sigma_{kk}^{+}\right)\alpha_d^t\right]\left(1-\alpha_d^c\right)^2} \end{array} \right\}\left[D_{ijmn}^{st}\right]^{-1} \tag{6.39}$$

In the above expression, all damage increments have been computed by solving the systems (6.34) and (6.35), and all derivatives are evaluated at the elastic trial point B. Normally, due to the linearization, the updated stress points do not lie on the yield/damage surfaces (they can be either above or below these surfaces) and relevant

techniques should be applied to return them to the loading surfaces. Repetition of the same process but with point B replaced with C, noting that there are no elastic stress increments in the subsequent steps, would be an appropriate and simple way to bring the stresses back to the loading surfaces. This simple but rather efficient stress returning algorithm is advocated here due to the complexity of the system of rate constitutive equations (6.26–6.29). Alternatively, further enhancement to the exactness of the integration scheme can also be obtained through the combination of sub-incrementation and the repetition of the above predictor-corrector processes, all of which have been implemented in the finite element code OXFEM used in this study. Furthermore, to reduce the errors in updating the stresses, in this study the integration scheme above will be carried out based on the incremental instead of iterative strains [see Crisfield (1997) for details].

6.4 Tangent and secant stiffness matrix

In finite element analysis using the Newton-Raphson iterative techniques, the employment of a consistent tangent stiffness matrix, which relates the forces and displacements at nodal points of a finite element, is an efficient way to achieve true quadratic convergence, although sometimes at high computational cost. In the numerical analysis with local constitutive models, this matrix can readily and explicitly be computed from the tangent moduli tensor C^t_{ijkl} (constitutive tensor relating the incremental stresses and incremental strains, see chapter 3) at integration points. In the case of nonlocal models, it is not always possible to explicitly derive the nonlocal tangent stiffness matrix as there is no local incremental stress-strain relationship and the moduli tensor C^t_{ijkl} can no longer be defined (Comi, 2001).

Jirásek and Patzák (2002) proposed a very sound procedure for the formulation of consistent tangent stiffness matrix for nonlocal models. However, they only illustrated the proposed procedure in a simple case with a nonlocal isotropic damage model and explicitly defined damage evolution rule. In practice it is difficult to apply that procedure to the general nonlocal damage-coupled-with-plasticity model (represented by equations 6.16–6.19) to derive the explicit nonlocal tangent stiffness matrix, especially in case the damage evolutions are governed by a system of differential equations (6.26–6.29) (see also Addessi *et al.*, 2002). Due to the complexity of the nonlocal model in this study, a nonlocal tangent stiffness matrix is difficult, even

impossible to be derived explicitly. Although numerical techniques using the above-proposed stress update scheme in combination with numerical perturbation techniques can also be employed as an alternative way to overcome the difficulty, the expected high computational cost in the numerical derivation of the tangent stiffness matrix prevents its wide use in practice. Therefore, use of a nonlocal tangent stiffness matrix is not pursued in this study.

Although there is no local stress-strain relationship in the nonlocal damage-plasticity model, the tangent moduli tensor of an equivalent local model can be employed for the calculation of the local tangent stiffness matrix in the numerical analysis using the nonlocal models developed in this study. The derivation of this tangent moduli tensor is similar to that for the stress-based damage-plasticity models in chapter 3. Even so, the expression of this local tensor is still too cumbersome (see that of stress-based model in chapter 3 as a simple example) to be straightforwardly implemented in the computer code OXFEM. In this study, the stiffness matrix used in the numerical analysis is computed based on the local constitutive moduli tensor, which is tangent with respect to plasticity and secant with respect to damage (see also the stress-based model in chapter 3). Although not as efficient as use of tangent stiffness matrix, the employment of the adopted stiffness matrix is preferred in this study due to its simplicity of implementation.

The derivation of this kind of constitutive moduli tensor is quite straightforward and is similar to that in plasticity models, with the damage indicators being kept frozen: $\dot{\alpha}_d^t = \dot{\alpha}_d^c = 0$. In this case, from the stress-strain relationship (6.16) we have

$$\dot{\varepsilon}_{ij} = \frac{D_{ijkl}\dot{\sigma}_{kl}}{\left[1 - H\left(\sigma_{kk}^{+}\right)\alpha_d^t\right]\left(1 - \alpha_d^c\right)} + \dot{\alpha}_{ij} \tag{6.40}$$

The consistency condition of the yield function without damage increments reads

$$\dot{y}_p^* = \frac{\partial y_p^*}{\partial \sigma_{ij}}\dot{\sigma}_{ij} + \frac{\partial y_p^*}{\partial \varepsilon_p^t}\dot{\varepsilon}_p^t + \frac{\partial y_p^*}{\partial \varepsilon_p^c}\dot{\varepsilon}_p^c = 0 \tag{6.41}$$

from which the plastic strain increment can be obtained

$$\dot{\alpha}_{ij} = \lambda_p \frac{\partial y_p}{\partial \chi_{ij}} = -\frac{\dfrac{\partial y_p}{\partial \chi_{ij}} \dfrac{\partial y_p^*}{\partial \sigma_{mn}} \dot{\sigma}_{mn}}{c\sqrt{\dfrac{\partial y_p}{\partial \chi_{kl}} \dfrac{\partial y_p}{\partial \chi_{kl}}} \left(F_4^t(\sigma_{pp}) \dfrac{\partial y_p^*}{\partial \varepsilon_p^t} + F_4^c(\sigma_{pp}) \dfrac{\partial y_p^*}{\partial \varepsilon_p^c} \right)} \tag{6.42}$$

From (6.40) and (6.42) one gets

$$\dot{\sigma}_{mn} = \left[D_{ijmn}^{st} \right]^{-1} \dot{\varepsilon}_{ij} \tag{6.43}$$

with D_{ijmn}^{st} being the compliance moduli tensor which is tangent with respect to plasticity and secant with respect to damage:

$$D_{ijmn}^{st} = \frac{D_{ijmn}}{\left[1 - H\left(\sigma_{kk}^{+}\right)\alpha_d^t\right]\left(1 - \alpha_d^c\right)} - \frac{\dfrac{\partial y_p}{\partial \chi_{ij}} \dfrac{\partial y_p^*}{\partial \sigma_{mn}}}{c\sqrt{\dfrac{\partial y_p}{\partial \chi_{kl}} \dfrac{\partial y_p}{\partial \chi_{kl}}} \left(F_4^t \dfrac{\partial y_p^*}{\partial \varepsilon_p^t} + F_4^c \dfrac{\partial y_p^*}{\partial \varepsilon_p^c} \right)} \tag{6.44}$$

6.5 Summary and discussion

The numerical implementation of the nonlocal constitutive model (represented by equations 6.16 – 6.19) proposed in chapters 4 and 5 has been presented in this chapter. A local arc-length control for the solution of nonlinear algebraic equations in finite element analysis and an implicit integration scheme for the rate constitutive equations have been adopted and detailed. For simplicity in the implementation, it has been proposed that the local stiffness matrix based on the constitutive moduli tensor which is secant with respect to damage and tangent with respect to plasticity would be used in the numerical solution.

The combination of local arc-length control and implicit integration scheme is expected to assure the stability of the incremental analysis based on the finite element method. Limit points and turning points on the equilibrium paths (figure 6.1), as results of the strain softening and localization, can now be overcome with ease using the local arc-length control in combination with relative nodal displacements, all of which will be numerically illustrated in the next chapter. Nevertheless, the convergence rate during iterative process within a load increment is expected to be very slow due to the use of the local stiffness matrix adopted and presented in section 6.4 above. Unfortunately, due

to time constraints, remedies for this drawback cannot be carried out at the present. Further research work is needed to improve the convergence rate.

Chapter 7: Numerical Examples

7.1 Introduction

This chapter is dedicated to the numerical validation of the model (represented by equations 4.25, 4.37, 5.19, and 5.20) proposed in the previous chapters. Analysis of real structures will be carried out to show the potential features and weaknesses of the proposed model. These tests range from simple to complex loading cases and hence require appropriate choice of constitutive models. The most complicated model in this study is the one with unilaterial damage coupled with plasticity (represented by equations 4.25, 4.37, 5.19, and 5.20), which can be used in most cases. However, this is not always necessary, as simple models (e.g. tensile damage model using equations 4.25 and 5.19; or tensile-compressive damage model using equations 4.25, 5.19 and 5.20; see table 7.1 for details) can also be employed in relevant cases, reducing the complication in the choice of model parameters while still being able to produce acceptable results.

The structural tests used here comprise those exhibiting important features in the behaviour of quasi-brittle materials in general and concrete materials in particular, which have been presented in chapter 2. They can be classified into groups of tension tests, bending tests, shear tests and compression-related tests, under monotonic or cyclic loading. The material models used can be pure tensile damage or tensile-compressive damage with plastic deformation being accounted for whenever the experimental cyclic loading data are available. A summary of the choice and determination of parameters corresponding to a variation of nonlocal models is provided at the end of this Chapter, with cross-references to procedures for the parameter identification in Chapters 4 and 5.

All the numerical tests in this section are carried out using the arc-length control for the incremental analysis and Newton-Raphson method for the iterative technique. The convergence tolerance parameter is 10^{-4} for the norm of the out of balance force vector in the Newton-Raphson iterative process. The same tolerance value is also used in the stress update routine to gauge the errors occurring in returning the stresses to the loading surfaces. In addition, automatic increments (see May and Duan, 1997; Crisfield, 1997, Chap. 9, Vol. 1), controlled by the number of iterations required for each load

increment, are used throughout the examples. A loading scheme consisting of three load stages (1st: fully elastic behaviour, 2nd and 3rd: peak and post-peak stages) is used, in which the controlling minimum and maximum numbers of iterations for the last two stages are normally 12-18 and 18-27, respectively.

To achieve convergence in severe cases with snap-back observed in the equilibrium paths, the constraint equation of the arc-length control is based on relative nodal displacements in the fracture process zone (FPZ), though crack mouth opening displacements (CMODs) or crack mouth sliding displacements (CMSDs) can also be used without any difficulty. The local stiffness matrix, which is tangent with respect to plasticity and secant with respect to damage (local secant stiffness matrix is used in case the dissipation is totally due to damage), will be used throughout the numerical examples in this chapter. For the adopted Newton-Raphson iterative method, the stiffness matrix is only recomputed at the beginning of the load increment and kept unchanged throughout the iterations. Furthermore, as mentioned in the previous chapter on the numerical implementation, the stress update here will be based on the incremental instead of iterative strains. This was strongly recommended by Crisfield (1997) for several numerical reasons, all of which can be found in the relevant books (Crisfield, 1997, Vol. 1 and 2).

7.2 Tensile test

7.2.1 Double-edge notched specimen under tension

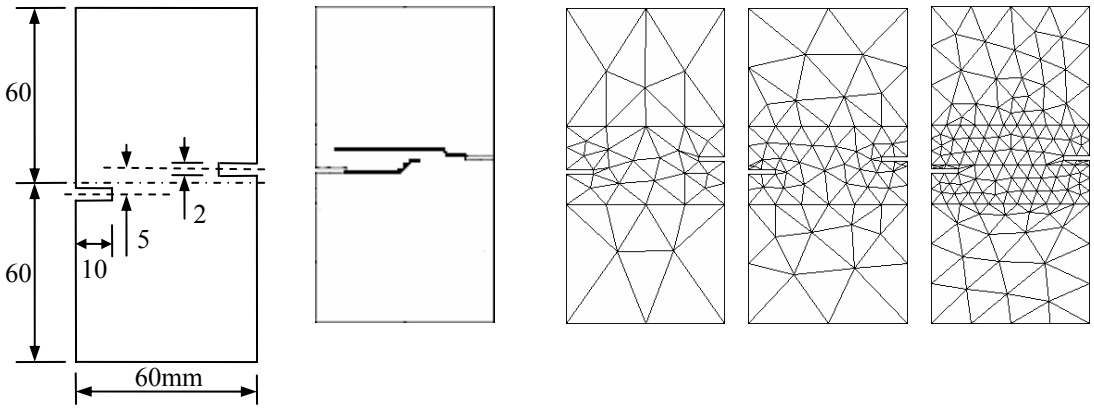

(a) (b) (c)

Figure 7.1: Double edge notched specimen (10mm thick) – geometry (a), experimental crack pattern (b) (Shi *et al.*, 2000) and FE meshes (c)

In this numerical example, the numerical simulations of a double edge notched specimen under tension (Shi *et al*., 2000) are presented. In the numerical models, the specimen is fixed in both directions at the bottom edge, and in horizontal direction at the top edge. The numerical analyses were carried out using three meshes of 6-node triangular finite elements, with prescribed vertical displacements on the top edge of the specimen.

The constitutive model used in this example is that presented in chapter 4, with only tensile damage mechanism being activated. In fact, it is also satisfactory to use an isotropic damage model with a single scalar damage variable for the analysis, as has been done in Nguyen and Houlsby (2004). The material properties used are: Young's modulus $E = 24\text{GPa}$, Possion's ratio $\nu = 0.2$, tensile strength $f_t = 2.0$ or 2.86MPa, fracture energy $G_f = 0.059\text{N/mm}$, nonlocal interaction radius $R = 1.5d_{\max} = 12\text{mm}$.

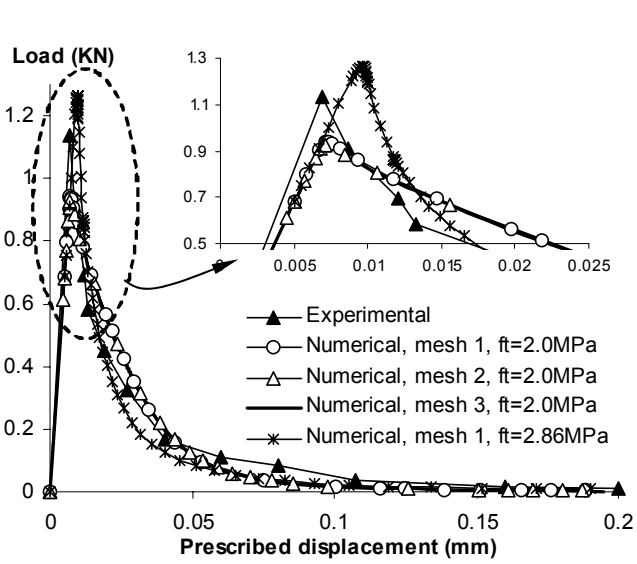

(a) Load-displacement curves

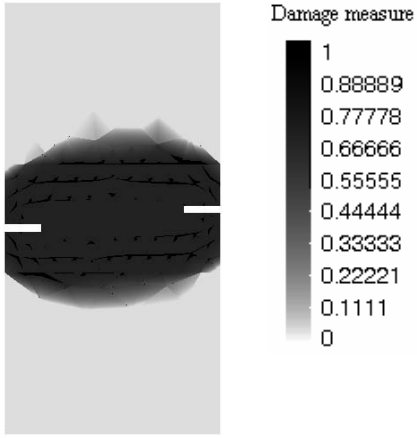

(b) Damage measure (mesh 3, prescribed displacement of 0.19mm)

Figure 7.2: Double edge notched specimen - Numerical results

There was no exact value for the ultimate tensile stress, and the tensile strengths above were obtained from two sources (Alfaiate *et al.*, 2002; and Shi, 2004), in which the higher one was in fact denoted as the peak stress in the report on the test (Shi, 2004). They are used in the numerical simulation here. The ratio $k = w_t / R = 2.02$ (1.98 for $f_t' = 2.86\text{MPa}$) was calculated using $t = g_{fnl} / g_F = 0.25$ and following the procedures in Chapter 5. The following model parameters were obtained based on the system (4.80-

4.81) in Chapter 4: $E_{pt} = 3090\text{MPa}$ and $n_t = 0.26$ ($E_{pt} = 9081\text{MPa}$ and $n_t = 0.36$ for $f_t' = 2.86\text{MPa}$).

The numerical results are depicted in figure (7.2), showing the agreement in the load-displacement curves obtained from different finite element meshes, thus proving the lack of mesh dependence of the proposed model. The experimental peak load (1.13KN) in the figure can be seen to be bounded by its two numerical counterparts (0.94KN and 1.26KN) corresponding to two used values of the tensile strength. In addition, the overall shape of the numerical load-displacement curves is consistent with the experimental one. The failure of the specimen can be seen in figure (7.2b). No clear macro crack can be observed, as attention here is paid to the structural response of the specimen under loading, rather than the crack propagation and interaction. A finer mesh and smaller nonlocal interaction radius can be used, of course at much higher computational cost, if the observation of crack propagation is interested (see figure 7.3).

Figure 7.3: Crack pattern obtained with very fine FE mesh

(5541 nodes, 2746 six-node triangular elements, nonlocal radius $R = 1mm$)

The numerical crack pattern in figure (7.3), however, does not agree well with its experimental counterpart (figure 7.1b, which was in fact redrawn based on the experimental crack pattern in the paper by Shi *et al.* (2000)), due to the use of an isotropic damage model and not-small-enough nonlocal radius. These issues will be discussed further in section (7.4.2). In figures (7.2b), due to the inadequacy of the procedures (of the commercial pre- and post-processor package GiD) used to extrapolate damage indicators from integration points to nodal points, some part of the damage zone in the figure may have damage indicators exceeding 1.0 or below 0.0,

which is not in fact allowed at Gauss points. Those parts are simply blackened in the figure.

7.3 Bending tests

7.3.1 Three-point bending test – notched beam

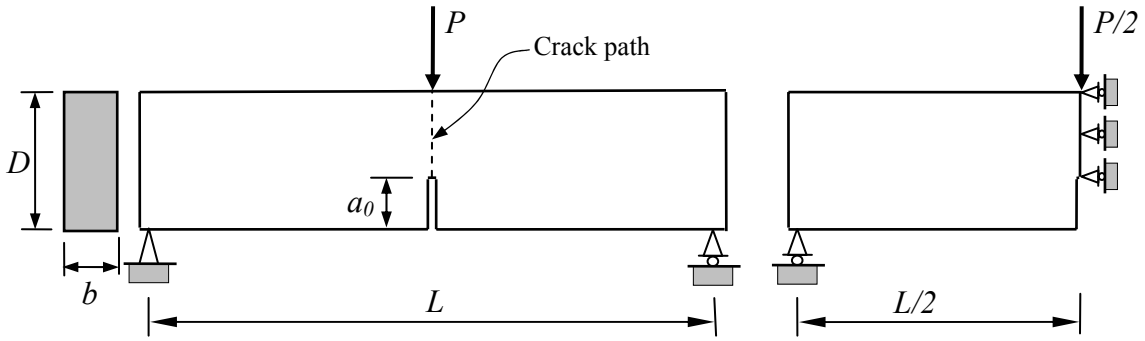

Figure 7.4: Geometrical data and half beam model used in the numerical analysis

The numerical simulations here are carried out on a notched beam in a three point bending test, aiming at investigating mode I fracture and crack propagation. The geometrical data and material properties are taken from the experimental test of Petersson (1981): $L = 2000\text{mm}$, $D = 200\text{mm}$, $b = 50\text{mm}$, $a_0 = 100\text{mm}$, $E = 30000\text{MPa}$, $\nu = 0.2$, $f_t' = 3.33\text{MPa}$, $G_F = 0.124\text{N/mm}$, with the fracture energy being measured eliminating the effect of the beam's self weight (see Petersson, 1981).

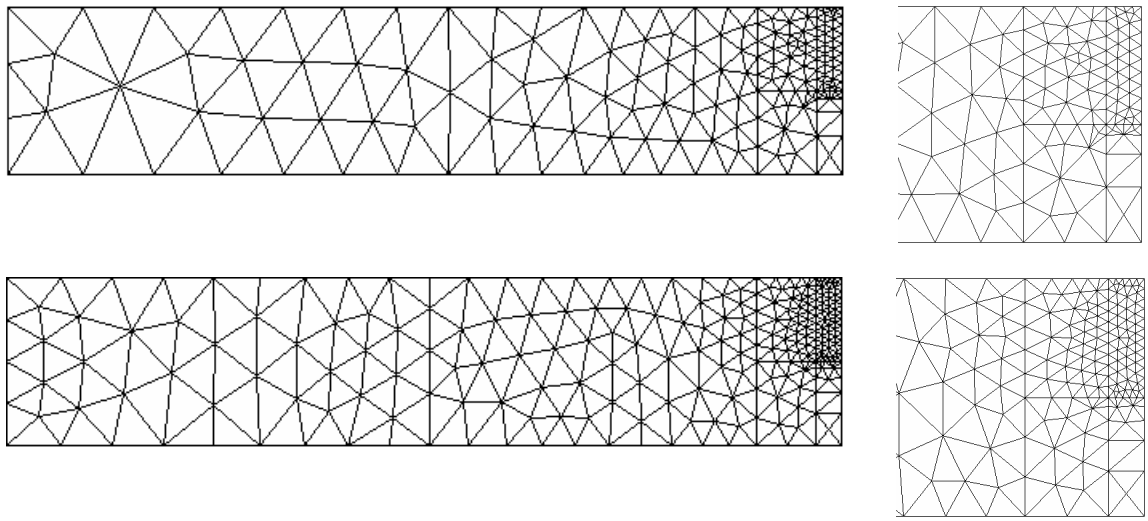

Figure 7.5: Finite element meshes: coarser (a), and denser (b)

The nonlocal interaction radius was taken as 2.0 times the maximum aggregate size ($d_{\max} = 8\text{mm}$, Petersson (1981)), resulting in $R = 16\text{mm}$ followed by the ratio $k = w_t / R = 1.96$ (using $t = g_{fnl} / g_F = 0.25$; see also the example in Chapter 5). As there was no experimental data on the unloading path, the constitutive model was assumed to be pure damage, with separation of tension and compression behaviour based on the decomposition of the stress tensor. Therefore, only two model parameters were derived from the system (4.80-4.81): $E_{pt} = 6899\text{MPa}$ and $n_t = 0.32$ (see section 5.3.3 in Chapter 5 for details).

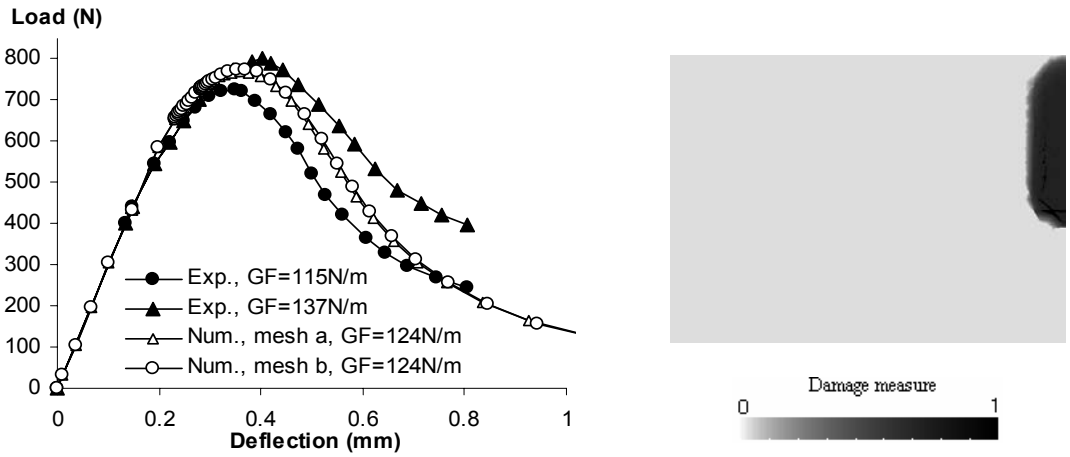

Figure 7.6: Load-deflection curve and damage pattern at very late stage of the numerical analysis (mesh b, zoomed-in at centre part of the half-beam)

The numerical analyses were carried out using two different finite element meshes of six-node triangular elements, with different mesh densities. Because of symmetry, only half of the beam was modelled (figure 7.5). Numerical results, in the form of load-deflection curve and damaged pattern, are shown in figure (7.6). The damage process zone can be clearly seen in the figure and the numerical crack path agrees well with the experimental one in figure (7.4). It is noted here that the crack paths in bending tests of notched beams are usually straight lines above the notch, running from the notch tip to the upper side of the beam (see figure 7.4). They were not included in research papers from which the experimental data and results on bending tests are extracted. This is the reason why the crack patterns in the numerical examples in this section (7.3) are drawn in the figures (7.4, 7.7 and 7.11) describing the geometry of the beams, instead of being scanned from the papers referred to.

The numerical load-deflection curves obtained from different meshes are almost identical, again demonstrating the lack of mesh-dependency of the proposed model. In addition, they also match quite well the experimental curves. In the model, the choice of the nonlocal radius obviously has some effect on the response of the model, but this influence has been considerably removed using the proposed procedures for the parameter identification (see Chapter 5).

7.3.2 Three-point bending test – un-notched beam

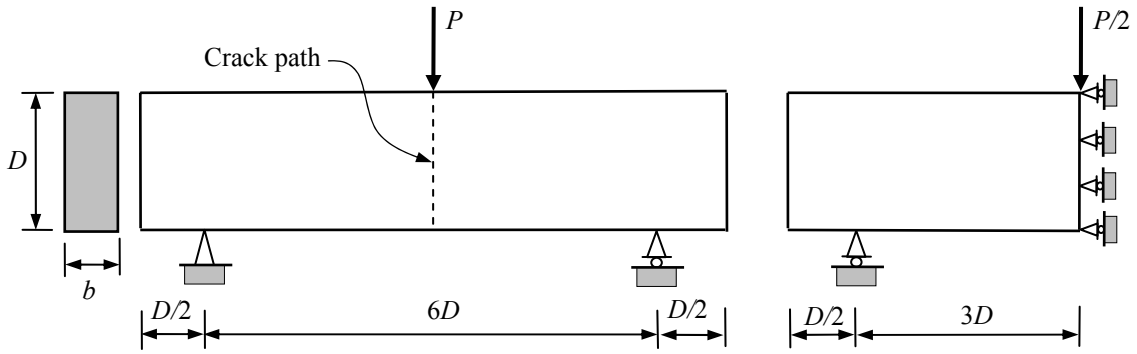

Figure 7.7: Geometrical data and half beam model used in the numerical analysis

This example is to test the response of an un-notched beam under three-point bending (figure 7.7). The experimental data in this case is extracted from Carpinteri's experiments (Carpinteri, 1989). The geometrical and mechanical data are: $D = 100\text{mm}$, $b = 150\text{mm}$, $E = 34300\text{MPa}$, $\nu = 0.2$, $f_t' = 5.3\text{MPa}$, $G_F = 0.09\text{N/mm}$. Compared to the material properties (smaller f_t' but higher G_F) in example 7.3.1 (Petersson, 1981), more brittle behaviour is expected in the load-deflection response of the beam. Because there was no experimental unloading data, the dissipation mechanism was again assumed to be due to damage only. Based on the proposed procedures in chapters 4 and 5 (using $t = g_{fnl}/g_F = 0.3$ and the assumed nonlocal radius $R = 7.5\text{mm}$), we obtain here the necessary model parameters: $E_{pt} = 10756\text{MPa}$ and $n_t = 0.32$ ($k = w_t/R = 2.10$ obtained from the procedure described in section 5.3.2, Chapter 5). The numerical results are shown in figure (7.8).

It can obviously be seen in figure (7.8) that the numerical and experimental results are greatly different from each other. A slight snap-back response can be observed on the numerical load-deflection curve, while the experimental softening curve is much less brittle. Nevertheless, the experimental fracture energy is appropriately reproduced

by the numerical model (through the area under the load-deflection curve); and the numerical and experimental peak loads are comparable: 11.02kN (numerical) and 11.38kN (experimental). This pattern was similar in several numerical models used for the simulation of this real test (Hawkins and Hjorteset, 1992). For comparison, the numerical result using Petersson's bilinear softening model (Hawkins and Hjorteset, 1992) is also shown in the same figure.

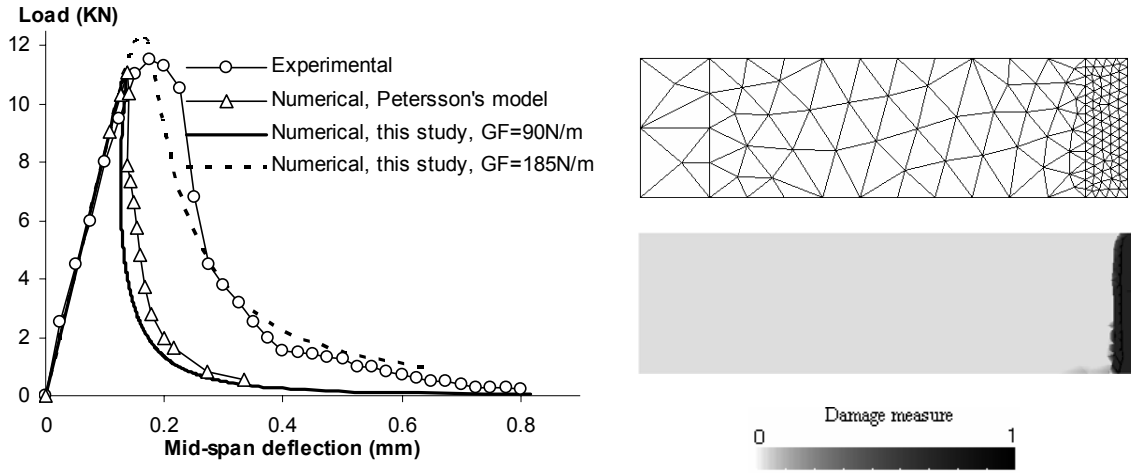

Figure 7.8: Finite element mesh, load-deflection curve and damage pattern (at deflection of 0.8mm)

The difference here possibly comes from different testing conditions and localization problems in the notched beam for measuring the fracture energy G_F and the un-notched beam examined in this example. In the notched beam, the failure is strongly forced to localize in a narrow area above the notch, while due to the mild stress distribution and the heterogeneity of the material, that in un-notched beam can spread out in a wider zone at the beginning of the analysis (pre-peak part in the load-deflection curve). In other words, the pre-peak behaviour of an un-notched beam is much more affected by the heterogeneity of the material than that of notched beam, where the artificial flaw dominates the material imperfection. Therefore the experimental load deflection curve of notched beam can be much more brittle than that of un-notched beam. As a consequence, the calculated fracture energy G_F can be different if one adopts the un-notched beam for the calculation of the fracture energy.

For illustration, the dissipated energy under the experimental load-deflection curve of the tested un-notched beam was used here to calculate the fracture energy G_{F1}, by simply dividing the area under the curve by the fracture surface (150*100mm^2),

yielding $G_{F1} \approx 0.185\text{N/mm}$. This is approximately double the experimentally provided fracture energy. The dashed curve in figure (7.8) shows the corresponding numerical response using $G_{F1} \approx 0.185\text{N/mm}$, which is closer to the experimental one.

7.3.3 Three-point bending test – notched beam – cyclic loading

This test was experimentally carried out by Perdikaris and Romeo (1995) and has also been used by several researchers (Meschke *et al.*, 1998; Hatzigeorgiou and Beskos, 2002) for the validation of their damage-plasticity constitutive models. The beam geometry is similar to that in section 7.3.1, with the following geometrical data (see figure 7.4) and material properties: $L = 1016\text{mm}$, $D = 254\text{mm}$, $b = 130\text{mm}$, $a_0 = 78\text{mm}$, $E = 43600\text{MPa}$, $\nu = 0.2$, $f_t' = 4.77\text{MPa}$, $f_c' = 63.4\text{N/mm}^2$, $f_{c0} = 0.3 f_c' = 19.02\text{N/mm}^2$, $G_F = 89.17\text{N/m}$ and $d_{\max} = 6\text{mm}$. The finite element meshes used are depicted in figure (7.9).

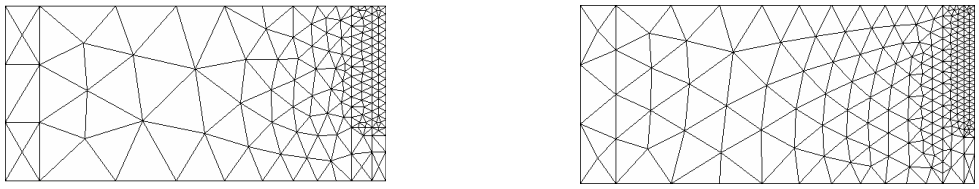

(a), (b): for nonlocal approach

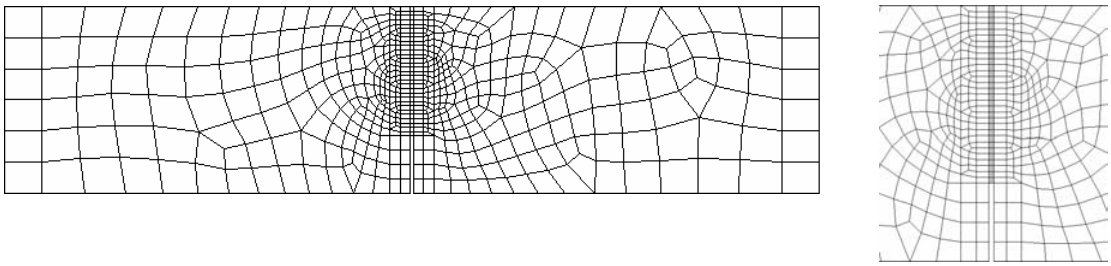

(c): for fracture energy approach

Figure 7.9: Finite element meshes

It should be noted here that an experimental test for the measurement of the tensile strength was not carried out and the tensile strength used here was in fact calculated from the compressive strength using the following empirical formula (Eurocode 2, ENV 1992-1-3)

$$f_t' = 0.3\left(f_c'\right)^{2/3}$$

where $f_c' = 63.4\text{N/mm}^2$ is the cylinder compressive strength obtained from experiment. In addition, since the self weight of the beam is not taken into account in the numerical

analysis, the experimentally-provided fracture energy ($G_F = 119.5\text{N/m}$) should be adjusted using the experimental data provided, giving $G_F = 89.17\text{N/m}$ (see also Petersson, 1981). This choice of material properties however was not clarified in the research work by the above-mentioned researchers, in which $G_F = 119.5\text{N/m}$ and $f_t' = 4.0\text{MPa}$ were used rather arbitrarily in their numerical examples.

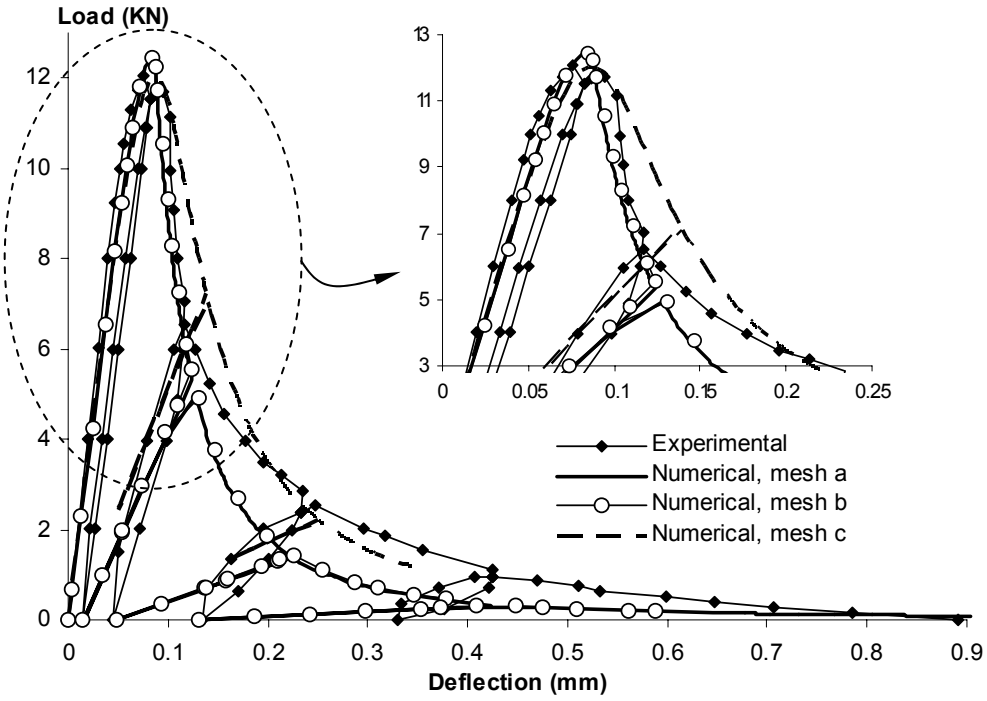

Figure 7.10a: Load-deflection curves

The numerical results using pure damage dissipation mechanism have been presented in Chapter 5 for the illustration of the proposed procedure used for the identification of parameters of nonlocal models. The obtained results, using three different nonlocal interaction radiuses, match rather well the observed experimental load-deflection curve. Here, a coupled damage-plasticity model was used, with the following assumptions on the unloading path (see Chapter 4 for details): $\varepsilon_{tu} = 1.1 f_t'/E$ and $E_{tu} = 0.91E$. The nonlocal interaction radius was taken as 2.0 times the maximum aggregate size, giving $R = 12\text{mm}$, with the corresponding ratio $k = w_t/R = 1.98$ (using $t = g_{fnl}/g_F = 0.25$) taken from the numerical example in Chapter 5. From the input data, we obtain the following model parameters from the system (4.80-4.82): $H_t = 59045\text{MPa}$, $E_{pt} = 29610\text{MPa}$ and $n_t = 0.39$. The nonlocal numerical analyses were carried out on two different finite element meshes to illustrate the mesh-independency of the proposed approach.

In a similar way, the nonlinear finite element analysis using the fracture energy regularization (or crack band approach) was also carried out for comparison with the nonlocal analysis. For that, the nonlocal interaction radius was set to zero in the implemented finite element code, restricting the localization to the band of elements at mid-span above the crack tip. The crack band width [equal to the width of the blackened 4-node quadrilateral elements in mesh (7.9c)] in this case is $w_t = 5\text{mm}$. This rather small width of the FPZ (compared to its nonlocal counterpart) requires another set of parameters for the constitutive model (see section 4.3.3, chapter 4). Using $t = g_{fnl} / g_F = 0.17$ and $w_t = 5\text{mm}$ ($R = 0$ for crack band model), from the system (4.80-4.82), we obtain: $H_t = 347789\text{MPa}$, $E_{pt} = 4620\text{MPa}$ and $n_t = 0.32$.

The numerically-obtained load-deflection curves are shown in figure (7.10a). There is almost no difference between results from the two meshes using the nonlocal approach, though their difference in tail behaviour from that of the fracture energy approach can be seen. In all cases, a good match between numerical and experimental peak-load can be observed. However, for deflections greater than about 0.13mm the descending part of the numerical curves underestimates the measured one. The unloading slopes on the numerical curves are also not close to the experimental ones, although the numerical models obviously produce residual deflections at zero-load state.

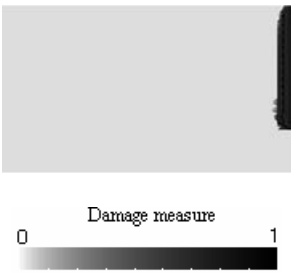

(b) Damage pattern

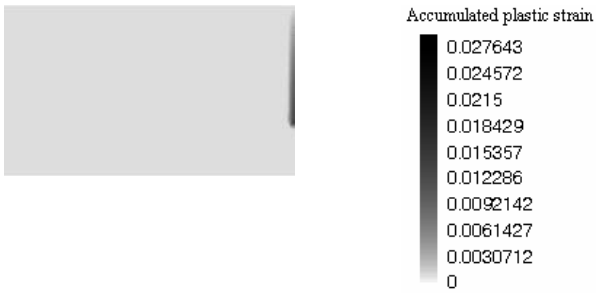

(c) Accumulated plastic strain at deflection of 0.9mm (mesh a)

Figure 7.10: Failure patterns

Those mismatches can be due to the following reasons. Firstly, fitting of the proposed stress-strain curve to the experimental one (based on the bilinear stress-separation curve in cohesive crack model) is particularly considered in the descending part just after peak stress (see section 4.3.3, Chapter 4). This is to assure the matching between the numerical peak load and its experimental counterpart. However, as there is

not enough experimental data, no attention has been paid to the tail of this stress-separation curve, which is controlled by the nonlinear function F_1^t in the proposed model. Secondly, the input parameters for the unloading slopes are possibly not relevant, resulting in damage-dominated dissipation in the failure of the structure. This is represented in the figure by very small residual deflections at zero-load state, compared to the measured ones. Choice of better sets of input parameters is in principle possible, but requires further studies on the relations between the unloading slopes of the stress-separation curve and stress-strain curve in continuum model. Last but not least, using nonlocal damage mechanisms and local plasticity mechanism also leads to damage-dominated dissipation in the failure process. This can be confirmed through examining the output results and through the distribution of the accumulated plastic strains and damage variable at the end of the numerical analysis (see figure 7.10c).

In figure (7.10b), loss of most of load carrying capacity at the centre cross-section of the beam is represented by damage reaching a critical value along the crack line. However, the accumulated plastic strains are not very high in the upper part of the crack line, compared to those in the lower part. Therefore, there must have been a considerable number of material points in the upper part undergoing pure damage dissipation while their parameters are in fact determined for coupled damage-plasticity model. This results in the underestimation of the experimental tail response (see Chapter 4 for more details on the effect of model parameters on the behaviour of the model). Use of crack band approach can remedy the mentioned problem (mesh c, figure 7.10 a), as both plasticity and damage in this case are local processes and forced to take place in the band of elements above the notch (figure 7.9c).

7.3.4 Four-point bending test – notched beam – cyclic loading

In this example, the four-point bending test experimentally performed by Hordijk (1991) is simulated using the coupled damage-plasticity model. The geometry of the specimen and finite element mesh of a half-beam model are depicted in figure (7.11). The following material properties were given (Hordijk, 1992): $E = 38000\text{MPa}$, $\nu = 0.2$, $f_t' = 3.0\text{MPa}$, $G_F = 125\text{N/m}$, with the assumed maximum aggregate size $d_{\max} = 5\text{mm}$ and assumed initial yield stress (in uniaxial compression) $f_{c0} = 11\text{N/mm}^2$.

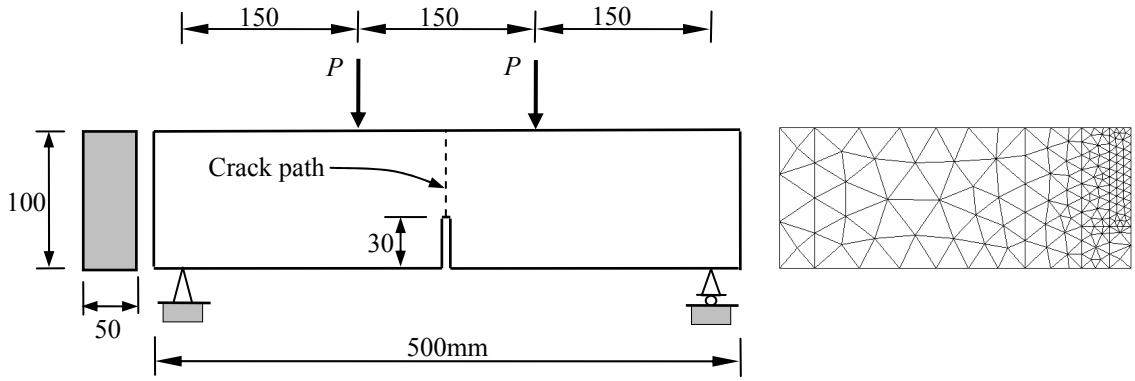

Figure 7.11: Four point bending test – Geometry and finite element mesh

Choice of the nonlocal interaction radius can be somewhat arbitrary without knowing the relevant maximum aggregate size, but the effect of this choice on the response of the model can be eliminated using the proposed procedure in chapter 5. For that reason, we take here $R = 6\text{mm}$, which is large enough for the adopted finite element mesh density in the critical zone. Using $\varepsilon_{tu} = 1.2\, f_t'/E$ and $E_{tu} = 0.9E$, the following model parameters were obtained (using $t = g_{fnl}/g_F = 0.2$, based on rough fitting of nonlinear stress-strain curve to the bilinear curve derived from given experimental data): $H_t = 33800\text{MPa}$, $E_{pt} = 6381\text{MPa}$ and $n_t = 0.33$ (with $k = w_t/R = 2.32$).

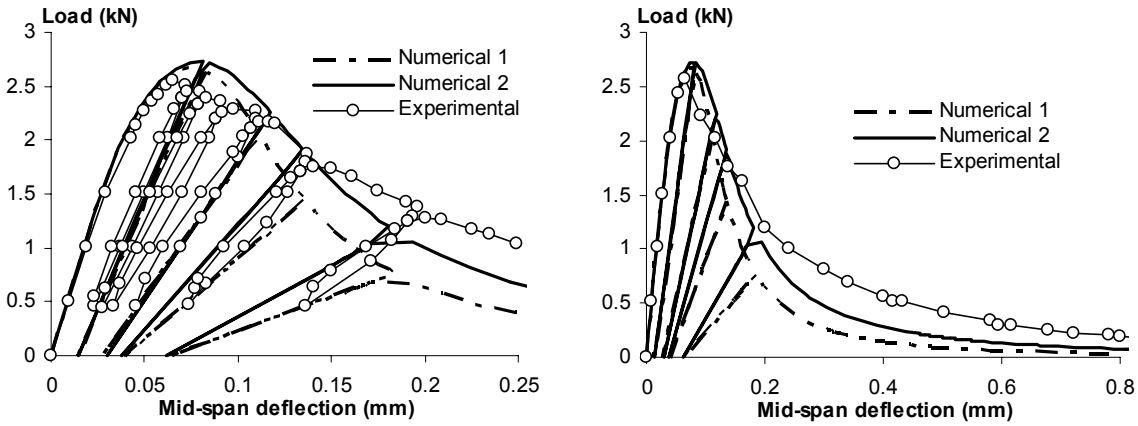

Figure 7.12: Four-point bending test - Load-deflection curves

The numerically obtained load-deflection curve (dashed-dot curve named "numerical 1" in figure 7.12) overestimates the experimental one in the post-peak region near peak load, while it underestimates the tail behaviour of the measured one (figure 7.12b). However, the numerical peak load (~2.7kN) in this case is rather close to

the value given by experiment (~2.55kN). A slight modification of the adopted procedures for the identification of model parameters can lead to better model response (solid curve named "numerical 2" in figure 7.12). This modification is based on the fact that the fracture energy in experiment can only be computed up to a certain stage in the very long tail of the experimental load-deflection curve. This has been mentioned in chapter 5 on the determination of the localization bandwidth. Following the modification, the critical damage used in the evaluation of local fracture energy g_F (see 4.80, chapter 4) is set to lower value, e.g. 0.999 instead of ~1.0 in theory. For this, only the tail behaviour of the model is significantly affected, represented by slight changes on H_t and E_{pt} ($H_t = 33840\text{MPa}$; $E_{pt} = 6377\text{MPa}$) and bigger change on n_t: $n_t = 0.37$ (see chapter 4 for the effect of parameters on the model behaviour). A slightly better model response can be clearly seen in the presented figure.

7.4 Mixed mode cracking

7.4.1 Four-point shear test

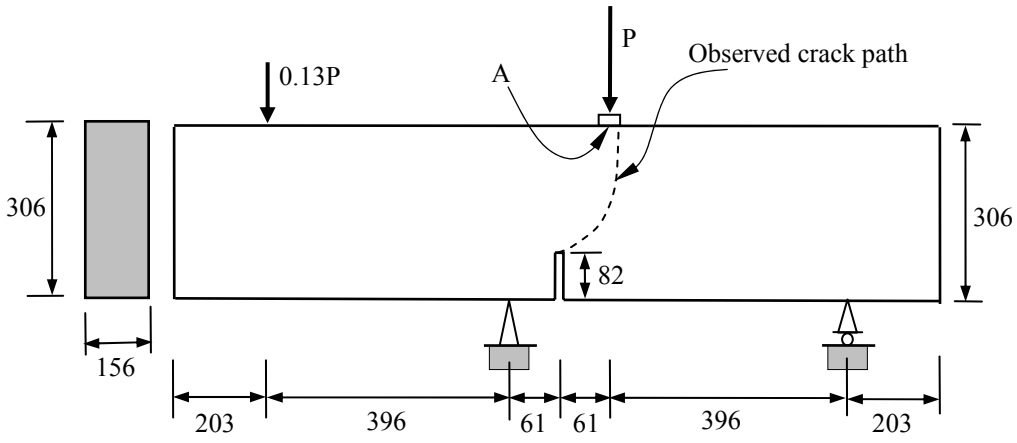

Figure 7.13: Four-point shear test – geometrical data

The four-point shear test of Arrea and Ingraffea (1982) is selected here to demonstrate the model capability in capturing the structural responses in shear loading. Partly, the snap back of the load point displacement curve helps to show the stability of the proposed numerical integration scheme and solution methods in dealing with highly nonlinear structural response. All the geometrical data of the analyzed structure are shown in figure (7.13) above. As the original report on the experimental test could not be obtained, all the above geometrical data are extracted from other sources (Saleh and

Aliabadi, 1995; Galvez *et al.*, 2002; Jefferson, 2003), which also show some negligible variations in the beam dimensions. The experimentally observed crack path is redrawn in figure (7.13) based on the crack pattern shown in the paper by Rots *et al.* (1985).

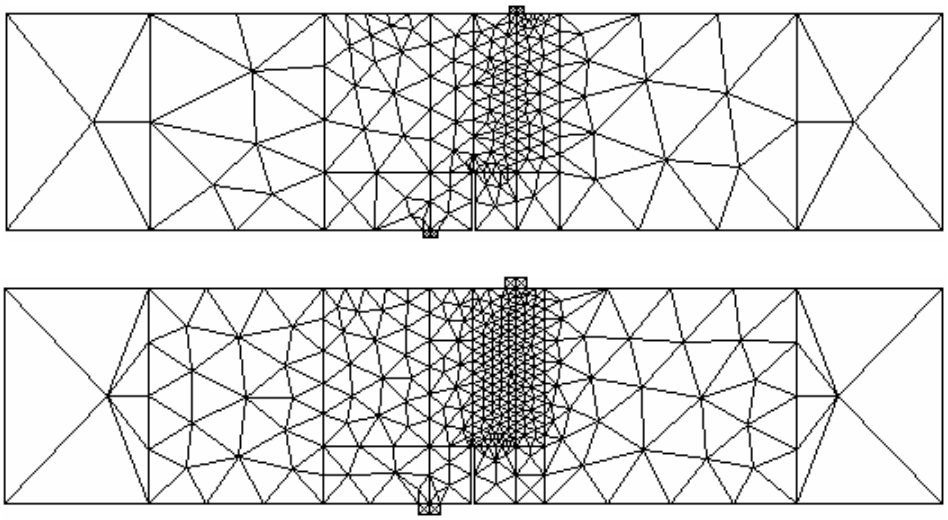

Figure 7.14: Finite element meshes

Most controversial is the choice of the tensile strength and fracture energy of the material, which have been rather arbitrarily adopted in different research work dealing with this shear test (Rots *et al.*, 1985; Saleh and Aliabadi, 1995; Jirasek and Patzak, 2002; Jefferson, 2003). For only compressive strength, Young modulus and Poisson's ratio having been experimentally provided, the tensile strength and fracture energy of the material can hardly be appropriately obtained, and therefore should be determined based on some code on concrete. In that way, we adopt here the following material properties as an averaging set between data on two test series B and C (Galvez *et al.*, 2002; CEB-FIP model code 1990): $E = 24800\text{MPa}$, $\nu = 0.18$, $f_t' = 3.55\text{MPa}$, and $G_F = 108.5\text{N/m}$. Assuming the nonlocal interaction radius to be $R = 25\text{mm}$, the material properties result in the following model parameters for pure damage behaviour ($k = w_t / R = 1.86$ in this case): $E_{pt} = 14129\text{MPa}$ and $n_t = 0.37$, with $t = g_{fnl} / g_F = 0.3$ having been adopted based on rough calibration of the nonlinear stress-strain curve to its experimentally derived bilinear counterpart.

The choice of nonlocal interaction radius in this case has little effect on the structural responses, illustrated hereafter with the use of two other different nonlocal radiuses ($R = 22\text{mm}$ and $R = 20\text{mm}$) in the numerical analyses. This proves the effectiveness of the proposed procedure in identifying parameters for nonlocal models.

Again two finite element meshes with different mesh densities were used in the numerical simulations (figure 7.14). To avoid local failure, the load distributors were also modelled in the two finite element meshes, and assumed to be made of steel ($E = 210000\text{MPa}$, $\nu = 0.3$). The numerical analyses were carried out with the applied load under indirect control of the relative displacements between nodal points of element in the fracture zone (local control). As mentioned in the introduction, the arc-length method was used for the incremental analysis and Newton-Raphson method for the iterative equilibrium. This helps to capture effectively the snap back on the load-displacement curve.

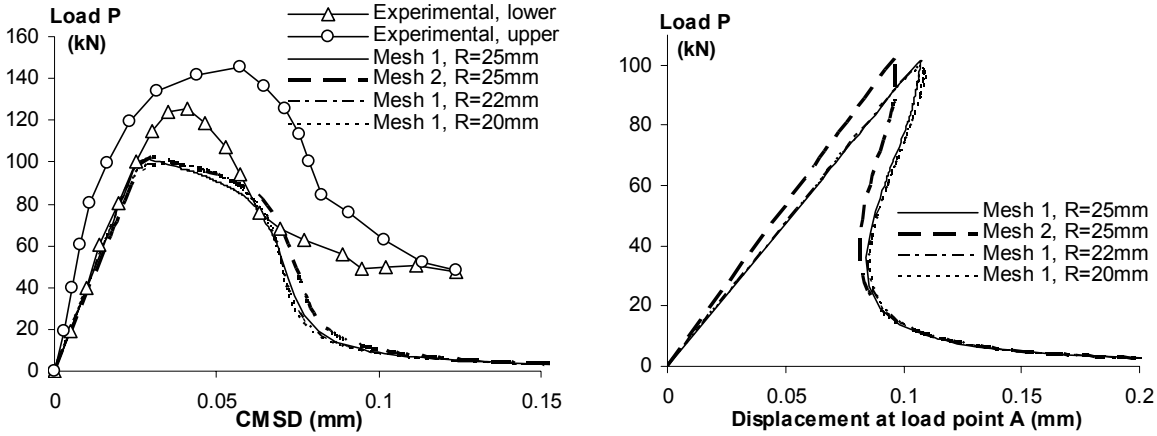

Figure 7.15: Load-CMSD responses (a) and Load-displacement curves (b)

Snap-back behaviour can be clearly seen on the load-displacement curves in the above figure, with the vertical displacement taken at point A on the upper side of the beam and under the steel load distributor (see figure 7.13). The difference in the load-displacement curves obtained from the analyses using two meshes mainly comes from the difference in size of the modelled load distributor. This is only a local effect, and the overall structural responses in figure (7.15a) are not significantly affected by the size of the load distributors and are almost identical.

Figures (7.15a) and (7.15b) also show very slight difference in the peak loads corresponding to different nonlocal interaction radii. This, however, can be in principle further reduced using appropriate calibration for the nonlinear stress-strain curves in all cases of nonlocal radii. On the other hand, there is also no match between the experimental and numerical load-CMSD curves; and this trend has also been found in some other research papers dealing with this mixed-mode test (Alfaiate *et al.*, 1992;

Jefferson, 2003). It can be supposed here that the observed numerical and experimental mismatch comes from the irrelevant use of pure mode I fracture energy in mixed-mode analysis. However, lack of relevant material properties from the real test means this mismatch cannot be fully explained.

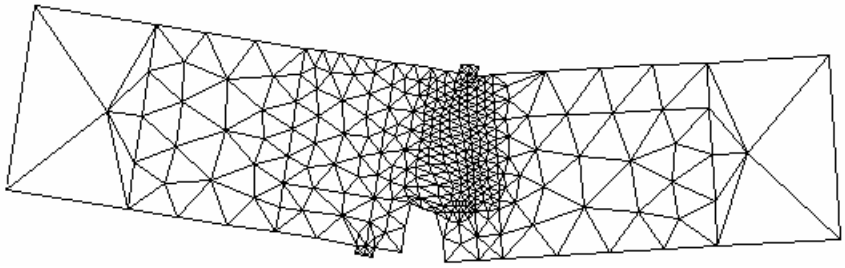

Figure 7.16: Deformed structure at CMSD of 0.26mm (mesh 2, magnification of 100)

The numerical crack pattern can be seen in figures (7.16) and (7.17), and compared with the experimentally-observed crack path in figure (7.13). The numerical crack path seems to be less curved than its experimental counterpart.

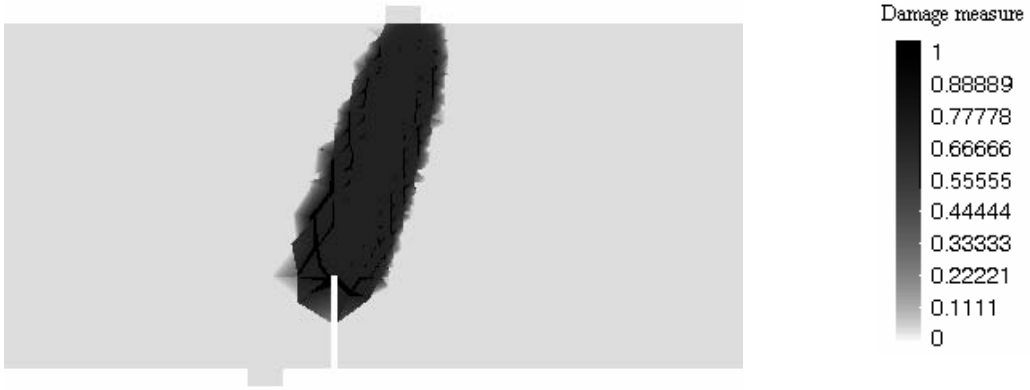

Figure 7.17: Four point shear test – Crack pattern at CMSD of 0.26mm (mesh 2)

7.4.2 Mixed-mode cracking test of Nooru-Mohamed

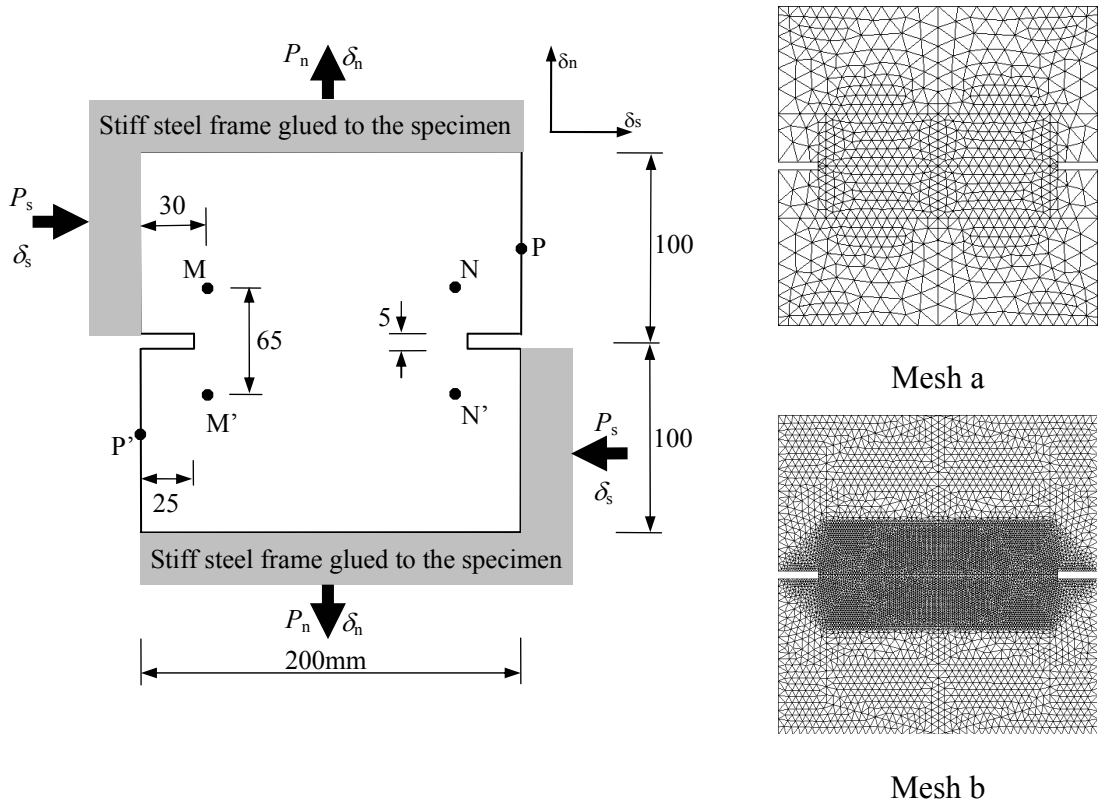

Figure 7.18: Double-edge notched specimen,
Geometrical data and finite element meshes

To examine further the responses of the proposed model in the numerical simulations of concrete structures, the mixed mode cracking of a double edge notched (DEN) specimen is numerically simulated in this example. The experimental tests of the DEN specimens examined were carried out by Nooru-Mohamed *et al.* (1993) and the corresponding data are extracted here. The geometrical data of the specimen along with the boundary conditions and finite element meshes are shown in figure (7.18) above. Only one loading path was considered in this example: biaxial loading (path 2a, Nooru-Mohamed *et al.* (1993)), in which the axial tensile P and lateral compressive shear load P_s were applied to the specimen so as to keep the ratio δ/δ_s unchanged throughout the test (δ/δ_s equals to 1.0 in load path 2a). The average deformations used to control the loading process are calculated as follows (Nooru-Mohamed *et al.*, 1993; di Prisco *et al.*, 2000): $\delta = \left(\delta^M - \delta^{M'} + \delta^N - \delta^{N'}\right)/2$, and $\delta_s = \delta_s^P - \delta_s^{P'}$. However in the numerical test, incorporation of the above deformation controls is difficult and an alternative way (Jefferson, 2003) has been adopted in this study with rigid movements of the upper left

edge and top edge of the specimen being prescribed, and the lower right edge and bottom edge being kept fixed in both directions.

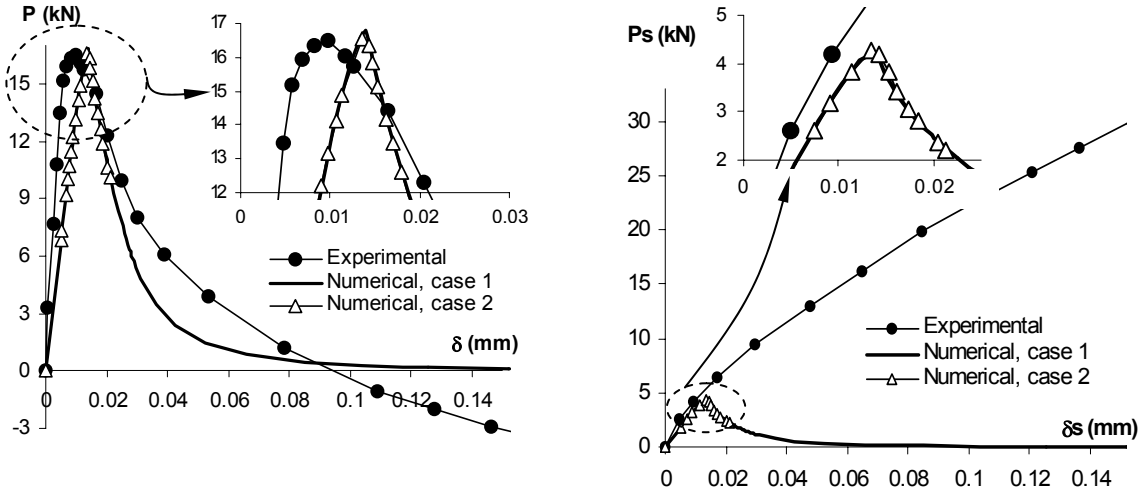

(a) $P - \delta$ (b) $P_S - \delta_S$

Figure 7.19: Load – deformation curves

The material properties provided by experiments ($E = 32000\text{MPa}$, $\nu = 0.2$, $f_t' = 3.0\text{MPa}$; $f_c' = 38.4\text{MPa}$ and $G_F = 0.11\text{N/mm}$) require the following model parameters for nonlocal model: $R = 7\text{mm}$; $t = g_{fnl}/g_F = 0.2$; $k = w_t/R = 2.24$; $E_{pt} = 3565\text{MPa}$ and $n_t = 0.31$ (see Chapters 4 and 5 for the procedures to determine these parameters). The simulations were carried out based on the nonlocal approach (case 1 and 2, using mesh (a) of 6-node triangular element) and fracture energy regularization (case 3, using mesh (b) of 3-node triangular element). For the sake of simplicity in the fracture energy regularization, a constant mesh density was adopted in the region near the notches of mesh (b), thus enabling us to use the same model parameters ($t = g_{fnl}/g_F = 0.15$; $w_t = \sqrt{2A} = 1.4\text{mm}$; $E_{pt} = 378\text{MPa}$ and $n_t = 0.25$; where A is the area of the element in the fracture zone) for all elements. In addition, premature cracking at the boundary was also prevented by introducing linear elastic behaviour to elements near the boundary (see also Nooru-Mohamed *et al.*, 1993; and Di Prisco *et al.*, 2000).

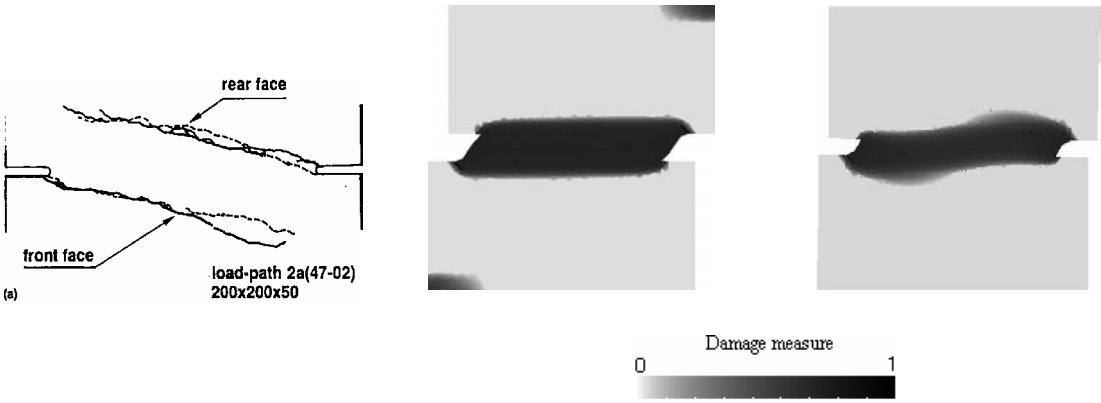

(a) Experimental (b) Numerical, case 1 (δ=δ_S=0.15mm, mag.=100) (c) Numerical, case 2 (δ=δ_S=0.02mm, mag.=500)

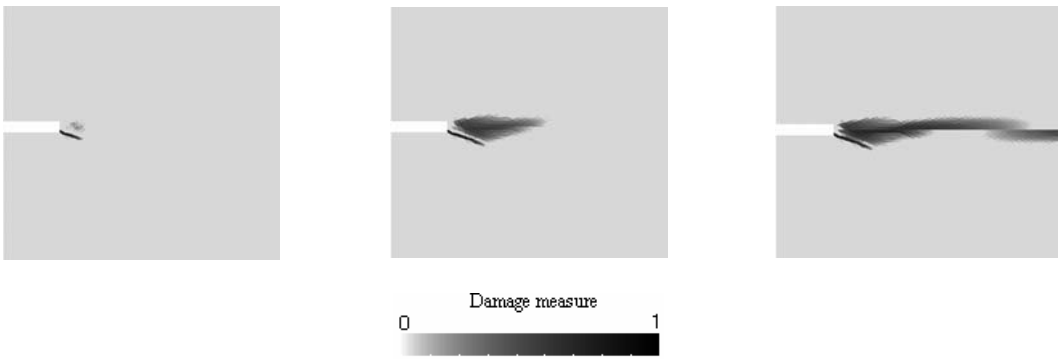

(d) Numerical, case 3: crack pattern at pre peak stage (left & middle) and peak load (right) (zoomed in at left notch)

Figure 7.20: Experimental and numerical crack patterns

The first numerical simulation (case 1) shows different responses of the simulated specimen compared to those obtained from experiments (figures 7.19 and 7.20b). Only the tensile peak load P matches the experimental one (figure 7.19a). In this numerical analysis, cracks occur first at two crack tips and propagate along the horizontal line connecting two notches. No curved or inclined macroscopic crack can be seen. This numerical response of the simulated specimen, as a result of the isotropic behaviour of the damage model used, directly results in decreasing shear resistance of the specimen after peak (figure 7.19b), which is contrary to experimental observations.

Two types of remedy have been examined (case 2 and 3, figure 7.20). In the first remedy (case 2), a slight modification of the failure envelope was done by setting $p_t = 0$ (see figure 4.7, chapter 4), along with forcing cracking process not to take place at the upper right and lower left edges (by introducing elastic behaviour to elements

near the boundaries). By setting $p_t = 0$, the shear strength of the material model (in compression-tension and tension-compression quadrants) is increased while the strength in the tension-tension quadrant is decreased (see figure 4.7, chapter 4). However, only limited success was achieved, with inclined cracks first occurring at the two crack tips but finally joining when propagating towards the centre of the specimen (figure 7.20c).

For the second remedy with a very fine finite element mesh, we used a local damage approach with fracture energy regularization. It can be seen in figure 7.20d that at early stages (pre peak response), the failure process begins with inclined macro cracks propagating from the two notches of the specimen. However, with increasing loads, secondary cracks occur and soon dominate the failure process (figure 7.20d) while the first two inclined cracks stop propagating.

Through the above numerical example, the isotropic damage model has been seen to show its weakness in capturing the real behaviour of the concrete specimen in mixed mode cracking. Mesh bias can be readily observed, which can only be partly remedied by modifying the failure envelope of the material model. Nevertheless, this modification leads to an unrealistic strength envelope of the material and hence should not be advocated in future research. Alternatively, refining the finite element mesh has also been shown to have effect on reducing the sensitivity of the model response to the mesh orientation but this simple method cannot be considered as a universal remedy (see also Grassl and Jirasek, 2004). On the other hand, it can readily be concluded that anisotropic behaviour of the model is the key to the enhancement of the numerical responses, and can be incorporated in the proposed constitutive model using the energy function (4.12) or (4.17) (see chapter 4). However, the realization of this enhancement is left here as future work on the model development.

7.5 Compression-related test

7.5.1 Splitting test on a concrete prism

This is the only structural problem in this chapter related to the compressive softening behaviour of the model. The splitting test (Brazilian test) here serves as an indirect testing method to measure the tensile strength of the material, helping to resolve disadvantages in the implementation of direct tensile test (Rocco *et al.*, 1995). The

resulting splitting strength can then be used to calculate the uniaxial tensile strength of the material (CEB-FIB, Rocco *et al.*, 2001). The testing arrangement was quite simple, as shown in figure (7.21), and test on the prism specimen was adopted for the numerical simulation, with $D = 75\text{mm}$, $B = 50\text{mm}$ and the following widths of the load bearing strip: $b_1 = 0.08D = 6\text{mm}$ (numerical test 1; named STP75-8 in Rocco *et al.*, 1995) and $b_2 = 0.16D = 12\text{mm}$ (numerical test 2; STP75-16 in Rocco *et al.*, 1995).

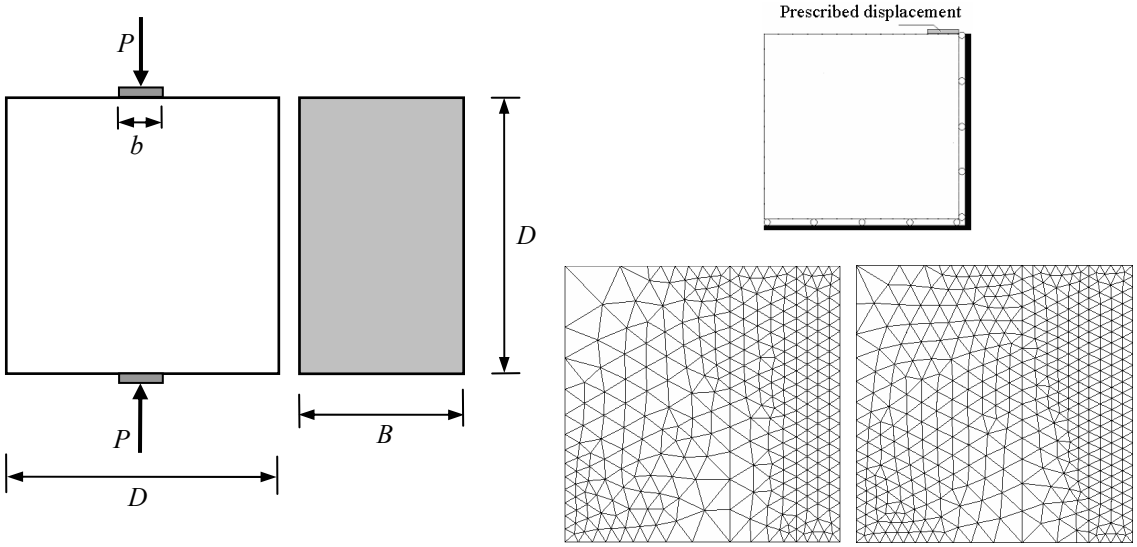

Figure 7.21: Splitting test – Geometry and finite element model

The following mechanical properties of the material are directly obtained from the test (Rocco *et al.*, 1995): $E = 31000\text{MPa}$, $f_c' = 38\text{MPa}$, $G_F = 0.072\text{N/mm}$, and $d_{\max} = 5\text{mm}$; the Poisson's ratio can be assumed to be $\nu = 0.2$. In addition, for the numerical simulations using constitutive model with two separate damage modes, more material properties are needed. The compressive fracture energy can be adopted here based on the experimental research by Jansen and Shah (1997): $G_c = 18\text{N/mm}$. This is the post-peak fracture energy, the derived local counterpart (g_c) of which has been illustrated in figure 4.20. However, the uniaxial tensile strength was not provided by the experiment and must be obtained from the splitting tensile strength f_{st}, based on CEB-FIP code or recent research by Rocco *et al.* (2001). Since tensile damage is the dominating mode of failure in the second numerical test (Comi and Perego, 2001), we have (from STP75-16; Rocco *et al.*, 1995): $f_{st} = 4.53\text{MPa}$, from which the uniaxial tensile strength can be derived: $f_t' = 0.9 f_{st} = 4.08\text{MPa}$ (CEB-FIB code) or $f_t' = 0.95 f_{st} = 4.31\text{MPa}$ (Rocco *et al.*, 2001). The CEB-FIB value was adopted in this study.

No permanent deformation is considered in this numerical example and the constitutive model used here is isotropic damage, with two separate failure mechanisms in tension and compression. The procedure developed in chapters 4 and 5 for the determination of model parameters were applied in this case to both tensile and compressive damage mechanisms, giving the following ratios between the widths of the fracture process zones and the adopted nonlocal interaction radius ($R = 2\text{mm}$): $k_t = w_t / R = 2.0$ and $k_c = w_c / R = 2.2$. In the determination of k_t and k_c, we have adopted the following values of parameters (see chapter 4 for details): $t = g_{fnl} / g_F = 0.25$ (for tensile damage); and $E_{pc} = 6000.0\text{MPa}$ and $m_c = 6.0$ (for compressive damage). The following sets of model parameters were obtained: $E_{pt} = 1988\text{MPa}$, $n_t = 0.28$, and $n_c = 0.24$.

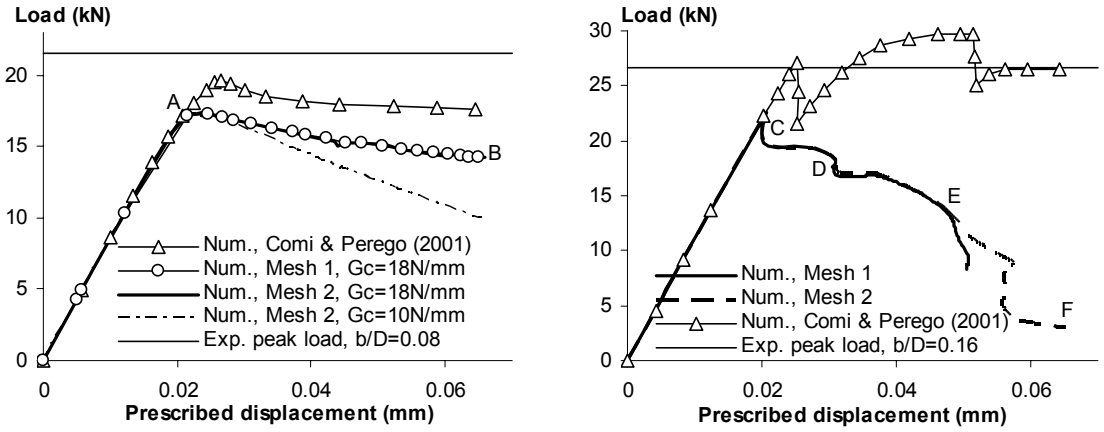

(a) $b/D = 0.08$ (b) $b/D = 0.16$

Figure 7.22: Load-displacement curves

The obtained peak loads in both numerical tests can be observed not to agree well with the experimental ones. In addition, only the numerical load-displacement curve of the first test ($b/D = 0.08$) show some resemblance with the numerical reference curve (Comi and Perego, 2001). Numerical analysis has also been carried out using a lower value of the compressive fracture energy (dashed dot curve, figure 7.22a). However, only the tail response is affected and the obtained numerical peak load only changes insignificantly. For the second test ($b/D = 0.16$), oscillation in the load-displacement response can be observed, which has also been found in the numerical results by other researchers dealing with this kind of splitting test (Feenstra and de Borst, 1996; Comi and Perego, 2001).

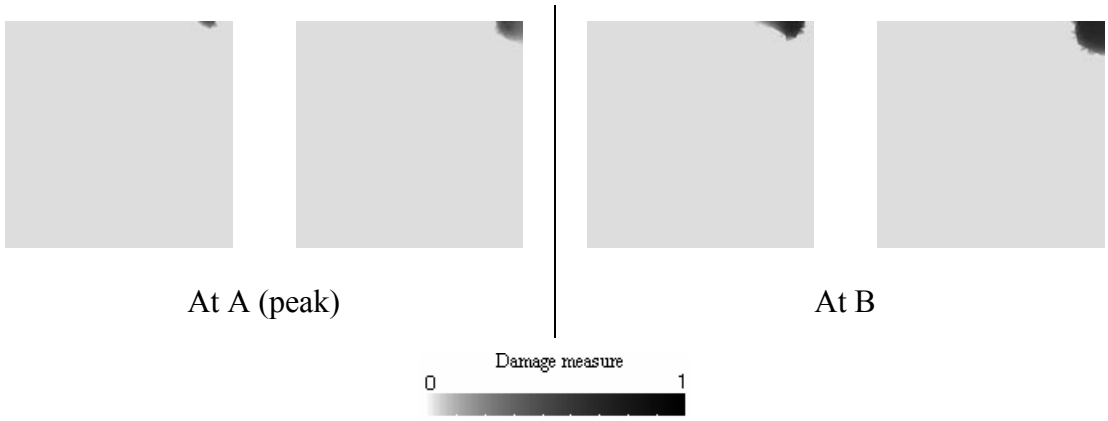

Figure 7.23: Tensile damage (left) and compressive damage (right) for *b/D*=0.08

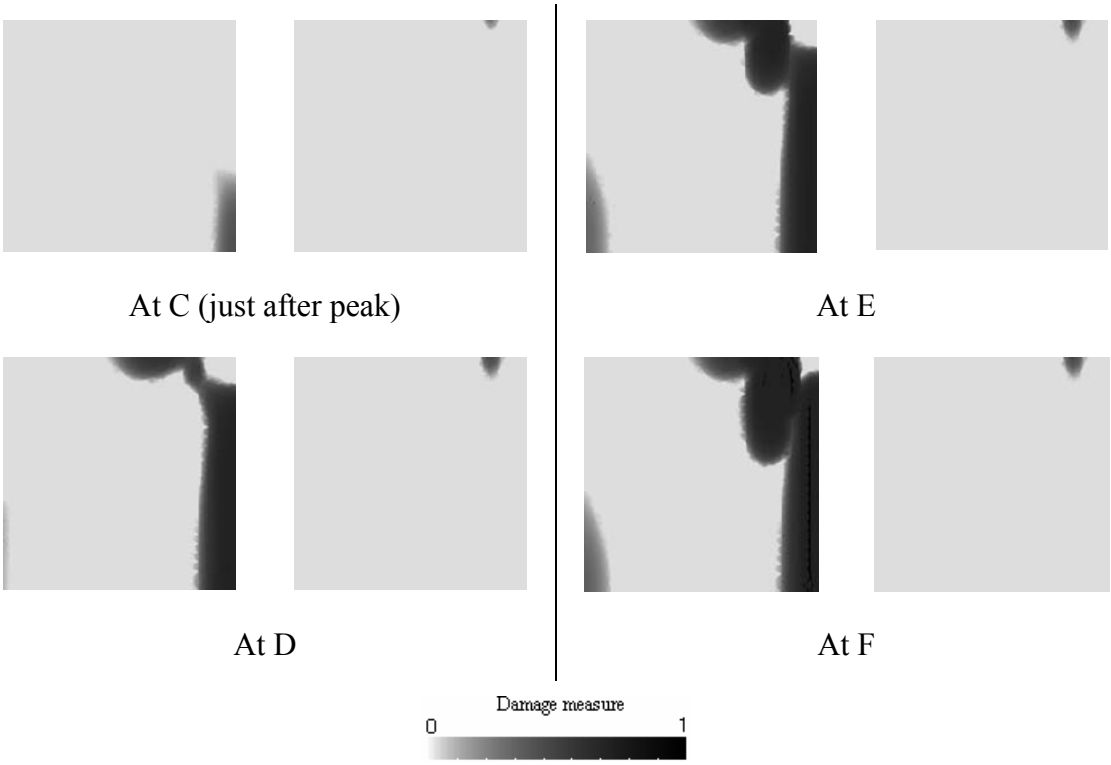

Figure 7.24: Tensile damage (left) and compressive damage (right) for *b/D*=0.16

In both tests, the results obtained from two finite element meshes are almost identical. Departure of two equilibrium paths obtained from two meshes is only found at late stage (point E, figure 7.22b) of the failure process in the second numerical test. Nevertheless, it is believed that this departure point is linked with the numerical instabilities instead of the capability of the proposed model in objectively capturing strain-softening behaviour. Full examination and explanation for this divergence requires further investigation and therefore cannot be covered by the scope of this study.

The paper by Rocco *et al.* (1995) does not provide any results on the load-displacement curves as well as crack pattern of the specimen. In this thesis, the damage

contours obtained from numerical analysis are presented to illustrate the failure processes in the specimen at different loading stages. This presentation is important as it helps to show the complicated failure process involving both tensile and compressive damage mechanisms, which are coupled in this example. The damage zones in both tests are depicted in the figures (7.23) and (7.24), where splitting effect can be clearly seen in figure (7.24) for *b/D*=0.16. Tensile damage in this case (*b/D*=0.16) occurs at the centre of the specimen and quickly develops through its height while failure due to compressive damage just happens at the corner of the load bearing strip. This is different from the first test (*b/D*=0.08) where failure due to both mechanisms of damage localizes underneath the load bearing strip (figure 7.23).

7.6 On the choice of model parameters

A summary of the models and parameters used in the numerical examples above is provided in this section. The aim is to show the whole picture of parameters of the constitutive model proposed in this study, and through that picture, indicate cases in which simplified versions of the full model can be appropriately used. We start here with the full version of the nonlocal model, which incorporates both dissipation mechanisms (damage and plasticity) and the capability to capture tensile and compressive behaviour separately. For the full version of the model, the necessary model parameters are:

a. Parameters defining the elastic behaviour of the material: Young's modulus E, and Poisson's ratio ν.

b. Parameters defining the initial loading surfaces: stress parameters f_t', f_c', and f_{c0}; and scalar parameters p_t and p_c. The initial shape of the parabolic Drucker-Prager yield surface used in the modelling is dependent on the uniaxial compressive yield stress f_{c0} and the uniaxial tensile strength f_t'. On the other hand, the uniaxial tensile and compressive strengths f_t' and f_c', along with two scalar parameters p_t and p_c are required to define the initial shape of the composite damage surface (section 4.2.3, Chapter 4). The stress parameters f_t', f_c' and f_{c0} are obtained directly from tensile and compressive tests on concrete, while the scalar parameters p_t and p_c are determined to yield best fit to the experimental biaxial strength envelope of the material. As such experimental data are not always available,

$p_t = 0.33$ and $p_c = 0.62$ [obtained based on the data from Kupfer and Gerstle (1973); see section 4.2.4, Chapter 4] are kept unchanged in all the numerical examples in this Chapter.

c. Nonlocal interaction radius R: this length parameter of nonlocal model is in principle obtained based on the procedure proposed in section 5.3.2, Chapter 5. Nonlinear relationships between R and the minimum widths w_t and w_c (in tension and compression) of the fracture process zones can be determined based on that procedure. From these nonlinear relationships, R is then chosen so that the corresponding widths w_t and w_c match their experimentally observed values [e.g. $w_t \approx 3d_{\max}$ following Bazant and Pijaudier-Cabot (1989)]. However, for the absence of an experimental value of w_c in compression and a possible wide range of w_t depending on the type of concrete (Bazant and Oh, 1983), the mentioned method is not worth pursuing. Therefore, in practice, the nonlocal radius R is assumed ($R = 0.5d_{\max}$ to $2d_{\max}$) and used, along with the procedure proposed in section 5.3.2, to calculate w_t and w_c. These widths are then used for the determination of other parameters of the model (see sections 4.3.3 and 4.3.4 in Chapter 4), provided that w_t and w_c lie in the experimentally observed ranges. Research in this study has shown that the ratio $k = w_t/R$ is not very sensitive with change on the nonlocal radius R (see the numerical examples for values of k), and usually lies in the range of 1.8 to 2.4. These values of R lead to the values of w_t in the range $w_t = 1.0d_{\max}$ to $5.0d_{\max}$, which is practically reasonable.

d. Parameters governing the tensile behaviour of the model: E_{pt}, n_t and H_t. Parameter H_t here controls the permanent deformations produced by the model. Two material properties (ε_{tu} and E_{tu}, see section 4.3.3, Chapter 4), which are respectively the strain and unloading slope at a point on the uniaxial stress-strain curve, are needed for the determination of this parameter. These properties (ε_{tu} and E_{tu}) are obtained from their relationships with the experimentally derived unloading slopes at points on the load-separation curves in cohesive crack model. As these relationships have not been worked out in this study, ε_{tu} and E_{tu} have been chosen rather arbitrarily in all the numerical examples. The values of ε_{tu} and E_{tu} can be (as experimented in this study): $\varepsilon_{tu} = 1.1f_t'/E$ to $1.2f_t'/E$, corresponding to $E_{tu} = 0.9E$. All three parameters (E_{pt}, n_t and H_t) are determined from the system

(4.80 – 4.82), using the fracture energy G_F and the width w_t of the fracture process zone. In addition, the ratio $t = g_{fnl}/g_F$ is also needed and can be chosen in the range t = 0.1 to 0.3 so that the nonlinear softening curve yields close fit to the first part of the experimentally derived bilinear softening curve (see section 4.3.3, Chapter 4).

e. Parameters governing the compressive behaviour of the model: E_{pc}, m_c, n_c and H_c. Similarly to the tensile case, H_c is used to control the residual strains in uniaxial compression. Its value is directly obtained from equation (4.97) and can be adjusted (based on the condition that $0 < f_{c0} < f_c'$; see section 4.3.4, Chapter 4) to yield an appropriate value of the residual strain ε_{cu} in uniaxial compression (see 4.99, Chapter 4). Another three parameters (E_{pc}, m_c, n_c) are determined from the condition that the model produces the same specific fracture energy g_c as provided by experiments ($g_c = G_c/w_c$). Equation (4.98) is used for this purpose, with E_{pc} and either m_c or n_c being assumed. As this choice of parameters is arbitrary, the parameter identification in compression is obviously not objective but simply adopted here for practical purpose. Experimental research on the compressive behaviour of the material is needed to cover this gap.

All the parameter sets above are not independent, but have tight relationships. They can be classified as local sets of parameters [sets (a), (b), (d) and (e)], and spatial set of parameter (c). The local parameters govern the pointwise behaviour of the model and are determined based on the procedures in sections 4.3.3 and 4.3.4 (Chapter 4), and 5.3.2 (Chapter 5), in which the widths w_t and w_c of the fracture process zones are obtained and then used to compute these local parameters. In that procedure, mutual effects of all parameters of the model (spatial set and local sets of parameters) on each other are accounted for. Table (7.1) overleaf summarizes important parameter sets needed for nonlocal models in this study. The physical meanings and dimensions of those parameters are summarized in table (7.2).

As can be seen in table (7.1), different simplified constitutive models can be derived from the full version by dropping out appropriate terms in the constitutive equations and setting appropriate values for some model parameters, e.g. setting $H_t = \infty$, $H_c = \infty$ and $f_{c0} = \infty$ to exclude plasticity from the full model (see sections

4.3.3 and 4.3.4 in Chapter 4 for details). This feature has been incorporated into the finite element code OXFEM used in this study.

Parameter sets → / Types of models ↓	Sets (a) and (b)	Set (c)	Set (d)	Set (e)
(1) **Full version**, using equations (4.25), (4.37), (5.19) and (5.20)	E, ν, f_t', f_c', f_{c0}, p_t and p_c	R	E_{pt}, n_t and H_t	E_{pc}, m_c, n_c and H_c
(2) **Tensile Damage**, using equations (4.25), and (5.19)	E, ν, f_t' and p_t	R	E_{pt} and n_t	
(3) **Tensile Damage & Plasticity**, using equations (4.25), (4.37), and (5.19)	E, ν, f_{c0}, f_t' and p_t	R	E_{pt}, n_t and H_t	
(4) **Compressive Damage**, using equations (4.25), and (5.20)	E, ν, f_c' and p_c	R		E_{pc}, m_c and n_c
(5) **Compressive Damage & Plasticity**, using equations (4.25), (4.37), and (5.20)	E, ν, f_t', f_c', f_{c0} and p_c	R		E_{pc}, m_c, n_c and H_c
(6) **Tensile Damage & Compressive Damage**, using equations (4.25), (5.19) and (5.20)	E, ν, f_t', f_c', p_t and p_c	R	E_{pt} and n_t	E_{pc}, m_c and n_c

Table 7.1: Parameters used for different nonlocal models

Parameters	Dimension	Physical meaning
E	N/mm^2	Elasticity modulus
ν		Poisson's ratio
f_t'	N/mm^2	Uniaxial tensile strength
f_c'	N/mm^2	Uniaxial compressive strength
f_{c0}	N/mm^2	Initial yield stress in uniaxial compression
p_t and p_c		Parameters governing the initial shapes of the damage loading surfaces
R	mm	Nonlocal interaction radius
E_{pt}	N/mm^2	Parameter governing the descending slope of the stress-strain curve in uniaxial tension
n_t		Parameter governing the rate of change of the softening tangent modulus in uniaxial tension
H_t	N/mm^2	Tensile hardening modulus, controlling the amount of plastic strain and the descending slope of the stress-strain curve in uniaxial tension
E_{pc}	N/mm^2	Parameter governing the descending slope of stress-strain curve in uniaxial compression
m_c		Parameter governing the ductile behaviour of the model in uniaxial compression
n_c		Parameter governing the rate of change of the tangent modulus in uniaxial compression
H_c	N/mm^2	Compressive hardening modulus, controlling the amount of plastic strain and the descending slope of the stress-strain curve in uniaxial compression

Table 7.2: Model parameters – Dimensions and physical meanings

Chapter 8: Conclusions and Further Work

8.1 Summary and Conclusions

An approach to the constitutive modelling of concrete has been presented in this study. A continuum approach based on damage mechanics and plasticity theory is adopted. Emphasis here is placed on the consistency and rigour of the approach, realized from the model formulation based on a thermodynamic framework to the specifications of the derived constitutive models and applications to real structural tests. The main contributions of this research are:

- The extension of an existing thermodynamic framework to incorporate both damage mechanics and plasticity theory (see section 8.1.1).
- The use of this framework to develop constitutive models for concrete. Different responses of concrete in tension and compression are appropriately modelled using damage mechanics and plasticity theory (see section 8.1.2).
- The incorporation of nonlocal regularization technique in a consistent way into the thermodynamic framework and the constitutive modelling (see section 8.1.3).
- The identification and determination of parameters of the nonlocal coupled damage-plasticity model: both set of local parameters controlling the pointwise behaviour of the model and set of spatial parameter (nonlocal radius) governing the spatial interaction of material points are determined in a rigorous manner (see section 8.1.4).
- The implementation of the nonlocal coupled damage-plasticity model into a finite element code (see section 8.1.5).

The main goals, contributions and weaknesses of the research in this thesis are summarized in the following sub-sections.

8.1.1 Thermodynamic aspects

It is desirable in this study to build constitutive models on a well established thermodynamic framework which can accommodate various forms of dissipation

mechanisms. This is to reduce the need for additional *ad hoc* assumptions during the model formulation. An existing thermodynamic framework (Houlsby and Puzrin, 2000) has been adopted for this purpose. To capture important features in the behaviour of concrete, it is essential to accommodate both continuum damage mechanics and plasticity theory in the adopted thermodynamic framework. For that, some slight modifications of the framework have been presented in Chapter 3. The derivation of constitutive models in this study follows procedures established beforehand in the adopted thermodynamic framework. Only two energy functions are needed for the derivation of a constitutive model, without introducing any further *ad hoc* assumption about the behaviour of the derived model. The evolutions of internal variables in this case are implicitly embedded in the derived constitutive relationships. Connections between the energy functions and the derived constitutive model have been well established (Houlsby and Puzrin, 2000) with the key feature being the use of the Legendre transformation, helping to exchange the dissipation function and the yield and damage functions. These connections are also illustrated in Chapter 3 of the thesis. In addition, research in this study (Chapter 3) has shown that both stress- and strain-based formulations can be described within the modified thermodynamic framework.

8.1.2 Constitutive modelling of concrete using damage mechanics and plasticity theory

To apply the adopted approach to the constitutive modelling of concrete, the specification and calibration of the proposed models have been carried out and presented in Chapter 4, based on micromechanical and experimental research. A stress-based model accommodating plasticity and two separate modes of damage is developed. The model utilizes the decomposition of the stress tensor into positive and negative parts, in combination with two scalar damage variables, to distinguish the damage dissipations in tension and compression respectively. However, this is only a simple and rather arbitrary way of modelling anisotropic behaviour at this stage of the model development, instead of using a more systematic approach with a tensorial form of damage, to capture the different material responses in tension and compression. In addition to the yield function, two separate damage loading functions naturally emerge from the thermodynamic-based formulation. Three dissipation mechanisms (plasticity,

tensile and compressive damage) are present in the specified dissipation function and control the dissipation process of the material model.

In addition, based on physical observations, the mutual effects of the three dissipation mechanisms on each other are also accounted for in the modelling. In this study, they are the reduction of tensile strength due to compressive damage, stiffness recovery as a result of closing of microcracks under load reversal from tension to compression, and a simple stress-induced linear hardening law of plasticity. The dissipation mechanisms and their coupling can be considered satisfactory at this early stage of the model development to capture the strain softening and stiffness degradation, as well as to model the different responses in tension and compression and the permanent deformations of the material in a simple manner. However, with two-dimensional material behaviour under consideration in this study, only the biaxial failure envelope is considered and calibrated from available experimental data. The present constitutive model in this case cannot take into account dissipation processes occurring in pure hydrostatic loading. In addition, no attention has been paid to the dilation of the material under loading, though this feature is also incorporated in the constitutive modelling through the use of a non-associated flow rule. Other shortcomings of the developed constitutive model, such as the abrupt transition of the energy function in switching between tension-dominant and compression-dominant stress states (see section 4.2.2, Chapter 4), the unrealistic shapes of the yield and failure surfaces in 3D principal stress space, the disagreement of the accumulated plastic strains in uniaxial and multiaxial cases, the lack of dependency of the hardening processes on direction and the isotropic behaviour of the damage model are acknowledged and will require a considerable amount of future work.

8.1.3 Nonlocal regularization technique

Properly and objectively capturing the strain softening behaviour of the material in structural tests is an important issue in the development of constitutive models. Due to the deficiency of conventional continuum mechanics in dealing with strain softening problems, regularization techniques are essential in the numerical analysis. The nonlocal approach is adopted and incorporated in the thermodynamic framework used in this study. This integration of a regularization technique into the thermodynamic framework and the constitutive modelling, however, does not require huge effort thanks

to the consistency of the established procedures for the derivation of constitutive models. In short, only slight modifications to the dissipation function are necessary, in which nonlocality is introduced through applying spatial integrals to terms related to the damage dissipation processes. The nonlocal regularization effect then occurs naturally in the derived damage loading functions.

8.1.4 Identification and determination of model parameters

The identification and determination of model parameters have been carefully taken into account during the model development. This process is considered very important for a consistent and rigorous approach towards the constitutive modelling of concrete materials. Relationships between the material properties and model parameters for a local constitutive model have been established in Chapter 4, helping to identify properly those parameters based on standard experiments. The parameter identification, however, requires slight modifications of standard experimental tests to separate the total dissipated energy into parts due to damage and plasticity. In particular, the unloading slopes on the load-deflection curves in the standard three-point bending test need to be measured for this purpose. The separation of the total dissipated energy, represented in the modelling through the fracture energy G_F in mode I cracking, helps us determine model parameters related to the macroscopic permanent deformations of the material. Therefore details on the test modifications and their connections to the constitutive modelling using coupled damage-plasticity models should obviously be accounted for in future research.

In addition to the elastic material properties (Young's modulus E, Poisson's ratio ν, uniaxial tensile and compressive strengths f_t' and f_c' respectively, and uniaxial yield stress f_{c0}), the full version of the proposed local constitutive model with the presence of plasticity deformation and two mechanisms of damage uses 9 parameters (p_t and p_c to define the composite failure surface; E_{pt}, n_t and H_t for tensile softening; E_{pc}, m_c, n_c and H_c for compressive softening; see section 7.6, Chapter 7 for details), all of which can be directly determined from modified standard tests. However, this number is only the minimum number of parameters required for the present model and can increase significantly depending upon the required accuracy in the constitutive modelling and the numerical simulation. Simpler constitutive models can be readily derived from the full version of the presented model and, of course, use

fewer parameters (i.e. p_t, E_{pt} and n_t for models with tensile damage as the only dissipation mechanism).

The employment of a nonlocal constitutive model requires relevant procedures for the identification and determination of model parameters. In addition to parameters for the local constitutive model, the identification of which is described in Chapter 4, the relationship between the nonlocal interaction radius R and other model parameters is also needed. This relationship, based on energy equivalence, helps derive the parameters of a nonlocal coupled damage-plasticity model in a consistent manner and significantly reduces the effects of change of nonlocal radius on the responses of the nonlocal model. This is an important feature which has not received much consideration in the literature. Furthermore, due to the different nature of failure in tension and compression, it is realistic and essential in modelling both tensile softening and compressive softening that the widths w_t and w_c of the fracture process zones in tension and compression be kept separate. This requirement is met using a single nonlocal interaction radius, based on the developed procedures for the determination of the two separate ratios w_t/R and w_c/R. This helps reduce the complication encountered when using two different nonlocal radii in the implementation and the numerical simulation. Nevertheless the consistency yet simplicity of the procedures for the identification of parameters of a nonlocal coupled damage-plasticity model are still preserved.

8.1.5 Implementation issues

For practical application with the use of nonlinear finite element analysis, the incremental form of the constitutive equations is usually required. However, with the use of a nonlocal constitutive relationship, no closed-form incremental relationship between the stresses and strains can be derived. As a consequence, the tangent moduli tensor C^t_{ijkl} can no longer be defined. Although it is possible to derive a nonlocal tangent stiffness matrix in some simple cases, i.e. strain-based isotropic damage without plasticity, the derivation procedure cannot be readily applied to the general coupled damage-plasticity in this study. Use of the constitutive matrix of an equivalent local model is an alternative way to cope with the difficulty, despite the fact that it is computationally inefficient. This is admitted as a weakness of the implementation for the nonlocal model developed in this study.

On the other hand, much care has been paid to the stress update routine. The implementation here uses a simple form of the backward Euler integration scheme. However, with the presence of nonlocal terms in the expressions of the damage functions, the single linearized constitutive equation normally encountered in local models is converted to a system of linearized equations relating all the damage increments in the fracture process zone (equations 6.34 and 6.35). The size of this system of algebraic equations depends upon the number of Gauss points undergoing damage in the whole structure. Moreover, although the accumulated errors due to the linearization are significantly eliminated by enforcing the yield and damage criteria in every iterative step, instead of using the consistency conditions, sub-incrementation is always required to reduce the drift of the stress points from the loading surfaces. This markedly increases the computer time spent on updating the stress, especially with the enlargement of the fracture process zone at late stages of the failure process. In combination with the use of local constitutive matrix and in "large scale" problems (i.e. the mixed mode cracking and splitting tests in Chapter 7), the stress update process turns out to be the slowest part of the numerical analysis. This deficiency obviously needs remedying in further work on the constitutive modelling pursued in this study.

Despite the very high computational cost due to the weakness of the model implementation, the adopted implicit integration for nonlocal rate constitutive equations has been shown to be stable through the simulation of structural real tests in Chapter 7. This stability is also thanks to the use of a local arc-length control (May and Duan, 1997) in the incremental analysis. On the other hand, the structural responses are objectively captured using the proposed nonlocal approach, proving the lack of mesh dependency of the nonlocal constitutive model. In addition, different nonlocal constitutive models can be derived from the full version of the model proposed, and this feature has been incorporated into the finite element code OXFEM used throughout this study. From the aspect of constitutive modelling, the model in this study shows its potential features in dealing with mode I cracking problems, such as the direct tensile tests or the standard three-point bending tests. In those circumstances, the constitutive modelling using G_F as mode I fracture energy furnishes a good way to describe the post-peak behaviour of the material. The permanent deformations in cyclic loading can also be accounted for thanks to the "yield" behaviour of the coupled damage-plasticity model.

Nevertheless, the proposed constitutive model also shows its deficiencies when the anisotropy in the material behaviour prevails and governs the structural responses to load excitations (i.e. in the mixed mode cracking test in Chapter 7). This is a direct result of using an isotropic form of damage in the constitutive modelling. In addition, it is also expected that damage-induced anisotropy is of particular importance when non-proportional loading is considered. This motivates further development of the constitutive model presented.

8.2 Further Work

The main goal of developing a consistent and rigorous approach to the constitutive modelling of concrete has only been partly achieved in this study. This is realized through the adoption and further development of a thermodynamic framework integrating nonlocal regularization technique, based on which nonlocal coupled damage-plasticity models can be derived. In parallel, the identification and determination of model parameters are conducted. However, the main weaknesses of the proposed approach have also been pointed out, lying in the incorporation of only two scalar damage variables in the thermodynamic framework used. In addition, the constitutive model described in this thesis and aiming at demonstrating the potential features of the proposed approach is a very simple one. Further research towards a more powerful approach and better responses of the derived constitutive model is hence necessary.

8.2.1 Damage-induced anisotropy

The incorporation of anisotropy features into the thermodynamic approach is of priority. This is required to faithfully capture the directional-induced responses of the material after the appearance of microcracks. In particular, both damage and plasticity parts of the model should account for the anisotropy in the post-peak behaviour. The introduction of damage variable as a tensor will require several modifications of the thermodynamic framework used in this study. To maintain the consistency and rigour of the framework, careful and critical review on the use of tensorial form of damage will need to be carried out (Cormery and Welemane, 2002; Challamel *et al.*, 2004).

Although it is essential to use the tensorial form of damage in this case, for practical purposes the stress-induced anisotropy can be incorporated in the modelling with much ease (e.g. using the energy functions 4.12 and 4.17, Chapter 4). Alternatively, the use of multiple scalar variables for the measurement of damage in different directions is also a simple and practical way to take into account the material anisotropy (di Prisco and Mazars, 1996). The incorporation of the scalar damage variables into the thermodynamic framework should be carefully considered to avoid the discontinuity of the energy function during the transition of stress states (see section 4.2.2, Chapter 4). In a similar way, the adoption of more hardening modes (other than 2 modes in the present model) for the multiple hardening behaviour of the plasticity part in the coupled damage-plasticity model also deserves examination.

8.2.2 Enhancements in the model behaviour

In addition, further work on the constitutive modelling in this study is also related to the enhancements in the model behaviour. The failure envelope and yield surface should be reconstructed so as to account for the dependence of the deviatoric sections on the Lode angle. In tandem with this modification, it is also necessary to include the "cap behaviour" in the responses of the model to pure hydrostatic compressive loading. To be in accordance with these changes, the evolution of the failure surface in compression should also be modified (see section 4.2.4, Chapter 4). More numerical examples on the compressive behaviour of the material are therefore needed to validate the model.

Other important features such as the nonlinear hardening law and the hysteresis in cyclic loading will also be expected to be captured through the employment of continuous kinematic hardening (Puzrin and Houlsby, 2001; Nguyen, 2002). Improvements in the hardening behaviour of the model will require further work on the identification of model parameters, which for plasticity can be based on the unloading slopes on the load-deflection curve in the standard three-point bending test.

8.2.3 Implementation issues

The stress update process has been shown to be the slowest part of the incremental analysis. To speed up the numerical analysis, further work should be spent on the model implementation, in particular the development of algorithms to compute the nonlocal

consistent tangent stiffness of the constitutive model. In addition, nonlocal constitutive equations which allow the stress update to be carried out pointwise [e.g. the strain-based isotropic damage model without plasticity in Chapter 3; or those of Comi (2001), Nguyen and Houlsby (2004)] are preferred in this case. The incorporation such kinds of constitutive equations in the present thermodynamic approach, while still maintaining the consistency and rigorousness of the approach, is expected to be a hard task.

8.2.4 Parameter identification

It can be predicted that the inclusion of many new behavioural features in the constitutive modelling will remarkably increase the number of parameters of the model under development. Consequently, more experimental research is required for the identification and determination of new model parameters. This is very time- and cost-demanding but seems to be inevitable in the macroscopic constitutive modelling of engineering materials. In addition, it is difficult, even impossible, to experimentally observe the underlying micro-structural phenomena of the material. Numerical microscopic analysis of the material behaviour is an alternative way to obtain some understanding on the underlying micro-structural phenomena, although at extremely high computational cost. In combination with experimental research, it is expected to help provide the closed-form constitutive modelling with sufficient data for the identification and determination of model parameters. Alternatively, the multi-scale modelling (Smit *et al.*, 1998; Kouznetsova, 2002; Massart, 2003), which loosely speaking is in between the full microscopic modelling and the macroscopic one, can bridge the gap between the macroscopic and microscopic modelling and bring in a fruitful way to capture the real behaviour of the material faithfully. This is however a totally new area of future research.

References

Addessi, D., Marfia, S., Sacco., E., 2002, A plastic nonlocal damage model, Comput. Methods Appl. Engrg. 191, 1291-1310

Alfaiate, J., Pires, E.B., and Martins, J.A.C., 1992, A finite element model for the study of crack propagation in concrete, Proc. 2nd Int. Conf. On Computer Aided Assesment and Control (Localized Damage 92), Vol. 1: Fatigue and Fracture Mechanics, pp. 291-280, Southampton, UK

Alfaiate, J., Simone, A., and Sluys L.J., 2003, Non-homogeneous displacement jumps in strong embedded discontinuities, Int. J. Solids Struct. 40, 5799-5817

Alfaiate, J., Wells, G.N., and Sluys L.J., 2002, On the use of embedded discontinuity element with crack path continuity for mode-I and mixed-mode fracture, Engineering fracture mechanics 69, 661-686

Alfano, G., and Crisfield M.A., 2003. Solution strategies for the delamination analysis based on a combination of local-control arc-length and line searches, Int. J. Num. Meth. Eng. 58, 999-1048

Ansari, F., and Li, Q., 1998, High strength concrete subjected to triaxial compression, ACI Materials Journal 95(6), 747-755

Arrea, M., and Ingraffea, A., 1982, Mixed mode crack propagation in mortar and concrete, Report 81-13, Department of Structural Engineering, Cornell University, Ithaca, NY

Bahn, B.Y, and Hsu, T.T.C., 1998, Stress-strain behavior of concrete under cyclic loading, ACI Materials Journal 95(2), 178-193

Barenblatt, G.I., 1962, The mathematical theory of equilibrium cracks in brittle fracture, Adv. Appl. Mech. 7, 55-129

Bazant, Z.P., 1976, Instability ductility and size effect in strain-softening concrete, ASCE Journal of engineering mechanics 102(2), 331-344

Bazant, Z.P., 1982, Crack band model for fracture of geomaterials, Proc. 4th Int. Conf. on numerical methods in geomechanics, Edmonton, Canada, Ed. Z. Eisenstein, Vol. 3, 1137-1152

Bazant, Z.P., 1984, Imbricate continuum and its variational derivation, ASCE Journal of the engineering mechanics division 110(12), 1693-1712

Bazant, Z.P., 1991, Why continuum damage is nonlocal: Micromechanics arguments, ASCE Journal of Engineering Mechanics 117(5), 1070-1087

Bazant, Z.P., 1994, Nonlocal damage theory based on micromechanics of crack interactions, ASCE Journal of Engineering Mechanics 120(3), 593-617

Bazant, Z.P., 1996, Analysis of work-of-fracture method for measuring fracture energy of concrete, ASCE Journal of engineering mechanics 122(2), 138-144

Bazant, Z.P., 2002, Concrete fracture models: testing and practice, Engineering fracture mechanics 69, 165-205

Bazant, Z.P., and Becq-Giraudon, E., 2002, Statistical prediction of fracture parameters of concrete and implications for choice of testing standard, Cement and concrete research 32, 529-556

Bazant, Z.P., and Cedolin, L., 1991, Stability of structures: Elastic, inelastic, fracture and damage theories, Oxford university press, Oxford, England

Bazant, Z.P., and Jirásek, M., 2002, Nonlocal integral formulation of plasticity and damage: survey of progress, ASCE Journal of engineering mechanics 128(11), 1119-1149

Bazant, Z.P., and Kim S.S., 1979, Plastic-fracturing theory for concrete, ASCE Journal of Engineering Mechanics 105(3), 407-428

Bazant, Z.P., and Oh, B.H., 1983, Crack band theory for fracture of concrete, Materials and structures (RILEM, Paris) 16, 155-177

Bazant, Z.P., and Pijaudier-Cabot, G., 1989, Measurement of characteristic length of nonlocal continuum, ASCE journal of engineering mechanics 115(4), 755-767

Bazant, Z.P., and Tabbara, M.R., 1992, Bifurcation and stability of structures with interacting propagating cracks, Int. J. Fract. 53, 273-289

Bazant, Z.P., Belytchko, T.B., and Chang, T.P., 1984, Continuum theory for strain softening, ASCE Journal of the engineering mechanics division 110(12), 1666-1692

Bazant, Z.P., Pijaudier-Cabot, G., 1988, Nonlocal continuum damage, localization instability and convergence, ASME Journal of Applied Mechanics 55, 287-293

Bazant, Z.P., Yu, Q., and Zi, G., 2002, Choice of standard fracture test for concrete and its statistical evaluation, International journal of fracture 118, 303-337

Benvenuti, E., Borino, G., Tralli, A., 2002, A thermodynamically consistent nonlocal formulation for damaging materials, European Journal of Mechanics A/Solids 21, 535-553

Bocca P., Carpinteri A., Valente S., 1991, Mixed mode fracture of concrete, Int. J. Solids Struct. 27 (9), 1139-1153

Borino, G., Failla, B., Parrinello, F., 2003, A symmetric nonlocal damage theory, Int. J. Solids Struct. 40, 3621-3645

Borino, G., Fuschi, P., and Polizzotto, C., 1999, A thermodynamic approach to nonlocal plasticity and related variational principles, ASCE Journal of Applied Mechanics 66, 952-963

Burlion, N., Gatuingt, F., Pijaudier-Cabot, G., and Daudeville, L., 2000, Compaction and tensile damage in concrete: constitutive modelling and application to dynamics, Comput. Methods Appl. Mech. Engrg. 183, 291-308

Carol, I., and Bazant, Z.P., 1997, Damage and plasticity in microplane theory, Int. J. Solids Struct. 34(29), 3807-3835

Carpinteri, A., 1989, Minimum reinforcement in reinforced concrete beams, RILEM TC 90-FMA, CODE WORK, Cardiff 20-22 September 1989, UK.

CEB-FIP model code 1990: design code / Comité Euro-International du Béton, 1993, Thomas Telford Pub., London, England

Chaboche, J.-L., 1992, Damage induced anisotropy: On the difficulties associated with the active/passive unilateral condition, International Journal of Damage Mechanics 1, 148-171

Challamel, N., Lanos, C., and Casandjian, C., 2004, Strain-based anisotropic damage modelling and unilateral effects, International Journal of Mechanical Sciences, in press.

Chen, W.F., 1982, Plasticity in Reinforced Concrete, McGraw-Hill Book Company

Chen, W.F., and Han, D. J., 1988, Plasticity for structural engineers, Springer-Verlag, Newyork Inc.

Collins, I.F., and Houlsby, G.T., 1997, Application of thermomechanical principles to the modelling of geotechnical materials, Proc. R. Soc. Lond. Serie A Vol. 453, 1975-2001

Comi, C., 2001, A non-local model with tension and compression damage mechanisms, Eur. J. Mech. A/Solids 20, 1-22

Comi, C., Perego, U., 2001, Fracture energy based bi-dissipative damage model for concrete, Int. J. Solids Struct. 38, 6427-6454

Cormery, F., and Welemane, H., 2002, A critical review of some damage models with unilateral effect, Mechanics Research Communication 29, 391-395

Crisfield, M.A., 1997, Non-linear Finite Element Analysis of Solids and Structures, Vol. 1 and 2, John Wiley & Sons Ltd.

Crisfield, M.A., and Wills, J., 1988, Solution strategies and softening materials, Comput. Methods Appl. Engrg. 66, 267-289

De Borst, R., 1986, Nonlinear analysis of frictional materials, PhD Dissertation, Delft university of technology, Delft, The Netherlands

De Borst, R., 2001, Some recent issues in computational failure mechanics, Int. J. Numer. Meth. Engrg 52, 63-95

De Borst, R., 2002, Fracture in quasi-brittle materials: a review of continuum damage-based approaches, Engineering fracture mechanics 69, 95-112

De Borst, R., and Muhlhaus, H-B., 1992, Gradient-dependent plasticity: formulation and Algorithmic aspects, Int. J. Num. Meth. Eng. 35, 521-539

De Borst, R., and Pamin, J., 1996, Gradient plasticity in numerical simulation of concrete cracking, Eur. J. Mech. A/Solids 15(2), 295-320

DeSimone, A., Marigo, J.J., and Teresi L., 2001, A damage approach to stress softening and its application to rubber, Eur. J., Mech. A/Solids 20, 873-892

Di Prisco, M., and Mazars, 1996, 'Crush-crack': a non-local damage model for concrete, Mechanics of Cohesive-Frictional Materials 1, 321-347

Di Prisco, M., Ferrara, L., Meftah, F., Pamin, J., De Borst, R., Mazars, J., and Reynouard, J.M, 2000, Mixed mode fracture in plain and reinforced concrete: some results on benchmark tests, International journal of fracture 103, 127-148

Dougill, J.W., 1976, On stable progressively fracturing solids, Zeitschrift fur angewandte mathematic und physic 27, 423-437

Dube, J-F., Pijaudier-Cabot, G., La Borderie, C., 1996, Rate dependent damage model for concrete in dynamics, ASCE Journal of engineering mechanics 122(10), 939-947

Edelen, D.G.B, and Laws, N., 1971, On the thermodynamics of systems with nonlocality, Arch. Rational Mech. Anal. 43, 24-35

Elices, M., Guinea, G.V., Gomez, J., and Planas, J., 2002, The cohesive zone model: advantages, limitations and challenges, Engineering fracture mechanics 69, 137-163

Eringen, A.C., 1972, Linear theory of nonlocal elasticity and dispersion of plane waves, Int. J. Engng. Sci. 10, 425-435

Eringen, A.C., 1981, On nonlocal plasticity, Int. J. Engng. Sci. 19, 1461-1474

Eringen, A.C., 1983, Theories of nonlocal plasticity, Int. J. Engng. Sci. 21(7), 741-751

Eurocode 2, Design of concrete structures, ENV 1992-1-3

Faria, R., Oliver, J., and Ceverra, M., 1998, A strain-based plastic viscous-damage model for massive concrete structures, Int. J. Solids Structures 35(14), 1533-1558

Feenstra, P.H., and de Borst, R., 1995, Constitutive model for reinforced concrete, ASCE Journal of Engineering Mechanics 121(5), 587-595

Feenstra, P.H., and de Borst, R., 1996, A composite plasticity model for concrete, Int. J. Solids Struct. 33(5), 707-730

Ferrara, L., and Di Prisco, M., 2001, Mode I fracture behaviour in concrete: nonlocal damage modelling, ASCE Journal of Engineering Mechanics 127(7), 678-692

Fremond, M., and Nedjar, B., 1995, Damage in concrete: the unilateral phenomenon, Nuclear eng. and design 156, 323-335

Galvez, J.C., Cervenka, J., Cendon, D.A., Sauma, V., 2002, A discrete crack approach to normal/shear cracking of concrete, Cement and concrete research 32, 1567-1585

Geers, M.G.D., de Borst, R., Peerlings, R.H.J., 2000, Damage and crack modeling in single-edge and double-edge notched concrete beams, Engng. Fracture Mech. 65, 247-261

GiD version 7.0, The personal pre- and post-processor, International Center for Numerical Methods in Engineering, Barcelona, Spain

Gopalaratnam, V.S., and Shah, S.P., 1985, Sofnening response of plain concrete in direct tension ACI Materials Journal 82(3), 310-323

Grassl, P., and Jirásek, M., 2004, On mesh bias of local damage models for concrete, pp. 255-262, Proc. of FRAMCOS-5 (International Conferences on Fracture Mechanics of Concrete and Concrete Structures), Vail Colorado, USA

Grassl, P., Lundgren K., and Gylltoft, K., 2002, Concrete in compression: a plasticity theory with a novel hardening law, Int. J. Solids Struct. 39, 5205-5223

Guinea, G.V., El-Sayed, K., Rocco, C.G., Elices, M., and Planas, J., 2002, The effect of the bond between the matrix and the aggregates on the cracking mechanism and fracture parameters of concrete, Cement and concrete research 32, 1961-1970

Han, D.J., and Chen, W.F., 1987, Constitutive modeling in analysis of concrete structures, ASCE Journal of Engineering Mechanics 113(4), 577-593

Hansen, E., Willam, K., Carol, I., 2001, A two-surface anisotropic damage/plasticity model for plain concrete, in "Fracture mechanics of concrete materials", de Borst, R. (Ed.), A.A. Balkema, Rotterdam, 549-556

Hatzigeorgiou, G.D., and Beskos, D.E., 2002, Static analysis of 3D damaged solids and structures by BEM, Engineering analysis with boundary elements 26(6), 521-526

Hawkins, N.M., and Hjorteset, K., 1992, Minimum reinforcement requirements for concrete flexural members, Chapter 15 in "Applications of Fracture Mechanics to Reinforced Concrete", Ed. by Carpinteri, Elsevier Applied Science, London, 1992

Hellweg, H.B., and Crisfield, M.A., 1998, A new arc-length method for handling sharp snap-backs, Computers & Structures 66(5), 705-709

Hillerborg, A., Modeer, M., and Pertersson, P.E., 1976, Analysis of crack formation and crack growth in concrete by means of fracture mechanics and finite element, Cement and concrete research 6, 773-782

Hordijk, D.A., 1991, Local approach to fatigue of concrete, PhD dissertation, Delft University of Technology, Delft, the Netherlands

Hordijk, D.A., 1992, Tensile and tensile fatigue behaviour of concrete; experiments, modeling and analyses, Heron 37(1), Stevin laboratory, Delft University of Technology, Delft, The Netherlands

Houlsby G. T., 2004, Notes on convex analysis, Civil Engineering Group, Oxford University, Oxford, UK

Houlsby, G.T., and Puzrin, A.M., 2000, A thermomechanical framework for constitutive models for rate-independent dissipative materials, Int. J. Plasticity 16, 1017-1047

Houlsby, G.T., and Puzrin, A.M., 2002, Rate-dependent plasticity models derived from the potential functions, J. Rheol. 46(1), 113-126

Hsieh, S.S., Ting E.C., and Chen W.F., 1982, A plastic-fracture model for concrete, Int. J. Solids Struct. 18(3), 181-197

Hu, X., and Duan, K., 2004, Influence of fracture process zone height on fracture energy of concrete, Cement and concrete research 34(8), 1321-1330

Hu, X., and Wittmann F.H., 2000, Size effect on toughness induced by crack close to free surface, Engineering fracture mechanics 65, 209-211

Imran, I., and Pantazopoulou, S.J., 1996, Experimental study of plain concrete under triaxial stress, ACI Materials Journal 93(6), 589-601

Imran, I., and Pantazopoulou, S.J., 2001, Plasticity model for concrete under triaxial compression, ASCE Journal of Engineering Mechanics 127(3), 281-290

Jansen, D.C., and Shah, S.P., 1997, Effect of length on compressive strain softening of concrete, ASCE Journal of engineering mechanics 123(1), 25-35

Jefferson, A.D., 2003, Craft – a plastic-damage-contact model for concrete. I. Model theory and thermodynamic considerations, Int. J. Solids Struct. 40, 5973-5999

Jefferson, A.D., 2003, Craft – a plastic-damage-contact model for concrete. II. Model implementation with implicit return-mapping algorithm and consistent tangent matrix, Int. J. Solids Struct. 40, 6001-6022

Jirásek, M., 1998a, Comparison of nonlocal models for damage and fracture, LSC Internal report 98/02, Laboratory of structural and continuum mechanics, Department of civil engineering, Swiss federal institute of technology (EPFL), Lausanne, Switzerland

Jirásek, M., 1998, Nonlocal models for damage and fracture: comparison of approaches, Int. J. Solids Structures 35(31-32), 4133-4145

Jirásek, M., 2000, Comparative study on finite elements with embedded discontinuities, Comput. Methods Appl. Mech. Engrg. 188, 307-330

Jirásek, M., 2001, Modeling of localized damage and fracture in quasibrittle material, In Continuous and discontinuous modeling of cohesive frictional materials, Lecture Notes in Physics 568, ed. P.A. Vermeer et al., Springer, Berlin, pp. 17-29

Jirásek, M., and Bazant Z. P., 2002, Inelastic analysis of structures, John Wiley & Sons Ltd.

Jirásek, M., and Patzák, B., 2001, Models for quasibrittle failure: Theoretical and computational aspects, ECCM-2001 European Conference on Computational Mechanics, June 26-29, Cracow, Poland

Jirásek, M., and Patzák, B., 2002, Consistent tangent stiffness for nonlocal damage models, Computers and Structures 80, 1279-1293.

Jirásek, M., Rolshoven, S., Grassl, P., 2004, Size effect on fracture energy induced by non-locality, Int. J. Numer. Anal. Meth. Geomech. 28, 653-670

Ju, J.W., 1989, On energy-based coupled elastoplastic damage theories: Constitutive modelling and computational aspects, Int. J. Solids Structures 25(7), 803-833

Kang, H.D., and Willam, K.J., 1999, Localization characteristics of triaxial concrete model, ASCE Journal of Engineering Mechanics 125(8), 941-950

Karihaloo, B.L., Abdalla H.M., and Imjai, T., 2003, A simple method for determining the true specific fracture energy of concrete, Magazine of concrete research 55(5), 471-481

Karsan I.D., and Jirsa J.O., 1969, Behavior of concrete under compressive loadings, ASCE journal of Structural engineering, Vol. 95(12),

Kotsovos, M.D., and Newman, J.B., 1977, Behavior of concrete under multiaxial stress, ACI Journal 74(9), 443-446

Kouznetsova, V., 2002, A Computational homogenization for the multi-scale analysis of multi-phase materials, PhD dissertation, Technical University of Eindhoven, Eindhoven, The Netherlands

Krajcinovic, D., and Fonseka, G.U., 1981, The continuous damage theory of brittle materials – Part 1: General Theory, ASME Journal of Applied Mechanics 48, 809-815

Kratzig, W.B., and Polling, R., 1998, Elasto-plastic damage-theories and elasto-plastic fracturing-theories – A comparison, Comp. Mater. Science 13, 117-131

Kratzig, W.B., and Polling, R., 2004, An elasto-plastic damage model for reinforced concrete with minimum number of material parameters, Computers and structures 82(15-16), 1201-1215

Kupfer, H., Hilsdorf, K., Rusch, H., 1969, Behavior of concrete under biaxial stresses, J. Am. Concr. Inst. 66(8), 656-666

Kupfer, H.B., and Gerstle, K.H., 1973, Behavior of concrete under biaxial stresses, ASCE Journal of engineering mechanics 99 (EM4), 853-866

Ladeveze, P., 1983, Sur une theorie de l'endommagement anisotrope, Rapport interne No. 34, LMT Cachan, France

Larsson, R., and Runesson, K., 1996, Element-embedded localization band based on regularized displacement discontinuity, ASCE Journal of engineering mechanics, 122(5), 402-411

Launay, P., and Gachon, H., 1972, Strain and ultimate strength of concrete under triaxial stresses, Special publication, SP-34, ACI, 1, 269-282

Lee, J., and Fenves, G.L., 1998a, A plastic-damage concrete model for earthquake analysis of dams, Earthquake Eng. and Struct. Dynamics 27, 937-956

Lee, J., and Fenves, G.L., 1998b, Plastic-damage model for cyclic loading of concrete structures, ASCE Journal of engineering mechanics 124(8), 892-900

Lemaitre, J. and Chaboche J. L., 1990, Mechanics of solid materials, Cambridge University Press, Cambridge

Lemaitre, J., 1971, Evaluation of dissipation and damage in metals, Proc. I.C.M. Kyoto, Japan, Vol. 1

Lemaitre, J., 1992, A course on damage mechanics, Springer Verlag

Li, Q., and Ansari, F., 1999, Mechanics of damage and constitutive relationships for high-strength concrete in triaxial compression, ASCE Journal of engineering mechanics 125(1), 1-10

Lowes, N.L., 1999, Finite Element Modeling of Reinforced Concrete Beam-Column Bridge Connections, PhD dissertation, University of California, Berkeley, U.S.A.

Luccioni, B., Oller, S., and Danesi, R., 1996, Coupled plastic-damaged model, Comput. Methods Appl. Mech. Engrg 129, 81-89

Massart, T.J., 2003, Multi-scale modeling of damage in masonry structure, PhD dissertation, Technical University of Eindhoven, Eindhoven, The Netherlands

Maugin, G.A., 1990, Internal variables and dissipative structures, J. Non-Equilib Thermodyn. 15 (2), 173-192

Maugin, G.A., 1992, The Thermodynamics of Plasticity and Fracture, Cambridge University Press, Cambridge

May, I.M., and Duan, Y., 1997, A local arc-length procedure for strain softening, Computers & Structures 64(1-4), 297-303

Mazars, J., and Pijaudier-Cabot, G., 1989, Continuum damage theory-Application to concrete, ASCE Journal of Engineering Mechanics 115(2), 345-365

Meftah, F., and Reynouard, J.M., 1998, A multilayered mixed beam element in gradient plasticity for the analysis of localized failure modes, Mech. Cohes.-Frict. Mater. 3, 305-322

Meschke, G., Lackner, R., and Mang, H.A., 1998, An anisotropic elastoplastic-damage model for plain concrete, International journal for numerical methods in engineering 42, 703-727

Mills, L.L., and Zimmerman, R.M., 1970, Compressive strength of plain concrete under multiaxial loading conditions, ACI Materials Journal 67(10), 802-807

Murakami, S., and Kamiya, K., 1997, Constitutive and damage evolution equations of elastic-brittle materials based on irreversible thermodynamics, Int. J. Mech. Sci. 39(4), 473-486

Nechnech W., 2000, "Contribution a l'etude numerique du comportement du beton et des structures en beton arme soumises a des solicitations thermique et mecaniques

couplees: une approche thermo-elasto-plastique endommageable" These de doctorat, L'institut national des sciences appliqués de Lyon, France

Nedjar, B., 2001, Elastoplastic-damage modelling including the gradient of damage: formulation and computational aspects, Int. J. Solids Structures 38, 5421-5451

Nguyen, G.D., 2002, Constitutive modelling of concrete, First year report, Department of Engineering Science, Oxford University

Nguyen, G.D., and Houlsby, G.T., 2004, A thermodynamic approach to constitutive modelling of concrete, Proceedings of the 12th conference, Association for Computational Mechanics in Engineering (ACME-UK), Cardiff, U.K.

Nooru-Mohamed, N.B., Schlangen, E., and Van Mier, J.G.M., 1993, Experimental and numerical study on the behavior of concrete subjected to biaxial tension and shear, Advanced cement based materials 1(1), 22-37

Ohmenhauser, F., Weihe, S., and Kroplin, B., 1999, Algorithmic implementation of a generalized cohesive crack model, Computational Materials Science 16, 294-306

Ohtani, Y., and Chen, W.F., 1988, Multiple hardening plasticity for concrete materials, ASCE journal of engineering mechanics 114(11), 1890-1910

Ortiz, M., 1985, A constitutive theory for the inelastic behavior of concrete, Mechanics of Materials 4, 67-93

Ottosen N.S., 1977, A failure criterion for concrete, ASCE Journal of engineering mechanics 103(4), 527-535

Palaniswamy, R., and Shah, S.P., 1974, Fracture and stress-strain relationship of concrete under triaxial compression, ASCE Journal of structural mechanics 100(5), 901-915

Peerlings, R.H.J., 1999, Enhanced damage modelling for fracture and fatigue, PhD dissertation, Eindhoven University of Technology, Eindhoven, The Netherlands

Peerlings, R.H.J., de Borst, R., Brekelmans, W.A.M., and de Vree J.H.P., 1996, Gradient enhanced damage for quasi-brittle materials, Int. J. Num. Meth. Eng. 39, 3391-3403

Peerlings, R.H.J., de Borst, R., Brekelmans, W.A.M., and Geers, M.G.D., 1998, Gradient enhanced damage modelling of concrete fracture, Mech. Cohes-Frict. Mater. 3, 323-342

Perdikaris, P.C., and Romeo, A., 1995, Size effect on fracture energy of concrete and stability issues in three-point bending fracture toughness testing, ACI Materials Journal 92(5), 483-496

Petersson, P.E., 1981, Crack growth and development of fracture zones in plain concrete and similar materials, Report TVBM-1006, Div. of Build. Mat., Lund Institute of Technology, Lund, Sweden.

Pijaudier-Cabot , G., and Bazant, Z.P., 1987, Nonlocal damage theory, ASCE Journal of Engineering Mechanics 113(10), 1512-1533

Planas, J., and Elices, M., 1990, Fracture criteria for concrete: mathematical approximation and experimental validation, Engineering fracture mechanics 35, 87-94

Polizzotto, C., 2003, Gradient elasticity and nonstandard boundary conditions, Int. J. Solids Structures 40, 7399-7423

Polizzotto, C., and Borino, G., 1998, A thermodynamics-based formulation of gradient-dependent plasticity, European Journal of Mechanics A/Solids 17, 741-761

Polizzotto, C., Borino, G., and Fuschi, P., 1998, A thermodynamically consistent formulation of nonlocal and gradient plasticity, Mechanics Research Communication 25(1), 75-82

Puzrin, A.M., and Houlsby, G.T., 2001, Fundamental of kinematic hardening hyperplasticity, Int. J. Solids Structures 38, 3771-3794

Que, N.S., and Tin-loi, F., 2002, An optimization approach for indirect identification of cohesive crack properties, Computers and Structures 80, 1383-1392

Ragueneau, F., La Borderie, C., and Mazars, J., 2000, Damage model for concrete-like materials coupling cracking and friction, contribution towards structural damping: first uniaxial applications, Mech. Cohes-Frict. Mater. 5, 607-625

Ramtani, S., 1990, Contribution a la modelisation du comportment multiaxial du beton endommage avec description du caractere unilateral, These de Genie Civil, Universite de Paris 6, E.N.S. de Cachan, France

Reinhardt, H., Cornelissen, H.A.W., and Hordjil, D.A., 1986, Tensile tests and failure analysis of concrete, ASCE journal of Structural Engineering 112(11), 2462-2477

Rice, J.R., 1976, The localization of plastic deformation, in Theoretical and applied mechanics, W.T. Koiter ed., North-Holland Publishing company

Riks, E., 1979, An incremental approach to the solution of snapping and buckling problems, Int. J. Solids Structures 15, 529-551

RILEM, 1985, Determination of the fracture energy of mortar and concrete by means of three-point bend tests on notched beams: TC-50-FMC, fracture mechanics of concrete, RILEM recommendation, Mat. And Struct. 18(106), Paris, France

Rocco, C., Guinea, G.V., Planas, J., and Elices, M., 1995, The effect of the boundary conditions on the cylinder splitting strength, Fracture Mechanics of Concrete Structures, Proceedings FRAMCOS-2, Ed. by Folker H. Wittmann, AEDIFICATIO Publishers, D-79104 Freiburg

Rocco, C., Guinea, G.V., Planas, J., and Elices, M., 2001, Review of splitting-test standards from a fracture mechanics point of view, Cement and concrete research 31, 73-82

Rots, J.G., Nauta, P., Kusters, G.M.A., Blaauwendraad, J., 1985, Smeared crack approach and fracture localization in concrete, Heron 30 (1), Stevin laboratory, Delft University of Technology, Delft, The Netherlands

Salari, M. R., Saeb, S., Willam, K. J., Patchet, S. J., and Carrasco, R. C., 2004, A coupled elastoplastic damage model for geomaterials, Comput. Methods Appl. Mech. Engrg 193(27-29), 2625-2643

Saleh, A.L., and Aliabadi, M.H., 1995, Crack growth analysis in concrete using boundary element method, Engineering fracture mechanics 51(4), 533-545

Santaoja, K., 2000, Thermomechanical formulation for the gradient theory, VII Finish Mechanics Day, Tampere University of Technology, Tampere, Finland, May 25-26, 113-123

Sfer, D., Carol, I., Gettu, R., and Etse, G., 2002, Study of the behaviour of concrete under triaxial compression, ASCE Journal of Engineering Mechanics 128 (2), 156-163

Shah, S.P., and Chandra S., 1968, Critical stress volume change and microcracking in concrete, ACI Journal 65(9), 770-781

Shao, J.F., Chiarelli, A.S., and Hoteit, N., 1998, Modeling of coupled elastoplastic damage in rock materials, Int. J. Rock Mech. Miner. Sci. 35(4-5), paper 115

Shi C., 2004, Tensile tests with offset double notched specimens, Personal communication.

Shi C., van Dam, A.G., van Mier, J.G.M., Sluys, L.J., 2000, Crack interaction in concrete, Wittmann, F.H. editor: Materials for Buildings and Structures EUROMAT, vol. 6, Weinheim, Germany: Wiley-VCH Verlag, 125-131

Simo, J.C., 1989, Strain softening and dissipation: a unification of approaches, in Cracking and damage – strain localization and size effect, ed. by J. Mazars and Z.P. Bazant, Elsevier, London and Newyork, 440-461

Simo, J.C., and Ju, J.W., 1987, Strain- and stress-based continuum damage models – I. Formulation, Int. J. Solids Struct. 23(7), 821-840

Simo, J.C., and Ju, J.W., 1987, Strain- and stress-based continuum damage models – II. Computational aspects, Int. J. Solids Struct. 23(7), 841-869

Sluys, L.J., 1992, Wave propagation, localization and dispersion in softening solids, PhD dissertation, Delft university of technology, Delft, the Netherlands

Smit, R.J.M., Brekelmans, W.A.M., and Meijer, H.E.H., 1998, Prediction of the mechanical behaviour of non-linear heterogeneous systems by multi-level finite element modelling, Comput. Methods Appl. Mech. Engrg. 155, 181–192

Tijssens, M.G.A., Sluys B.L.J., van der Giessen, E., 2000, Numerical simulation of quasi-brittle fracture using damaging cohesive surfaces, Eur. J. Mech. A/Solids 19, 761-779

Tin-loi, F., and Que, N.S., 2001, Parameter identification of quasibrittle materials as a mathematical program with equilibrium constraints, Comput. Methods Appl. Mech. Engrg. 190, 5819-5836

Ung-Quoc, H., 2003, Theorie de degradation du beton et developpement d'un nouveau modele d'endommagement en formulation incrementale tangente – Calcul a la rupture appliqué au cas des chevilles de fixation ancrees dans le beton, PhD dissertation, L'ecole nationale des ponts et chausses, France

Valanis, K.C., 1985, On the uniqueness of solution of the initial value problem in softening materials, ASME Journal of applied mechanics 52, 649-653

Van Mier, J.G.M., 1984, Complete stress-strain behavior and damaging status of concrete under multiaxial conditions, RILEM-CEB-CNRS, International conference on concrete under multiaxial conditions, Vol. 1, Presses de l'Universite Paul Sabatier, Toulouse, France, 75-85

Van Mier, J.G.M., 1986, Fracture of concrete under complex stress, Heron 31(3), 1986, Delft University of Technology, Delft, The Netherlands

Vardoulakis, I., 1999, 2nd gradient constitutive models, In Constitutive modelling of granular materials, Dimitrios Kolymbas (Ed.), Springer-Verlag, 225-248

Vonk, R.A., 1992, Softening of concrete loaded in compression, PhD dissertation, Delft university of technology, The Netherlands

Walsh, S.D.C., and Tordesillas, A., 2004, A thermomechanical approach to the development of micropolar constitutive models of granular media, Acta Mechanica 167(3–4), 145–169

Weihe, S., Kroplin, B., and De Borst, R., 1998, Classification of smeared crack models based on material and structural properties, Int. J. Solids Struct. 35(12), 1289-1308

Willam, K.J., and Warnke E.P., 1975, Constitutive model for the triaxial behavior of concrete, International association of bridge ans structural engineers, Seminar on concrete structure subjected to triaxial stresses, paper III-1, Bergamo, Italy, May 1974, IABSE Proc. 19

Yang, Z.J., and J., Chen, 2004, Fully automatic modeling of cohesive discrete crack propagation in concrete beams using local arc-length methods, Int. J. Solids Struct. 41, 801-826

Yang, Z.J., and Proverbs, D., 2004, A comparative study of numerical solutions to non-linear discrete crack modeling of concrete beams involving sharp snap-back, Engineering fracture mechanics 71, 81-105

Yazdani, S., and Schreyer, H.L., 1988, An anisotropic damage model with dilatation for concrete, Mechanics of Materials 7(3), 231-244

Yazdani, S., and Schreyer, H.L., 1990, Combined plasticity and damage mechanics model for plain concrete, ASCE Journal of Engineering Mechanics 116(7), 1435-1450

Yin, W.S., Su, E.C.M., Mansur, M.A., and Hsu, T.T.C, 1989, Biaxial tests of plain and fiber concrete, ACI Materials Journal 86(3), 236-243

Zhao, J., Sheng, D., and Zhou, W., 2005, Shear banding analysis of geomaterials by strain gradient enhanced damage model, Int. J. Solids Struct., article in press

Ziegler, H., 1983, An introduction to thermomechanics, 2nd Ed., North Holland, Amsterdam